# Aeroelastic Analysis of Wind Turbine Smart Blades Utilising Multiple Control Surfaces

Terence Macquart

PhD

2014

# Aeroelastic Analysis of Wind Turbine Smart Blades Utilising Multiple Control Surfaces

Terence Macquart

A thesis submitted in partial fulfilment of the requirements of the
University of Northumbria at Newcastle
for the degree of
Doctor of Philosophy

Research undertaken in the school of
Mechanical and Construction Engineering

October 2014

# Abstract

The aeroelastic control of wind turbine blades employing active flow controllers is part of an ongoing research effort aiming to alleviate blade loads. Over the past years, the growing body of literature has confirmed the preliminary potential of active flow controllers and, in particular, of control surfaces in relieving wind turbine fatigue and extreme loads. The aim of present research is to investigate the feasibility, design and capability of a multi-component aero-structural load control system utilising light control surfaces such as trailing edge flaps and microtabs. This is achieved through the design of load alleviation control systems, and a detailed understanding of the aeroelastic dynamic of wind turbine blades equipped with control surfaces.

As part of this research, a Wind Turbine Aeroelastic Control (WTAC) simulator has been developed. WTAC is the combination of an unsteady aerodynamic module, a structural finite element analysis module, and a control module incorporating the aerodynamic models of control surfaces. The aeroelastic study of the NREL 5MW wind turbine whose blades are equipped with trailing edge flaps and microtabs is carried out using WTAC.

The prime contributions of this research are threefold:

(i) The development and validation of models describing the steady state and dynamic responses of microtabs and trailing edge flaps deploying on wind turbine aerofoils.

(ii) The detailed examination of the wind turbine control system designs which revealed that: (a) both continuous and discontinuous actuation mechanisms can efficiently be used for load alleviation. (b) Two or more Pitot tubes and strain gauges sensors distributed along the blades spans are necessary for wind and state estimations. It also showed that (c) the optimal location of active flow controllers along the blade span is strongly dependent on the chord distribution. In addition, it was found that (d) the control system load alleviation capability does not increase linearly with the number of active flow controller but is limited due to its destabilising effect on the controlled blades.

(iii) The characterisation of the wind turbine blade load alleviation problem as a loop-shaping control problem. The proposed loop-shaping approach revealed that the vibrating aeroelastic dynamic of wind turbine blades is critical for designing dedicated load alleviation control systems. Most importantly, it was demonstrated that the multi-input multi-output control problem of wind turbine blades equipped with multiple control surfaces could be decoupled into single-input single-output control problems.

# Table of Contents

# List of Figures

# List of Tables

# List of Algorithms

# Nomenclature

| | |
|---|---|
| $a$ | Axial Induction Factor |
| $a'$ | Tangential Induction Factor |
| [A] | State Matrix |
| [B] | Input Matrix |
| [C] | Output Matrix |
| [D] | Damping Matrix |
| [Dd] | Disturbance Matrix |
| [K] | Stiffness Matrix |
| [M] | Mass Matrix |
| $A_r$ | Wind Turbine Rotor Area |
| $B$ | Wind Turbine Number of Blades |
| $B_M$ | Microtab Input Matrix |
| c | chord length |
| $C_D$ | Drag Coefficient |
| $C_L$ | Lift Coefficient |
| $C_{L,0}$ | Linear lift coefficient under fully attached flow |
| $C_{L,d}$ | Dynamic Lift Coefficient |
| $C_{L,ss}$ | Steady State Lift Coefficient |
| $C_{L0,d}$ | Dynamic Linear Lift Coefficient |
| $C_P$ | Power Coefficient |
| $C_P$ | Pressure Coefficient |
| $C_{P,opt}$ | Optimal Power Coefficient |
| $C_T$ | Thrust Coefficient |
| D | Drag Force |
| $dr$ | Wind Turbine Blade Segment Size |
| E | Elastic Modulus |
| EI | Bending Stiffness |
| $f$ | Aerofoil Attachment Degree |
| F | Force Vector |
| $F_N$ | Normal Force |
| $F_T$ | Tangential Force |
| $H_M$ | Microtab Maximal Deployment Height |
| $I$ | Moment of Inertia |
| I | Area Moment of Inertia |
| iseg | Segment Number |
| $K_D$ | Derivative Gain |
| $K_I$ | Integral Gain |
| $K_P$ | Proportional Gain |
| $L$ | Finite Element Length |
| L | Lift Force |
| $M$ | Finite Element Mass |
| $M_i$ | Nodal Moment |
| $M_s$ | Mode Shapes |
| $N_i$ | Shape Functions |
| Nsec | Numbers of Section used in Steady BEMT |
| Nseg | Numbers of Segments used in BEMT |
| $P$ | Power |
| $P_{gen}$ | Power Generator |
| $P_L$ | System Plant |
| $P_{mech}$ | Wind Turbine Mechanical Power |
| $P_{wind}$ | Wind Power |
| $q$ | Dynamic Pressure |

| | |
|---|---|
| Q | Modal Coordinate Vector |
| r | Blade Radial Coordinate |
| R | Blade Radius |
| Re | Reynolds Number |
| $r_f$ | Relaxation Factor |
| $T$ | Normalised Time |
| t | Time |
| $T_{Aero}$ | Aerodynamic Torque |
| $T_{deploy}$ | Microtab Normalised Deployment Time |
| $T_{Gen}$ | Generator Torque |
| $V_\infty$ | Wind Speed |
| $V_{axial}$ | Axial Wind Speed |
| $V_e$ | Eigenvector Matrix |
| $V_i$ | Nodal Shear Force |
| $V_{rel}$ | Relative Wind Speed |
| $V_{tan}$ | Tangential Wind Speed |
| $w$ | Nodal Displacement |
| X | Rotational Plane Downwind Axis |
| X | State Vector |
| Y | Output Vector |
| Y'Z' | Rotational Plane |
| YZ | Original Rotor Plane (no cone, no tilt, no yaw angles) |
| $z$ | Trailing Edge Flap Model Aerodynamic Variable |

## Subscript

| | |
|---|---|
| A | Augmented |
| Ae | Aeroelastic |
| d | Dynamic Structure |
| ds | Dynamic Stall |
| edge | Edgewise |
| F | Trailing Edge Flap |
| flap | Flapwise |
| Fr | Reduced Trailing Edge Flap |
| ip | In-plane |
| M | Microtab |
| oop | Out-of-Plance |
| q | Modal |
| qr | Reduced Modal |

## Greek Symbols

| | |
|---|---|
| ϕ | Beam Plane Angle |
| $u_{beam}$ | Beam Axial Displacement |
| $w$ | Beam Transversal Displacement |
| α | Angle of Attack |
| $\alpha_0$ | Zero Lift Angle of Attack |
| $\beta$ | Blade Pitch and Pretwist Angle |
| $\gamma$ | Yaw Angle |
| $\gamma_f$ | Filter Dynamic Parameter |
| $\Delta C_{D,ss}$ | Steady State Drag Coefficient Generated by a Control Surface |
| $\Delta C_L$ | Dynamic Lift Coefficient Generated by a Control Surface |
| $\Delta C_{L,ss}$ | Steady State Lift Coefficient Generated by a Control Surface |
| $\Delta C_{L,v}$ | Dynamic Lift Coefficient Generator by Leading Edge Vortex |
| $\delta_F$ | Trailing Edge Flap Deployment Angle |
| $\delta_F$ | Trailing Edge Flap Quasi-Steady Deployment Angle |

| | |
|---|---|
| $\delta_M$ | Microtab Deployment Height |
| $\eta$ | Tilt Angle |
| $\theta$ | Blade Pitch Angle |
| $\theta_d$ | Dynamic Flow Separation Angle |
| $\theta_{pt}$ | Blade Pretwist Angle |
| $\theta_s$ | Aerofoil Flow Separation Angle |
| $\lambda$ | Tip Speed Ratio |
| $\lambda_{opt}$ | Optimal Tip Speed Ratio |
| $\rho$ | Air Density |
| $\Phi$ | Inflow Angle |
| $\Psi$ | Azimuth Angle |
| $\omega_{gen}$ | Generator Angular Speed |
| $\omega_{rot}$ | Wind Turbine Rotor Angular Speed |

## Abbreviations

| | |
|---|---|
| 1*N* | First Natural Frequency |
| 2*N* | Second Natural Frequency |
| 1*P* | First Rotational Frequency |
| 2*P* | Second Rotational Frequency |
| 3*P* | Third Rotational Frequency |
| AFC | Active Flow Controller |
| ATEG | Adaptive Trailing Edge Geometry |
| BB | Bang-Bang |
| BEMT | Blade Element Momentum Theory |
| BP | Band-Pass |
| C | Controller |
| CAA | Convergence Accelerator Algorithm |
| CFD | Computational Fluid Dynamics |
| COE | Cost of Energy |
| CS | Control Surface |
| DOF | Degree of Freedom |
| FE | Finite Element |
| GDP | Gross Domestic Product |
| GWEC | Global Wind Energy Council |
| GWEO | Global Wind Energy Outlooks |
| HP | High-Pass |
| *IP* | In-Plane |
| IPC | Individual Pitch Control |
| LP | Low-Pass |
| LQR | Linear Quadratic Regulator |
| MEM | Micro-electro-mechanical |
| MIMO | Multi-Input Multi-Output |
| MPC | Model Predictive Control |
| MT | Microtabs |
| MWR | Method of Weighted Residual |
| N*P* | N-th Rotational Frequency |
| NREL | National Renewable Energy Laboratory |
| ODE | Ordinary Differential Equation |
| *OOP* | Out-of-Plane |
| PC | Pitch-Controlled |
| PD | Proportional Derivative |
| PDE | Partial Differential Equation |
| PID | Proportional Integral Derivative |
| PSD | Power Spectrum Density |
| R | Rotor Radius |

| | |
|---|---|
| RMS | Root Mean Square |
| RPM, rpm | Rotation Per Minute |
| SISO | Single-Input Single-Output |
| SMA | Shape Memory Alloys |
| SMC | Sliding Mode Controller |
| SR | Stall-Regulated |
| TEF | Trailing Edge Flap |
| UAV | Unmanned Aerial Vehicle |
| VS | Variable-Speed |
| VS-PC | Variable-Speed Pitch-Controlled |
| WTAC | Wind Turbine Aeroelastic Control |

# Acknowledgment

Foremost, I would like to express my sincere gratitude to my principal supervisor Dr. Alireza Maheri for his support and guidance throughout my PhD. His knowledge and experience have been of great values and this, I am sure, will continue to serve me well in the future.

My sincere thanks also go to Professor Krishna Busawon and Professor Mohamed Djemai for their advices and guidance during this research.

Last but not the least I would like to thank all my relatives and friends that have supported me during these three years.

# Declaration

I declare that the work contained in this thesis has not been submitted for any other award and that it is all my own work. I also confirm that this work fully acknowledges opinions, ideas and contributions from the work of others.

Word Count: 46,137

Name: Terence Macquart

Signature:

Date: 17 October 2014

# 1. Introduction

## 1.1 Structure of the Thesis

The first chapter of this thesis is devoted to the background and current state of wind energy. The world-wide wind energy state and the potential outcomes resulting from the enhancements of wind power systems are highlighted. The prime challenges to be faced in order to reduce the cost of wind energy are identified and some of the proposed solutions are presented. The second chapter of this thesis is dedicated to the development of a wind turbine unsteady aerodynamic module. The steady state and dynamic modelling of active flow controllers, namely microtab and trailing edge flap, are presented in Chapter 3. Chapter 4 details the structural and aeroelastic model of wind turbine blades. A finite element code is developed and benchmarked. The control analysis of wind turbine blades equipped with active flow controllers is carried out in Chapter 5. The locations and types of sensors required for the load alleviation of wind turbine blades employing active flow controllers are also investigated. Chapter 6 presents the wind turbine blade load alleviation results. The optimal location of active flow controllers and the closed-loop control designs are examined. The efficiencies of several closed-loop control designs for load alleviation are evaluated. Finally, Chapter 7 summarises the overall research work, the results obtained, the findings, and the contributions. It also includes a critical appraisal of the work and suggested future developments.

## 1.2 Background

The last 15 years have seen a substantial amount of effort being invested into the research and development of renewable energy technologies (Turner, 1999, Nema et al., 2009, Liserre et al., 2010). In one form or another, green energies are available virtually everywhere. Moreover, with the foreseen increasing instability of the fuel market the renewable energy market price stability is certainly attractive (Kaminsky and Schmukler, 2002). While this market has been undergoing substantial growth, the future of green energy highly depends on technological advances as well as political and economic support (Changliang and Zhanfeng, 2009).

In an effort to predict the future of wind energy and provide a recognised planning tool for the power sector, the Global Wind Energy Council (GWEC) and Greenpeace International have released the Global Wind Energy Outlooks (GWEO) (Greenpeace and the Global Wind Energy Council, 2010, Greenpeace and the Global Wind Energy Council, 2012). Three major markets, namely Europe, North America, and Asia have dominated the global wind power markets for the past several years. Three baseline scenarios including, energy policies, economic market and political support are considered in the GWEO predictions. The first scenario, namely the conservative scenario, takes into account existing policies as well as electricity and gas market reforms. The second or moderate scenario includes all existing and in-progress policies supporting the development of renewable energy. It also assumes that the targets set by many countries, for both reductions of CO2 emissions and wind energy generations, are successfully achieved. The last or advanced scenario refers to the most optimistic ones where industries and politics strongly support the development of wind energy. Projections for the installed cumulative wind power of the three scenarios are shown in Figure 1.1. The conservative scenario features the slowest growth with an average capacity of 20 GW installed per year which corresponds to about 573 GW installed by 2030. As clearly seen in Figure 1.1, there is a significant gap between the conservative predictions and the predictions for the moderate and advanced scenarios. In both the moderate and advanced scenarios, the amount of annually installed wind capacity is shown to increase significantly over the next 20 years (see Figure 1.1). Resulting in a cumulative installed wind capacity of more than two and three times the conservative predictions for 2020 and 2030 respectively.

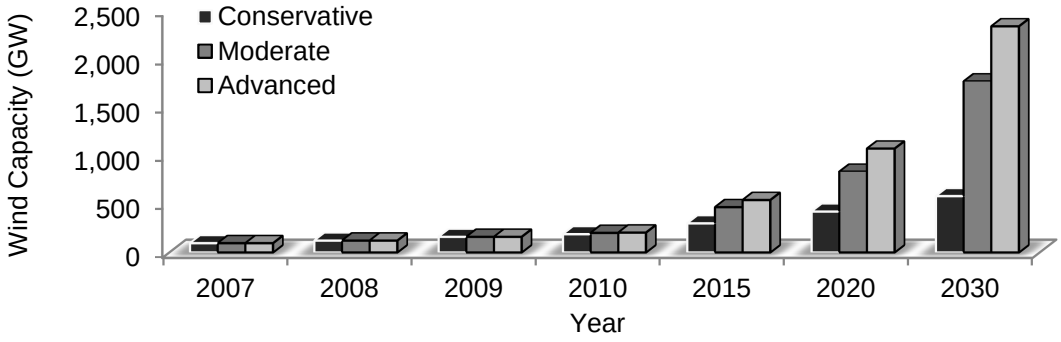


Figure 1.1 - World-wide installed cumulative wind capacity projection
(Greenpeace and the Global Wind Energy Council, 2010)

In addition to the installed cumulative wind capacity, it is also relevant to estimate the share of the wind power energy in the context of the continuously increasing electricity demand (Koomey, 2011). According to the International Energy Agency predictions on GDP (Gross Domestic Product) growth and electricity demand, the GWEO estimates the share of wind energy for electricity generation as presented in Figure 1.2. It can be observed that the wind energy share under the conservative scenario flattens towards 2020 where the number of new annually installed wind energy generation becomes insufficient to overcome the electricity demand growth. On the other hand, the moderate and advanced scenarios predict an increase of the wind energy share with a percentage up to 8% by 2020 and up to 15% by 2030. It is clear that increasing the share of renewable energy as part of the global electricity generation will require significant investments in new power generation to overcome the increasing power demand.

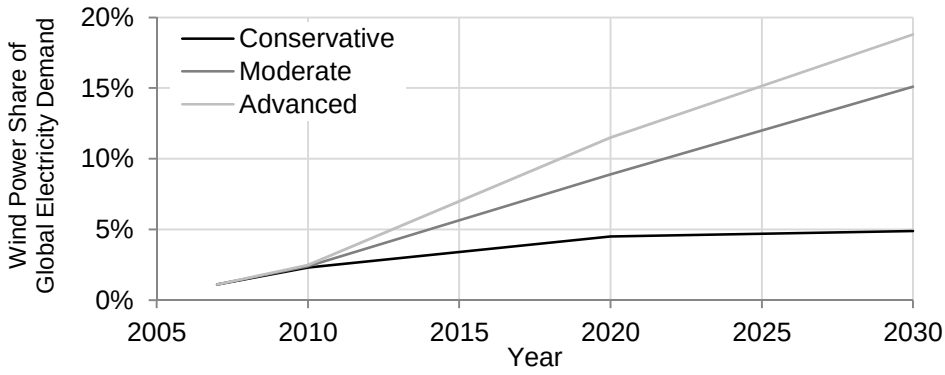


Figure 1.2 - Prediction of the wind energy share of global electricity production
(Greenpeace and the Global Wind Energy Council, 2010)

Considering the significant incoming increase installed wind power capacity according to the GWEC predictions, additional reduction of the cost of energy (COE) could attract substantial levels of investment. The COE is an index used to estimate the profitability of an energy

investment (Maki et al., 2012). The COE takes into account the investment capital and maintenance costs as well as the production and price of energy over the whole system lifespan as shown in Figure 1.3. Several studies summarised by Lantz et al. (Lantz et al., 2012) predict a slow fall of the COE over the next 20 years. However, the rate at which the COE is predicted to fall varies significantly between studies.

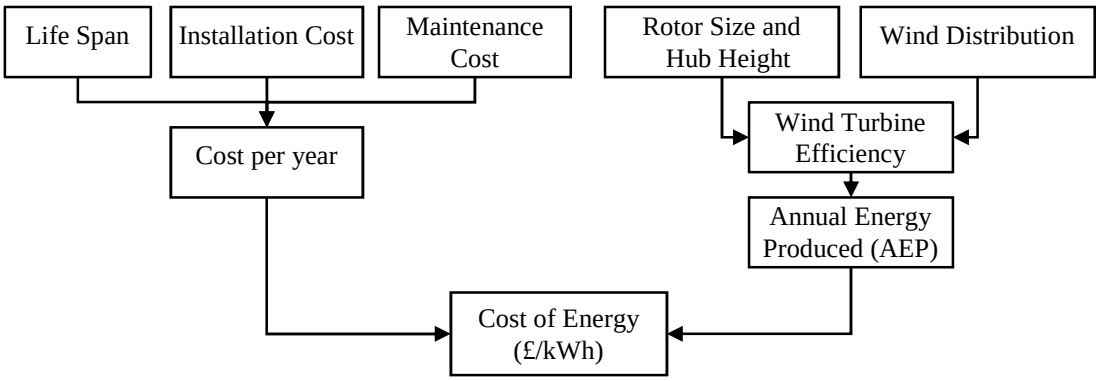


Figure 1.3 - Typical model for determining the cost of wind energy

Reducing the COE of wind technology in order to be competitive with fossil fuels and nuclear power sources is the main research driver towards improving wind turbine designs. The issue of wind energy generation at a reduced cost has led to a rapid increase of wind turbine rotor size. As a result of this increase, wind turbines can harness more regular and significant amount of wind energy. However, the square-cube law shows that as the wind turbines rated power increases proportionally to the square of the blade's radius, the mass increases proportionally to the radius cubed (Veers et al., 2003, Schubel and Crossley, 2012). Scaling up wind turbine designs without technological improvement is therefore ineffective in reducing the COE (Sieros et al., 2012). Figure 1.4 illustrates the power-to-mass ratio scaling with rotor radius (Fingersh et al., 2006). Both arguments, in favour and against increasing wind turbine rotors size, are valid and it is necessary to find a trade-off between the two when designing wind turbines.

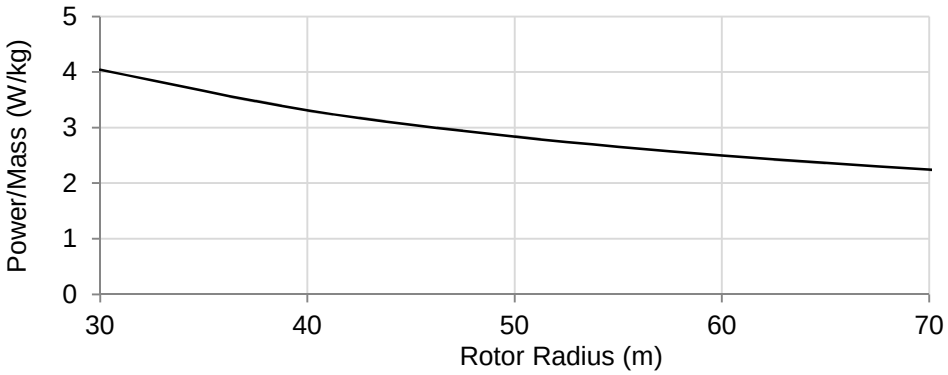


Figure 1.4 - Blade power-to-mass ratio (Fingersh et al., 2006)

Blades, worth about 20% of the total cost of wind turbines (IRENA, 2012), are key aerodynamic and structural components(Sieros et al., 2012). Reducing the blade weight while maintaining the blade high stiffness in order to reduce fatigue and prevent blade failure is critical. Fatigue is due to the cumulative structural damage experienced due to repeated loadings. Wind turbine blades are now so long that the incoming wind conditions vary along each blade (Leishman, 2002). At the same time, the dynamic motion of the blades also changes the airflow conditions by dynamic interaction. These two effects create aerodynamic inputs to the blades' loading, which feed fatigue loads into the blades and into the power train. The increasing loads resulting from wind turbine growth have triggered the investigation of innovative control strategies in order to reduce fatigue and therefore the COE (Barlas and van Kuik, 2010, Barlas and Van Kuik, 2007).

### 1.2.1 Wind Turbine Blade Loads

The power output quality and aero-structural dynamics of wind turbines are influenced by the wind stochastic nature. Figure 1.5 is an example of wind frequency spectrum based on data acquired at the National Laboratory of Brookhaven at New York in 1957. Large time scale variations (i.e. over 10 minutes) are often easily predictable, which is used for predicting the variation of large amounts of power into the electric network. Smaller time scale variations or turbulences do not have a significant effect on average power. Nevertheless, turbulences are responsible for transient aerodynamic forces that feed loads into the mechanical part of the wind turbines and result in fatigue damage. In wind analysis, turbulence refers to an irregular fluctuation of wind speed at a fast time scale typically less than about 10 minutes. The research interest in generating unsteady wind fields peaked during the 90's (Deodatis, 1996, Di Paola, 1998) and turbulence models based on the Von Karman and the Kaimal models are

still used nowadays. Figure 1.6 shows a longitudinal turbulent wind generated using TurbSim (Foley and Gutowski, 2008).

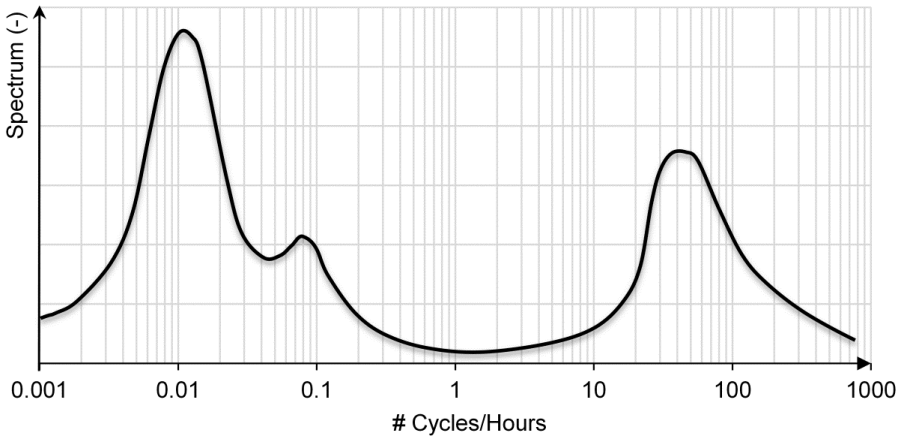


Figure 1.5 - Cleaned experimental wind spectrum (van der Hoven, 1957)

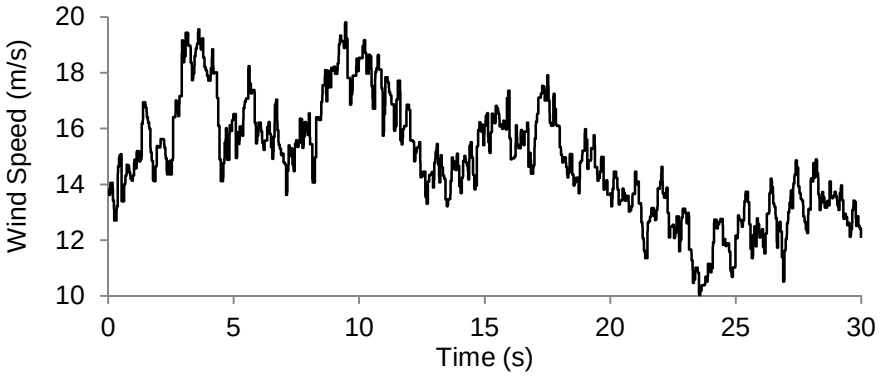


Figure 1.6 - Generated turbulent wind (15m/s mean wind speed) (Foley and Gutowski, 2008)

Despite the stochastic nature of turbulence, the primary wind turbine blade loads caused by the blades' cyclic motions in a non-axisymmetric wind field are mostly periodic. That is, the changes in velocity and load caused by the cyclic motion are often greater than stochastic changes (Castaignet et al., 2014). For instance, the ground produces friction forces that delay the winds in the lower atmospheric layers creating a wind gradient also referred to as wind shear (Figure 1.7). As a wind turbine blade sweeps up and down, it experiences a cyclic wind speed variation resulting in cyclic loadings (Figure 1.8). A list of the loads experienced by wind turbine blades is given in Figure 1.9.

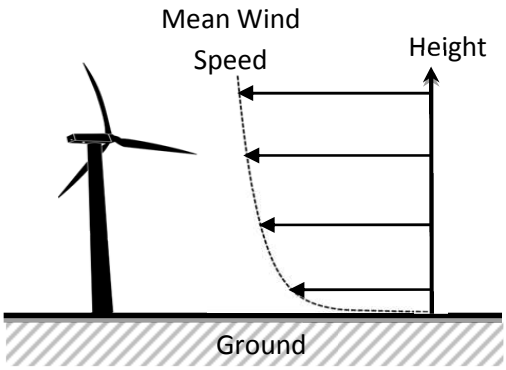


Figure 1.7 - Wind shear illustration

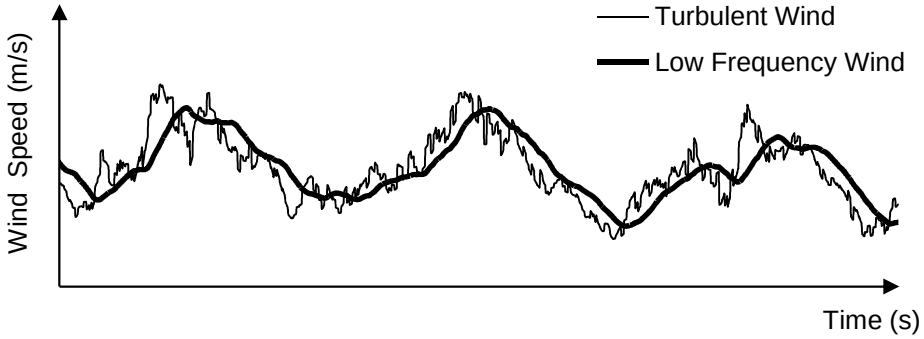


Figure 1.8 - Typical wind speed experienced along the span of a rotating wind turbine blade simulated using the Von Karman model (Foley and Gutowski, 2008)

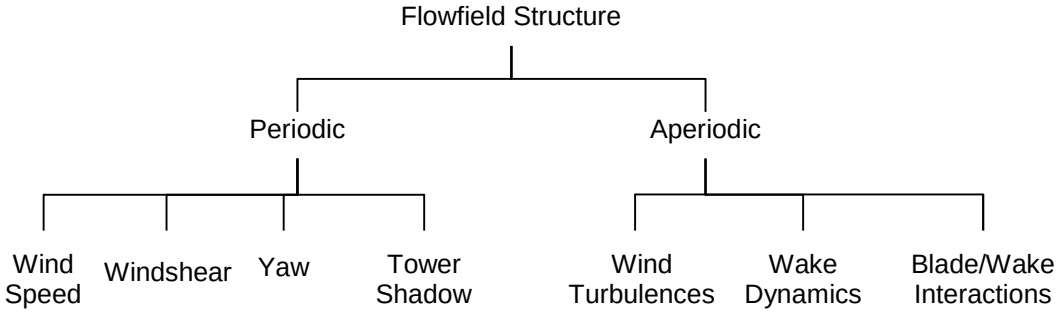


Figure 1.9 - Sources of wind turbine unsteadiness (Leishman, 2002)

Cyclic loads are so substantial that the frequency spectrum of the loads experienced by a wind turbine blade features characteristic peaks at the wind turbine rotational frequency (1*P*) and higher harmonics (2*P*, 3*P*, *NP*) as illustrated in Figure 1.10.

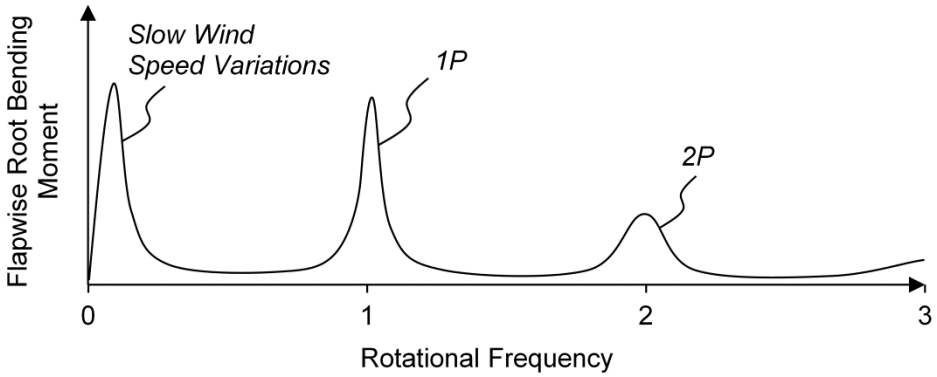


Figure 1.10 - Typical flapwise wind turbine blade root bending moment frequency spectrum (without mean value)

Over time the damage due to the repeated blade loads (i.e. fatigue) causes the material to show microscopic cracks which grow until failure occurs. Since increasing wind turbine rotor size causes greater fatigue loads, there is a major challenge in supporting rotor size growth while ensuring that the blade fatigue does not result in failure. S-N curves are generally used to estimate the structural damage caused by blade loads as shown in Figure 1.11. S-N curves link the magnitude of a cyclic stress (S) against its number of cycles before failure occurs (N). According to the S-N curve fatigue calculation, it is clear that decreasing the load amplitudes will result in lifespan increases.

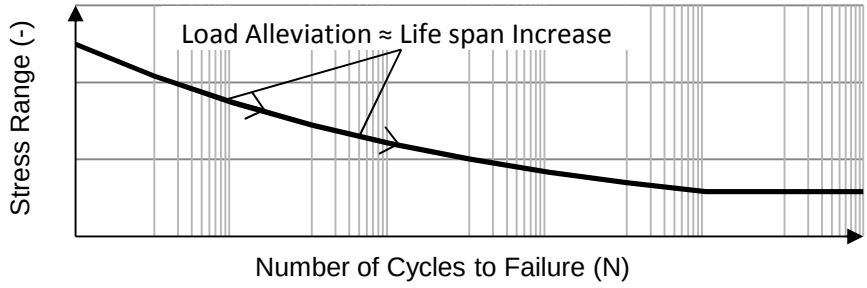


Figure 1.11 - Typical SN curve

The prime idea behind the active load alleviation of wind turbine blades is to employ control devices in order to reduce the blades loads and therefore increase the blades' life span. Research has shown that the blade loads can be reduced by employing load control techniques such as individual pitch control (Bossanyi, 2003, Larsen et al., 2005, van Engelen, 2006) and control surfaces (Andersen, 2005, Johnson et al., 2010, Mayda et al., 2005). Control surfaces (CSs) are deployable structures installed on wind turbine blades capable of modifying the flow kinematics locally. Advantageous features in terms of modularity, cost, size, and response time have led to a growing research interest in employing CSs for load alleviation of wind turbine blades. However, unsteady applications on wind turbine blades are

still at an experimental level (Johnson et al., 2010, Castaignet et al., 2013, Thill et al., 2010). A non-exhaustive list of wind turbine blade load alleviation techniques is given in Figure 1.12.

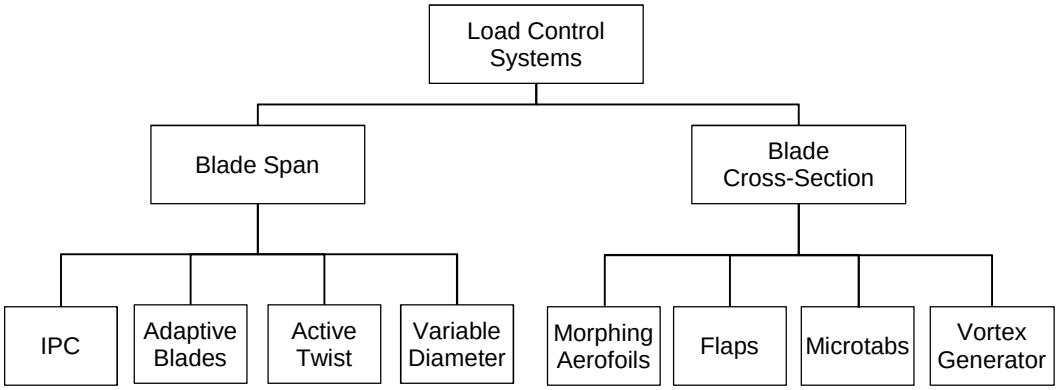


Figure 1.12 - Non-exhaustive list of devices and techniques for wind turbine blade load alleviation

### 1.2.2 Wind Turbine Control Systems

The wind turbine operating modes are divided into four regions (Laks et al., 2009) as shown in Figure 1.13. No energy is generated in the first region. The rotation starts at the beginning of the second region when the mean wind speed exceeds the cut-in wind speed (e.g. 3m/s). At low wind speeds (e.g. 3-11m/s), the extractable wind energy is lower than the generator nominal power. In this region the wind turbine may be controlled to maximise power generation (Bottasso et al., 2012). As the wind speed increases, the wind turbine power increases until rated wind speed and power are reached. The wind turbine then enters in the third operating region in which it is controlled in order to maintain rated power and limit aerodynamic forces. The control, either passive or active, forces the blades into less aerodynamically efficient operating conditions. By doing so the driving aerodynamic force (i.e. lift) decreases. Finally, when the mean wind speed reaches the wind turbine cut-out wind speed threshold (e.g. 25 m/s) the wind turbine is shut-down to avoid damage. The main wind turbine control system's aims are to maximise the power extraction over the operating region 2 and to maintain power at nominal in region 3. Well-known control techniques such as variable speed and collective pitch control are now standards for multi-megawatt modern wind turbines (Zhang et al., 2008, Muljadi and Butterfield, 2001).

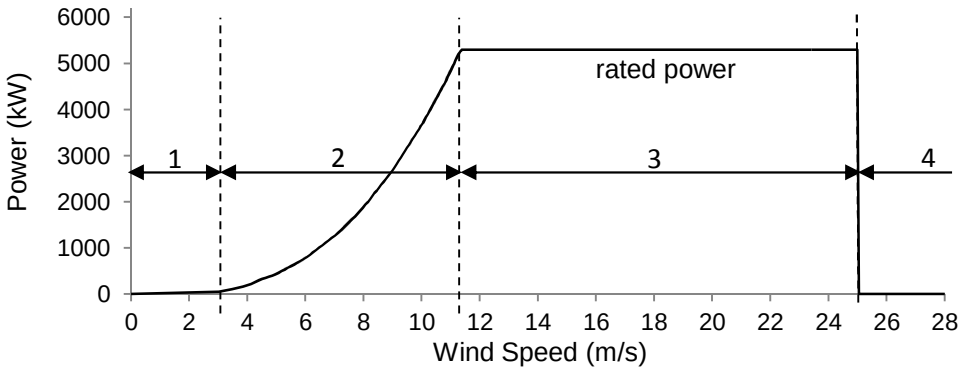


Figure 1.13 - Wind turbine operating regions example (Jonkman et al., 2009)

The power coefficient ($C_p$) of a wind turbine reflects its efficiency in converting wind energy (Schubel and Crossley, 2012). The wind turbine power coefficient is calculated as the wind turbine mechanical power ($P_{mech}$) over the total amount of available wind power ($P_{wind}$) as in Equation (1.1). The wind turbine power can be calculated as a function of the power coefficient, rotor area $A_r$, air density $\rho$ and freestream velocity $V_\infty$ as shown in Equation (1.2).

$$C_P = \frac{P_{mech}}{P_{wind}} \tag{1.1}$$

$$P_{mech} = C_P \frac{1}{2} \rho A_r V_\infty^3 \tag{1.2}$$

### 1.2.3 Passive Load Control - Stall-Regulated Wind Turbines

Blades of stall-regulated wind turbines are designed to enter stall after rated wind speed in order to limit power generation (Bang et al., 2007, Merz, 2011). Static stall describes a reduction of the lift force generated by an aerofoil as the angle of attack quasi-steadily increases above a critical value. When the angle of attack reaches its critical value, the flow separates from the aerofoil surface as shown in Figure 1.14. As the wind speed increases, blades progressively enter into stall as illustrated in Figure 1.15.

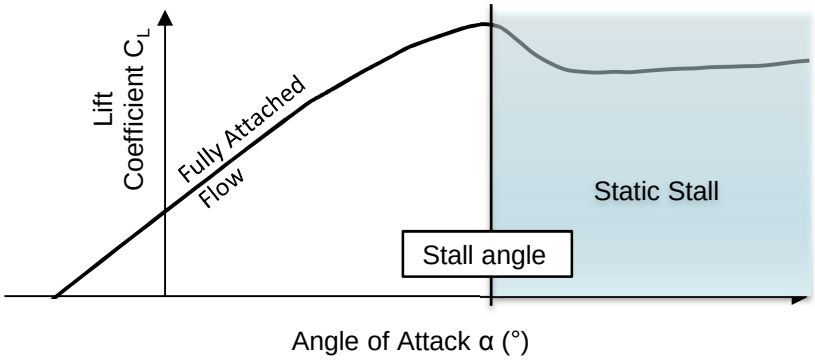


Figure 1.14 - Typical steady state two-dimensional lift curve

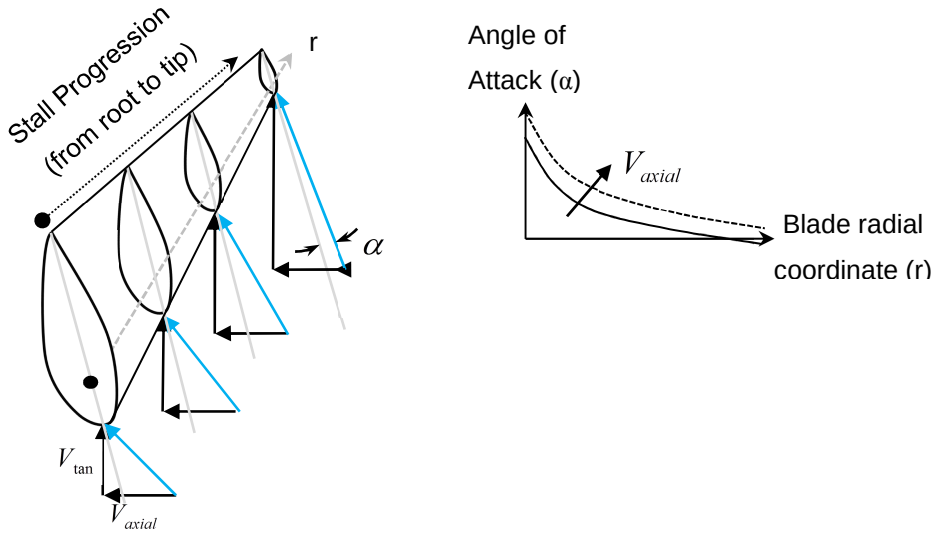


Figure 1.15 - Angle of attack and stall progression along the blade span

The performance of the 300 kW AWT-27 wind turbine design (Poore, 2000) calculated with the steady state BEMT code WTAero (Maheri et al., 2006b) is shown in Figure 1.16. Moreover, the angle of attack distribution along the blade span and the propagation of the stall as the wind speed increases are given in Figure 1.17

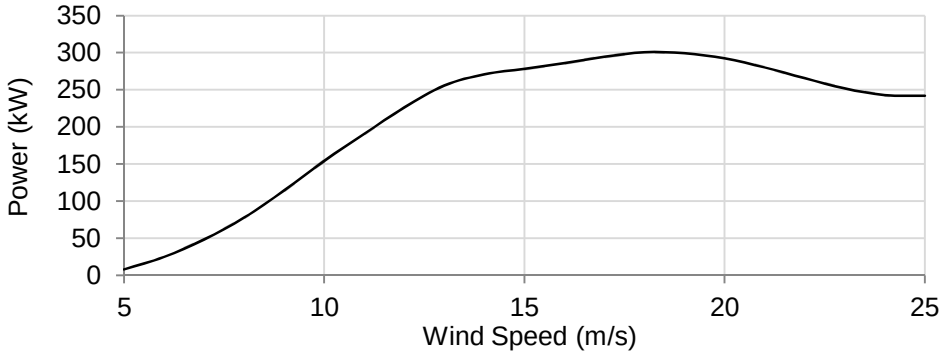


(a)

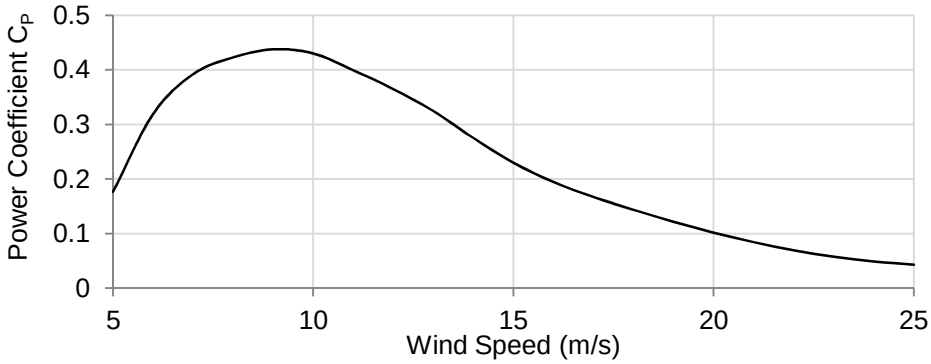


(b)

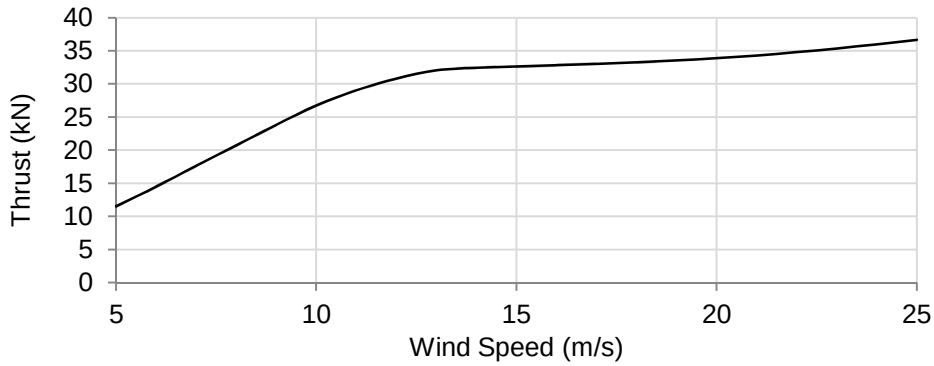


(c)

Figure 1.16 - AWT-27 wind turbine (a) power, (b) power coefficient and (c) thrust as functions of the mean wind speed: generated using WTAero

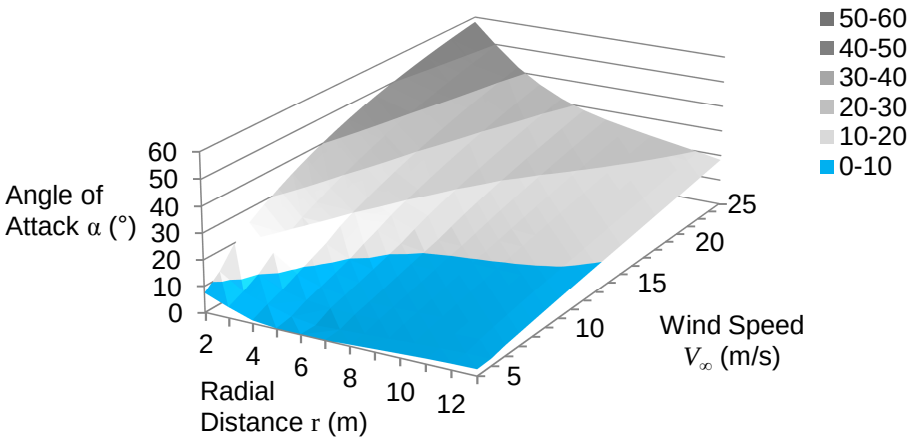


Figure 1.17 - AWT-27 wind turbine angle of attack distribution along the blades: generated using WTAero

As shown in Figure 1.16, the AWT-27 wind turbine power generation in the low wind speed region is not maximised since it only operates in optimal conditions (i.e. maximum $C_p$ or $C_{p,opt}$) for the unique wind speed of about 8.5 m/s. As the wind turbine enters region 3 (≈ 11 m/s), it can be seen that the power is much lower than rated (i.e. 300 kW) and does not reach its nominal value until 17 m/s. Moreover, as the wind speed keeps increasing above 17 m/s the passive stall control does not maintain the power at nominal value (Pierce and Migliore, 2000). Entering into stall is a progressive process and therefore the blades must operate much closer to stall conditions even before the wind turbine rated wind speed (Poore, 2000). As a consequence, stall-regulated wind turbines have poor performance near their rated wind speeds. However, stall-regulated wind turbines feature advantages such as un-modified blades, no active control systems or sensors. On the other hand, because stall corresponds to a reduction of the lift coefficient only, aerodynamic forces related to the drag (i.e. thrust) keep increasing even after stall (see Figure 1.16.c). Over the past decades, the

interest in stall-regulated wind turbines has rapidly declined in favour of pitch-controlled wind turbines (Zhang et al., 2008, Şahin, 2004). With the exception of simple small scale designs, fixed-speed stall-regulated wind turbines are not generally used for the control of modern wind turbines.

### 1.2.4 Collective Pitch Control

In response to quasi-steady changes in wind speed, the pitch control mechanism changes the pitch angle of all blades simultaneously for the purpose of adjusting the output power and load (Figure 1.18) (Laks et al., 2009, Zhang et al., 2008, Muljadi and Butterfield, 2001). As Figure 1.19 shows, pitching the blade to feather by an angle $\theta$ results in a reduction of the angle of attack from $\alpha_1$ to $\alpha_2$. In doing so, the aerodynamic lift force is reduced as illustrated in Figure 1.20. Pitch control is mainly used in the wind turbine's operating region 3 where the power can be maintained to nominal values as shown in Figure 1.21. In the operating region 2, the pitch angle may be allowed to vary a few degrees from the fixed pitch angle in order to maximise power.

The most conventional pitch control, namely pitch-to-feather, consists of pitching the blades to reduce the angle of attack (Figure 1.20). In so doing both the lift and drag forces decrease. By contrast, pitch-to-stall consists of increasing the angle of attack for the blade to enter into stall where the lift decreases. Pitch-to-feather is often preferred over pitch-to-stall for aeroelastic stability reasons.

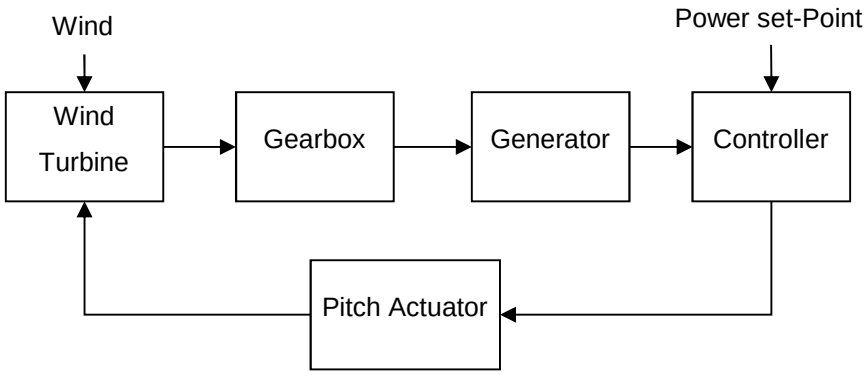


Figure 1.18 - Fixed-speed pitch-regulated wind turbine feedback control loop (Burton et al., 2001)

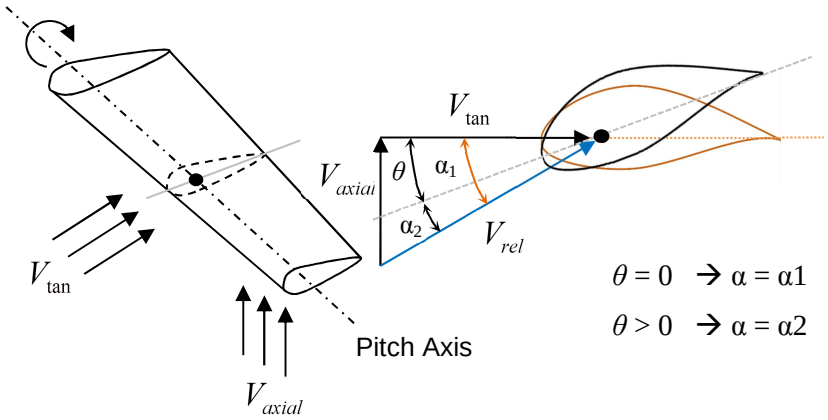


Figure 1.19 - Pitch angle illustrative scheme

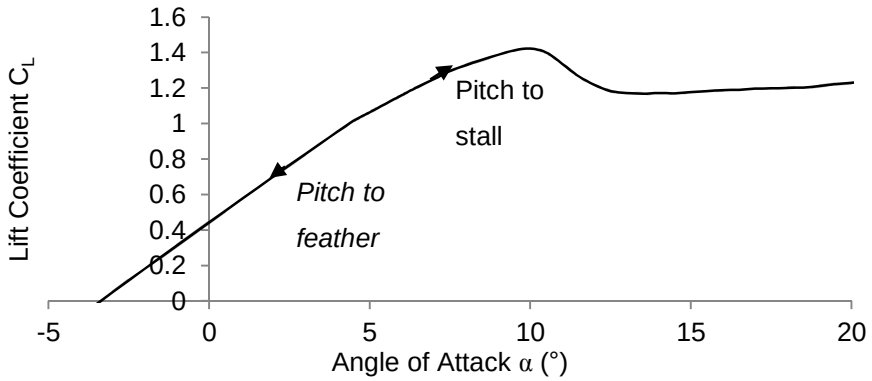


Figure 1.20 - Pitch control strategies

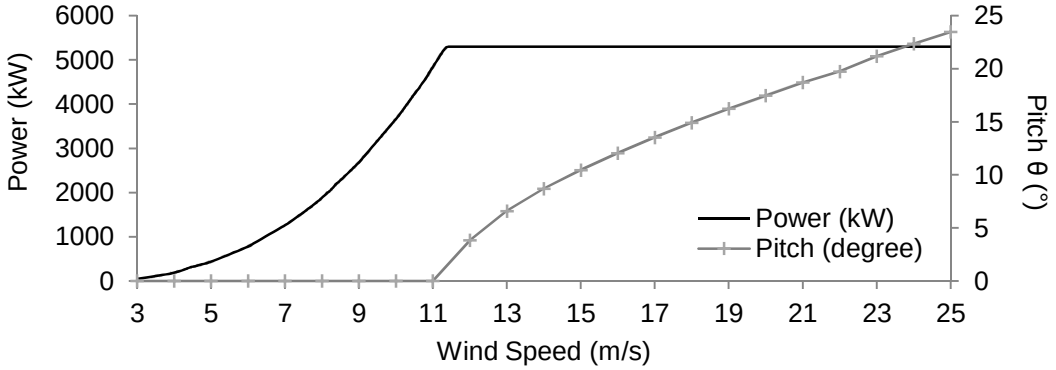


Figure 1.21 - Pitch-controlled NREL 5MW wind turbine power curve and pitch angle (Jonkman et al., 2009)

### 1.2.5 Variable-Speed Stall-Regulated Wind Turbines

The variable-speed control system maximises power extraction over the low wind speed region by tracking the optimal power coefficient. Since the power coefficient reflects the wind turbine blades aerodynamic efficiencies, different wind speeds or rotational speeds result in different inflow angles and aerodynamic efficiencies. The aerodynamic efficiency of wind turbines is, therefore, generally expressed as a function of the tip speed ratio (λ) as follows:

$$\lambda = \frac{[V_{\tan}]_{Tip}}{V_{\infty}} = \frac{\omega_{rot} R}{V_{\infty}} \tag{1.3}$$

where, the tip speed ratio is defined as the blade tangential tip wind speed (i.e. rotor angular speed $\omega_{rot}$ times the blade radius *R*) divided by the free stream velocity. There is a unique operating condition for which the power coefficient of a wind turbine is optimal as illustrated in Figure 1.22.

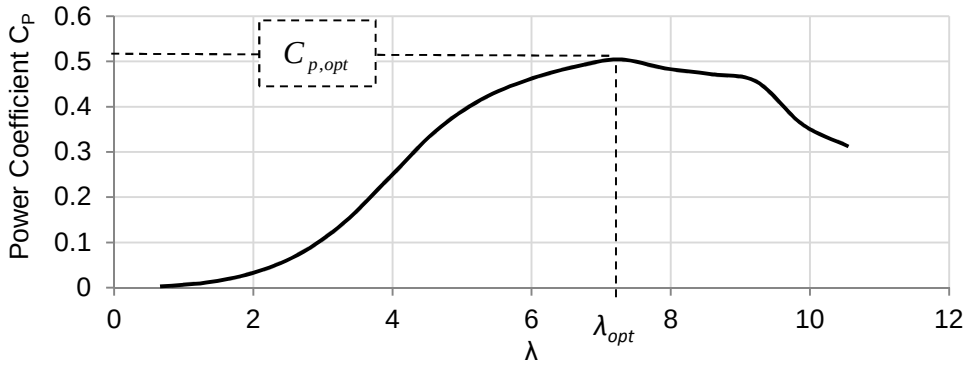


Figure 1.22 - AWT-27 wind turbine power coefficient as a function of the tip speed ratio: generated using WTAero

Wind turbines with fixed angular speeds only maximise the power coefficient for a unique wind speed ( $\lambda = \lambda_{opt}$ ). In comparison, by using a variable-speed wind turbine and controlling the rotor angular speed $\omega_{rot}$ the power coefficient can be maintained near optimum as the wind speed varies. In addition to the tip speed ratio, the pitch angle also impacts on the turbine aerodynamic efficiency as illustrated in Figure 1.23.

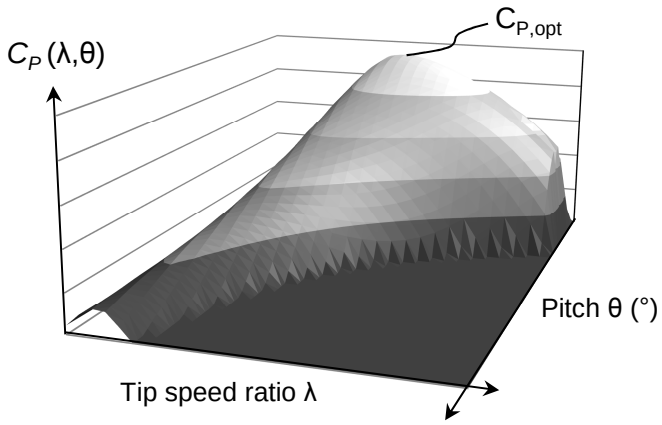


Figure 1.23 - Typical power coefficient surface as a function of the tip speed ratio and pitch angle

Assuming the variable-speed control system maintains the power coefficient equal to optimal, the optimal power can then be written as:

$$P_{opt} = \frac{1}{2}\rho A_r C_{p,opt} V_\infty^3 = \frac{1}{2}\rho A_r C_{p,opt} \left(\frac{R}{\lambda_{opt}}\right)^3 \omega_{rot}^3 = K_{opt}\omega_{rot}^3 \tag{1.4}$$

It can be seen that the optimal power can be expressed as a factor $K_{opt}$, depending only on the wind turbine steady state performance, and the rotational speed. By controlling the wind turbine rotational speed one can therefore track the optimal power coefficient. Employing a variable-speed stall-regulated wind turbine, power extraction can be maximised in the low wind speed region. Above rated power, the angular speed is reduced to increase the angle of attack and bring the blades into stall. Although this has not often been done in practice, variable-speed stall-regulated wind turbines can maximise power at low wind speed while maintaining nominal power in operating region 3 without the need for the pitch mechanism (Burton et al., 2001). However, the main disadvantage of this control strategy is that when a wind gust hits the turbine in operating region 3, the generator torque has to suddenly increase to match the mechanical torque in order to prevent the wind turbine from accelerating and also has to increase further to slow the rotor down into stall. As a consequence, the torque and power transients experienced by variable-speed stall-regulated wind turbines are often substantial.

In addition to achieving high aerodynamic efficiency over the low wind speed region, the variable speed control also has numerous advantages. The generator torque can be controlled in region 3 to maintain power close to nominal. The rotor can also act as a flywheel in order

to smooth mechanical torque entering the drive train. Furthermore, the low wind turbine rotational speed in region 2 reduces noise generation.

There are two main methods, namely broad and narrow range, for achieving variable-speed control (Burton et al., 2001). The broad range variable-speed allows the rpm to be controlled from zero to rated speed. The narrow range control limits the rpm variations about $\pm 30\%$ / $\pm 50\%$ of the generator synchronous speed. The narrow range variable-speed is the most commonly used method as it requires a much cheaper frequency converter while featuring most of the advantages of the broad range. From the early investigations (Muljadi and Butterfield, 2001) to more recent and complex tracking control (Abdullah et al., 2012, Hand, 1999, González et al., 2010), many strategies have been proposed in order to maximise power extraction. One of which, a variable-speed closed-loop control system using the filtered wind speed as reference, is shown in Figure 1.24. The aerodynamic and generator torque are denoted by $T_{Aero}$ and $T_{gen}$ while the rotor and generator angular speeds are referred to as $\omega_{rot}$ and $\omega_{gen}$. At the present time, maximum power point tracking (MPPT) control strategies are generally used due, in part, to their robustness to inaccuracies in predicting the performance of wind turbines (Abdullah MA et al., 2012).

The commonly employed MPPT control strategies can be divided into 4 classes: (i) tip speed ratio (TSR) control, (ii) optimal torque (OT) control, (iii) power signal feedback (PSF) control and (iv) perturbation and observation (P&O) control. The tip speed ratio control strategy aim is to track the optimal tip speed ratio by changing the rotational speed in order to maximise the energy yield. This strategy uses wind speed measurements and is relatively straightforward to implement. However, the TSR control is limited by the fact that precise measurements of the wind speed are rarely available (Raza Kazmi et al., 2010). In comparison, the optimal torque MPPT regulates the generator torque based on a maximum power reference. This methods is also straightforward and simple to implement. On the other hand, since the OP control uses the torque instead of wind speed it features a much slower response time than TSR (Nakamura et al., 2002). By contrast, as its name suggest the power signal feedback control track the optimum power using the wind turbine optimum power curve previously obtained experimentally (Tan and Islam, 2004). This PSF methods is generally considered of similar complexity and efficiency as the OP control. The perturbation and observation control strategy is relatively different to the other three. P&O uses optimisation such as hill-climbing search in order to determine the maximum power point.

This methods is widely popular since it does not require any previous knowledge about the wind turbine power curve. Nevertheless, different tuning the hill-climbing optimisation can lead to significantly different outcomes and many works are focused on this topic (Hui and Bakhshai, 2008, Hong and Lee, 2010).

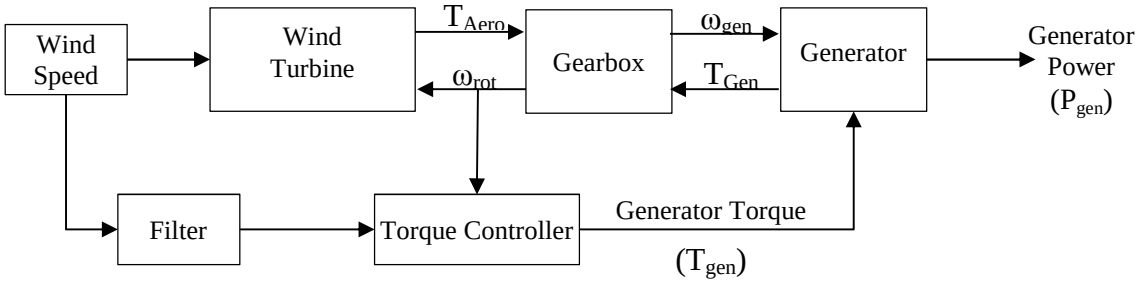


Figure 1.24 - Variable-speed control loop using the filtered wind speed as reference

### 1.2.6 Variable-Speed Pitch-Controlled Wind Turbines

Most modern wind turbines are now equipped with both variable-speed and pitch control systems. Below rated wind speeds, the torque control tracks the optimal power coefficient. Once rated power is reached, the generator torque is held constant and the pitch control system maintains the aerodynamic torque close to the rated generator torque. The pitch and variable-speed control combination provides the best smoothing performance for torque and power transients. The pitch controller is used to smooth gusts and the variable-speed control uses the rotor inertia to smooth out faster and smaller power transients. Figure 1.25 illustrates the power curve, as well as the pitch and the variable-speed control values for a 5 MW wind turbine (Jonkman et al., 2009).

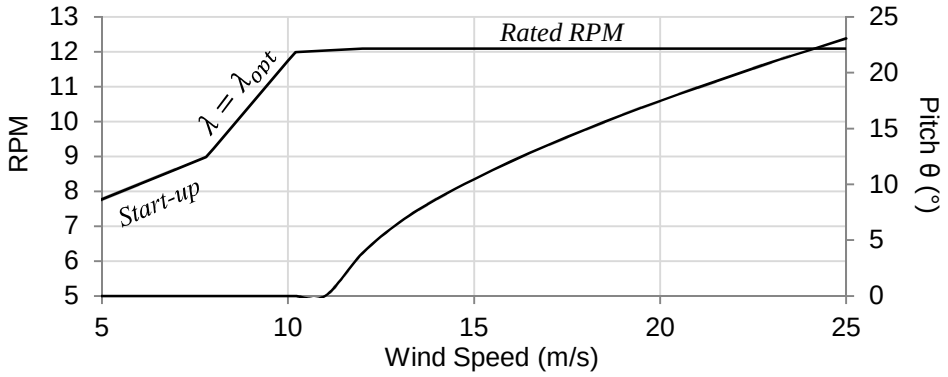


(a)

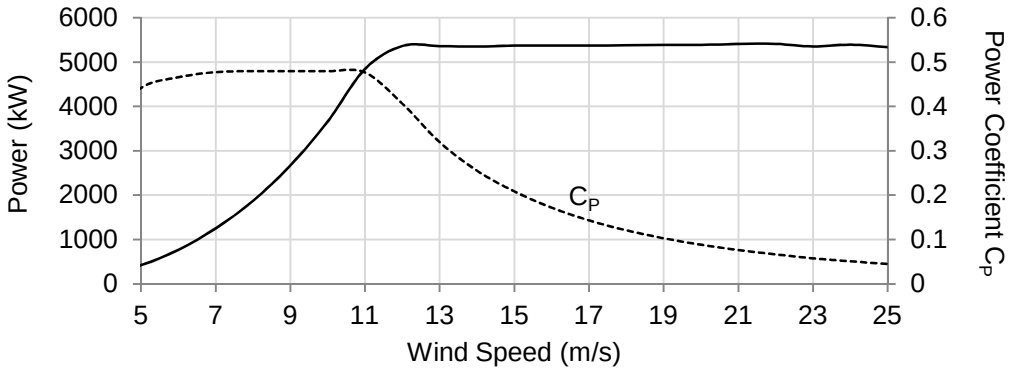


(b)

Figure 1.25 - NREL 5MW wind turbine (a) rotor angular speed and pitch angle, and (b) power coefficient and power curve: generated using WTAero

## 1.3 Wind Turbine Blade Load Alleviation Studies

The conventional wind turbine control systems presented above are not designed for load alleviation purposes and are therefore ineffective at relieving fatigue loads. Instead, innovative control techniques are being proposed and developed. The most common load alleviation control systems referred to in the literature are presented in this section.

### 1.3.1 Individual Pitch Control

The individual pitch control (IPC) system can be seen as the evolution of the collective pitch control in order to reduce fatigue loads. In the presence of windshear, the cyclic loads due to the blades rotation are deterministic loads as shown in Figure 1.26. While the collective pitch controller modifies the blade pitch angles simultaneously for controlling quasi-steady loads, the IPC system allows each blade to pitch independently in order to alleviate cyclic loads. Research by Bossanyi (Bossanyi, 2003) has shown that significant load reduction can be achieved providing accurate measurements of the blade loads. In 2005 Larsen et al. (Larsen et al., 2005) proposed an IPC control strategy based on local inflow measurements along the blade span. In particular, the angle of attack and the local wind velocity are measured using a Pitot tube. Since the inflow measurements are correlated to the wind turbine cyclic loads (Larsen et al., 2005), it is used as a reference signal for the IPC controller. The inflow measurement-based control strategy permits faster and more adequate IPC response compared to the strategy originally proposed by Bossanyi. Research has shown that the IPC has a significant capability in reducing loads from 1P (rotor rotational frequency) up to 3P (van Engelen, 2006). While the IPC has shown potential in reducing cyclic loads, load

alleviation using IPC still remains difficult to achieve in practice due to the dominance of turbulence and rapid dynamics which wear on the pitch actuators.

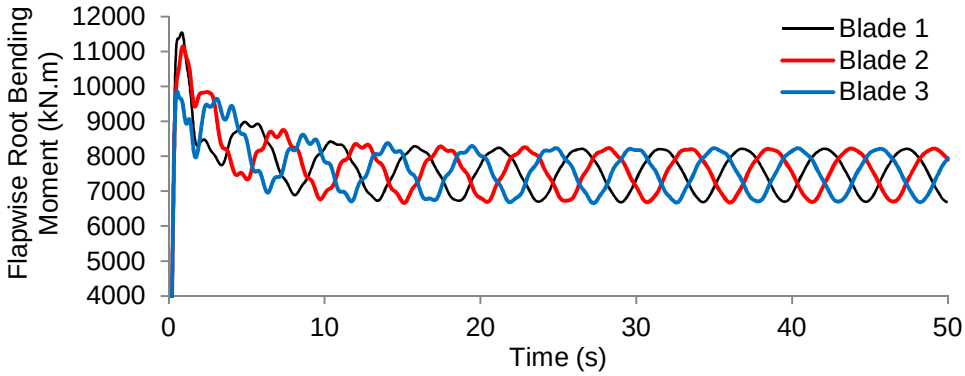


Figure 1.26 - Flapwise root bending moment for a three bladed 5MW NREL wind turbine: generated by FAST (Jonkman and Buhl, 2005)

### 1.3.2 Control Surfaces

Control surfaces (CSs) are deployable parts implemented on wind turbine blades able to control aerodynamic forces locally by changing the geometry of aerofoils (Barlas and van Kuik, 2010). Changing the camber of aerofoils located along the blade span affects the local aerodynamic forces as illustrated in Figure 1.27. Since small variations in the trailing edge aerofoil geometry can significantly change the aerofoil aerodynamic performance (Yen et al., 2000), active load control devices are generally located at the trailing edge (Castaignet et al., 2013). Two of the most commonly used CSs for wind turbine blade applications are the trailing edge flap and microtab. These CSs share common features such as modularity, fast actuation and are lightweight. In contrast to CSs, the IPC is more expensive, has higher operating energy consumption and has a slower response time.

The performance of CSs varies with their host aerofoil. However, there is no analytical model able to accurately predict the changes in lift and drag forces generated by deploying CSs. The aerodynamic performance of a particular CS equipped on an aerofoil is evaluated using numerical or experimental methods (Chow and van Dam, 2007). The aerodynamic efficiency of CSs is given in terms of lift-drag ratio, aerodynamic response time and control space. The lift-drag ratio is used as an aerodynamic performance index. The response time refers to the time at which the flow reaches its steady state after the CS deployment. A short response time, and therefore the capability to quickly modify aerodynamic forces, is crucial in order to counteract high frequency loads. The control space refers to the CS capability in generating aerodynamic force (i.e. $\pm\Delta C_{L,ss}$) with respect to the baseline aerofoil as shown in Figure 1.28.

A large control space is necessary because it directly affects the CS capability in alleviating load. When CSs are coupled with a sensing system, a closed-loop control system can be designed in order to achieve load alleviation (Andersen, 2010a) as shown in Figure 1.29.

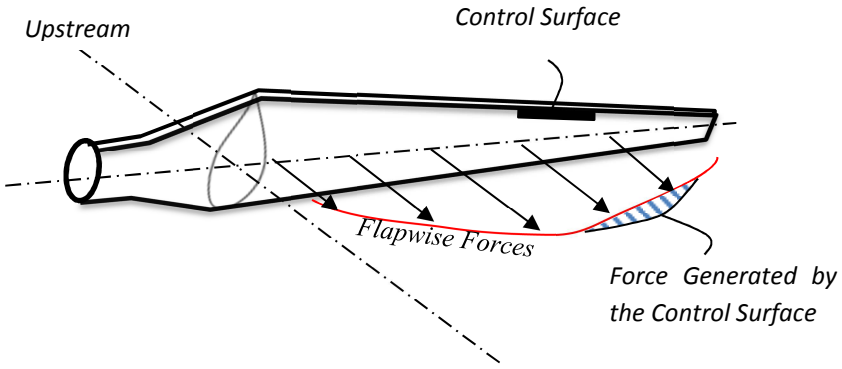


Figure 1.27 - Wind turbine blade equipped with a control surface

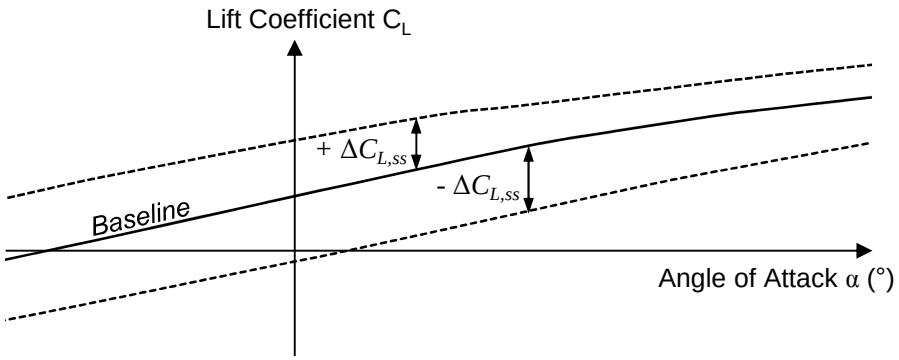


Figure 1.28 - Typical variation of the baseline lift coefficient of an aerofoil due to the deployment of a control surface

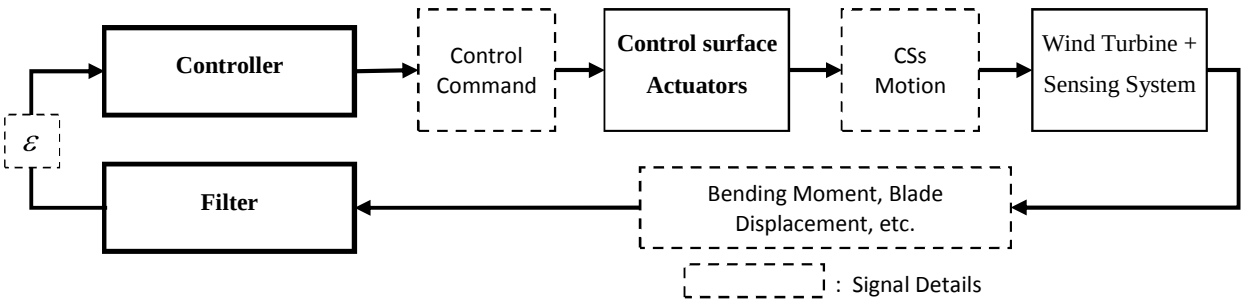


Figure 1.29 - Typical control structure for blade load alleviation employing control surfaces

### 1.3.2.1 Trailing Edge Flap

The trailing edge flap (TEF) has shown great potential as an aerospace control device and it is therefore logical to investigate TEFs as a possible means for the load alleviation of wind

turbine blades. TEFs are mounted at the aerofoil trailing edge and can deploy (i.e. rotate and translate) with respect to their host aerofoil to effectively change its camber. Figure 1.30 shows a single slotted TEF. In this figure, the TEF is hinged on the aerofoil and an actuator is used to generate a moment for controlling the TEF deployment angle.

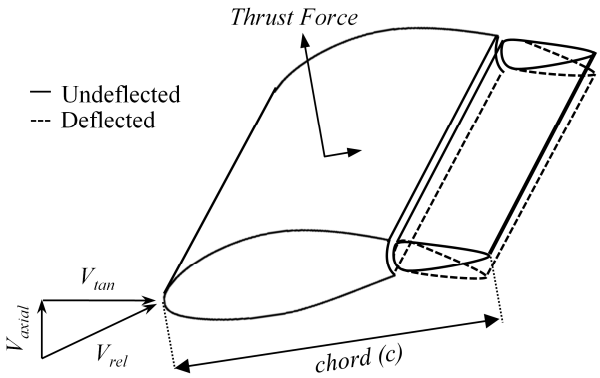


Figure 1.30 - Aerofoil equipped with a single slotted trailing edge flap

Due to its previous aerospace application as a lift enhancing device, the steady and dynamic modelling of TEF was already under-investigation in the 1930s (Theodorsen, 1935). Many models based on Theodorsen's work have been proposed since. One of which, Leishman's model is an indicial model predicting the lift generated by TEFs equipped on thin aerofoils and operating under attached flow (Leishman, 1994).

In the nineties, investigations of TEFs implemented on wind turbine aerofoils were also performed by the National Renewable Energy Laboratory (NREL). The potential use of TEF for aerodynamic braking and power regulation were first evaluated (Migliore et al., 1995). However, the original research efforts on power regulation and aerodynamic braking were rapidly supplanted by wind turbine blade load alleviation.

The possibility of employing TEFs in order to control the aeroelastic response of wind turbine blades to a gust of wind was first investigated in 1996 (Stuart et al., 1996). Results of this investigation demonstrated the load alleviation potential of TEFs at an early stage of modern wind turbine technology. Since then, the growing interest in reducing wind turbine blade loads has led to numerous proofs of concept. The works published in this period can be summarised as (i) simulations, (ii) reduced-scale experiments and (iii) full-scale experiments.

Simulations are by far the most common type of investigation of wind turbine blade load alleviations. Due to their simplicity, preliminary steady state load alleviation studies are often

carried out. These investigations utilise the two dimensional steady state data of aerofoils equipped with TEFs and neglect aerodynamic lags (i.e. response of the flow due to the TEF deployment) (Castaignet et al., 2011, Wilson et al., 2009, Wilson et al., 2010). One of which, the research conducted in 2011 by Castaignet, has evaluated the potential of TEF to reduce the blade flapwise root bending moment of a Vestas V27 wind turbine. Castaignet, employing a frequency weighing model-predictive controller (MPC), showed evidences of the load alleviation potential of TEFs. Barlas et al. (Barlas et al., 2012) have also shown similar load alleviation results employing MPC.

Simulations investigating the potential of TEFs while considering the flaps' dynamic responses were also carried out. In 2009, Barlas and van Kuik investigated the dynamic control of TEFs on a 5 MW wind turbine (Barlas and van Kuik, 2009). Several control distribution strategies were proposed when implementing multiple TEFs onto the same blade. Two of them considered the TEFs located on the same blade to act as a unique entity ("large flap" assumption). By contrast, the decentralised multiple feedback control used the local flapwise deformations as control references. Load alleviation results showed a 20% maximum load reduction of the root bending moment using the decentralised multiple feedback control. A year later, Resor et al. (Resor et al., 2010) used the aeroelastic code (DU_SWAMP), developed by researchers at the Delft University Wind Energy Research Institute, to simulate several active aerodynamic control scenarios. Results showed a 30% reduction of the 1*P* flapwise root bending moment standard deviation when employing classical controllers with 10% chord wise TEFs covering 25% of the blade span.

Reduced scale experiments of wind turbine blades or aerofoils load alleviation are also commonly found in the literature (Andersen, 2010b, Frederick et al., 2010, van Wingerden et al., 2011). In 2010, Frederick et al. (Frederick et al., 2010) experimentally investigated the load alleviation capability of a small (4% chord-wise) TEF. The TEF was allowed to deploy ± 90° with respect to the host aerofoil. The experiment set up a NACA 0012 of 0.3m span and 0.22m chord in a water tank. An inviscid state-space model combined with a finite element model was used to model the aero-structural system. The TEF was controlled using PID and LQR controllers using a strain gauge measurement. Even though the work produced by Frederick demonstrated promising load alleviation capability, some concerns remained to be noted for applications on wind turbine aerofoils. First, the deployment of a TEF at such large angles could be responsible for substantial drag increase and premature stall. Second, wind

turbine aerofoils generally experience flow at higher Reynolds numbers than those used in the experiment. A year later, van Wingerden et al. (van Wingerden et al., 2011) conducted another experiment setting up a reduced-scaled model of the 5MW wind turbine designed by NREL (Jonkman et al., 2009). The proposed control system combined two multi-input multi-output (MIMO) H-infinity controllers taking into account the deterministic and stochastic disturbances of the measurement obtained using strain gauges located at the blades' root. The load alleviation results presented by van Wingerden were substantial (i.e. from 50 to 90% load reduction). There are, nonetheless, obvious differences with the large scale implementation of TEFs. First, the TEF coverage and size on the reduced scale were much greater than the commonly assumed 10-20% span-wise and chord-wise coverage. Second, the small blade size results in a relatively stiff structure with rapid dynamic responses (i.e. low phase system) compared to full scale dynamics.

Due to their high cost, there are only a limited number of reported full-scale experiments of CSs equipped on wind turbine blades. In a continuing effort by Castaignet et al. (Castaignet et al., 2013), the full-scale load alleviation of a 225 kW Vestas V27 wind turbine was carried out in 2013. Assuming no interactions with the classic control systems, the conventional blade pitch control was not modified. Due to some issues encountered during the test, only 5% of the blade span was covered with TEFs. Nevertheless, the 38-minute test successfully demonstrated an average load alleviation of about 13.8%. While the experimental work of Castaignet can be considered as a milestone, experimental applications on multi-megawatt wind turbines have not yet been carried out. Moreover, the control strategy was only applied for a SISO case (i.e. one TEF) and assumed negligible aerodynamic lags. Better load alleviation performance may, therefore, be achieved using more suitable control strategies.

In view of the above literature on load alleviation of wind turbine blades employing TEFs, it is clear that TEFs have a significant potential for load alleviation. While many proofs of concept have demonstrated the load alleviation capabilities of TEFs, further work is needed in order to promote TEFs for industrial applications. In particular, the research conducted during this PhD addresses this issue by providing a better understanding of the dynamic control of wind turbine blades equipped with TEFs. Specific load alleviation control systems are designed in order to maximise load alleviation performance in Chapter 5 and 6.

#### 1.3.2.2 Microtabs

Microtabs, proposed by Yen et al. (Yen et al., 2000) are small tabs located near the aerofoil trailing edge and are considered the evolutionary descendant of Gurney flaps. Gurney flaps were first used in automobile racing by the pilot Dan Gurney in the early seventies. The small solid non-movable device installed pointing upward on the rear wing of his car improved the car traction by generating downward aerodynamic forces, achieving greater manoeuvrability at high speed. The device was later investigated on aerofoils and brought to the aerodynamic field by Liebeck (Liebeck, 1978) who named it the Gurney flap. The implementation of Gurney flaps on aerofoils consist of small size flaps attached to the trailing edge and almost perpendicular to the aerofoil chord line (Wang et al., 2008) as shown in Figure 1.31. The implementation of a Gurney flap modifies the Kutta condition and increases the lift and drag generation (Van Dam et al., 1999). While heavier and more complex active flow controllers such as TEFs had already shown great results as high-lift control devices, the Gurney flap was an innovative micro-scale device capable of macro-scale aerodynamic performance. Additionally, the Gurney flap has a simple design, low installation and maintenance costs, and is lightweight (Yen et al., 2000).

The location and height of the Gurney flap along aerofoils are the two primary design parameters. As the Gurney flap is moved away from the trailing edge towards the leading edge, the drag steadily increases and the lift remains unchanged up to a point where aerodynamic performance rapidly decreases (Yen et al., 2000). When the Gurney flap height increases, both lift and drag increase steadily up to a height about the boundary layer thickness where drag starts to significantly increase. Accordingly, it is generally accepted that the Gurney flap should be located between 90 and 100% of the aerofoil chord and should be kept lower than 2% of the chord length (Van Dam et al., 1999, Yen et al., 2000).

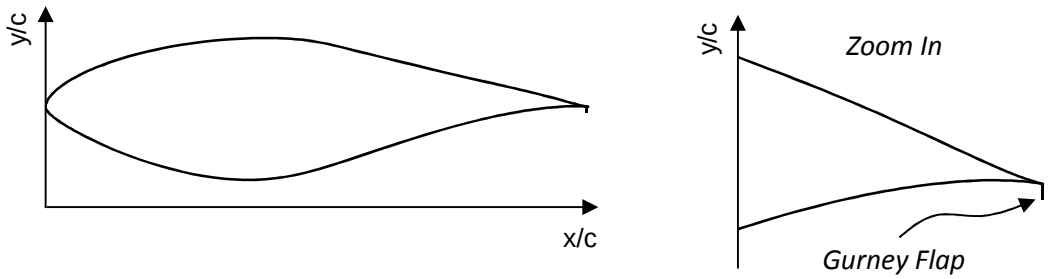


Figure 1.31 - Gurney flap implemented on a S809 aerofoil

The original Gurney flap is a passive device employed to increase the lift generation of aerofoils. However, the drag penalty during cruise flight is one of the main factors limiting Gurney flap applications to a few airplanes. Further research starting in the year 2000 has since led to the development of an actively controlled Gurney flap or microtab (micro-electro-mechanical (MEM) translational tabs) for wind turbine and rotorcraft applications (Nakafuji et al., 2000, Nakafuji et al., 2001, Yen et al., 2000, Thiel et al., 2006, Mayda et al., 2005). Yen et al. (Yen et al., 2000) published research including the numerical and experimental proofs of concept in addition to a fabrication process and actuation mechanism for microtabs. Being actively deployable, the new concept provides the possibility to control aerodynamic forces locally towards regulating rotor vibrations (Frederick et al., 2010, Van Dam et al., 2002, Johnson et al., 2010, Mayda et al., 2005, Thiel et al., 2006).

Microtabs deploy approximately normal to the aerofoil surface. As shown in Figure 1.32, a microtab can either be: (i) deployed upward on the suction side of the aerofoil, (ii) deployed downward on the pressure side of the aerofoil and (iii) neutral, where the microtab is inside the aerofoil with no effect on the lift and drag coefficients.

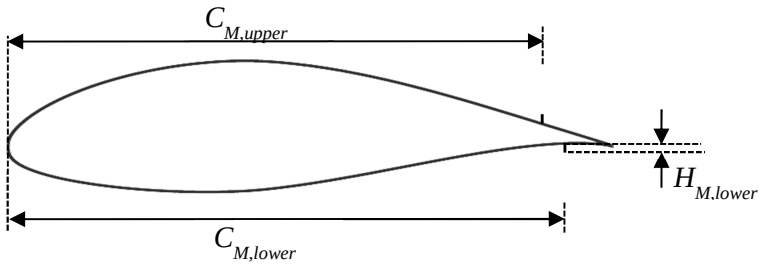


Figure 1.32 - Microtab implemented on an aerofoil

The potential of microtabs for load control was first demonstrated by Van Dam et al. (Van Dam et al., 2002) and then by Baker et al. (Baker et al., 2007) who carried out extensive numerical and experimental analyses with microtabs installed on the S809 aerofoil. They addressed the issues of optimal positioning and sizing for maximum lift/drag performance. Similar to the Gurney flap, the tab height should be close to the boundary layer thickness (i.e. 1% to 2% of the local chord length) while being located near the trailing edge as this location provides a good lift/drag ratio and enough volume for the microtab to retract. Nevertheless, optimal sizing and positioning is difficult to achieve due to its dependency on geometric and aerodynamic parameters and will more often result in a lift/drag ratio trade-off.

During the last decade, the load alleviation performance of microtabs was investigated. As for TEF, preliminary steady state load alleviation studies were carried out. Wilson et al. (Wilson et al., 2009, Wilson et al., 2008) have shown that microtabs installed on a 600 kW wind turbine could achieve a reduction of the flapwise root bending moment by up to 50%. The load alleviation results presented by Wilson, although promising, were obtained assuming instantaneous microtab response. By contrast, other studies have investigated the dynamic response of microtab (Zayas et al., 2006, Chow and van Dam, 2007, Bæk and Gaunaa, 2011). Considering the microtab aerodynamic response, Baek et al.(Bæk et al., 2010), and Baek and Gaunaa (Bæk and Gaunaa, 2011) have compared the load alleviation performance of TEFs and microtabs. Both studies have concluded that, despite their disadvantages (i.e. short delay and transient adverse response), microtabs can be used to reduce the loads experienced by wind turbine blades. While the investigations mentioned above have greatly contributed to the microtab proofs of concept, the control system design and frequency response of actively controlled blade equipped with microtabs remain to be investigated. Moreover, no mathematical model has been proposed in order to describe the microtab dynamic response. Both issues are addressed in this thesis. A dynamic model for the aerodynamic response of deploying microtab is proposed in Chapter 3 and used for control system analyses in Chapter 5 and 6.

### 1.3.3 Morphing Technology

While aircraft morphing has long been the subject of research (Weisshaar, 2013), wind turbine morphing is a more recent subject of interest. According to Lachenal et al.(Lachenal et al., 2013) the morphing of wind turbines is divided into two main groups: In-plane and Out-of-plane morphing as shown in Figure 1.33.

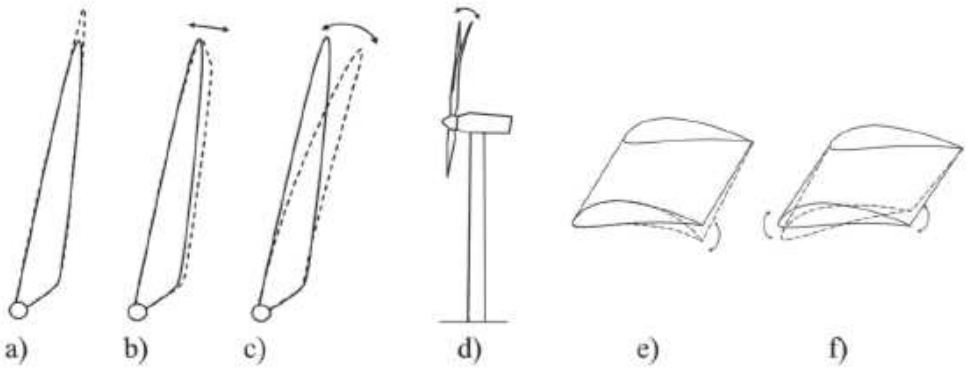


Figure 1.33 - Morphing classification In-plane: (a) span-wise, (b) edgewise (c) sweep and Out-of-plane: (d) span-wise, (e) chord-wise and (f) twist (Lachenal et al., 2013)

Since morphing technologies have a broad range of applications, the past few years have witnessed a growing interest in morphing technologies and its applications to wind turbines. Investigations for wind turbine applications (e.g. adaptive trailing edge geometry) have started less than a decade ago (Andersen, 2005, Andersen et al., 2010, Andersen, 2010b). One particular advantage of a morphing trailing edge is to maintain structural integrity while ensuring a smooth deformable shape as shown in Figure 1.34. The smooth deformation often guarantees that the flow around the aerofoil remains attached, which in comparison with other discrete control surfaces that feature gaps and external mechanisms, results in lower drag. Although morphing technologies are promising, the practical implementations face numerous challenges. For instance, manufacturing a lightweight wing or blade structure flexible enough to morph without losing its capacity to withstand aerodynamic loads is difficult. The main features of a morphing aerofoil include:

- High out-of-plane stiffness to resist aerodynamic loads
- Low cross-sectional stiffness to reduce actuation forces
- High strain capability
- Short response time
- Fatigue resistance

The study of deformable TEF started in 2005 with the work of Andersen on the 33m-radius Vestas 66 wind turbine (Andersen, 2005). In 2006, a more recent model based on thin aerofoil theory was developed by Gaunaa for describing the aerodynamic response of a deforming TEF (Gaunaa, 2006). This model was later used for load alleviation studies (Andersen et al., 2010, Andersen, 2010b). A few other works have also investigated the use of deformable TEFs in order to alleviate wind turbine blade loads (Barlas et al., 2012, Andersen, 2010b). As for the hinged TEFs, simulations of the deformable TEF have shown great load alleviation potential on medium and large scale wind turbines.

The aerodynamic advantage of a morphing structure is not questioned and there are many potential candidates for morphing structures. For instance, piezoelectric, anisotropic material (Thill et al., 2010), bi-stable plates (Diaconu et al., 2008), composite (Bettini et al., 2010) cellular structures and shape memory alloys (SMA) (Barbarino et al., 2009, Mohd Jani et al., 2014) are potential candidates for morphing structures. There is, however, no actual consensus about a suitable mechanism that would allow the contradictory objectives of a morphing aerofoil to be satisfied.

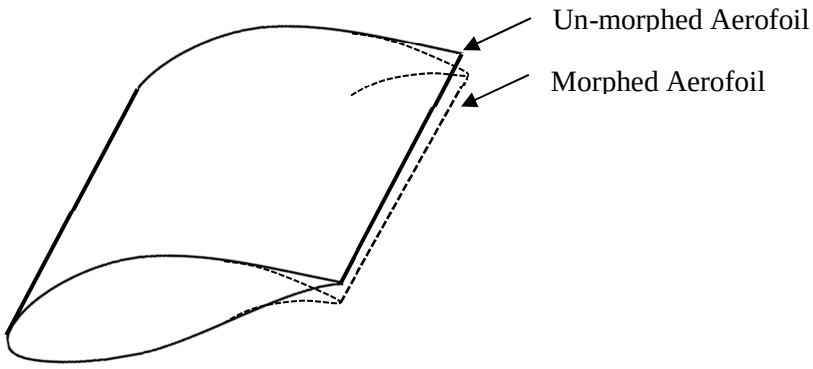


Figure 1.34 - Illustration of an aerofoil design with morphing trailing edge

## 1.4 Aim and Objectives of this Research

As mentioned in the previous sections, research has shown that wind turbine blade fatigue loads can be reduced by employing load control systems such as individual pitch control and control surfaces. Moreover, advantageous features in terms of modularity, cost, size and response time, has led to a growing research interest in employing control surfaces for load alleviation of wind turbine blades. While this research area holds great promise, the implementation of control surfaces on wind turbine blades remains experimental and much work has to be done before a consensus regarding the benefits of wind turbine blades equipped with control surfaces can be reached. The research conducted during this PhD is part of a global research effort towards reaching this consensus and focuses on the control of wind turbine blades equipped with multiple control surfaces.

Before the load alleviation performance of control surfaces equipped on wind turbine blades can be evaluated, two problems must be solved:

i) How should wind turbine blades equipped with control surfaces be modelled?

In this thesis, the answer is obtained by breaking down the original question and answering the following ones:

- How can the steady state control surfaces aerodynamic performance be modelled?
- What are the control surfaces dynamic response models?
- How can the structural dynamic of wind turbine blades be mathematically described?
- How can the structural model be coupled with the aerodynamic wind turbine model?

ii) Which are the control architectures suitable for the load alleviation of wind turbine blades equipped with control surfaces?

In this thesis, contributions are achieved by breaking down the above question and answering the following ones:

- How can the load alleviation of wind turbine blades be defined as a control problem?
- What types of sensors are required? How many sensors are needed? Where should the sensors be located?
- What is the optimal location of control surfaces along the blades span in order to maximise load alleviation, and how many control surfaces should be used?
- What is the impact of different control architectures on the dynamic response of wind turbine blades?

The aim of this PhD is to investigate the feasibility, design and capability of a multi-component aero-structural load control system utilising control surfaces such as trailing edge flaps and microtabs. In the process of this PhD, questions (i) and (ii) are answered through achieving the following objectives:

1. To develop a code (WTAC) capable of simulating the aeroelastic response of wind turbine blades equipped with control surfaces operating in unsteady environments. Figure 1.35 is a schematic of WTAC (in this figure the numbers in brackets refer to the Chapter numbers in this thesis).

2. To model the steady state and dynamic responses of microtabs and trailing edge flaps deploying on aerofoils and to couple this model with the aeroelastic wind turbine blade model of WTAC.

3. To investigate the dynamic capability of wind turbine blades, equipped with multiple control surfaces, in rejecting fatigue loads using WTAC. To propose, design and evaluate control architectures for the load alleviation of wind turbine blades employing control surfaces. To explain the aero-structural dynamics of actively controlled wind turbine blades.

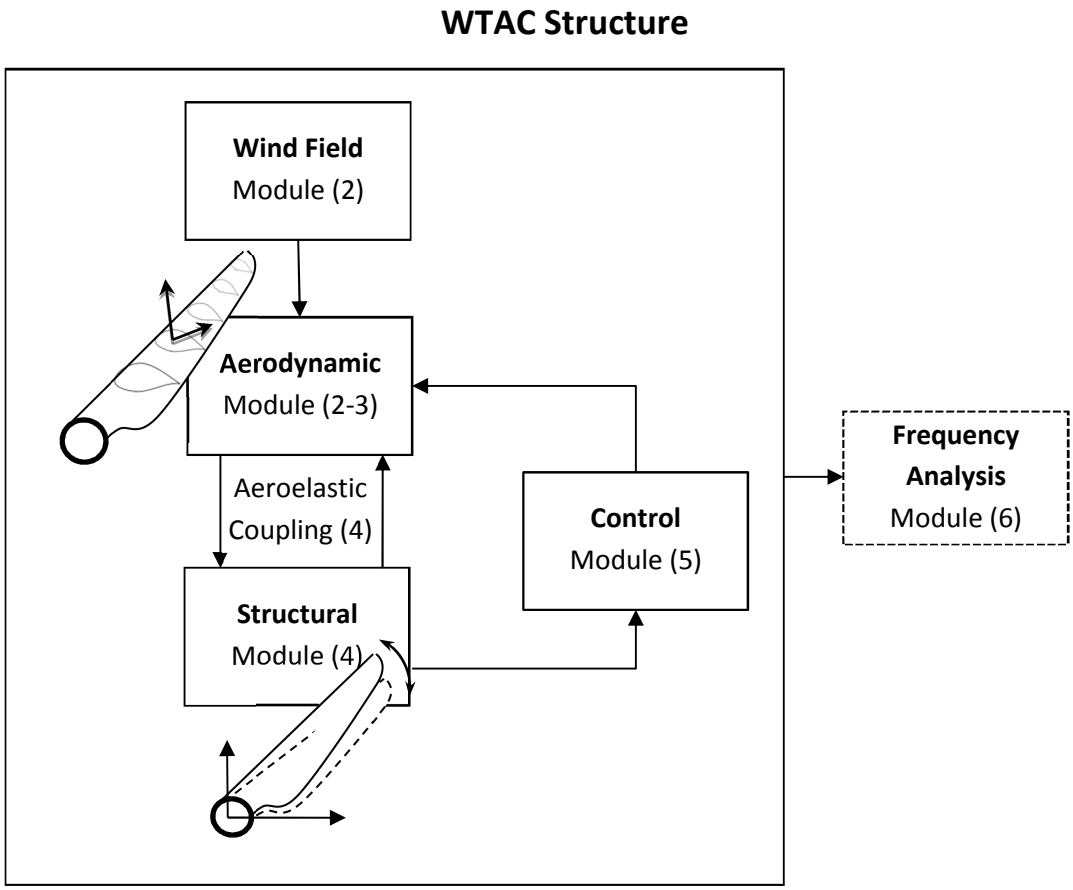


Figure 1.35 - WTAC and thesis structure

# 2. Unsteady Aerodynamics of Wind Turbines

## 2.1 Introduction

The aerodynamic module of WTAC is based on the steady state BEMT code WTAero (Maheri et al., 2006b). The following modifications have been implemented in order for WTAC to accurately model wind turbine blades operating in unsteady flow conditions:

Common modifications

- Misaligned rotor
- Rotating blades
- Space-time wind field interpolation
- Viterna-Corrigan aerodynamic data extension
- 3D stall
- Dynamic stall

Modifications specific to this work

- Coupling with TurbSim
- Coupling with XFoil
- Convergence accelerator algorithm

This chapter starts with the definition of the wind turbine coordinate systems used in this study. It then continues with a brief background on the steady state BEMT in Section 2.3 and detailed explanations regarding the above mentioned modifications through Sections 2.4 and 2.5. The final version of the unsteady aerodynamic module developed during this PhD is then benchmarked in Section 2.6.

## 2.2 Wind Turbine Coordinate Systems

Figure 2.1 illustrates the blades' rotational plane and non-alignment angles (i.e. tilt and yaw) for an upwind rotor configuration. The YZ plane corresponds to the blade rotational plane only if all misalignment angles are equal to zero. Otherwise, the rotational plane is the Y'Z' plane. The tilt angle $\eta$ denotes the angle by which the original rotor plane (YZ) is rotated with respect to the *Z*-axis. Tilting the wind turbine rotor increases tower clearance but also increases the out-of-plane bending moment due to gravitational forces. The yaw angle $\gamma$ denotes the wind turbine misalignment with incoming flow (i.e. rotation with respect to the *Y*-axis). The azimuth angle $\psi$ is used to represent the angular position of blades. The three-dimensional wind fields are described as vector fields. Each point in the global coordinate system (X-Y-Z) is associated with a velocity vector composed of three components. The in-plane (tangential) and out-of-plane (normal) vectors to the wind turbine blades are calculated, in WTAC, in order to determine the local velocity induced by the vector fields along the blade span as shown in Figure 2.2.

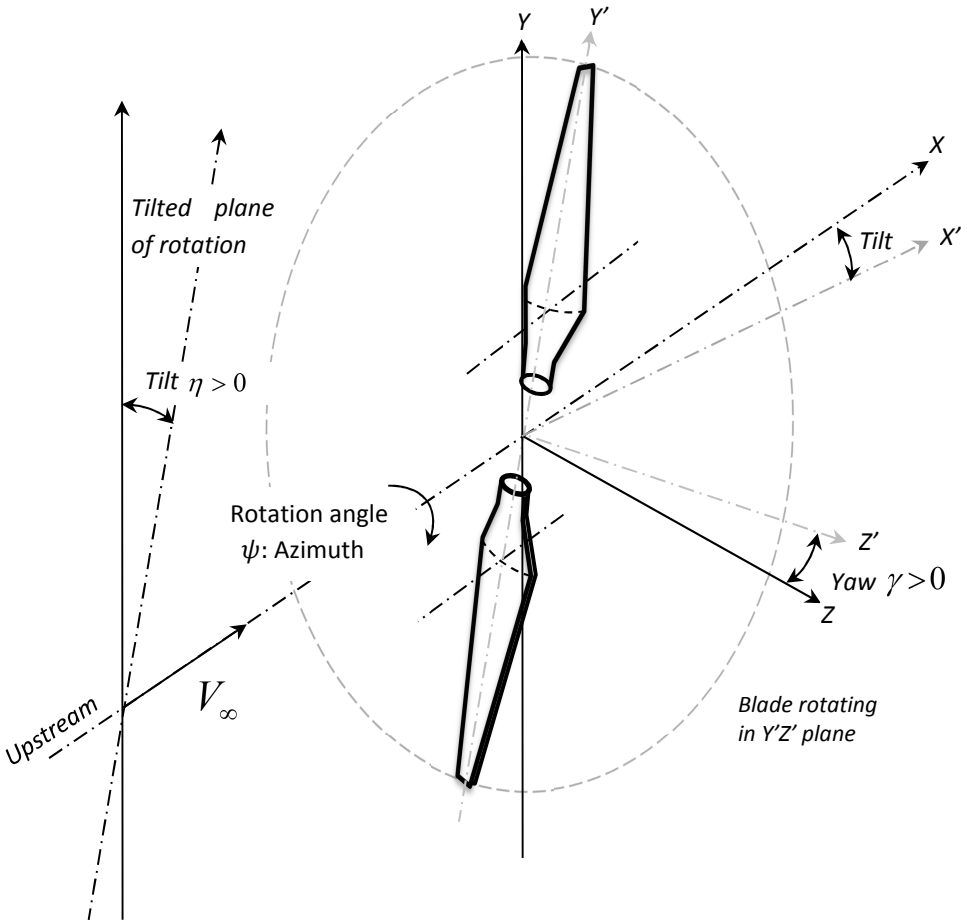


Figure 2.1 - Global wind turbine coordinate system

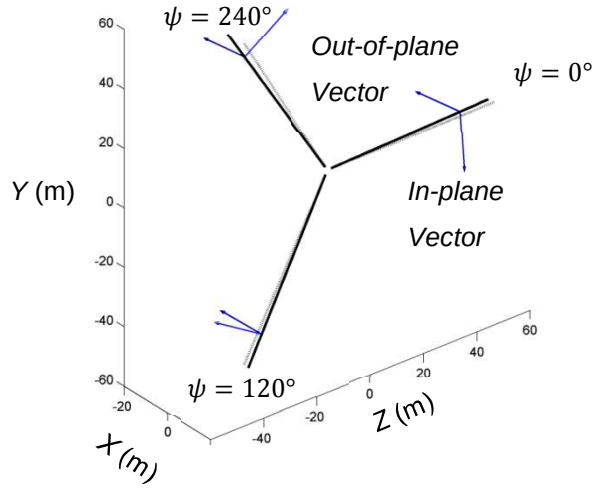


Figure 2.2 - Three-bladed wind turbine spatial representation (WTAC) of the rotational plane without (grey) and with tilt, yaw and cone angles (black)

Figure 2.3 shows the rotating blade coordinate system (*X'-Y''-Z''*) and Figure 2.4 is a detailed illustration of the blade cross-sectional coordinate system. The two dimensional lift (**L**) and drag (**D**) forces acting on aerofoils are respectively perpendicular and parallel to the local flow velocity. The flapwise and edgewise directions refer to the aerofoil principal elastic axis. In general, the internal aerofoil structures are designed such that the aerofoil principal elastic axes are similar to the chord axis. The In-Plane (*IP*) and Out-Of-Plane (*OOP*) forces are used to calculate the thrust and mechanical torque of wind turbines.

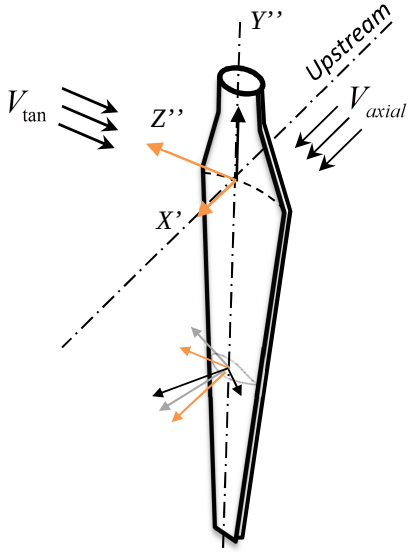


Figure 2.3 - Wind turbine blades rotating coordinate system: $\psi = 90°$

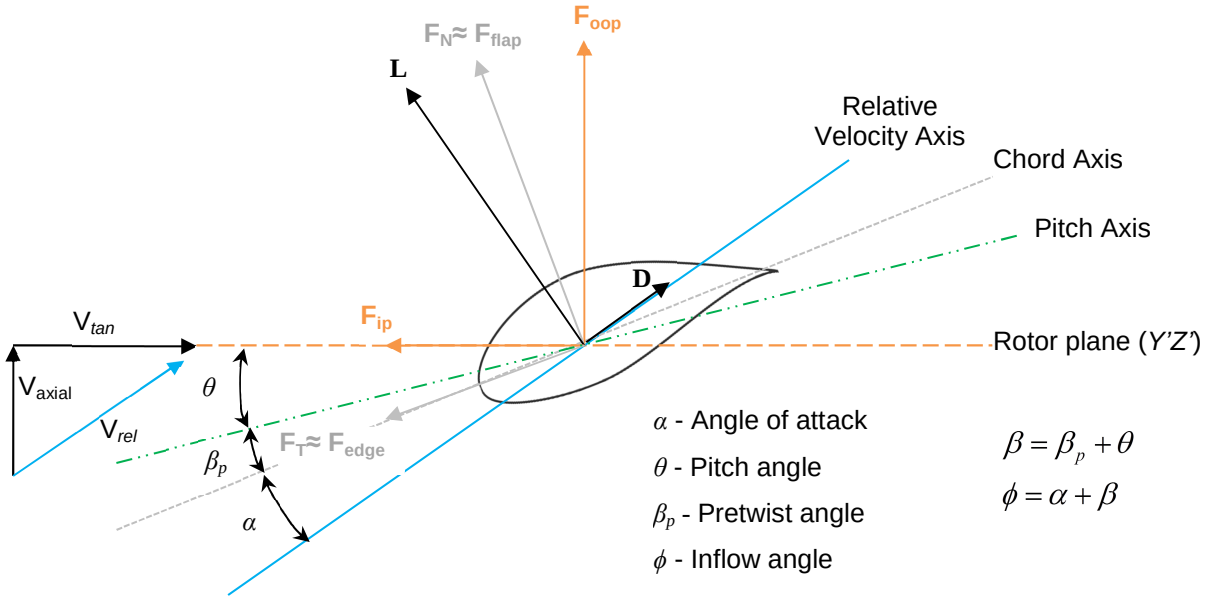


Figure 2.4 - Aerofoil coordinate system

## 2.3 Steady State Blade Element Momentum Theory (BEMT)

This Section gives a general overview of the steady state blade element momentum theory (BEMT) as it can be found in the literature. BEMT is a two-dimensional steady state based aerodynamic evaluator for propellers and is by far the most common method used for calculating the performance of wind turbines. Although more advanced methods such as Computational Fluid Dynamics (CFD) are available, the simplicity, computational efficiency and insightful features of BEMT-based codes are often preferred (Leishman, 2002). CFD is probably the most accurate method for evaluating the aerodynamic performance of wind turbines as long as the three-dimensional effects such as dynamic stall and vortical wake resulting from the blades' rotations are accurately predicted (Leishman, 2002). Even though CFD methods are certainly attractive, CFD wind turbine models have not yet reached the necessary level of computational efficiency for design purposes and time dependent analyses. Consequently, there is value in the development of simpler models employing a BEMT-based core in order to enable the evaluation of developing ideas at reasonable computing efforts (Buhl, 2004, Jonkman and Buhl, 2005, Leishman, 2002, Resor et al., 2010, Barlas et al., 2013).

The general procedure used for solving the steady state BEMT is now explained (Moriarty PJ and Hansen AC, 2005, Buhl ML, 2004). BEMT postulates the effects of the presence and the rotation of wind turbine blades on the flow field around the rotor by introducing and calculating the field of induced velocities. This evaluation is based on an iterative algorithm in which the induced velocities are initially assumed and re-calculated by iteration. In BEMT each blade is divided into segments used to approximate the two-dimensional aerodynamic forces along the blade span as illustrated in Figure 2.5. The flow kinematics of each segment are assumed to be independent of that of the other segments. When analysing each segment of the blade, BEMT deals with 6 unknown parameters. These unknowns are the axial induction factor ($a$), rotational induction factor ($a'$), inflow angle ($\phi$), angle of attack ($\alpha$), and lift and drag coefficients ($C_L$ and $C_D$). For a segment centred at span *r*, these unknowns are correlated through a set of two discrete data equations ($C_L(\alpha)$ and $C_D(\alpha)$ lookup tables) and four algebraic equations (Maheri et al., 2006b):

$$\phi = \phi\,(a, a', \mathrm{k}_f, \mathrm{k}_r) \tag{2.1}$$

$$\alpha = \alpha\,(\phi, \mathrm{k}_f, \mathrm{k}_r) \tag{2.2}$$

$$a = a\,(C_L\,, C_D, \phi, \mathrm{k}_f, \mathrm{k}_r) \tag{2.3}$$

$$a' = a'\,(a\,, C_L\,, C_D, \phi, \mathrm{k}_f, \mathrm{k}_r) \tag{2.4}$$

$$C_L = C_L\,(\alpha) \tag{2.5}$$

$$C_D = C_D\,(\alpha) \tag{2.6}$$

where $\mathrm{k}_f$ and $\mathrm{k}_r$ are subsets of known fixed parameters $\mathrm{k}_f = \{w_{rot}, \#\,Blades, R, \rho\}$ and known $r$-dependent parameters $\mathrm{k}_r = \{r, V_\infty, c, \beta\}$ respectively.


Figure 2.5 - Typical blade segments in BEMT

Equations (2.1) to (2.6) form a nonlinear system of equations with two sets of tabulated data that makes BEMT analysis iterative in nature (Maheri et al., 2006b). The induction factors $a$ and $a'$ are the most common choices of iterative parameters (Laino, 2005, Burton et al., 2001, Hau and von Renouard, 2013, Lanzafame and Messina, 2007). BEMT is based on three main assumptions: a steady flow, an infinite number of blades and an axisymmetric flow. However, most of these limitations can be removed by (i) applying some corrections, (ii) averaging, and (iii) employing further assumptions to the original concepts (Maniaci, 2011). For instance, ground shear and rotor misalignment contradict the basic assumption of axisymmetric flow. Dividing the rotor disk area into a number of sectors (i.e. *Nsec*, virtual blades) and averaging the results is a means of including non-axisymmetric effects. Corrections are also required for large induced velocities, tip and hub losses, and skewed wake (Moriarty and Hansen, 2005). Some of the limitations typically encountered by BEMT based codes include calculations for flow dominated by unsteady and three dimensional phenomena (Simms et al., 2001, Yang et al., 2014). Non-axisymmetric rotors, high wind speeds and three dimensional stall are potential sources of discrepancies with experimental data. The accuracy of BEMT predictions strongly depends on the accuracy of the lift and drag coefficients (Tangler, 2002, Tangler and Kocurek, 2005).

Lift and drag steady state aerodynamic coefficients can be obtained by carrying out wind tunnel experiments (Timmer, 2009). Although this may seem the best choice in terms of accuracy, comparison between the data generated with different wind tunnels can also show discrepancies (McCroskey, 1987, Duraisamy et al., 2007). Experimental testing is also the most expensive means of generating aerodynamic data. By contrast, computer based codes are inexpensive for generating aerodynamic coefficients. XFoil (Drela, 1989) is one of the well-known freeware using the panel method to calculate aerofoils' aerodynamic coefficients. The NACA 64-618 aerofoil shown in Figures 2.6 is of particular interest to this research since it is the tip aerofoil of the 5 MW wind turbine case study investigated later on. We, therefore, evaluate the accuracy of XFoil in predicting the aerodynamic coefficient of this aerofoil as presented in Figures 2.7 and 2.8 for the lift and drag coefficients respectively.

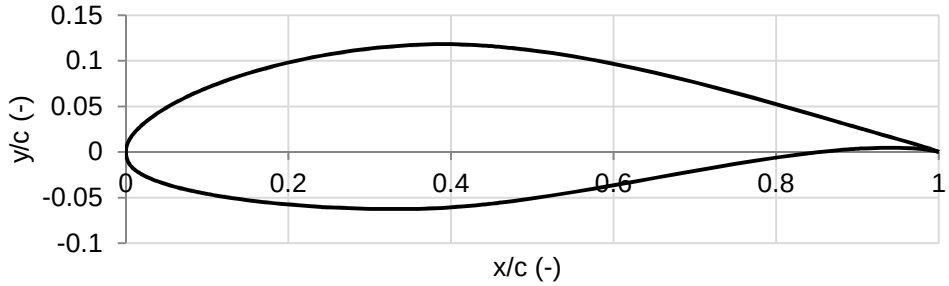

Figure 2.6 - NACA 64-618 aerofoil normalised coordinates

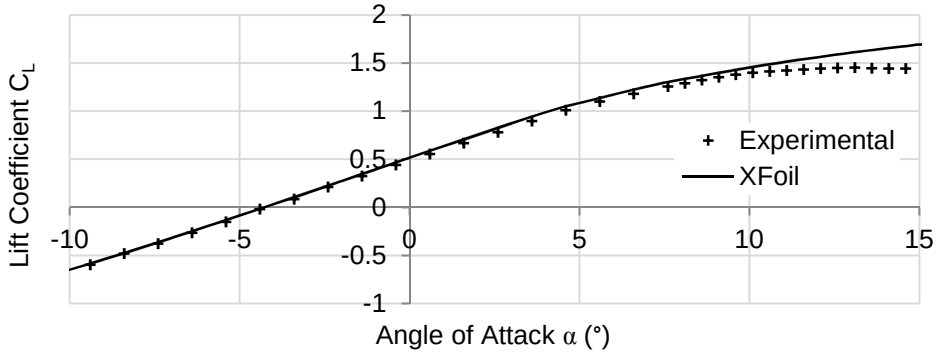

Figure 2.7 - NACA 64-618 lift coefficient, Re= $6.5\times10^6$. Experimental results (Timmer, 2009)

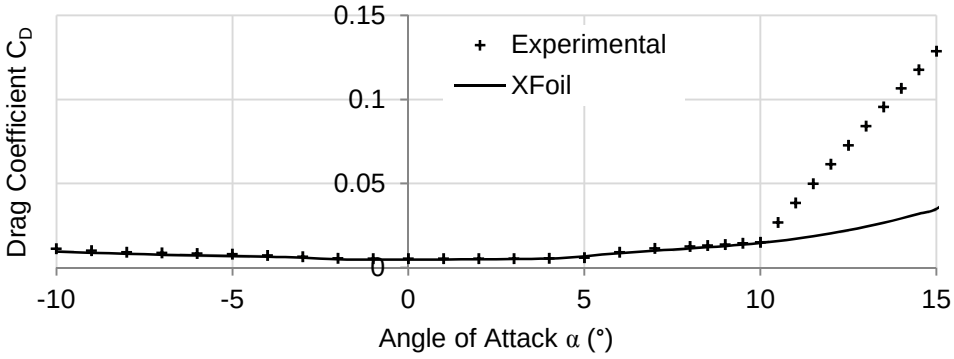

Figure 2.8 - NACA 64-618 drag coefficient, Re= $6.5\times10^6$. Experimental results (Timmer, 2009)

Aerofoils' aerodynamic coefficients are generally calculated for pre-stall angles of attack as shown in Figure 2.9. However, aerofoils on wind turbine blades experience a wide range of angles of attack and the pre-stall data are generally extended to post-stall angles of attack by using extrapolation models (Jonkman JM et al., 2009, Buhl, 2004). The NREL code AirfoilPrep (Hansen, 2012) uses the Viterna model (Viterna and Janetzke, 1982) in order to extend the pre-stall data to ± 180° angle of attack as shown in Figure 2.9.

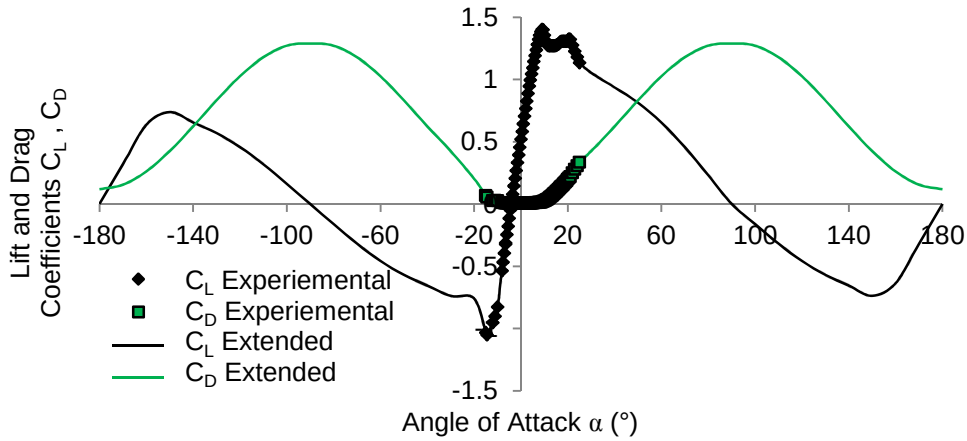


Figure 2.9 - Extension of the experimental aerodynamic coefficient using Viterna's model

Experiments have shown that using two-dimensional aerodynamic coefficients may result in under-prediction of power and thrust (Lindenburg, 2004). The centrifugal and Coriolis effects taking place on rotating wind turbine blades affect the flow dynamics. The Coriolis acceleration term alleviates the adverse pressure gradient and consequently delays flow separation and stall (Snel et al., 1994, Leishman, 2002).. As a result, the lift and drag forces experienced at stalled sections of wind turbine blades (e.g. inboard) are significantly higher than predicted when using two-dimensional data(Merz, 2011). The performance of stall-regulated wind turbines are therefore highly affected by three-dimensional stall (Dumitrescu and Cardos, 2012). Although many attempts to model the three dimensional stall effects have been made (Tangler and Kocurek, 2005, Snel et al., 1994, Corrigan and Schillings, 1994, Du and Selig, 1998, Chaviaropoulos and Hansen, 2000), Breton et al. (Breton et al., 2008) have shown that there are still significant discrepancies between numerical and experimental results. The three-dimensional stall model employed in WTAC is identical to the one used in AirfoilPrep (Hansen, 2012). This model combines Selig Du (Du and Selig, 1998) correction with modifications for the drag coefficient according to Eggers et al (Eggers et al., 2003). Figures 2.10 and 2.11 compare the lift and drag coefficients from two-dimensional data with the corrected data for three dimensional stall.

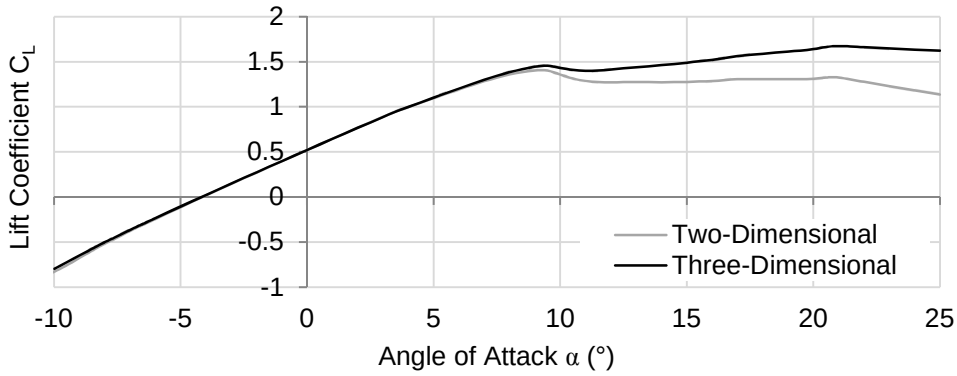


Figure 2.10 - DU21 - A17 two and three-dimensional lift coefficients

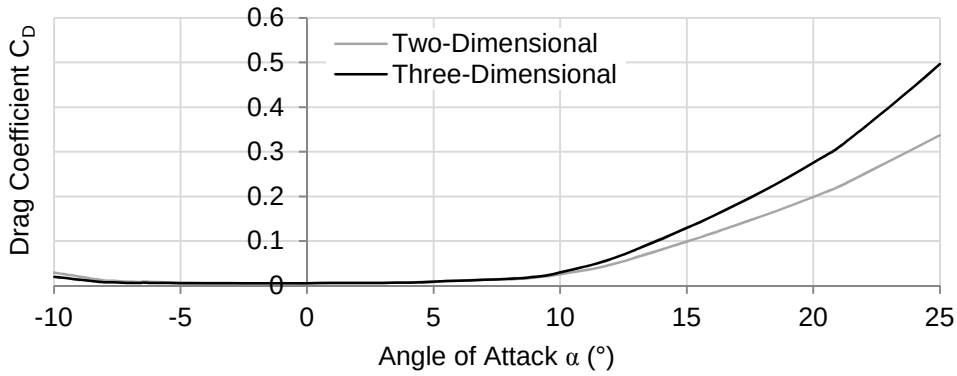


Figure 2.11 - DU21 - A17 two and three-dimensional drag coefficients

## 2.4 Unsteady Blade Element Momentum Theory

Applying the required corrections, a steady BEMT can reasonably predict the annual energy production of wind turbines. However, in order to realistically compute the structural behaviour of wind turbines it is necessary to also include unsteady phenomena. Amongst the various unsteady modifications, those that have been considered in this study (listed in Section 2.1) are presented in this section.

The wind field generator TurbSim developed by the NREL (Foley and Gutowski, 2008) is used to generate unsteady wind fields. TurbSim produces a collection of planes, each containing the vector fields representing the wind velocity vectors over that plane. Each plane is separated by a constant time step as illustrated in Figure 2.12. The unsteady wind fields thereby generated are used as input to wind turbine analysis codes suitable for Taylor's frozen turbulence hypothesis model (e.g. WTAC and AeroDyn (Laino, 2005)).

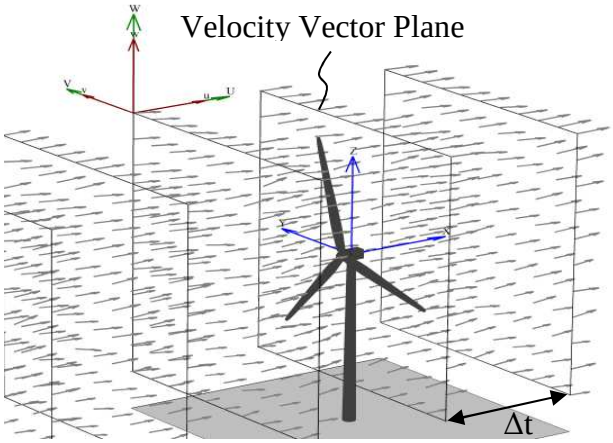


Figure 2.12 - Wind field output generated by TurbSim (Foley and Gutowski, 2008)

The non-moving sectors used in the classic BEMT are replaced by rotating blades in order to simulate the blades' cyclic loading and rotational effects. The blades' spatial positions are calculated based on the tilt, yaw, cone, and azimuth angles. The local relative velocity along each blade is then obtained through space-time interpolation with the wind field.

**Dynamic Stall**

In contrast to static stall, dynamic stall occurs when the aerofoil angle of attack rapidly changes due to flow unsteadiness or structural vibrations. Experiments (Andersen et al., 2009, Leishman and Beddoes, 1989) have shown that when the angle of attack of an aerofoil rapidly increases above its static stall angle, the flow remains substantially attached to the aerofoil before separating and reaching a steady state. The dynamic stall model proposed by Larsen (Larsen et al., 2007) is used in WTAC. Figures 2.13 and 2.14 compare the steady and dynamic lift coefficients of the aerofoil Vertol 23010-1.58 under cyclic variations of the angle of attack at a reduced frequency (i.e. the cyclic frequency times the chord length divided by two times the velocity) of 0.062.

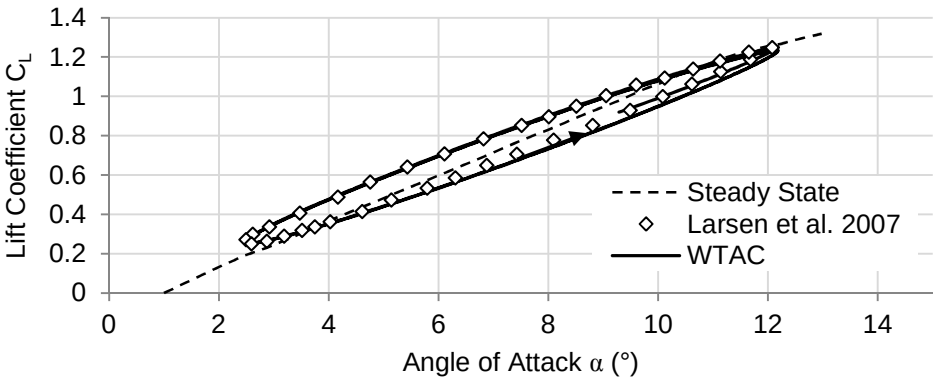


Figure 2.13 - Steady state and dynamic lift coefficients subject to cyclic variations of the angle of attack (pre-stall)

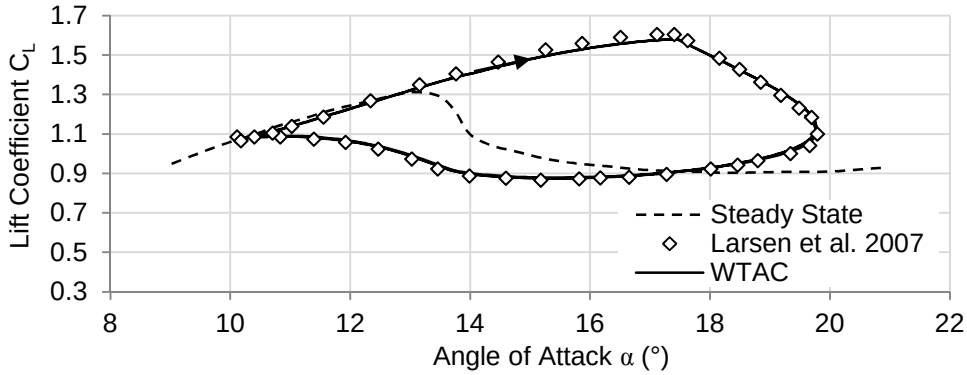


Figure 2.14 - Steady state and dynamic lift coefficients subject to cyclic variations of the angle of attack (stall & post-stall)

Figures 2.15 and 2.16 show a qualitative comparison between the steady and dynamic lift coefficients for a step change of the angle of attack. It can be seen that a step increase of the angle of attack under attached flow results in an increased lift coefficient following the dynamic behaviour of two combined first order differential equations. On the other hand, when the angle of attack abruptly increases above the stall angle one can see that the lift coefficient substantially out-reaches its steady state value as shown in Figure 2.16.

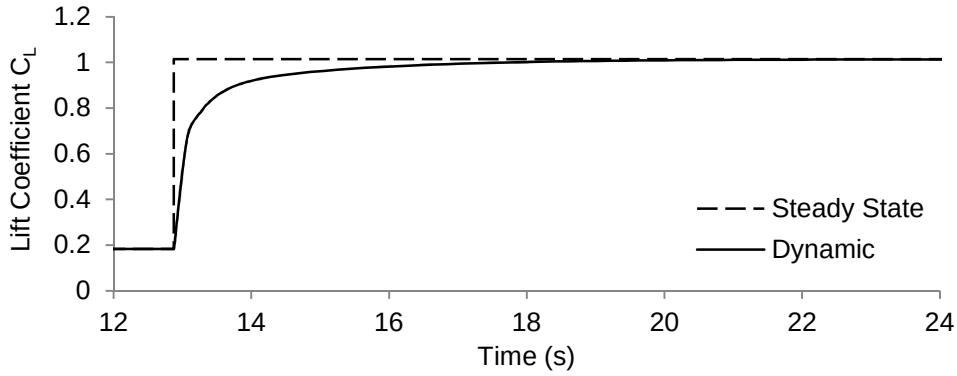


Figure 2.15 - Steady state and dynamic lift coefficient responses to a step change of the angle of attack (pre-stall)

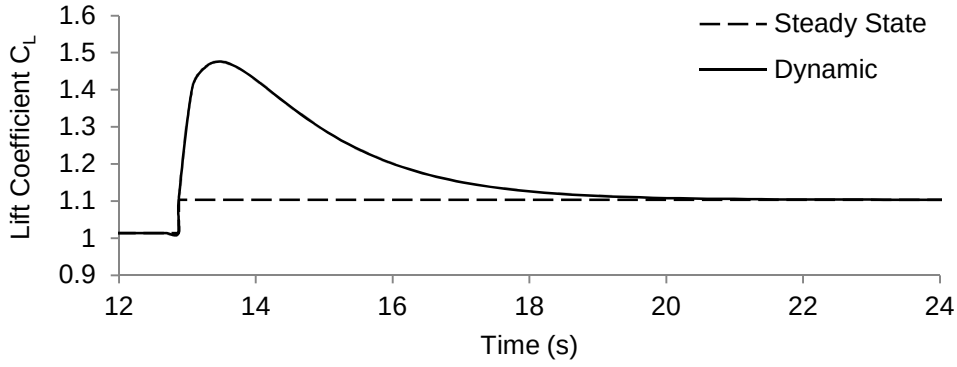


Figure 2.16 - Steady state and dynamic lift coefficient responses to a step change of the angle of attack (stall)

## 2.5 Convergence Accelerator Algorithm (CAA)

The convergence accelerator algorithm (CAA) has been especially developed during this thesis in order to reduce the computational time taken by the unsteady BEMT aerodynamic module. Considering the computational power available to date, using BEMT to find the blade aerodynamic loads for a given wind turbine run condition (wind speed, rotor speed, blade pitch angle, etc.) takes only a fraction of a second. However, when using BEMT as the aerodynamic analyser of a simulation-based optimal design code, this can be very time consuming. Considering this, there is potential interest in reducing the computation time of BEMT. The convergence accelerator algorithm (CAA) is an improvement on the relaxation factor method proposed by Maheri et al. (Maheri et al., 2006a). The fluctuating behaviour of the axial induction factor (see Figure 2.17) is explained as follows. Momentum theory predicts a parabolic variation for thrust coefficient $C_T$ with a maximum value of 1 at $a = 0.5$, while experimental data shows that $C_T$ keeps increasing for $a > 0.5$. For small axial induction factors, $0 < a < a_c \cong 0.4$, known as the light loading state, the predicted thrust coefficient by the momentum theory is in good agreement with experimental data. On the other hand, in the heavy loading state (i.e. $a > a_c$), the predicted $C_T$ departs dramatically from its actual value. For the heavy loading state the momentum-based equation is therefore replaced by the Glauert's empirical formula. Separating light and heavy loading states imposes a singular point of $a_c$ in the domain and therefore when two successive predicted axial induction factors lie in different sides of $a_c$ a fluctuating behaviour, as shown in Figure 2.17, is observed. Fluctuation of the axial induction factor causes unnecessary computation and decreases accuracy when convergence does not occur. The original method proposed by Maheri et al.(Maheri et al., 2006a) consists of using a constant relaxation factor $r_f$ in order to damp these fluctuations. Using a relaxation factor as an intermediary step (2.7) between the current (n) and newly (n+1) calculated induction factor, results in damping the fluctuating behaviour observed and ensures the convergence as shown in Figure 2.18.

$$a_{n+1} = r_f a_{n+1} + \left(r_f - 1\right) a_n; \quad r_f = 0.5 \tag{2.7}$$

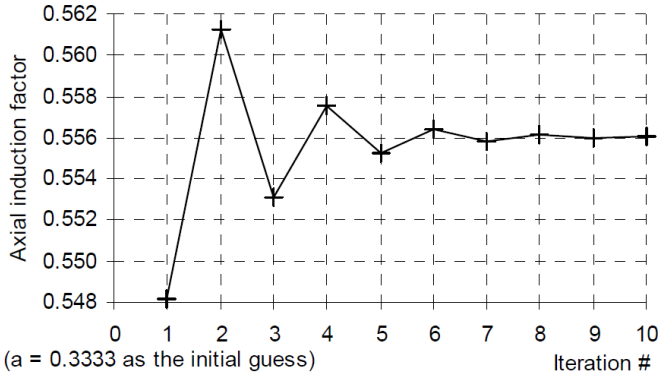


Figure 2.17 - Converging oscillatory behaviour of the axial induction factor (Maheri et al., 2006a)

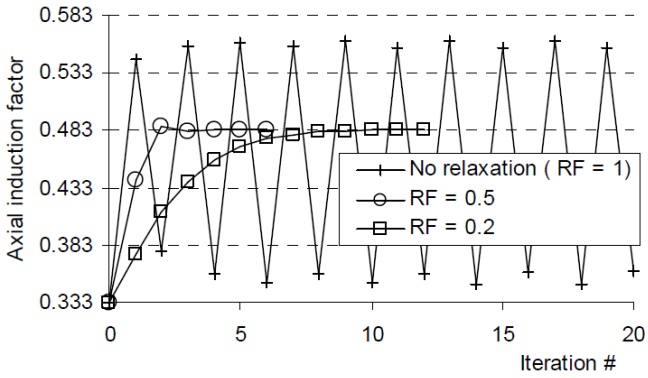


Figure 2.18 - Effect of different values of relaxation factor on the fluctuating behaviour of the axial induction factor (Maheri et al., 2006a)

Employing a relaxation factor guarantees convergence of the solution when fluctuating convergence occurs, however it may result in slower convergence in other conditions. The key improvement of the CAA consists of using a variable relaxation factor depending on the observed type of convergence. The different convergences of the axial induction factor are categorised into four types as shown in Table 2.1. Each behaviour is detected using the history of the axial induction factor using previously computed values. For instance the non-fluctuating slow convergence can be identified via the monotonicity of the axial induction history as shown Table 2.2.

Table 2.1 - Impact of the induction factor behaviour on the time and accuracy of BEMT

| Fluctuating convergence | Increases Computational Time |
|---|---|
| Slow convergence | Increases Computational Time |
| Fluctuating Divergence | Increases Computational Time and reduces accuracy |
| Oscillatory behaviour | Increases Computational Time and reduces accuracy |

Table 2.2 - Detection of the induction factor behaviour

| Behaviour Type | Detection | New value of relaxation factor |
|---|---|---|
| Non-Fluctuating Convergence | $a_k < a_{k-1}$ & $a_{k-1} < a_{k-2}$ *or* $a_k > a_{k-1}$ & $a_{k-1} > a_{k-2}$ | 1 |
| Fluctuating Divergence | $a_k < a_{k-1}$ & $a_k < a_{k-2}$ *or* $a_k > a_{k-1}$ & $a_k > a_{k-2}$ | 0.4 |
| Fluctuating Convergence | $a_k < a_{k-2}$ & $a_k > a_{k-1}$ & $a_{k-1} < a_{k-2}$ & $a_{k-2} > a_{k-3}$ | 0.5 |

The CAA is compared to the classic BEMT iteration loop and the original method proposed by Maheri et al. (Maheri et al., 2006a) using the NREL 5 MW wind turbine design (Jonkman et al., 2009). Figures 2.19 and 2.20 compare the convergence between the different methods for fluctuating and non-fluctuating convergences. As can be observed in both cases, the CAA achieves faster convergence by choosing the appropriate relaxation factor. In Figure 2.19 both methods converge faster than the classic iteration loop by damping the oscillations. In Figure 2.20 the CAA converges faster by detecting the slow convergence and using the maximal relaxation factor. Additionally, Figure 2.21 shows the average number of iterations required per segment for the iteration loop to converge as a function of the wind speed. Noticeably, the solution proposed by Maheri et al. (Maheri et al., 2006a) accelerates convergence for low wind speeds while slowing it down for higher wind speeds. The CAA clearly out-performs both methods.

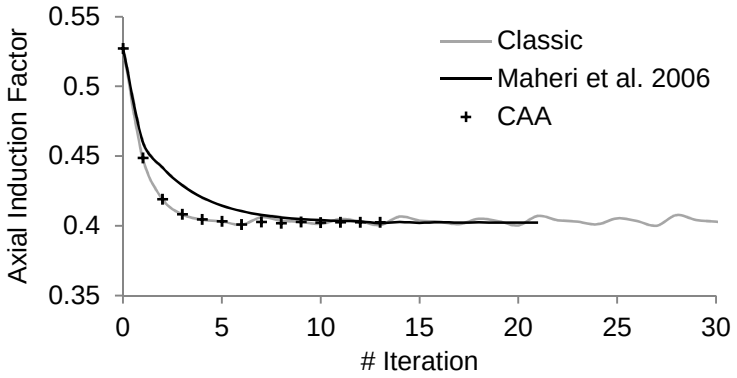

Figure 2.19 - Fluctuating convergence of the axial induction factor

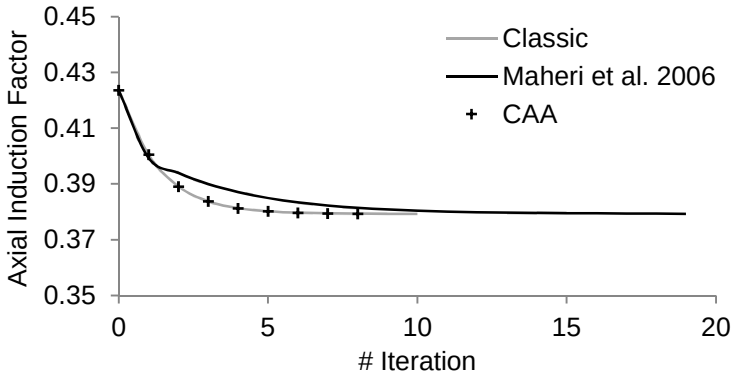


Figure 2.20 - Non-fluctuating convergence of the axial induction factor

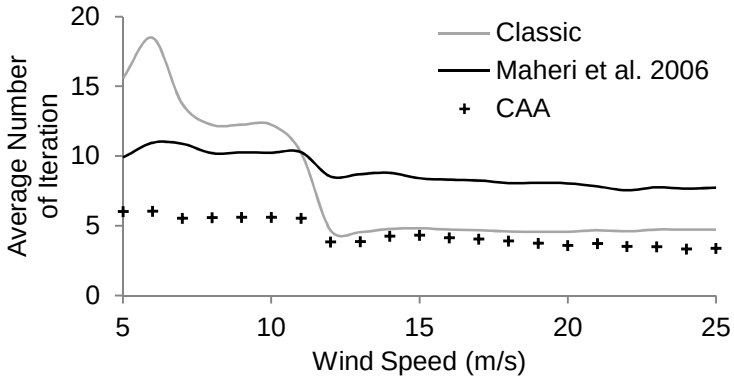


Figure 2.21 - Average number of iterations to convergence

## 2.6 WTAC - Aerodynamic Module Validation

Figure 2.22 summarises all the modifications that have been integrated to the original steady BEMT code WTAero (Maheri et al., 2006b) during the course of this PhD.

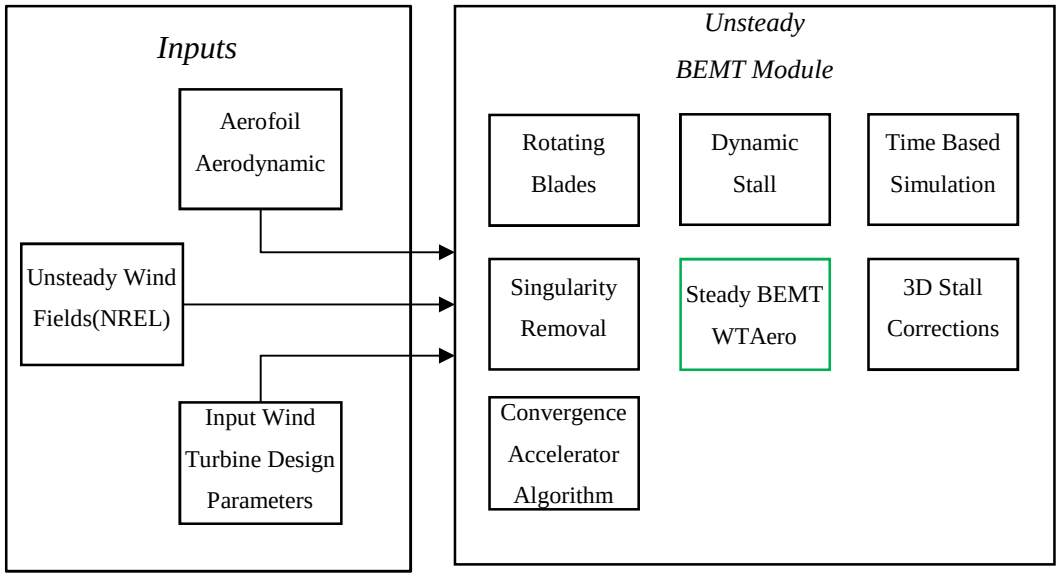


Figure 2.22 - WTAC unsteady BEMT features added to WTAero

In this section WTAC predictions are compared against the NREL code WT_Perf (Buhl, 2004). Three wind turbine case studies are compared:

- The constant-speed stall-regulated 300 kW AWT-27 wind turbine (Poore, 2000)
- The variable-speed pitch-controlled 1.5 MW WindPACT wind turbine (Malcolm and Hansen, 2002)
- The variable-speed pitch-controlled 5 MW NREL wind turbine (Jonkman et al., 2009)

Figures 2.23 and 2.24 compare the power and thrust curves predicted by WT_Perf and WTAC for the AWT-27 wind turbine. As these figures show, the two software predictions agree. For the control values (i.e. pitch and rotor rpm) shown in Figure 2.25, the power and thrust curves for the WindPACT 1.5 MW are respectively presented in Figures 2.26 and 2.27. Similarly, the NREL 5 MW wind turbine control values (i.e. pitch and rpm), power and thrust curves are also presented in Figures 2.28 to 2.30. It can be observed that the steady state predictions between WT_Perf and WTAC agree well for the three case studies.

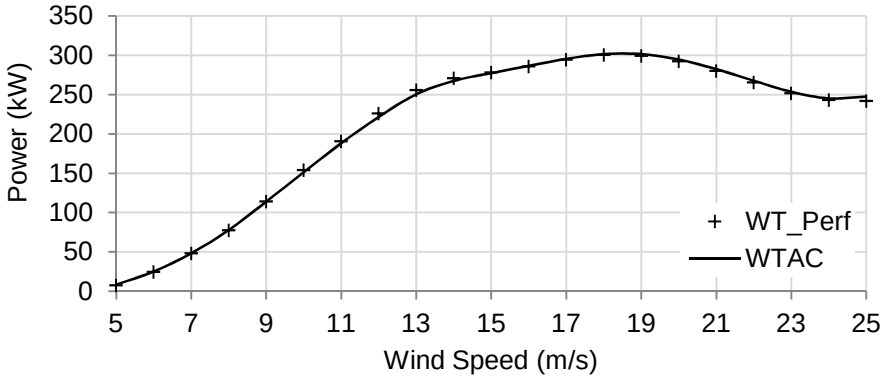

Figure 2.23 - AWT-27 power curve

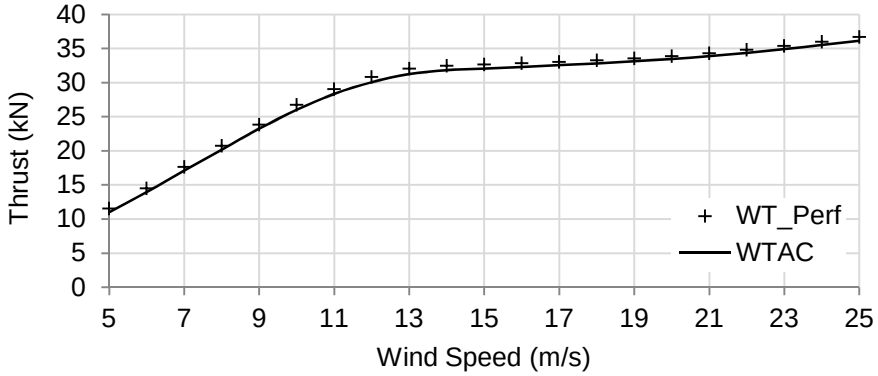

Figure 2.24 - AWT-27 thrust curve

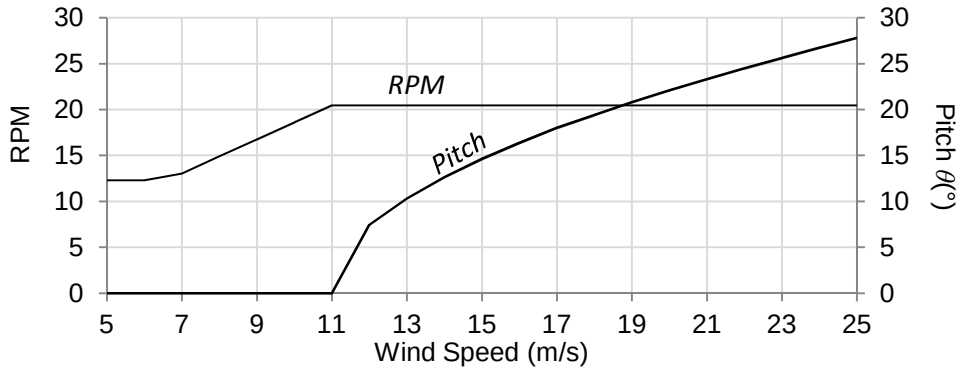

Figure 2.25 - WindPACT 1.5 MW control parameters (Malcolm and Hansen, 2002)

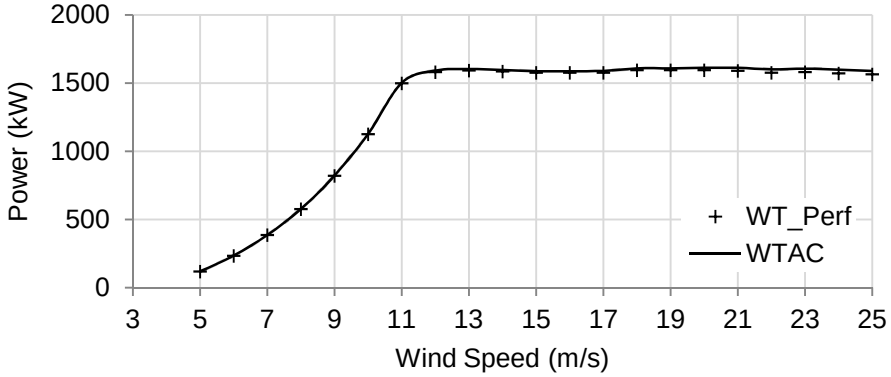

Figure 2.26 - WindPACT 1.5 MW power curve

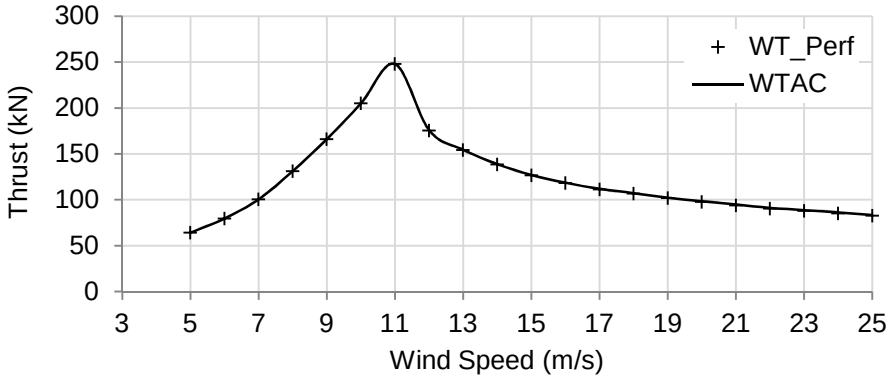

Figure 2.27 - WindPACT 1.5 MW thrust curve

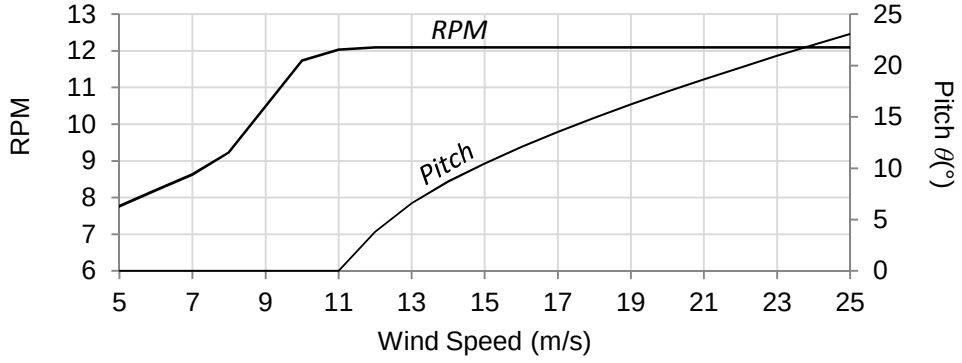

Figure 2.28 - NREL 5 MW control parameters (Jonkman et al., 2009)

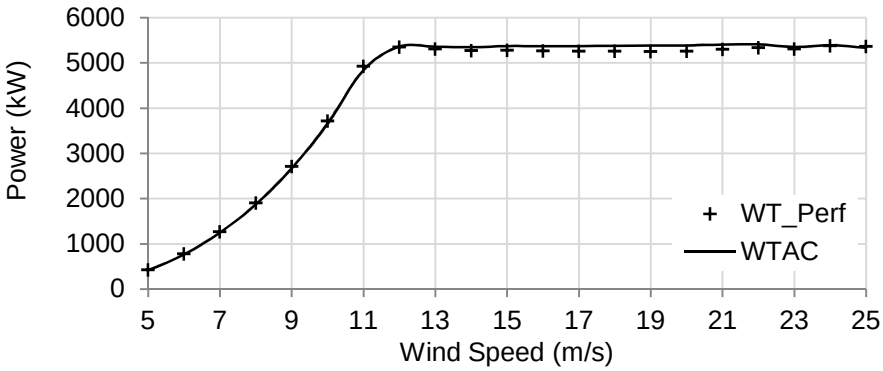

Figure 2.29 - NREL 5 MW power curve

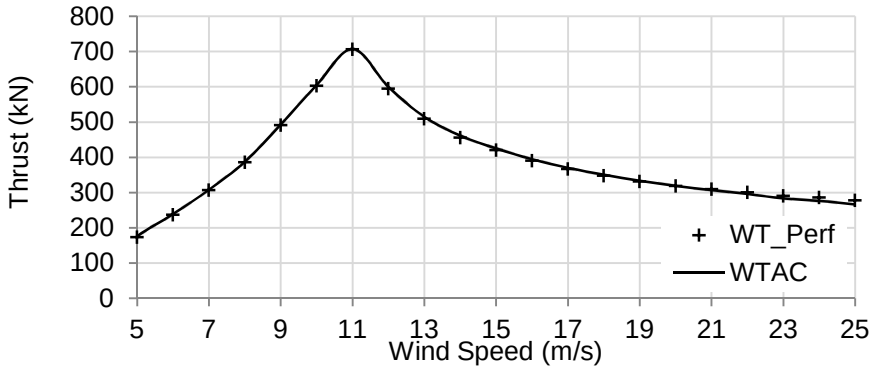

Figure 2.30 - NREL 5 MW thrust curve

In addition to the steady state results, the dynamic power and thrust generated by the NREL 5MW wind turbine under windshear are shown in Figures 2.31 and 2.32. As expected due to the windshear, the power and thrust experienced by each of the three blades is out of phase by 120 degrees and the summation of the power and thrust produced by the three blades is equal to the predicted quasi-steady state value.

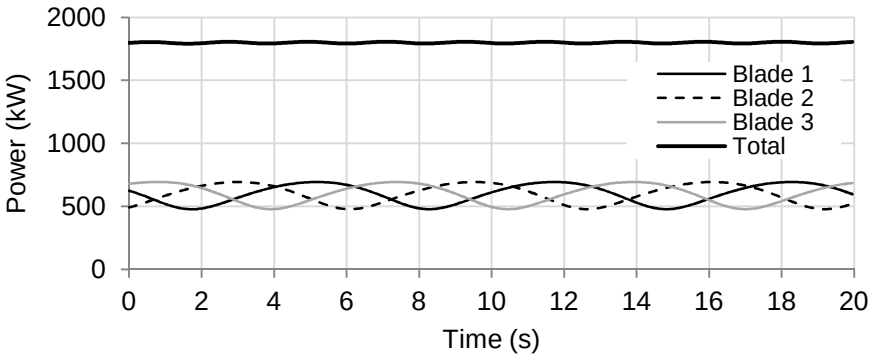

Figure 2.31 - WTAC power prediction for the NREL 5 MW wind turbine

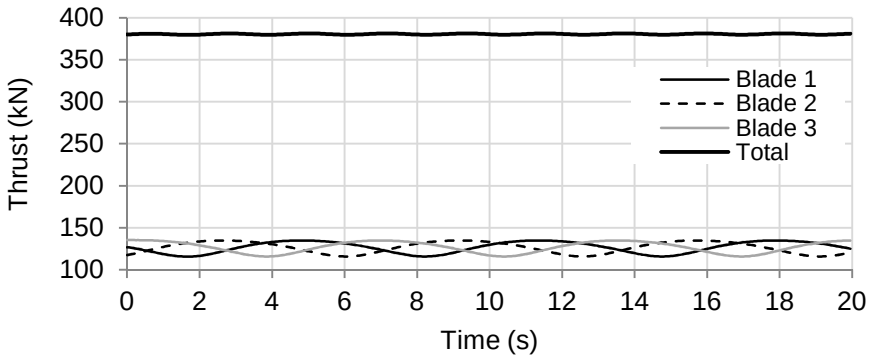

Figure 2.32 - WTAC thrust prediction for the NREL 5 MW wind turbine

## 2.7 Summary - Aerodynamic Module

The present chapter served as a brief reminder of wind turbine dynamics and as an introduction to the wind turbine unsteady BEMT simulator included in WTAC. The unsteady aerodynamic module developed during this PhD is the evolution of the original steady state BEMT code WTAero. The WTAC unsteady aerodynamic model is coupled with the wind field generator TurbSim and includes unsteady dynamics such as dynamic stall and three-dimensional stall corrections for rotating blades.

In this chapter, it was shown that the NACA 64-618 aerofoil aerodynamic data obtained using XFoil was satisfactory and could be used in this study. Additionally, a convergence accelerator algorithm was proposed and shown to improve the accuracy and computational efficiency of the BEMT iteration loop. Finally, the steady state results of the WTAC aerodynamic module were evaluated against the NREL code WT_Perf and it was shown that WTAC can be used for the aerodynamic analysis of wind turbines.

# 3. Microtab and Trailing Edge Flap Transient Aerodynamic Models

## 3.1 Introduction

This chapter presents the steady state and transient aerodynamic models of aerofoils equipped with microtabs and trailing edge flaps that have been developed during the course of this PhD. These aerodynamic models are necessary in order to evaluate the potential load alleviation of CSs while taking into account aerodynamic lags. While the optimal positioning of CSs is investigated later on in Chapter 5, it is known that CSs should be located in the blades' aerodynamic region of efficiency (i.e. from mid-span to tip). In this region of the blades, aerofoils are generally of medium or thin thickness (i.e. normalised thickness < 25%) and the flow remains attached during the wind turbine operating conditions (i.e. pitch to feather control). This is clearly visualised in Figure 3.1 which plots the average angle of attack distribution along the NREL 5MW (Jonkman et al., 2009) wind turbine blade span. As a result, the aerodynamic tools and models presented in this chapter are developed for attached flow conditions.

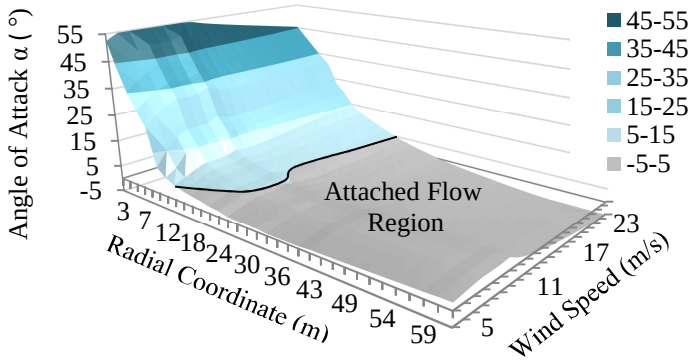


Figure 3.1 - Average angle of attack distribution along the NREL 5 MW wind turbine blades (generated using WTAC)

## 3.2 Aerofoil Lift and Drag Coefficients

Where no experimental data is available, the steady state aerodynamic coefficients of aerofoils are obtained using numerical methods (e.g. panel method, CFD). XFoil is a well-known code developed for the purpose of analysing two-dimensional aerofoils under subsonic flow using the panel method (Drela, 1989). The extensive experimental and numerical comparison conducted by Bertagnolio et al. (Bertagnolio et al., 2001) is one of the many published works that shows XFoil to be sufficiently accurate for thin aerofoils under attached flow regime. The general procedure used to generate the lift and drag coefficients of

a given aerofoil is illustrated in Figure 3.2. Figure 3.3 shows the lift coefficient look-up table for the aerofoil DU93_W210 equipped with a plain trailing edge flap.

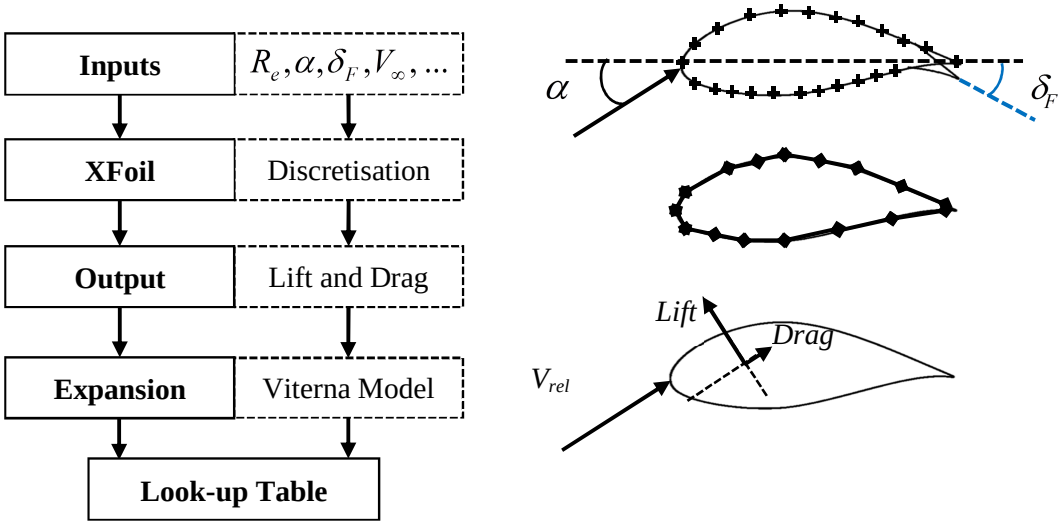


Figure 3.2 - Procedure to generate aerodynamic lookup tables for aerofoils using XFoil

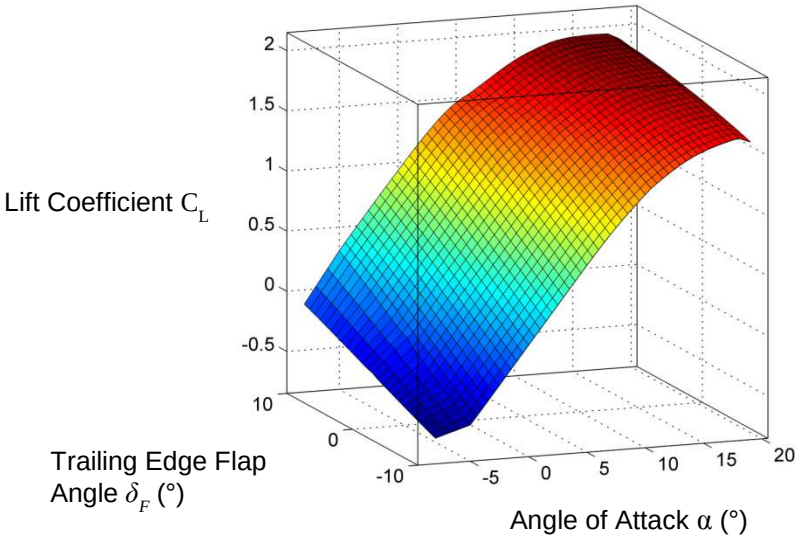


Figure 3.3 - Lift coefficient lookup table (aerofoil DU93_W210 equipped with a trailing edge flap, $Re = 6 \times 10^6$)

The aerodynamic performance of wind turbine blades varies with the magnitude of the flow velocity (i.e. axial and tangential velocities). Using the NREL 5 MW wind turbine as a case study, the differences in flow experienced along the blades' span are characterised by variations of the Reynolds number as shown in Figure 3.4. It can be seen that the Reynolds number remains high (i.e. $Re > 10^6$) over the majority of the wind turbine operating range. Furthermore, the aerodynamic performance of aerofoils operating under attached flow and high Reynolds numbers is little changed by variations of the Reynolds number as illustrated

Figure 3.5. Consequently, it is decided that for the NREL 5 MW wind turbine case study an average Reynolds number (e.g. of 6 million) will used during the aerofoil aerodynamic coefficient calculations.

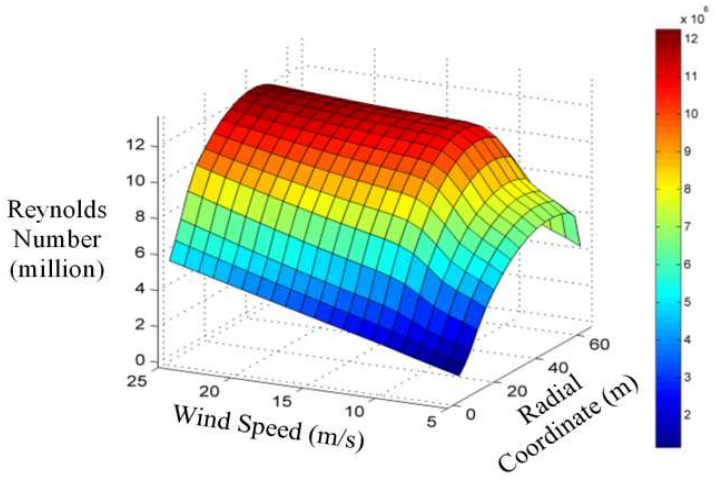


Figure 3.4 - Reynolds numbers experienced by the NREL 5 MW wind turbine blades (generated using WTAC)

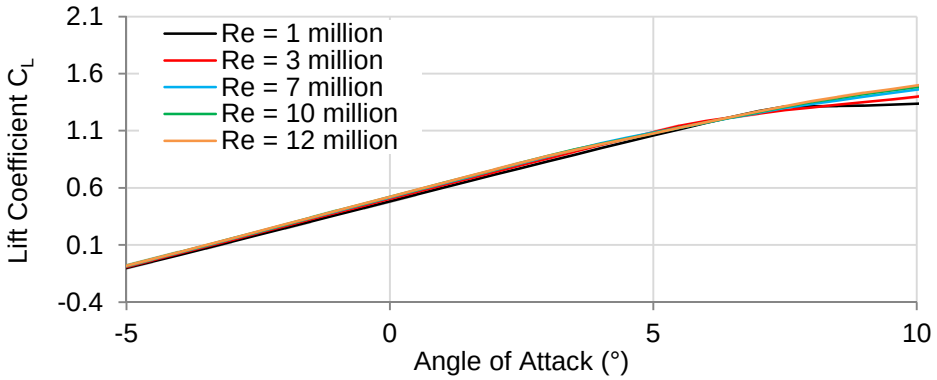


(a)

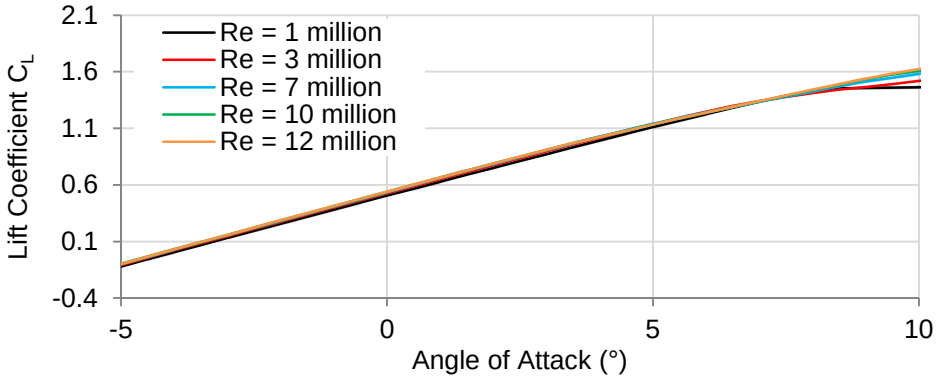


(b)

Figure 3.5 - NACA 64-618 and DU 21-A17 aerofoil sensitivity to Reynolds number (generated using XFoil)

In order to ensure that XFoil will provide accurate aerodynamic coefficients for the NREL 5 MW wind turbine aerofoils, three aerofoils, namely the NACA64-618, DU 93-W-250 and

DU 99-W-350, are used for benchmarking. These aerofoils are respectively located at the tip, middle and root of the blade. The following figures compare results generated using XFoil with experimental data reported in the literature (Kooijman et al., 2003). The contours of the three aerofoils are shown in Figure 3.6. The respective lift and drag coefficients for each aerofoil are presented through Figures 3.7, 3.8, and 3.9. With these comparisons, it is shown that XFoil can reasonably predict the aerodynamic coefficients of the NREL 5 MW wind turbine aerofoils for angles of attack between $[-5, 10]$ degrees.

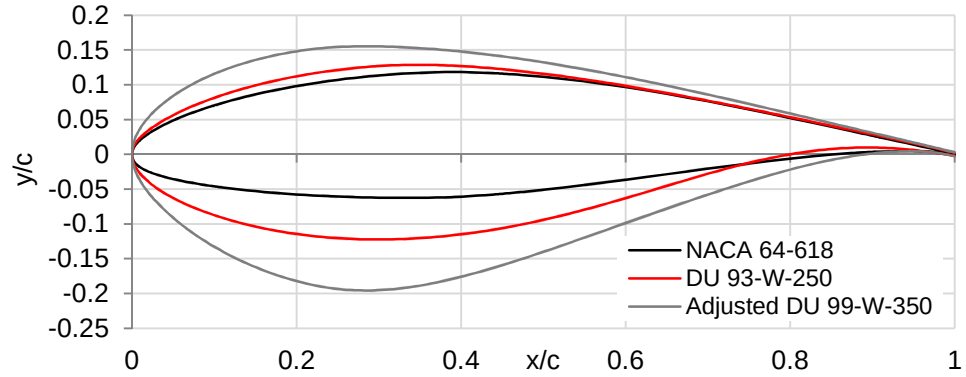


Figure 3.6 - Aerofoils contours

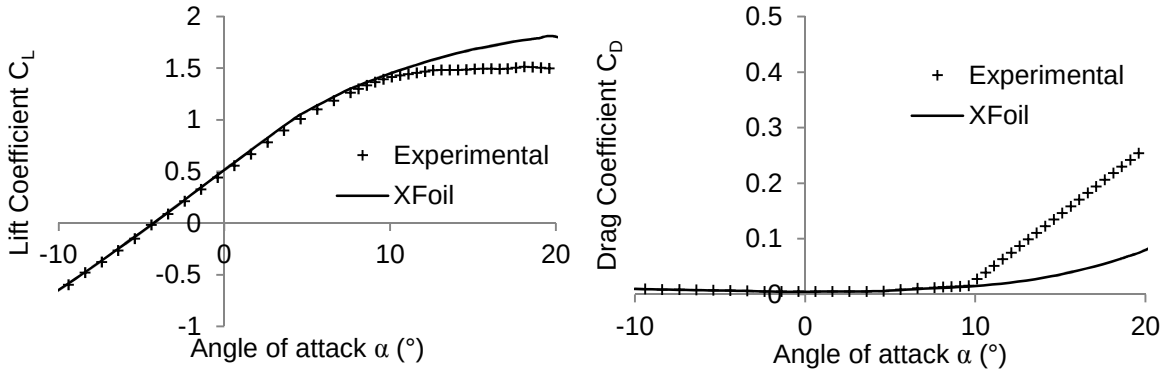


Figure 3.7 - Aerodynamic coefficients of the NACA 64-618 aerofoil
(Re = $6\times10^6$, experimental results from Kooijman et al. 2003)

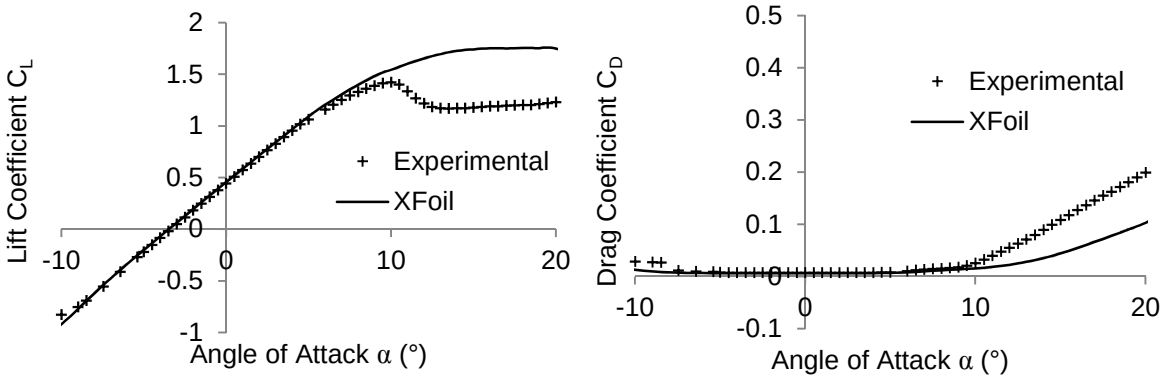

Figure 3.8 - Aerodynamic coefficients of the DU 93-W-250 aerofoil
(Re = $6\times10^6$, experimental results from Kooijman et al. 2003)

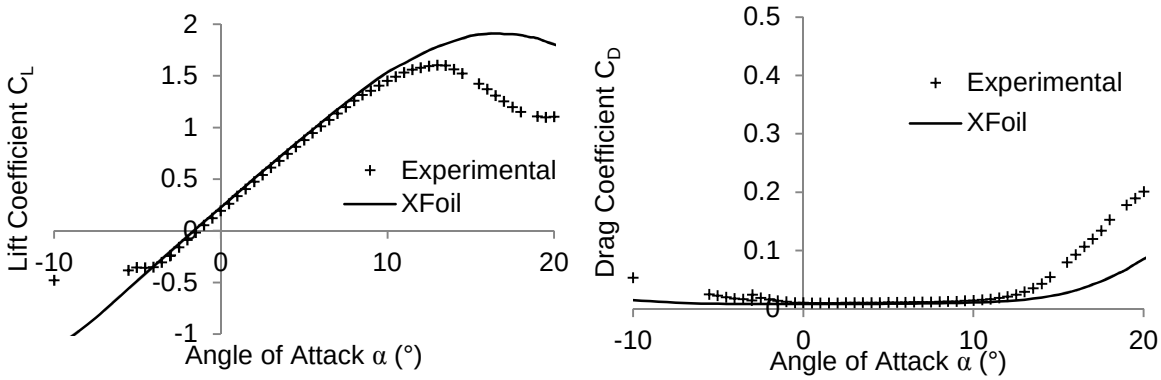


Figure 3.9 - Aerodynamic coefficients of the adjusted DU 99-W-350 aerofoil
(Re = $6\times10^6$, experimental results from Kooijman et al. 2003)

The outer blade part of variable-speed pitch-controlled wind turbines mostly operates under attached flow conditions. Although it is known that XFoil does not provide accurate results for thick aerofoils and high angles of attack, aerofoils located towards the root of wind turbine blades are mainly operating under these conditions (see Figure 3.1). We, therefore, investigate the error induced by XFoil inaccuracies when evaluating the performance of wind turbines. The NREL 5MW wind turbine is used as a case study. The original lift and drag coefficients of the six aerofoils making up the blades are replaced by the coefficient generated by XFoil. The two power curves for both the original data and XFoil generated data are presented in Figure 3.10. It can be observed that the errors induced by XFoil predictions (i.e. toward root) have a negligible effect on power calculations.

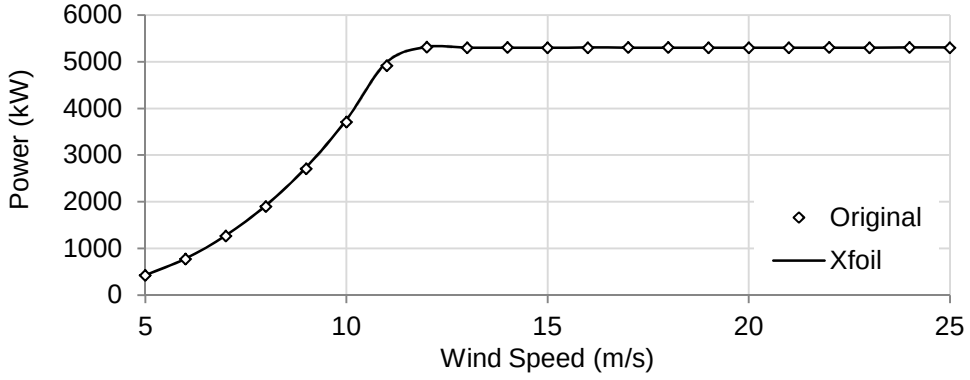


Figure 3.10 - NREL 5 MW wind turbine power curve

## 3.3 Microtab

Microtabs have been the subject of several numerical and experimental investigations. Experiments and simulations, in particular for the S809 and DU-96-W-180 aerofoils, have shown that microtab heights above 2% of the chord length results in a significant increase in drag (Van Dam et al., 2002, Baker et al., 2007). Furthermore, a 1% height microtab located at 95% of chord of the pressure side of the S809 has been shown to provide a good (≈ 50) lift/drag trade-off. The NREL 5MW wind turbine blade tip aerofoil (i.e. the NACA 64-618) is chosen to illustrate the method used to obtain the microtabs' steady state aerodynamic coefficients. This aerofoil, compared to S809 is thinner and towards the trailing edge has a different curvature on the lower surface as shown in Figure 3.11.

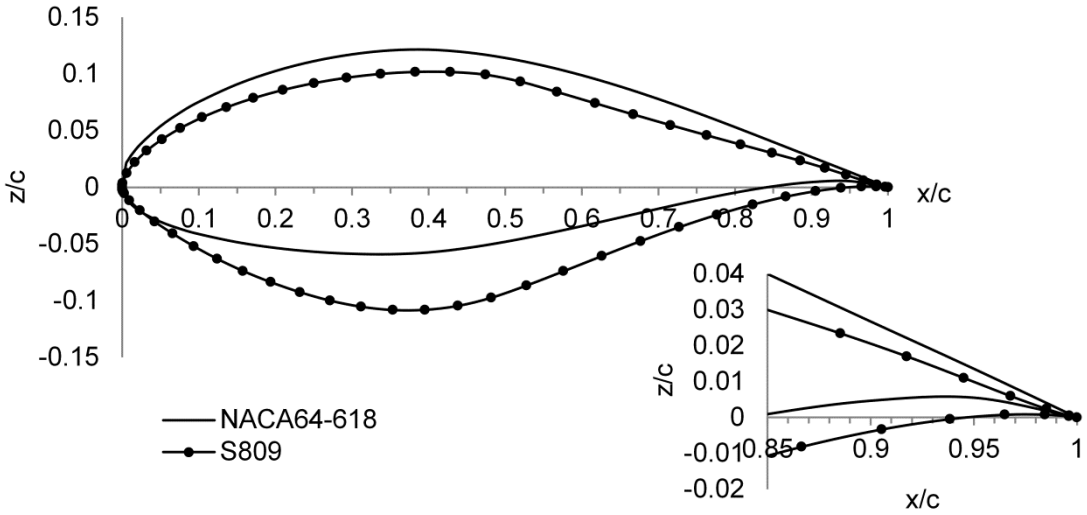


Figure 3.11 - Aerofoils S809 and NACA 64-618 profiles

### 3.3.1 Microtab Steady State Aerodynamic Model

Two dimensional analyses of aerofoils equipped with microtabs are carried out to generate the steady state coefficients required for control purposes. Microtabs introduce a geometric discontinuity of the aerofoil contour which does not lend itself to panel-based solvers. Instead, CFD is chosen to compute the steady state microtab lift and drag coefficients. The baseline aerofoil contour is modified in SolidWorks in order to integrate the microtab as illustrated in Figure 3.12. As shown in this figure, both the microtab maximal height $H_M$ and location the aerofoil leading edge $C_M$ are parameters to be set. From SolidWorks, the geometry is imported into ICEM CFD 13.0 and create a C-mesh grid (Bæk et al., 2010) as shown in Figure 3.13 and Figure 3.14. A typical grid contains about 80000 nodes and extends 12 chords before and after the aerofoil. Once the mesh is complete, it is imported into

ANSYS Fluent for CFD simulations. Mesh sensitivity analysis and convergence comparison studies between the several solvers and experimental data are then carried out. It was generally found that the results obtained using CFD simulations with the k-ω SST model were the most accurate when compared with experimental data as shown in Figures 3.15 and 3.16.

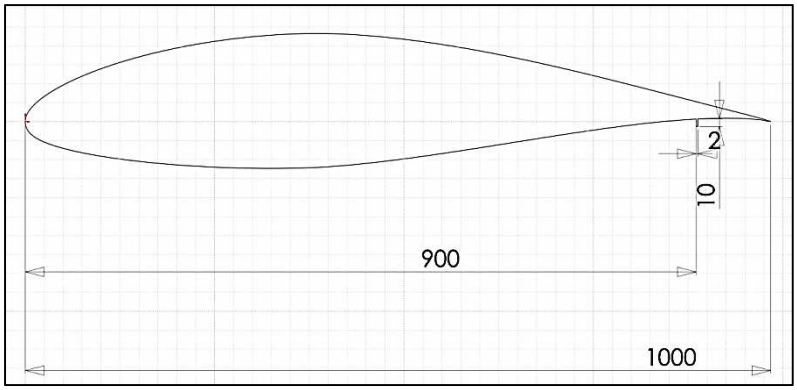

Figure 3.12 - SolidWorks two dimensional sketch of a NACA 64-618 aerofoil equipped with microtabs

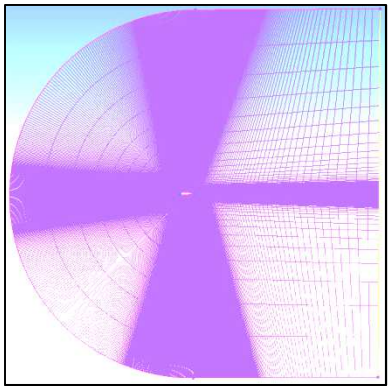
Figure 3.13 - ICEM meshing for a NACA 64-618aerofoil equipped with a microtab

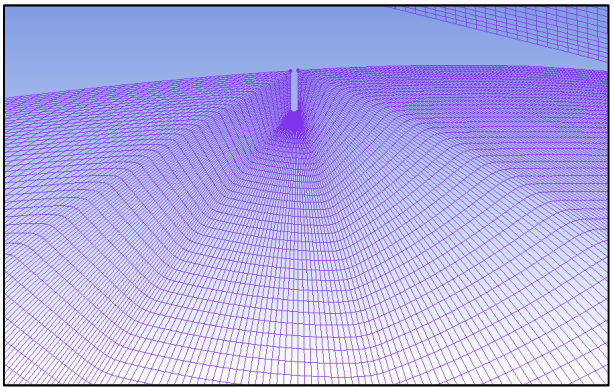
Figure 3.14 - ICEM meshing for a NACA 64-618 aerofoil equipped with a microtab (zoom in)

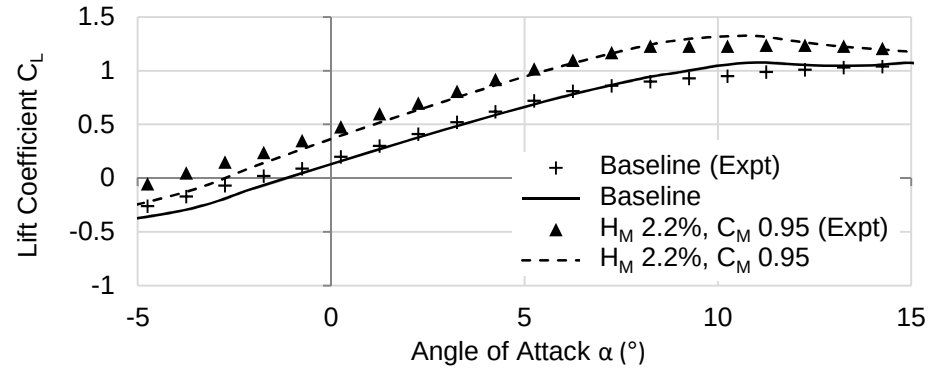


(a)

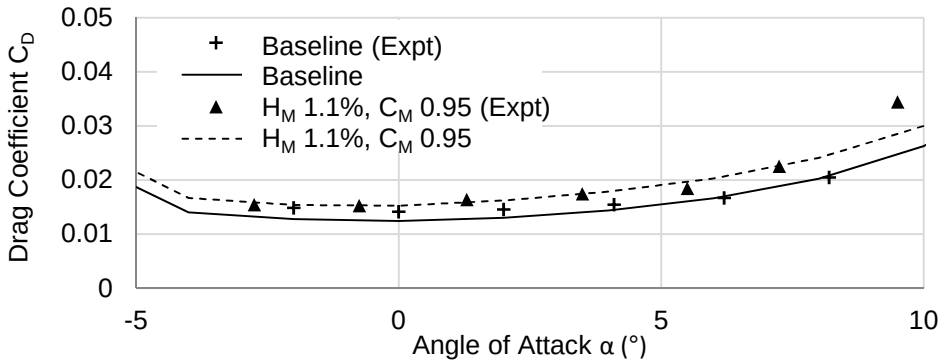


(b)

Figure 3.15 - Experimental (Zayas et al., 2006) and numerical (a) lift and (b) drag coefficients (S809 aerofoil equipped with a microtab on the pressure side, Re = $6\times10^6$, k-ω SST model)

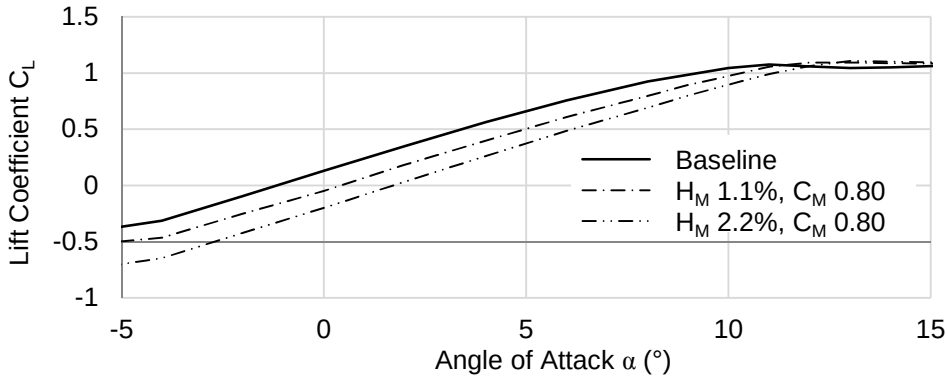


(a)

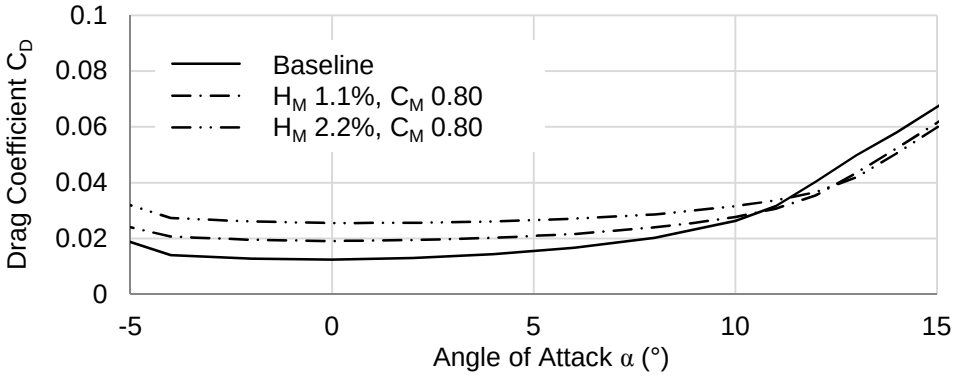


(b)

Figure 3.16 - Numerical (a) lift and (b) drag coefficients
(S809 aerofoil equipped with a microtab on the suction side, Re = $6\times10^6$, k-ω SST model)

Following the same procedure, the two-dimensional CFD analyses for several deployment heights and chord locations of microtabs on the NACA 64-618 aerofoil are carried out. Figure 3.17 shows the lift and drag coefficients for the microtab located on the pressure side and Figure 3.18 presents the results for the microtab positioned on the suction side of the aerofoil.

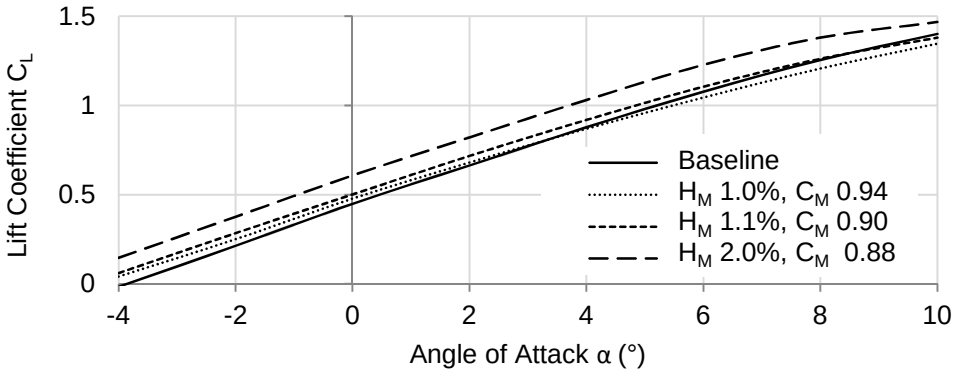


(a)

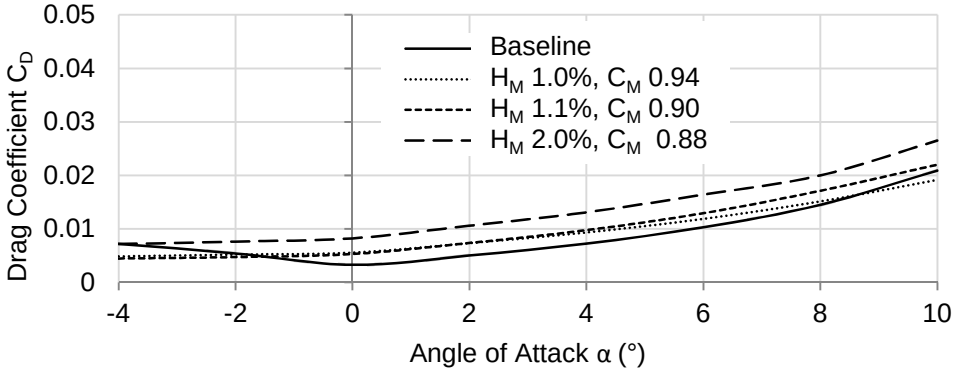


(b)

Figure 3.17 - Steady state (a) lift and (b) drag coefficients
(NACA 64-618aerofoil equipped with a microtab on the pressure side, Re = $6\times10^6$, k-ω SST model)

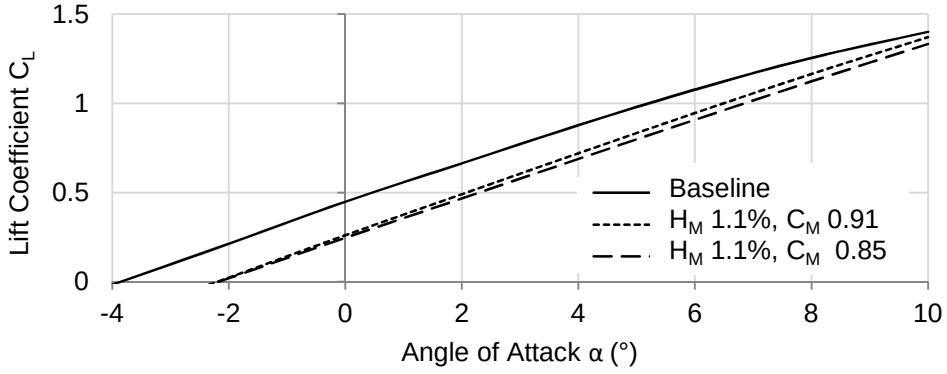


(a)

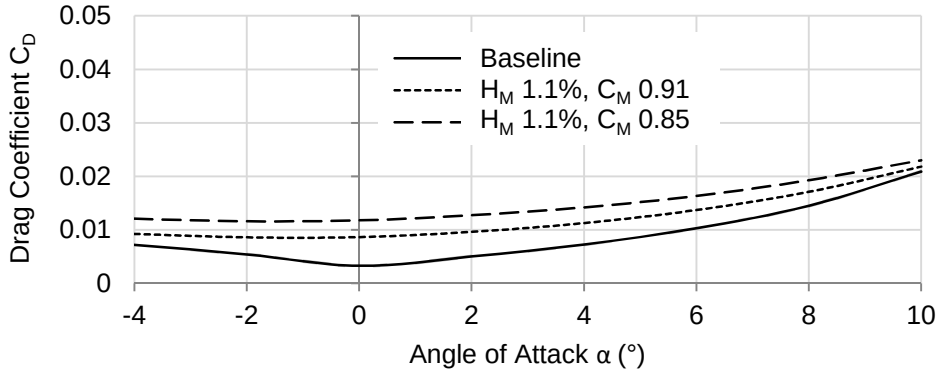


(b)

Figure 3.18 - Steady state (a) lift and (b) drag coefficients
(NACA 64-618 aerofoil equipped with a microtab on the suction side, Re = $6\times10^6$, k-ω SST model)

Amongst the several configurations of microtabs evaluated on the NACA 64-618 aerofoil, it is found that a microtab located at 88% of chord from the leading edge with a deployment height of 2% chord length on the aerofoil pressure side provides one of the best trade-off between lift increase and drag penalty. On the other hand, a location of 91% and height of 1.1% are found to give the best lift/drag trade-off for a microtab on suction side. Figure 3.19 shows the lift and drag coefficients generated by the microtab for these two configurations.

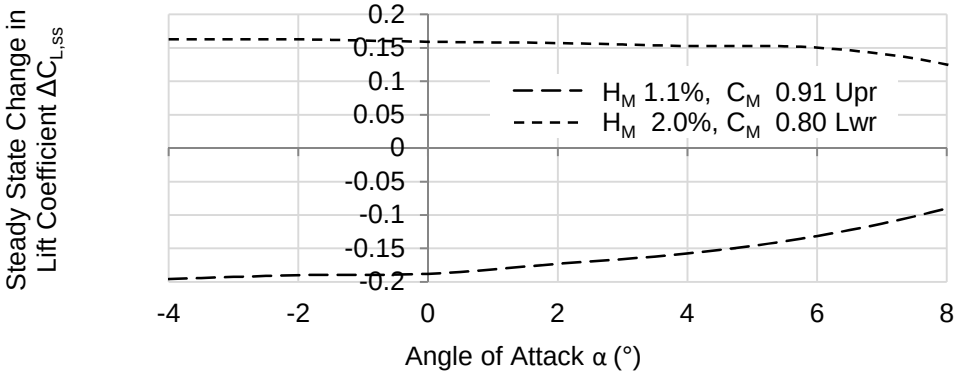


(a)

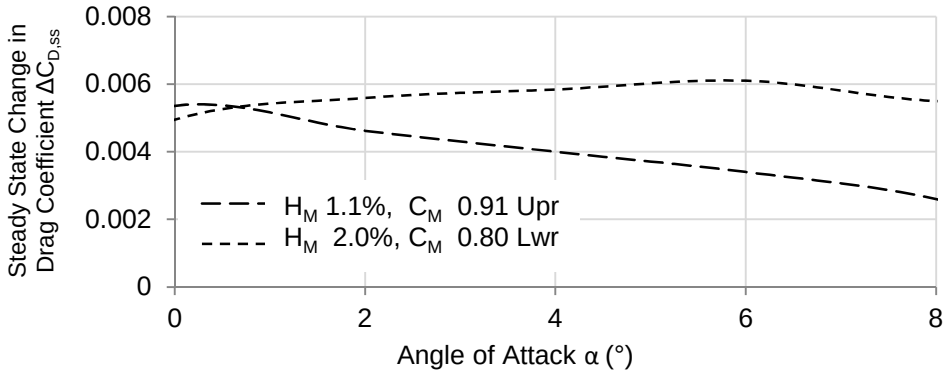


(b)

Figure 3.19 - Steady state changes in (a) lift and (b) drag coefficients
(NACA 64-618aerofoil equipped with microtabs, Re = $6\times10^6$)

Two dimensional CFD analyses are used to generate steady state aerodynamic lookup tables. Each table contains the steady state changes in lift $\Delta C_{L,ss}$ and drag coefficients $\Delta C_{D,ss}$ of aerofoils as functions of the normalised microtab deployment height $\delta_M$ and the angle of attack. Figure 3.20 shows one of the look-up tables obtained for the NACA 64-618 aerofoil. The normalised deployment height $\delta_M$ is equal to 1 when the microtab is fully deployed on the suction side and equal to -1 when fully deployed on the pressure side. The lookup table is approximated in the form of Equations (3.1) and (3.2) in order to later be used in designing controllers. The function used for approximation is linear with respect to the microtab deployment height $\delta_M$ and nonlinear with respect to the aerofoil angle of attack. This choice is justified as it gives a reasonably accurate approximation (i.e. RMS error < 0.02) and simplifies the control design (i.e. linear system). The CFD steady state surface and its linear approximation are superimposed in Figure 3.20.

$$\Delta C_{L,ss}(\delta_M, \alpha) = K_M \delta_M \tag{3.1}$$

$$K_1 = a_{M1}\alpha^5 + a_{M2}\alpha^4 + a_{M3}\alpha^3 + a_{M4}\alpha^2 + a_{M5}\alpha + a_{M6} \tag{3.2}$$

where, $a_{M1}$ to $a_{M6}$ are constants found to minimise the error in surface fitting.

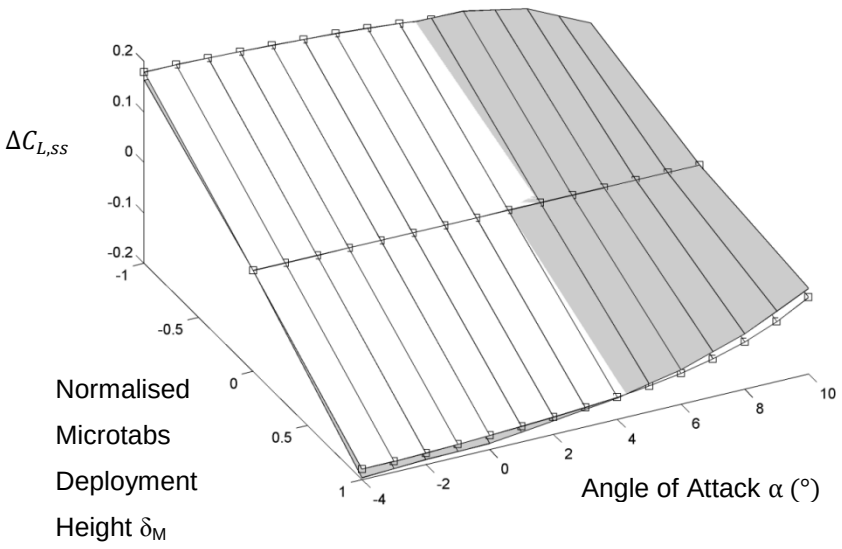


Figure 3.20 - Microtab steady state lift coefficient linear approximation
(NACA 64-618 aerofoil, Re = $6\times10^6$, *rms* = 0.01071)

The two dimensional steady state lift coefficient, as shown in Figure 3.20, provides a means of evaluating the capability of microtabs to change aerodynamic forces. Other features such as the microtab response time and dynamic response are also critical for load alleviation applications. The general model used to describe the microtab dynamic response based on its steady state data is shown in Figure 3.21. The angle of attack and microtab deployment height are used to obtain the aerodynamic steady state coefficient. The steady state value $\Delta C_{L,ss}$ is then fed as reference to the microtab transient aerodynamic model which outputs the dynamic lift coefficient $\Delta C_L$.

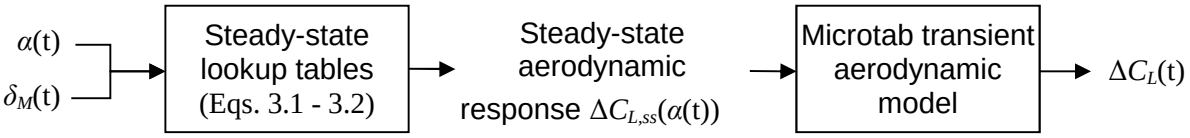


Figure 3.21 - Dynamic lift coefficient generated by microtabs

### 3.3.2 Microtab Transient Aerodynamic Response

Investigations (Chow and van Dam, 2007, Bæk et al., 2010) have shown that the dynamic lift response due to the microtab deployment has four prime features: a delay, an adverse response, a rapid dynamic and a slow dynamic (see Figure 3.22). The microtab deployment time ($T_{deploy}$), given in terms of the normalised time defined in Equation (3.3), strongly affects these four dynamics. During the microtab deployment, the transient lift response is characterised by a delay and an adverse response due to the formation of a vortex behind the tab. The microtab lift and drag aerodynamic responses are remarkably rapid, with a significant change occurring during the tab deployment. The lift rapidly climbs up to about 50% of its steady state value quickly after tab deployment (at normalised time $T_{50\%}$) before rising asymptotically to the steady state lift at a much slower rate.

$$T = V_{rel} t / c \tag{3.3}$$

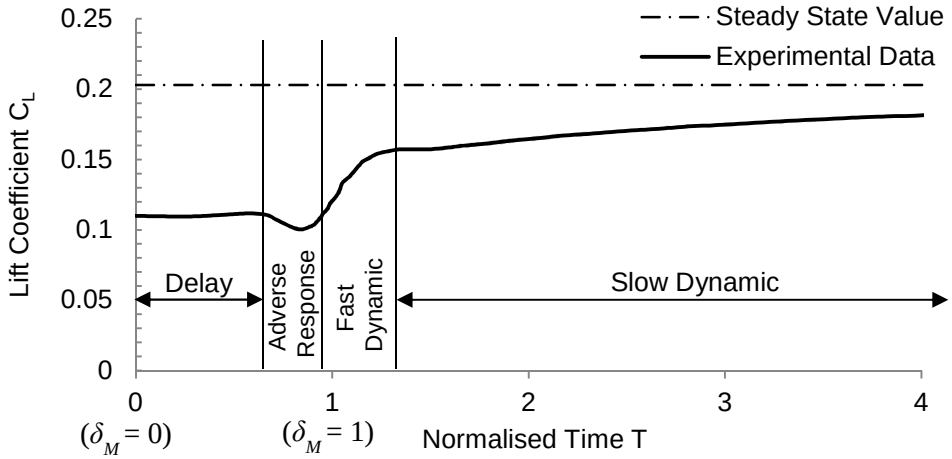


Figure 3.22 - Microtab transient lift aerodynamic response ($T_{deploy}$= 1, Re = 1×10$^6$, experimental value from (Chow and van Dam, 2007))

Table 3.1 and Figure 3.23 demonstrate the effect of the microtab deployment time on the aerodynamic lift response for a microtab deployment height $H_M$ of 1.1%, installed on the S809 aerofoil (Chow and van Dam, 2007).

Table 3.1 - Temporal lift response of microtab (Re = 1×10$^6$)

| $T_{deploy}$ | $C_{L,adverse}$ | $\lvert C_{L,adverse} / C_{L,retract} \rvert$ | $T_{delay}$ | $T_{50\%}$ |
|---|---|---|---|---|
| 1 | -0.00978 | 0.0895 | 0.836 | 1.7 |
| 2 | -0.00625 | 0.0572 | 1.304 | 2.34 |
| 4 | -0.00341 | 0.0312 | 2.078 | 3.76 |

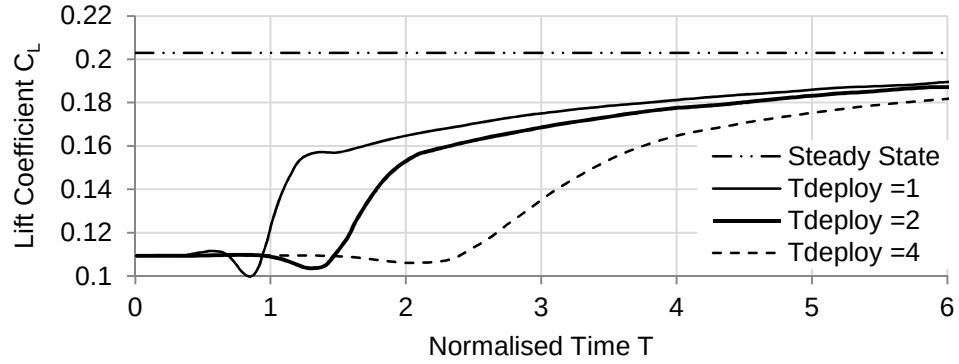


(a)

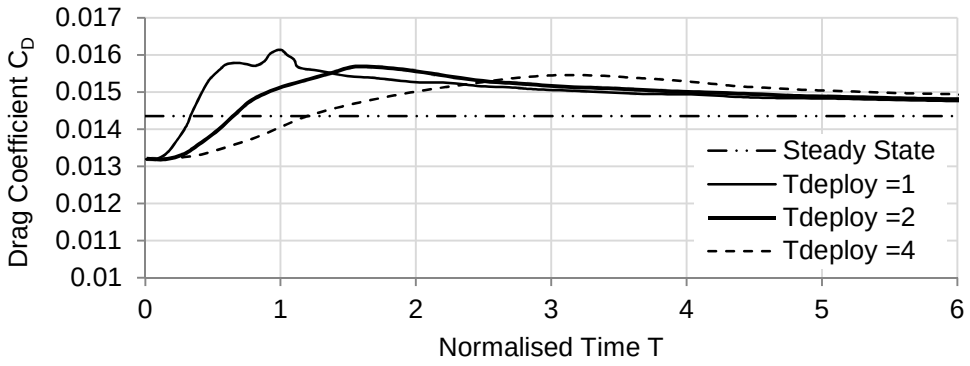


(b)

Figure 3.23 - Microtab transient response to deployment (base aerofoil S809, Re = $1\times10^6$, original data from (Chow and van Dam, 2007))

While the microtab dynamic response has been investigated (Bæk and Gaunaa, 2011, Chow and van Dam, 2007), no mathematical model suitable for control purpose has been proposed. It was, therefore, decided to develop a dynamic model of microtab for this purpose. In this model the deploy time is set to 1 ($T_{deploy}$=1) because it will ensure the fastest response and consequently permit the counteraction of higher frequency loads.

First, the transient microtab dynamic is investigated. The transient aerodynamic response times of several microtab configurations are calculated using Equation (3.3) as shown in Table 3.2. The duration of the transient dynamics is compared to the cyclic loads period of the NREL 5MW wind turbine. At rotor rated speed, the first and second rotational frequencies have periods of approximately 5 and 2.5 seconds. It can be seen that in the worst case scenario the duration of the transient microtab dynamic response does not exceed 5% of the second natural frequency period. As a result, it can be assumed that the adverse lift response and delay have little influences on the blade loads. As a matter of fact, the investigation by Chow and van Dam also demonstrated that the inverse response and the delay observed in microtab dynamic have no significant impact on load rejection due to their short existences (Chow and van Dam, 2007).

Table 3.2 - Microtab transient time ($T_{deploy}$=1)

| Chord $c$ (m) | $V_{rel}$ (m/s) | Time (s) | Transient Time / Cyclic Period (%) | |
|---|---|---|---|---|
| | | | 1$P$ (5s) | 2$P$ (2.5s) |
| 2 | 30 | 0.11 | 2.20% | 4.40% |
| 2 | 40 | 0.09 | 1.80% | 3.60% |
| 2 | 50 | 0.07 | 1.40% | 2.80% |
| 2 | 60 | 0.06 | 1.20% | 2.40% |
| 2 | 70 | 0.05 | 1.00% | 2.00% |
| 1 | 30 | 0.06 | 1.20% | 2.40% |
| 1 | 40 | 0.04 | 0.80% | 1.60% |
| 1 | 50 | 0.03 | 0.60% | 1.20% |
| 1 | 60 | 0.03 | 0.60% | 1.20% |
| 1 | 70 | 0.02 | 0.40% | 0.80% |

Comparing the results reported in the literature, similar normalised aerodynamic response under different Reynolds numbers are observed (Bæk and Gaunaa, 2011, Chow and van Dam, 2007). For developing the dynamic model, it is further assumed that the response of a microtab is insensitive to variation in Reynolds numbers values for Re > $10^6$. Moreover, the transient dynamics of microtabs deploying on the upper and lower surface are assumed to be equivalent. Considering the above assumptions, the lift dynamic is approximated using a second order model expressed as a transfer function:

$$\frac{\Delta C_L}{\Delta C_{Lss}} = \frac{c_{M1}s + c_{M2}}{1 + \frac{2\xi}{w_n}s + \frac{1}{w_n^2}s^2} \tag{3.4}$$

The coefficients $c_{M1}$, $c_{M2}$, $w_n$ and $\xi$, as explained later in this section, are calculated such that the model fits the dynamic response of experimental data presented in Table 3.1. The microtab response features two dynamics, one being much faster than the other (see Figure 3.22). Consequently, the microtab response can be separated into two distinct dynamics without loss of accuracy: a fast transient response occurring at the same time and shortly after the deployment of microtabs, and a slow response starting after the deployment as shown in Figure 3.22. In the fast dynamic region, the lift increases sharply half way to the steady state value whereas in the slow dynamic region it varies with a much slower rate to reach the steady state value. Moreover, since no outreaching or oscillations are observed in the response of $\Delta C_L$, the second order model of Equation (3.4) can be broken down to the summation of two single orders as in Equation (3.5).

$$\frac{\Delta C_L}{\Delta C_{Lss}} = \frac{c_{M1}s + c_{M2}}{1 + b_{M2}s + b_{M1}s^2} = \frac{c_{Mf}}{1 + \tau_{Mf}s} + \frac{c_{Ms}}{1 + \tau_{Ms}s} \tag{3.5}$$

where $\tau_{Mf}$ and $c_{Mf}$ are the parameters representing the fast dynamic and $\tau_{Ms}$ and $c_{Ms}$ are the parameters for the slow dynamic. As shown in Figure 3.22, both dynamics almost equally contribute to the total response, hence $c_{Mf} = c_{Ms} = 0.5$ seems a reasonable assumption. The constant time parameters are then calculated based on $T_{deploy}$, the response time of the system from Table 3.2 and based on the well-established knowledge that the response of a 1st order model reaches 90% of the steady state value around $3\tau$ (i.e. three times the time constant). Combining the model of Equation (3.1) with the flow dynamic response of Equation (3.5), the overall microtab dynamic from deployment to impact on the lift coefficient can be obtained. Additionally, the microtab dynamic model takes into account two constraints: (i) the effect of microtab on the local lift coefficient is limited to the steady state value of $\Delta C_{L,ss}$ at maximum tab deployment, and (ii) the microtab deployment time is fixed (i.e. $T_{deploy}$).

The procedure used to calculate the dynamic model parameters is detailed in Algorithm 3.1. In this algorithm, a pattern search method is used to minimise the difference between the experimental data of Table 3.1 and the predicted data by the model through identifying the best coefficients. The search stops when the difference between the modelled and reported experimental data $|\Delta C_{L,} - \Delta C_{L,exp}|$ is less than a tolerance $\varepsilon$.

**Algorithm 3-1 - Microtab dynamic model identification**
Given: $T_{deploy}$, the local relative velocity $V_{rel}$ and the local chord length $c$

Step 1- Use Table 1 to read off $T_{50\%}$.
Step 2- Calculate real times: $t_{50\%} = cT_{50\%} / V_{rel}$ , $t_{ss} = cT_{ss} / V_{rel}$ , $T_{ss} = 30\ T_{deploy}$
Step 3- Assign initial values for $\tau_{Mf}$ and $\tau_{Ms}$
Step 4- Calculate: $b_{M1} = \tau_{Mf}\tau_{Ms}$ , $b_{M2} = \tau_{Mf} + \tau_{Ms}$ , $c_{M1} = 0.5(\tau_{Mf} + \tau_{Ms})$ , $c_{M2} = 1$,

$$\Delta C_L = \Delta C_{L,ss} \frac{c_{M1}s + c_{M2}}{1 + b_{M2}s + b_{M1}s^2}$$

Step 5- Calculate $|\Delta C_{L,} - \Delta C_{L,exp}|$ ; If $|\Delta C_{L,} - \Delta C_{L,exp}| \le \varepsilon$ End; otherwise: employing pattern search find new values for time constants and go back to Step 4.

It is found that initial values $\tau_{Mf} = t_{50\%}/3$ and $\tau_s = (t_{ss} - t_{50\%})/3$ lead to the fastest convergence. In this study a tolerance $\varepsilon = 0.01$ is used. The model procedure is flexible and can be easily modified in order to fit new experimental data. Since the model developed above is linear, one can write the microtab dynamic model in a state space form as:

$$\dot{X}_M = A_M X_M + B_M u \tag{3.6}$$

$$\dot{X}_M = \begin{bmatrix} 0 & 1 & a_M \\ b_M & c_M & d_M \\ 0 & 0 & \tau_M \end{bmatrix} X_M + \begin{bmatrix} 0 \\ 0 \\ 1 \end{bmatrix} u \tag{3.7}$$

$$X_M = \begin{bmatrix} \Delta C_L & \Delta \dot{C}_L - r_M \Delta C_{Lss} & \delta_M \end{bmatrix}^T \tag{3.8}$$

where, the microtab deployment height is controlled by the control variable $u$. Figure 3.24 shows the microtab dynamic response model, obtained by Algorithm 1, compared with experimental data (Chow and van Dam, 2007). The deployment of the microtab is modelled by a first order ordinary differential equation (i.e. $\tau_M$) such that the non-dimensional deployment time equals $T_{deploy}$. As can be observed in Figure 3.24, the proposed model shows good agreement with experimental data for predictions after the microtab full deployment. Figure 3.25 shows the aerodynamic response of a microtab deploying in response to unsteady flow conditions. Once the steady state aerodynamic data for a given aerofoil is generated, the model described by Equation (3.5) is used to calculate its dynamic response to a change in flow conditions.

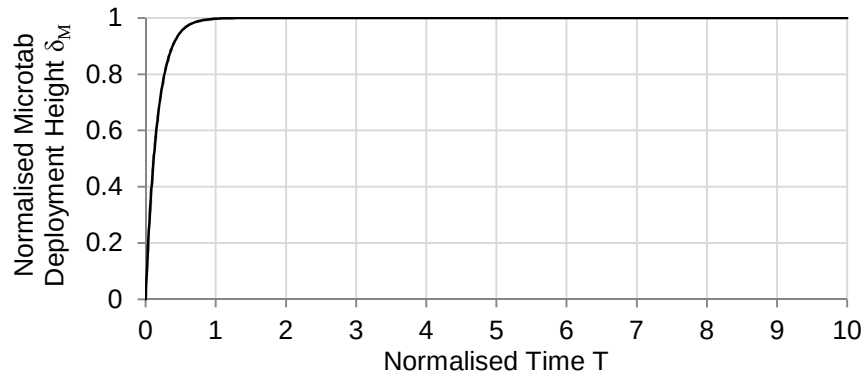


(a)

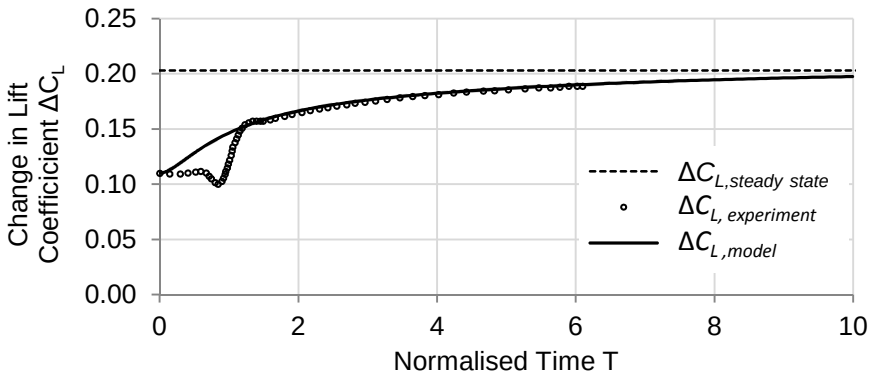


(b)

Figure 3.24- Microtab actual and modelled aerodynamic response

(based aerofoil S809, 1.10% deployment height, microtab located on the pressure side, Re = $1\times10^6$)

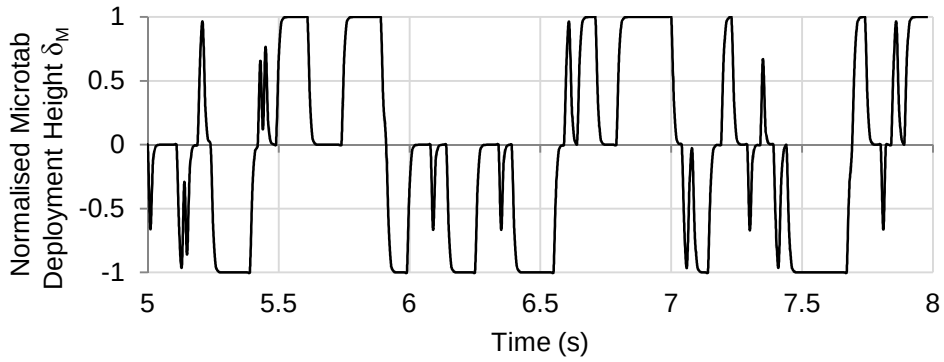


(a)

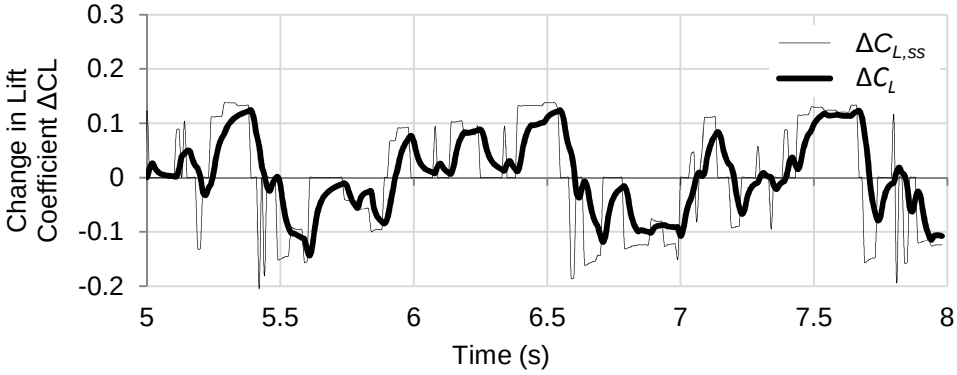


(b)

Figure 3.25 - (a) Microtab deployment and (b) aerodynamic response to turbulent wind (base aerofoil S809)

## 3.4 Trailing Edge Flap

As discussed in Section (1.3.2.1) several trailing edge flap (TEF) types are commonly employed in the aerospace industry. For low wind speed, high-lift flaps often refer to the double and triple slotted flaps (Stanewsky, 2001). While slotted and Fowler flaps are generally employed when high-lift increase is required (i.e. aircraft take-off), there are major drawbacks to their use on wind turbines. First, the actuation mechanism is relatively costly, complex to install and maintain. Second, the weight and space required for their implementations is prohibitive for wind turbine applications. In comparison, plain or single slotted flaps have a simpler actuation mechanism, are lighter and yet effective lift-enhancing devices.

### 3.4.1 Trailing Edge Flap Steady State Aerodynamic Model

Wind tunnel test facilities were not accessible during this research, however, TEFs have been intensively studied for many decades and the numerical tools available nowadays such as panel methods and CFD can be used to generate reasonably accurate aerodynamic data. In

order to validate XFoil predictions for aerofoils equipped with TEF, two case studies are chosen for benchmarking. Xfoil is used to generate the aerodynamic coefficients of the aerofoils DU96-W-180 and NACA 0009 equipped with TEF. As shown in Figures 3.26 and 3.27, XFoil predictions are compared against experimental results (Bæk et al., 2010, Lafountain et al., 2012). As expected, it is found that under attached flow the lift increase predicted by XFoil agrees well with experiments. Although XFoil can only be used for aerofoils equipped with plain flaps and sealed gap, the generated data can be used for preliminary wind turbine blade load alleviation studies. Figure 3.28 shows the steady state changes in lift and drag coefficients employing a plain flap on the DU96-W-180 aerofoil. Clearly, the changes in lift coefficient are much greater than the changes in drag. This is ideal for wind turbine blade load alleviation purposes. As it will be shown in the following chapters, the lift force is one of the primary sources of fatigue loads.

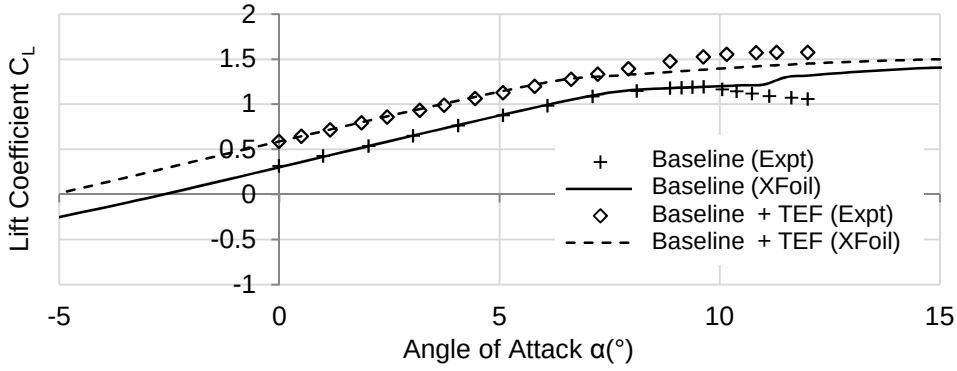


Figure 3.26 - XFoil and experimental lift coefficients (Bæk et al., 2010)
(base aerofoil DU96-W-180 equipped with TEF, Re = $3\times10^6$)

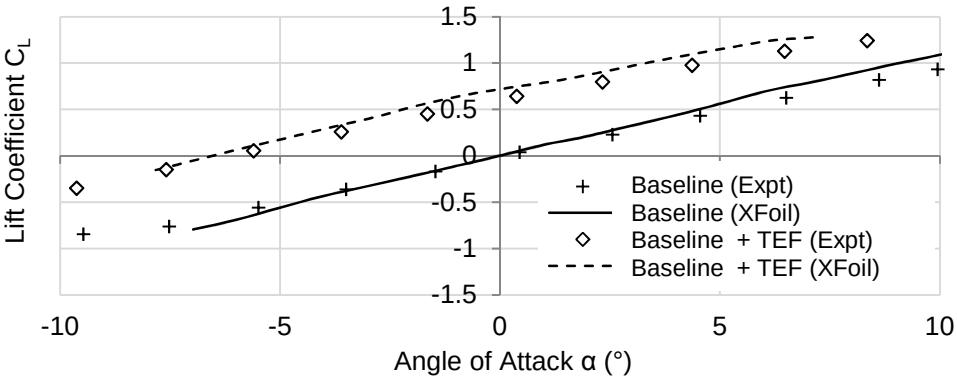


Figure 3.27 - XFoil and experimental lift coefficients (Lafountain et al., 2012)
(base aerofoil NACA 0009 equipped with TEF, Re = $2.7\times10^6$)

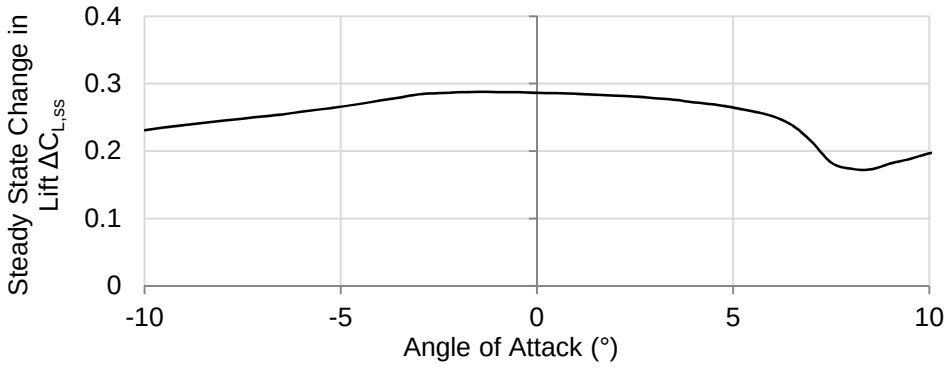


(a)

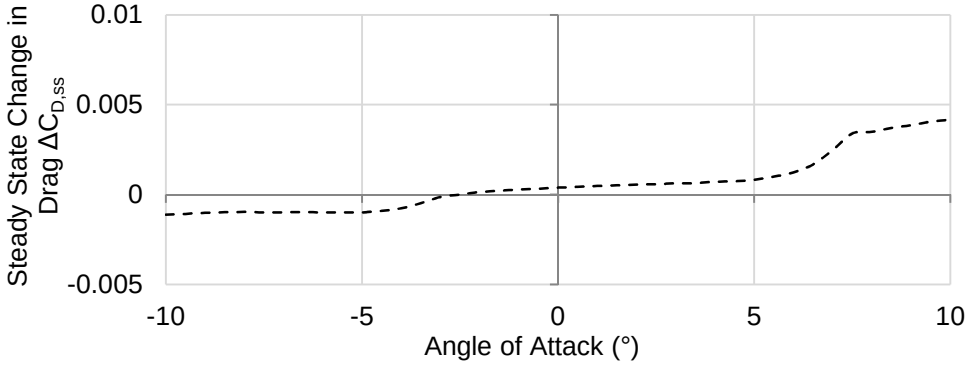


(b)

Figure 3.28 - Lift and drag coefficients generated for the DU96-W-180 aerofoil equipped with a 10% chord size TEF using XFoil (Re = 3×106)

### 3.4.2 Trailing Edge Flap Dynamic Model

The dynamic lift $\Delta C_L$ generated by the TEF deployment $\delta_F$ is modelled based on the work of Leishman (Leishman, 1994), a modified version of Theodorsen's model (Theodorsen, 1935). This indicial model, assuming a thin aerofoil and attached flow, describes the TEF dynamics in a linear state space form as in Equations (3.9) to (3.16).

$$\begin{bmatrix} \dot{z} \\ \ddot{z} \end{bmatrix} = \begin{bmatrix} 0 & 1 \\ -b_{F1}b_{F2}\left(V_{rel}/b_F\right)^2 & -\left(b_{F1}+b_{F2}\right)\left(V_{rel}/b_F\right) \end{bmatrix} \begin{bmatrix} z \\ \dot{z} \end{bmatrix} + \begin{bmatrix} 0 \\ 1 \end{bmatrix} \delta_{Fqs} \tag{3.9}$$

The circulatory part of the lift coefficient generated by flap motion is given by:

$$\left(\Delta C_L\right)_c = 2\pi \left[ \left(b_{F1}b_{F2}/2\right)\left(V_{rel}/b_F\right)^2 \quad \left(A_{F1}b_{F1} + A_{F2}b_{F2}\right)\left(V_{rel}/b_F\right) \right] \begin{bmatrix} z \\ \dot{z} \end{bmatrix} + \pi\delta_{Fqs} \tag{3.10}$$

with,

$$\delta_{Fqs} = \frac{F_{10}\delta_F}{\pi} + \frac{b_F F_{11}\dot{\delta}_F}{2\pi V_{rel}} \tag{3.11}$$

$$F_{10} = \sqrt{(1 - e^2)} + \cos^{-1}(e) \tag{3.12}$$

$$F_{11} = (1 - 2e)\cos^{-1}(e) + (2 - e)\sqrt{(1 - e^2)} \tag{3.13}$$

The non-circulatory part of the lift coefficient generated by flap motion is given as:

$$(\Delta C_L)_i = \frac{b_F}{V_{rel}^2}\left(- V_{rel} F_4 \dot{\delta}_F - b_F F_1 \ddot{\delta}_F\right) \tag{3.14}$$

$$F_1 = e\cos^{-1}(e) - (1/3)(2 + e^2)\sqrt{(1 - e^2)} \tag{3.15}$$

$$F_4 = e\sqrt{(1 - e^2)} - \cos^{-1}(e) \tag{3.16}$$

where, $z$ contains the aerodynamic state variables, $b_{F1,F2}$ and $A_{F1,F2}$ represent the exponents and coefficients of the function used to approximate the Wagner function. The Wagner function provides a solution for the indicial lift on a thin-aerofoil undergoing a step change in angle of attack when operating under incompressible flow. In addition, $\delta_{Fqs}$ is the quasi-steady flap deployment angle, $b_F$ the semi-chord $(c/2)$ and $e$ is the flap hinge location expressed in terms of semi-chord. The $F_i$ terms represent geometric parameters. For more details on the aerodynamic model please see Leishman JG, 1994.

For the TEF actuator the author consider a zero overshoot hard constraint and its dynamic is modelled as a single order system dynamic. However, since the flap deployment speed and acceleration are required to compute Equation (3.14), it was decided to virtually augment the actuator model with fast dynamics for $\dot{\delta}_F$ and $\ddot{\delta}_F$ to appear in the state vector. Combining the dynamic lift model and the TEFs' actuator model, a 5$^{th}$ order state space representing the dynamic lift coefficient generated by the TEF position and motion is obtained, see Equations (3.17) to (3.22). In Equation (3.20), $[A_{act}]_{3\times3}$ denotes the actuator dynamic and $[A_{aero}]_{2\times5}$ represents the dynamic of the flap aerodynamic state variables. More details about the coefficients of matrices $A_F$ and $C_F$ are given in Table 3.3. Additionally, the TEF deployment angle and corresponding aerodynamic response generated during this research are presented in Figure 3.29 and Figure 3.30.

$$\dot{X}_F(t) = A_F(t) X_F(t) + B_F u(t) \tag{3.17}$$

$$\Delta C_L(t) = (\Delta C_L)_c + (\Delta C_L)_i = C_F X_F(t) \tag{3.18}$$

where,

$$X_F = \begin{bmatrix} \delta_F & \dot{\delta}_F & \ddot{\delta}_F & z & \dot{z} \end{bmatrix}^T \tag{3.19}$$

$$A_F = \begin{bmatrix} [A_{act}]_{3\times3} & [0]_{3\times2} \\ [A_{aero}]_{2\times5} \end{bmatrix} = \begin{bmatrix} 0 & 1 & 0 & 0 & 0 \\ 0 & 0 & 1 & 0 & 0 \\ a_{F1} & a_{F2} & a_{F3} & 0 & 0 \\ 0 & 0 & 0 & 1 & 0 \\ a_{F4} & a_{F5} & 0 & a_{F6} & a_{F7} \end{bmatrix} \tag{3.20}$$

$$B_F = \begin{bmatrix} 0 & 0 & 1 & 0 & 0 \end{bmatrix}^T \tag{3.21}$$

$$C_F = \begin{bmatrix} c_{F1} & c_{F2} & c_{F3} & c_{F4} & c_{F5} \end{bmatrix} \tag{3.22}$$

Table 3.3 - Trailing edge flap aerodynamic model coefficients

| Matrix $A_F$ coefficients | Matrix $C_F$ coefficients |
|---|---|
| $a_{F1} = -10^6$ | $c_{F1} = F_{10}$ |
| $a_{F2} = -11\times10^4$ | $c_{F2} = \left(\frac{bF_{11}}{2V_{rel}} - \frac{bF_4}{V_{rel}}\right)$ |
| $a_{F3} = -1100$ | $c_{F3} = -b^2 F_1 / V_{rel}^2$ |
| $a_{F4} = F_{10}/\pi$ | $c_{F4} = \pi b_{F1} b_{F2} (V_{rel}/b)^2$ |
| $a_{F5} = b_F F_{11}/(2V_{rel}\pi)$ | $c_{F5} = 2\pi(A_{F1}b_{F1} + A_{F2}b_{F2})(V_{rel}/b)$ |
| $a_{F6} = -b_{F1}b_{F2}(V_{rel}/b_F)^2$ | |
| $a_{F7} = -(b_{F1} + b_{F2})(V_{rel}/b_F)$ | |

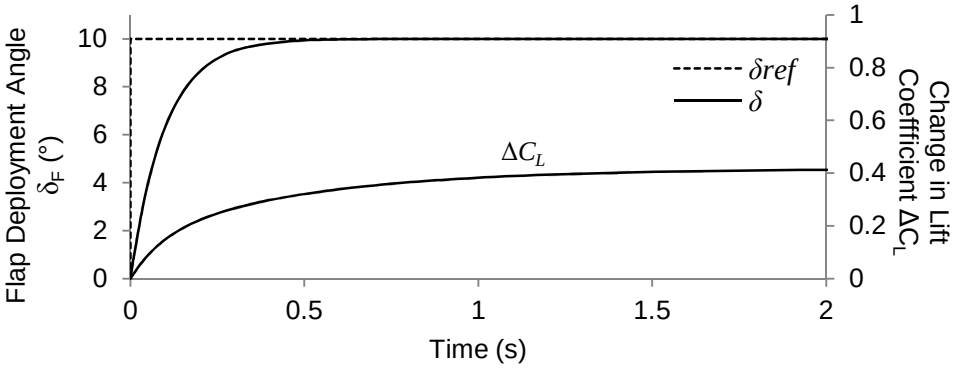


Figure 3.29 - Dynamic lift generation due to the deployment of a TEF (base aerofoil S808, Re = $1\times10^6$)

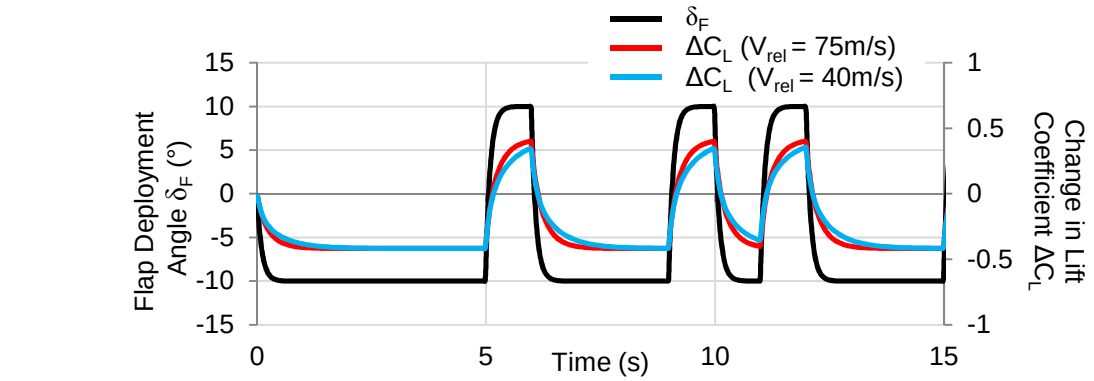


(a)

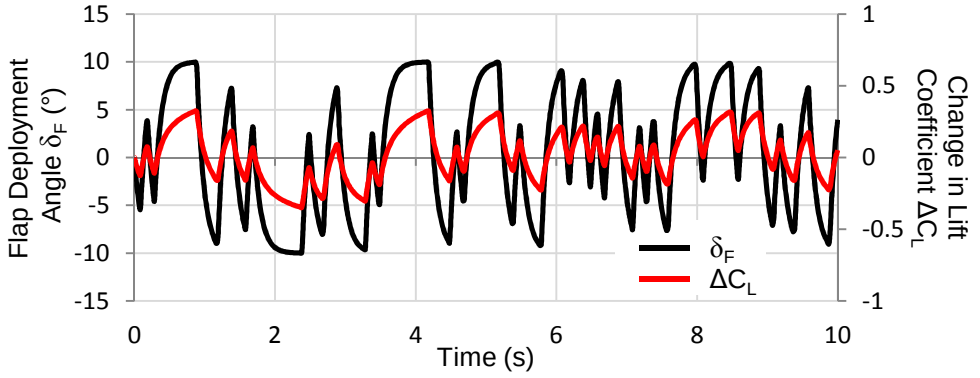


(b)

Figure 3.30 - Aerodynamic response due the deployment of a trailing edge flap (base aerofoil S808)

Without loss of accuracy the 5th order model presented above can be reduced to a 3rd order model described through Equations (3.23) to (3.26), where the subscript $r$ stands for reduced. For the 3rd order model the author assumes the lift produced by the TEF speed and acceleration to be negligible compared to the other states contributions $(i.e.\ c_{F2} = c_{F3} = 0)$. Figure 3.31 compares the dynamic lift results obtain by the 5th and 3rd order models for random input signals of 10 and 50 Hz. It can be seen that simplifying from the 5th to the 3rd order model is found to be an accurate approximation if acceleration and deployment speed are not the dominant source of lift. Therefore, the 3rd order model predictions are accurate as long as the frequency of actuation remains lower than a given frequency (e.g. 20 Hz). This condition is satisfied for medium and large wind turbines where the frequency bandwidth containing the first three rotational frequencies is generally lower than 10 Hz (Jonkman et al., 2009).

$$X_{Fr} = \begin{bmatrix} z & \dot{z} & \delta_F \end{bmatrix}^T \tag{3.23}$$

$$A_{Fr} = \begin{bmatrix} 0 & 1 & 0 \\ a_{F6} & a_{F7} & a_{F4} \\ 0 & 0 & \tau_F \end{bmatrix} \tag{3.24}$$

$$B_{Fr}{}^{T} = [0 \quad 0 \quad 1] \tag{3.25}$$

$$C_{Fr} = [c_{F4} \quad c_{F5} \quad c_{F1}] \tag{3.26}$$

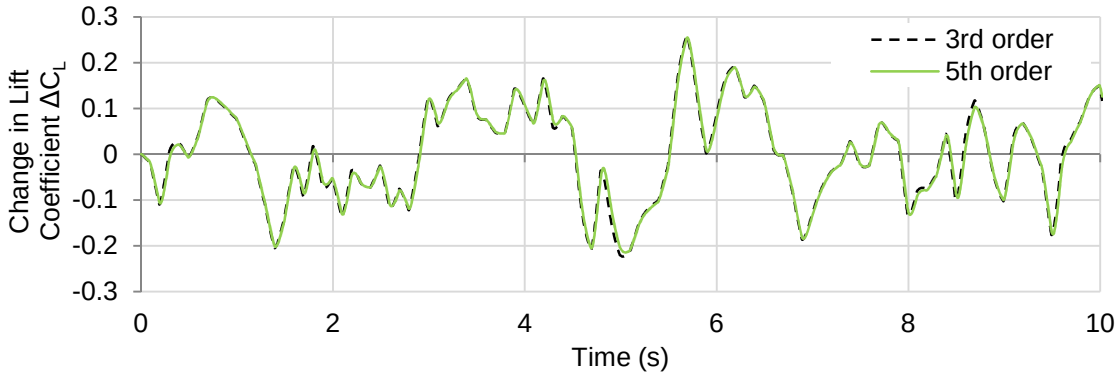


(a)

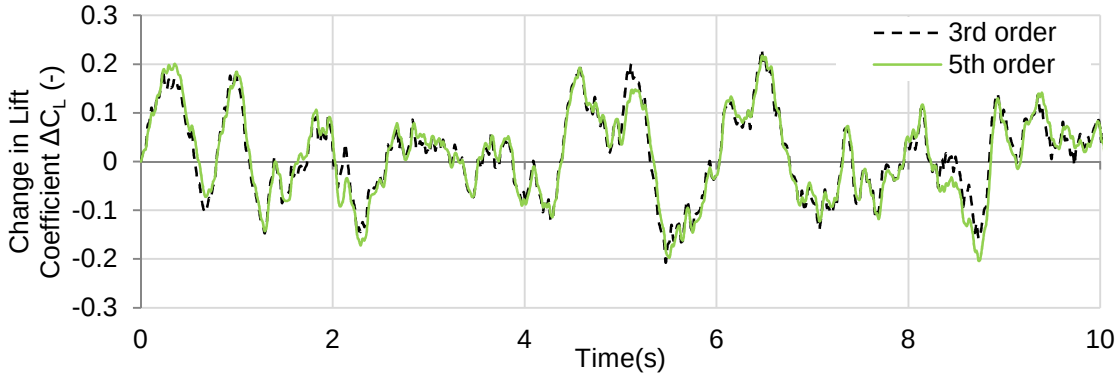


(b)

Figure 3.31 - Fifth and the third order indicial model subject to input signal of frequency equal to (a) 10Hz and (b) 50Hz (base aerofoil S808, Re = $1\times10^{6}$)

Using the above linear model the use of control theory is simplified. However, the model may lose accuracy when employed for wind turbine applications where the assumptions of attached flow and thin aerofoils are not always satisfied. For instance, in Figure 3.32 the author compares the indicial model calculations with XFoil for the S808 aerofoil (thickness ratio of 21%). In order to increase the accuracy of the indicial model compared to numerical and experimental data, the model is modified using an optimisation technique. Although the optimisation should increase the model accuracy, it should not change its dynamic response. In this context, it was preferred to introduce a new dependent parameter denoted by $p_1(\alpha)$ in the output matrix as follows $C_{Fr} = [p_1(\alpha) c_{F4} \quad c_{F5} \quad c_{F1}]$. The position of $p_1(\alpha)$ is chosen such that it modifies the linear steady state slope of $\Delta C_L$ by varying the contribution of the aerodynamic state variable $z$. The optimisation aim is to find $p_1(\alpha)$ such that the root mean

square error (RMS) between the model and XFoil predictions are minimised. The detail of the search algorithm developed during this PhD is described by Algorithm 3.2.

**Algorithm 3-2 - Trailing edge flap dynamic model optimisation**
Given: The numerical/experimental steady state prediction.

Step 1- Define a search range, $\delta_F \in \lfloor \delta_F{}^-, \delta_F{}^+ \rceil$, $\alpha \in \lfloor \alpha_0, \alpha_f \rceil$ and the increments $\Delta\alpha$ and $\Delta\delta_F$

Step 2- Define the dynamic and geometric parameters: $c, V_{rel}, e, b_F$ and $F_1, F_4, F_{10}, F_{11}$

Step 3- Initialise the index and coefficient value: $ii \leftarrow 1$; $coef_{ii} \leftarrow 1$; $\chi \leftarrow \chi_0$

Step 4- Simulate the model until RMS is less than $\varepsilon$ or maximum number of iterations $N$ reached

*for* $\alpha = \alpha_0$ to $\alpha_f$

*while* $RMS_{ii} > \varepsilon$ *and* $ii < N$

Step 4.1- $[p_1]_{ii} \leftarrow coef_{ii}$

Step 4.2- Simulate the model until steady state convergence over $\delta_F \in \lfloor \delta_F{}^-, \delta_F{}^+ \rceil$

Step 4.3- $RMS_{ii} \leftarrow$ Calculate the RMS error between the model and XFoil's predictions

Step 4.4- $coef_{ii+1} = coef_{ii} + \chi$ *(Use gradient descent to modify $\chi$)*

Step 4.5- $ii \leftarrow ii + 1$

*end*

Step 4.6- $[p_1]_\alpha \leftarrow$ Save the best value of $[p_1]_{ii}$ that minimise the RMS.

*end*

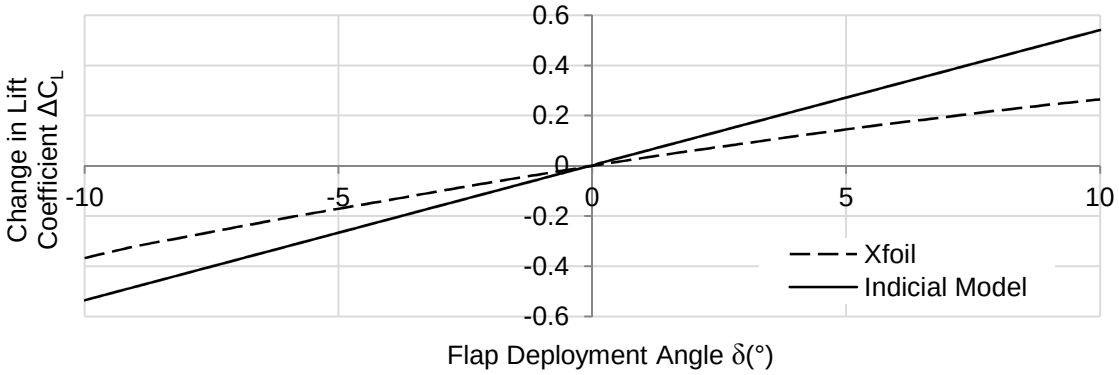


Figure 3.32 - Indicial model and XFoil quasi-steady lift coefficients
(base aerofoil S809, angle of attack of 15°)

The optimisation results obtained with $\delta_F \in [-10,10]$, $\alpha \in [0,15]$, $\chi_0 = 0.5$, $\varepsilon = 0.005$ and $N = 20$, are presented in the following figures. Figure 3.33 gives the average root mean square error of $\Delta C_L(\delta_F)$ over $\alpha$ and Figure 3.34 shows the improvement of predictions for $\alpha$ equals to 5 and 15 degrees. As observed in Figure 3.33, it can be seen that the proposed optimisation algorithm shows significant improvements for $\alpha \in [6,15]$. The proposed

optimisation algorithm minimises the root mean square error while keeping the system linear, therefore the greatest inaccuracies still occur at maximal flap deployment angles as shown in Figure 3.34.

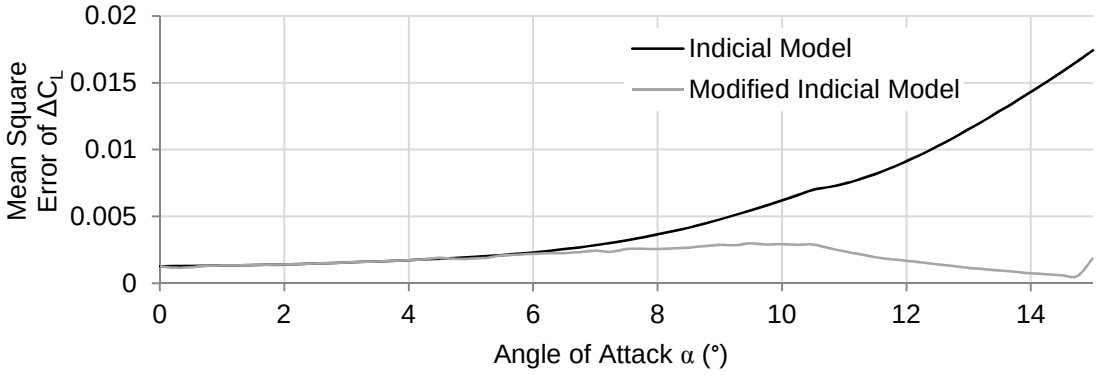


Figure 3.33 - Modified indicial model and XFoil steady state results (base aerofoil S808, Re = $1\times10^6$)

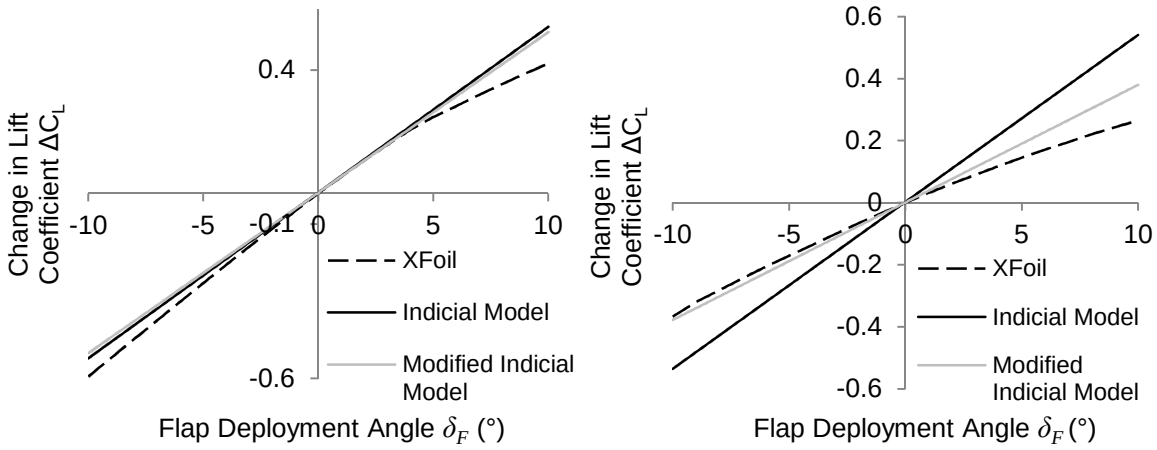


(a) (b)

Figure 3.34- Modified indicial model and XFoil steady state results for angles of attack of (a) 5 and (b) 15degrees (base aerofoil S808, Re = $1\times10^6$)

Although good results are obtained for low angles of attack, significant deviations are still observed for high angles of attack. As a consequence, it was decided to modify the previous optimisation code to obtain multiple linearised models for various deployment angles. Figure 3.35 presents the results of the piece-wise linearisation for constant angles of attack of 5 and 15 degrees. As seen in this figure, the piece-wise linearisation significantly improves predictions accuracy for high angles of attack. Moreover, by dividing the domain in a continuity of linear subdomains, the simplicity of the original model as well as its suitability for linear control theory is conserved. Although the steady state predictions of the piece-wise model closely match the steady data, the dynamic of the model is only valid under attached

flow. This limitation therefore excludes the use of the piece-wise linearised modelling for high angles of attack (after stall) despite its good steady state predictions.

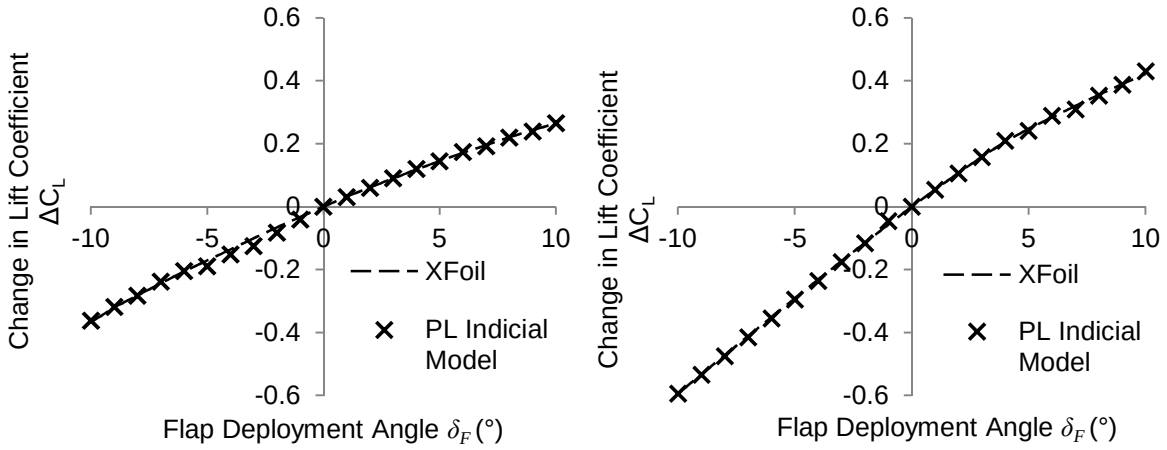


Figure 3.35 - Piecewise linear approximation of the lift coefficient generated by flaps using the indicial model for angle of attacks of (a) 5 and (b) 15 degrees (base aerofoil S808, Re = $1\times10^6$)

## 3.5 Summary - Aerodynamic Modelling of Control Surfaces

Chapter 3 was dedicated to the development of the aerodynamic models for microtabs and trailing edge flaps.

First, the author showed that the majority of aerofoils located along the variable-speed pitch-controlled NREL 5 MW wind turbine operate under attached flow. As a result, it was decided to assume attached flow conditions when developing the microtab and trailing edge flap aerodynamic models. Next, it was found that the NREL 5 MW wind turbine blades experience Reynolds numbers in-between 1 to 12 million and demonstrated that its aerofoils aerodynamic coefficients are insensitive to change in Reynolds numbers in this range. As a consequence, it was decided to assume an average Reynolds numbers of 6 million for the aerodynamic calculations. The author then compared the accuracy of XFoil predictions against experimental data for the NREL 5 MW aerofoils. The results showed that XFoil is suitable to generate aerodynamic data for these aerofoils when operating under attached flow conditions. It was also shown that XFoil inaccuracies have a negligible effect on the wind turbine power predictions.

In order to investigate the potential of microtabs operating on the NREL 5 MW wind turbine, it was decided to generate steady state aerodynamic data of the NACA 64-618 aerofoils

equipped with microtabs. Several microtab configurations (i.e. position and size) were then evaluated using CFD. During the results analysis, the author found that locating microtabs at 88% of chord from the leading edge with a deployment height of 2% chord length on the pressure side provided one of the best side trade-offs between lift increase and drag penalty. On the other hand, a location of 91% and height of 1.1% was found to give the best lift/drag trade-off for a microtab on suction side.

A dynamic model of the microtab aerodynamic response was also developed as part of this research. The aerodynamic response of a deploying microtab was previously shown to have four prime features. However, this research showed that for the load alleviation of large wind turbine blades employing microtabs, both the delay and transient dynamics have negligible impacts due to their short transient existences. Experimental data of the two remaining dynamics were then used to develop a general model for the dynamic response of microtabs. The proposed model is the linear combination of two single order differential equations. In addition, an algorithm that automatically tunes the parameters of our model in order to match available experimental data was also developed.

After validating the accuracy of XFoil predictions for aerofoil equipped with flaps, it was decided to generate the steady state aerodynamic data of the NACA 64-618 aerofoil equipped with a trailing edge flap. The dynamic modelling of trailing edge flap used in this study is based on the previous work of Leishman. Due to discrepancies observed between Leishman's model and XFoil predictions, the author chose to modify Leishman's model in order to match XFoil results. For that purpose, a new variable was introduced in the model in order to control the slope of the steady state response as a function of the angle of attack. The author also developed an algorithm in order to automatically tune this new variable such that the error between both models would be minimised. The final results showed significant accuracy improvement for angles of attack above 6 degrees.

# 4. Aero-Structural Model of Blades Equipped with Control Surfaces

## 4.1 Introduction

This chapter includes the modelling details of the wind turbine blades structural model and coupling with control surfaces. During this research, the author chose to developed an in-house structural model instead of using the available NREL software FAST (Jonkman and Buhl, 2005) for the following reasons:

- Acquire a more in-depth understanding of the dynamic of wind turbine blades
- Ease the implementation of control surfaces onto blades
- Develop and test aeroelastic controllers for blades equipped with control surfaces
- Investigate control properties such as controllability and observability
- Remove the limitation regarding the number of DOFs

Wind turbine blades are slender structures which can be approximated as cantilever beams using lumped mass or finite elements methods (Andersen, 2005, Andersen et al., 2009, Barlas and van Kuik, 2009). In this research, a finite element (FE) code has been developed to analyse the blades' structural dynamics as rotating tapered beams. The FE model is later transformed into its modal form for which the model complexity is reduced and accuracy conserved. Section 4.2 gives a brief reminder of the Euler-Bernoulli beam FE modelling. The modal transformation and reduction of the FE model are explained in Section 4.3. The wind turbine blades' structural parameters used as input to the FE model are detailed in Section 4.4. The developed aero-structural wind turbine blade model is then compared to the NREL code FAST in Section 4.5. Finally, the wind turbine blade aeroelastic model is coupled with the CS models of Chapter 3 in Section 4.6.

## 4.2 Finite Element Formulation

The uniform Euler-Bernoulli beam model is a fourth order partial differential equation (PDE) as shown in Equation (4.1); in which $M$, $F$, $w$ and $EI$, respectively, stand for the transversal bending moment, distributed force, beam deflection and bending stiffness. The uniform Euler-Bernoulli PDE is analytically solvable in order to compute the static deformation of simple structure-like beams. In case of a wind turbine, the blade structure varies along its span (i.e. taper) and the blade rotation results in centrifugal and Coriolis forces which have to be taken into account (Merz, 2011). The existence of analytical solutions is not always guaranteed for modified version of Equation (4.1). Methods such as the method of weighted residual (MWR), the lumped mass modelling or finite element (FE) modelling have to be used for approximating the solutions of these PDEs (Resor et al., 2010). An FE method is

chosen because of its suitability for numerical implementation and its high accuracy. Consider the beam element of length $L$ shown in Figure 4.1. This element has 2 nodes, each with 2 DOFs, namely, the vertical displacement $w(x)$ and deflection angle $\phi(x)$. If the axial deflection $u_{beam}(x)$ is also considered the element is then referred to as a planar frame element.

$$F(x) = -\frac{d^2M(x)}{dx^2} = \frac{d^2}{dx^2}\left(-EI\frac{d^2w(x)}{dx^2}\right) \tag{4.1}$$

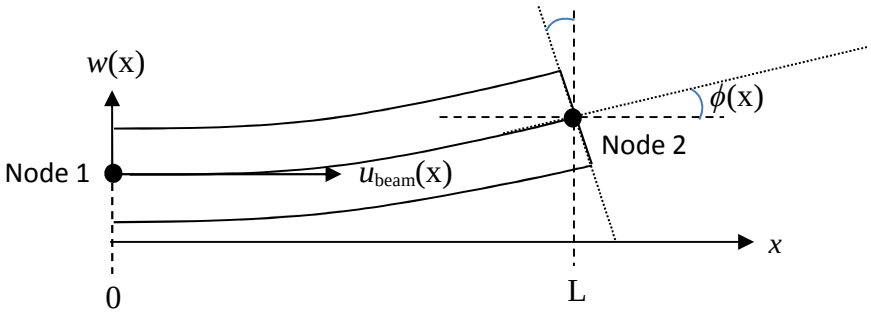


Figure 4.1 - Beam element, $u_{beam}(x)$ axial displacement, $w(x)$ transversal displacement and $\phi(x)$ plane angle

In the FE method, the trial function used to represent the beam displacement over one element is a polynomial function that contains the same number of coefficients as the number of unknown parameters. A 3rd order polynomial function is therefore used as trial function:

$$w(x) = a_0 + a_1x + a_2x^2 + a_3x^3 \tag{4.2}$$

The coefficients $a_i$ are found by substituting the coordinates of the nodal point into (4.2) as in the following set of equations:

$$w(0) = w_1 = a_1 \tag{4.3}$$

$$w(L) = w_2 = a_1 + a_2L + a_3L^2 + a_4L^3 \tag{4.4}$$

$$\left.\frac{\partial w(x)}{\partial x}\right|_{x=0} = \phi_1 = a_2 \tag{4.5}$$

$$\left.\frac{\partial w(x)}{\partial x}\right|_{x=L} = \phi_2 = a_2 + 2a_3L + 3a_4L^2 \tag{4.6}$$

$$a_3 = \frac{3}{L^2}(w_2 - w_1) - \frac{1}{L}(2\phi_1 + \phi_2) \tag{4.7}$$

$$a_4 = \frac{1}{L^2}(\phi_1 + \phi_2) + \frac{2}{L^3}(w_1 - w_2) \tag{4.8}$$

Substituting the coefficients in Equation (4.2) one can rewrite the displacement function:

$$w(x) = w_1 N_1(x) + \phi_1 N_2(x) + w_2 N_3(x) + \phi_2 N_4(x) \tag{4.9}$$

$$w(x) = \vec{N}(x)\vec{X}(t) = \begin{bmatrix} N_1 & N_2 & N_3 & N_4 \end{bmatrix} \begin{bmatrix} w_1 \\ \phi_1 \\ w_2 \\ \phi_2 \end{bmatrix} \tag{4.10}$$

where, the shape functions $N_i$ are defined as in Equation (4.11) - (4.14) and shown in Figure 4.2. Each shape function corresponds to one of the DOFs. For instance, the shape function $N_1$ corresponds to the transversal displacement of node 1 ($w_1$).

$$N_1(x) = 1 - 3\frac{x^2}{L^2} + 2\frac{x^3}{L^3} \tag{4.11}$$

$$N_2(x) = \left(\frac{x}{L} - 2\frac{x^2}{L^2} + \frac{x^3}{L^3}\right)L \tag{4.12}$$

$$N_3(x) = 3\frac{x^2}{L^2} - 2\frac{x^3}{L^3} \tag{4.13}$$

$$N_4(x) = \left(-\frac{x^2}{L^2} + \frac{x^3}{L^3}\right)L \tag{4.14}$$

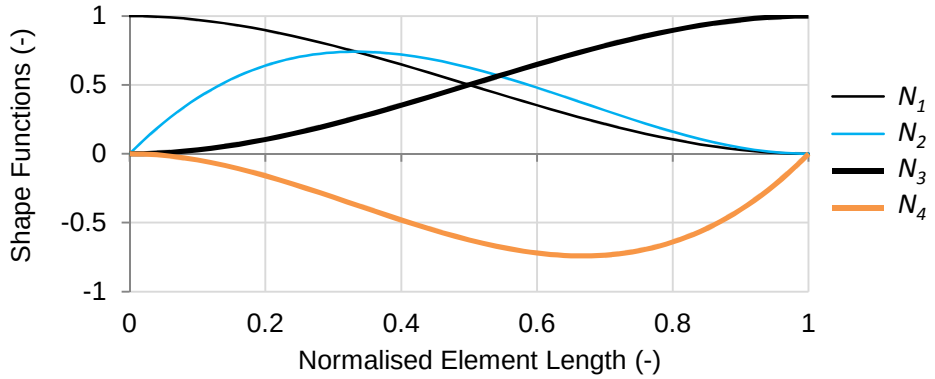


Figure 4.2 - Euler-Bernoulli beam element shape functions (generated using WTAC)

Substituting the boundary conditions of the beam element with the shear forces $V_{1,2}$ and moments $M_{1,2}$ obtained for an Euler-Bernoulli beam with Equation (4.1) one can derive the stiffness matrix [$K$] of the beam element of Equation (4.15). Similarly, the consistent mass matrix can be obtained by utilising the kinetic energy expression of Equation (4.16) and the force vector of Equation (4.17) which is calculated using the work-equivalence method.

$$\begin{bmatrix} V_1 \\ M_1 \\ V_2 \\ M_2 \end{bmatrix} = \frac{EI}{L^3}\begin{bmatrix} 12 & 6L & -12 & 6L \\ 6L & 4L^2 & -6L & 2L^2 \\ -12 & -6L & 12 & -6L \\ 6L & 2L^2 & -6L & 4L^2 \end{bmatrix}\begin{bmatrix} w_1 \\ \phi_1 \\ w_2 \\ \phi_2 \end{bmatrix} = [K_{EB}]\begin{bmatrix} w_1 \\ \phi_1 \\ w_2 \\ \phi_2 \end{bmatrix} \tag{4.15}$$

$$T_e = \frac{1}{2}\int_0^L \rho A\dot{w}^2 dx = \frac{1}{2}\int_0^L \rho A\dot{w}^2 dx = \frac{1}{2}\int_0^L \rho A\left[\dot{\vec{X}}^T\vec{N}^T\right]\left[\vec{N}\dot{\vec{X}}\right]dx$$

$$[M] = \int_0^L \rho A\left[\vec{N}^T\right]\left[\vec{N}\right]dx = \frac{\phi AL}{420}\begin{pmatrix} 156 & 22L & 54 & -13L \\ 22L & 4L^2 & 13L & -3L^2 \\ 54 & 13L & 156 & -22L \\ -13L & -3L^2 & -22L & 4L^2 \end{pmatrix} \tag{4.16}$$

$$[F] = \begin{pmatrix} f1 \\ f2 \\ f3 \\ f4 \end{pmatrix} = \begin{pmatrix} \int_0^L f(x,t)N_1(x)dx \\ \int_0^L f(x,t)N_2(x)dx \\ \int_0^L f(x,t)N_3(x)dx \\ \int_0^L f(x,t)N_4(x)dx \end{pmatrix} \tag{4.17}$$

In comparison to the uniform beam description detailed above, blades are modelled as tapered and rotating beams. The taper is used to approximate the continuous parameter variation along the blade span. Centrifugal or stress stiffening occurs when a thin structural member undergoing transverse motion is subject to an axial load ($F_{axial}$). Centrifugal stiffening consequently increases the transversal stiffness by:

$$[K_S] = \frac{F_{axial}}{L}\begin{bmatrix} \frac{6}{5} & \frac{L}{10} & -\frac{6}{5} & \frac{L}{10} \\ \frac{L}{10} & \frac{2L^2}{15} & -\frac{L}{10} & -\frac{L^2}{30} \\ -\frac{6}{5} & -\frac{L}{10} & \frac{6}{5} & -\frac{L}{10} \\ \frac{L}{10} & -\frac{L^2}{30} & -\frac{L}{10} & \frac{2L^2}{15} \end{bmatrix} \tag{4.18}$$

Based on the above, an FE code has been developed to model the blade structural dynamics as rotating tapered beams. The dynamic equations of motion take the well-known form of Equation (4.19).

$$[M]\ddot{\vec{X}}_d + [K]\vec{X}_d = \vec{F} \tag{4.19}$$

with,

$$[K] = [K_{EB}] + [K_S] \tag{4.20}$$

where, the variable $\vec{X}_d$ is the state vector containing nodal displacements and rotations. Finally, it was decided to benchmark the developed FE code (Table 4.1) against the rotating tapered beam case studies available in the literature (Gunda et al., 2007, Wang and Wereley, 2004). As it can be observed, the results obtained by WTAC closely match the published results within a 1% error margin.

Table 4.1 - WTAC Structural Validation for Rotating Tapered Beams

| **Normalised Rotational speed** | **1st mode** | | | **2nd mode** | | | **3rd mode** | | |
|---|---|---|---|---|---|---|---|---|---|
| | Gunda *et al.(Gunda et al., 2007)* | Wang and Wereley (Wang and Wereley, 2004) | WTAC | Gunda *et al.* (Gunda et al., 2007) | Wang and Wereley (Wang and Wereley, 2004) | WTAC | Gunda *et al.* (Gunda et al., 2007) | Wang and Wereley (Wang and Wereley, 2004) | WTAC |
| **0** | 3.8238 | 3.8238 | 3.8437 | 18.3173 | 18.3173 | 18.451 | 47.2649 | 47.2648 | 47.643 |
| **4** | 5.8788 | 5.8788 | 5.9329 | 20.6852 | 20.6852 | 20.918 | 49.6457 | 49.6456 | 50.116 |
| **8** | 9.554 | 9.554 | 9.6398 | 26.5437 | 26.5437 | 26.992 | 56.1595 | 56.1595 | 56.878 |
| **12** | 13.4711 | 13.4711 | 13.578 | 34.0877 | 34.0877 | 34.778 | 65.5237 | 65.5237 | 66.597 |

## 4.3 Reduced Order Model (ROM)

The FE model is a large system of equations of the size of $3N_nN_{Dof}$, where $N_n$ stands for the number of nodes kept after boundary conditions are applied and $N_{Dof}$ is the number of DOFs per node. While the static analysis of thousands of equations is relatively quick, the time required for the dynamic analysis of a vibrating continuous system increases drastically with the numbers of DOFs. A modal transformation is used to reduce the size of the FE model and obtain a reduced order model which provides a trade-off between accuracy, complexity and computational efficiency (Castaignet et al., 2011). In order to take advantage of the techniques developed for such transformation, the structural damping matrix is assumed to be a linear combination of the mass and stiffness matrices:

$$[D] = a_d [M] + b_d [K] \tag{4.21}$$

where, $a_d$ and $b_d$ are chosen such that the damping ratios of natural frequencies defined in Equation (4.22) are the same as the structural damping ratios of the wind turbine blades to be simulated. Considering the lack of data in early wind turbine design phase and the variability of the structural damping, the linear assumption is a well-established assumption (Adhikari, 2001).

$$\xi_i = \frac{\left(a_d + b_d \omega_i\right)^2}{2\omega_i} \tag{4.22}$$

The wind turbine blade structural system of equations becomes:

$$[M]\ddot{\vec{X}}_d + [D]\dot{\vec{X}}_d + [K]\vec{X}_d = \vec{F} \tag{4.23}$$

When equipped with CSs the forces acting on the blades are divided into the controlled $\vec{F}_c$ and external $\vec{F}_{ext}$ forces as shown below:

$$\vec{F} = \vec{N}_{ext}\vec{F}_{ext} + \vec{N}_c\vec{F}_c \tag{4.24}$$

where, the $\vec{N}_c$ and $\vec{N}_{ext}$ vectors are the respective transformation vectors for the external and the controlled forces. The initial state space model of the blade structure employed in this research is described as follows:

$$\begin{bmatrix} \dot{X}_d \\ \ddot{X}_d \end{bmatrix} = [A_d]\begin{bmatrix} X_d \\ \dot{X}_d \end{bmatrix} + [B_d]\vec{F}_c + [D_d]\vec{F}_{ext} \tag{4.25}$$

$$[A_d] = \begin{bmatrix} 0 & I \\ -[M]^{-1}[K] & -[M]^{-1}[D] \end{bmatrix} \tag{4.26}$$

$$[B_d] = [M]^{-1}\vec{N}_c \tag{4.27}$$

$$[D_d] = [M]^{-1}\vec{N}_{ext} \tag{4.28}$$

$$\vec{y}_d = [C_d]\vec{X}_d \tag{4.29}$$

where, $D_d$ stands for the state disturbance matrix and $y_d$ is the state space output. The output matrix $C_d$ depends on the available measurement(s) and position of strain sensor(s) located along the blade span. To the best of the author's knowledge, this is the first time the structural and aerodynamic CS models are written in this form.

As for a full rank continuous linear system of equation, there exists a transformation matrix $[V_e]$ that can be used to transform [$K$], [$M$] and [$D$] into the modal matrices [$K_q$], [$M_q$] and [$D_q$]:

$$[V_e]^T [K][V_e] = [K_q] = \begin{bmatrix} k_{q1} & 0 & 0 \\ 0 & ... & 0 \\ 0 & 0 & k_{qn} \end{bmatrix} \tag{4.30}$$

$$[V_e]^T [M][V_e] = [M_q] = \begin{bmatrix} m_{q1} & 0 & 0 \\ 0 & ... & 0 \\ 0 & 0 & m_{qn} \end{bmatrix} \tag{4.31}$$

$$[V_e]^T [D][V_e] = [D_q] = \begin{bmatrix} d_{q1} & 0 & 0 \\ 0 & ... & 0 \\ 0 & 0 & d_{qn} \end{bmatrix} \tag{4.32}$$

Applying the transformation to Equation (4.23) and defining the modal coordinate vector $\vec{Q}$ as $\vec{Q} = [V_e]^{-1} \vec{X}_d$ one obtains

$$[M_q]\ddot{\vec{Q}} + [D_q]\dot{\vec{Q}} + [K_q]\vec{Q} = \vec{F}_q \tag{4.33}$$

The modal transformation of Equation (4.33) results in a series of independent dynamic equations whose solutions are complex conjugates representing the dynamics of the damped natural frequencies of the FE model. Furthermore, it can be shown that the transformation matrix $[V_e]$ is unique and is the eigenvector matrix of the system. Since the blade structural dynamic is described by the combination of the blade mode shapes vibrating at the natural frequencies, it is possible to neglect particular frequencies that do not significantly contribute to the overall blade dynamic. Previous works as well as numerical results show that for wind turbine blades operating in unsteady conditions the first two or three natural frequencies are usually sufficient for accurate calculations of the flapwise deflection and bending moment (Castaignet et al., 2014, Jonkman and Buhl, 2005). The reduced modal blade-CSs aero-structural model (subscript *qr*) is then given as:

$$\begin{bmatrix} \dot{Q}_r \\ \ddot{Q}_r \end{bmatrix} = \left[A_{qr}\right]\begin{bmatrix} Q_r \\ \dot{Q}_r \end{bmatrix} + \left[B_{qr}\right]\vec{F}_c + \left[D_{qr}\right]\vec{F}_{ext} \tag{4.34}$$

$$\vec{y}_{qr} = \left[C_{qr}\right]\vec{Q}_r \tag{4.35}$$

$$\vec{Y}_B = \left[C_B\right]\vec{X}_d = \left[C_B\right]\left[V_e\right]\vec{Q} = \left[C_B\right]\left[\vec{V}_{e,1} \quad \vec{V}_{e,2} \quad \ldots \quad \vec{V}_{e,n}\right]\begin{bmatrix} Q_1 \\ Q_2 \\ \ldots \\ Q_n \end{bmatrix} = \left[C_B\right]\left[\vec{V}_{e,1}Q_1 + \vec{V}_{e,2}Q_2 + \ldots + \vec{V}_{e,n}Q_n\right] \tag{4.36}$$

$$\vec{Y}_B = \vec{M}_{s1}Q_{r,1} + \vec{M}_{s2}Q_{r,2} + \vec{M}_{s3}Q_{r,3} + \ldots + \vec{M}_n Q_{r,\mathrm{n}} \tag{4.37}$$

where, $\vec{y}_{qr}$ is the vector of measured outputs and $\vec{Y}_B$ is the vector containing the transversal displacement of each node of the finite element model. The output matrix $C_B$ is a sparse matrix of zeros and ones used to extract the transversal displacement when multiplied by $\vec{X}_d$. Equation (4.37) is the common form of Equation (4.36) where the $\vec{M}_{si}$ terms are the blades' mode shapes. Mode shapes are the physical shapes that a structure takes when vibrating at natural frequencies. The mode shapes depend only on the radial coordinate as depicted in Figure 4.3 for the first three flapwise mode shapes of the NREL 5 MW wind turbine blades. It is important to note that the modal coordinates are independent of the blade span at which the displacement is observed. The flapwise blade displacement at any point along the blade span is a linear combination of the modal coordinates obtained through the output matrix $C_{qr}$. Therefore, for case of $Q_r = 0$ the blade displacement at any span location is zero.

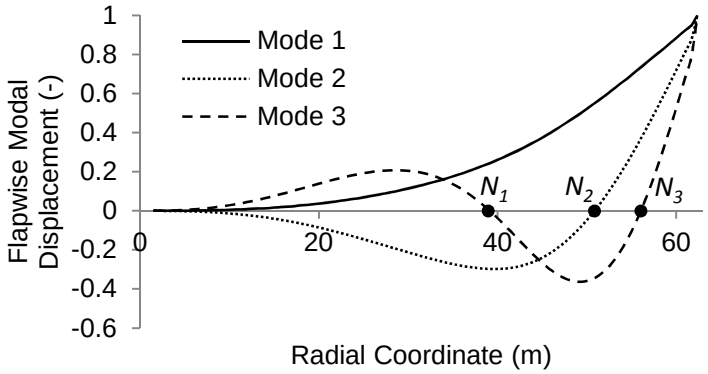


Figure 4.3 - Normalised mode shapes of the NREL 5MW wind turbine blade

## 4.4 Wind Turbine Blade Structural Parameters

The two previous sections introduced the general analytical form of the structural wind turbine blade model. In this section, the calculations of the model parameters are explained. The internal structure of blades is generally divided into several parts as shown in Figure 4.4 and must be carefully designed in order to obtain high bending stiffness while limiting the blade mass.

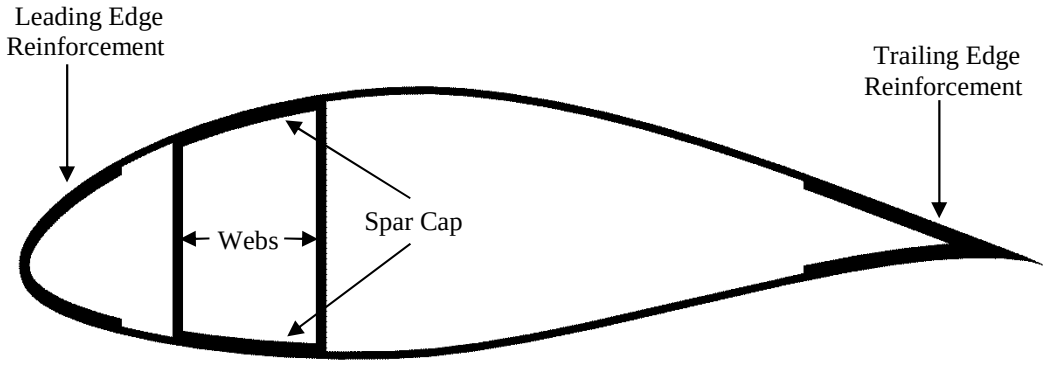


Figure 4.4 - Aerofoil internal layout example

The structural properties of a composite blade cross-section at various locations along its span are calculated and integrated over the blade span in order to approximate the entire blade structural properties such as weight, flapwise/edgewise mass moment of inertia $\left(I_{flap}, I_{edge}\right)$ and bending stiffness $\left(EI_{flap}, EI_{edge}\right)$. The cross-sectional mass moment of inertia about the *x*-axis and *y*-axis can be calculated as in the following two equations:

$$I_{xx} = \iint_A \rho_{mat}\, y^2 dA \tag{4.38}$$

$$I_{yy} = \iint_A \rho_{mat}\, x^2 dA \tag{4.39}$$

where, $\rho_{mat}$ and A denote the material density and the cross-sectional aerofoil surface area. The location of the centre of mass $\left(x_{cm}, y_{cm}\right)$ and bending centroid$\left(x_e, y_e\right)$ must also be calculated:

$$x_e = \frac{1}{[EA]} \iint_A xE(x,y)\, dA \tag{4.40}$$

$$y_e = \frac{1}{[EA]} \iint_A yE(x,y)\, dA \tag{4.41}$$

where, [*EA*] is the cross-sectional elastic modulus in the blade span direction:

$$[EA] = \iint_A E(x,y)\,dA \tag{4.42}$$

The flapwise and edgewise cross-sectional bending stiffnesses are calculated according to:

$$EI_{Edge} = \iint_A E(\bar{x}_e,\bar{y}_e)\bar{x}_e^2 dA \tag{4.43}$$

$$EI_{Flap} = \iint_A E(\bar{x}_e,\bar{y}_e)\bar{y}_e^2 dA \tag{4.44}$$

where the integrals are calculated with respect to the elastic centre. An example comparing WTAC with the renown PreComp and SolidWorks (Gunjit, 2006, Cansizoglu et al., 2008) software for the aerofoil defined in Figure 4.5 and Table 4.2 is shown in Table 4.3. It can be seen that the three software are in agreement.

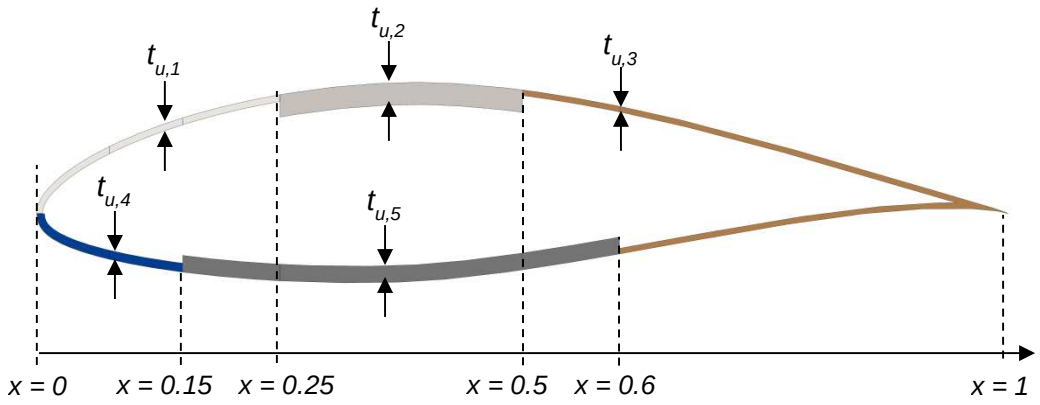


Figure 4.5 - Blade cross-section used for comparison between the developed code, SolidWorks, and PreComp.

Table 4.2 - Material properties and thickness

| | Thickness | Material | Elastic modulus in *x*-axis (MPa) | Elastic modulus in the *y*-axis (MPa) | Density (kg/m$^3$) |
|---|---|---|---|---|---|
| $t_{u,1}$ | 6mm | SNL Triax | 27 700 | 13 650 | 1850 |
| $t_{u,2}$ | 20mm | ETL 5500 (UD) | 41 800 | 14 800 | 1920 |
| $t_{u,3}$ | 15mm | Saertex | 13 600 | 13 300 | 1780 |
| $t_{u,4}$ | 8mm | Foam | 256 | 256 | 200 |
| $t_{u,5}$ | 5mm | Carbon (UD) | 114 500 | 8690 | 1220 |

Table 4.3 - Cross-sectional blade properties comparison between WTAC, SolidWorks and PreComp

| | Lineal Density (kg/m) | Flapwise Inertia (kg.m) | Edgewise Inertia (kg.m) | Flapwise Stiffness ($Nm^2$) | Edgewise Stiffness ($Nm^2$) | $x_{cm}$ (m) | $y_{cm}$ (m) | $x_e$ (m) | $y_e$ (m) |
|---|---|---|---|---|---|---|---|---|---|
| WTAC | 28.854 | 0.12609 | 1.5284 | 4.48E+06 | 2.69E+07 | 0.4459 | 0.0364 | 0.3847 | -0.00957 |
| PreComp | 29.45 | 0.13 | 1.69 | 4.46E+06 | 2.83E+07 | 0.455 | 0.036 | 0.387 | -0.009 |
| SolidWorks | 28.8 | 0.126 | 1.526 | 4.48E+06 | 2.69E+07 | 0.4459 | 0.0364 | 0.3848 | -0.00953 |

In order to model the wind turbine blades accurately with the FE method, the cross-sectional properties of aerofoils must be calculated at each node. Figure 4.6 through 4.9 show the lineal density (i.e. mass per unit length), cross-sectional bending stiffness and mass moment of inertia of the NREL 5 MW wind turbine blades. As it can be observed, the lineal density and stiffnesses are relatively high in the first portion of the blade span before substantially decreasing around 10% of the blade span and then smoothly decreasing as the radius increases. The blade geometry is mostly responsible for this observed trend. Since the bending moments are maximal at the blades' root, a reinforced circular cross-section is used in order to reduce stress. As it moves along the blade span in the tip direction, aerofoils progressively replace the circular and elliptic root geometry. The maximal chord and thickness occur at about 18% of the blade span where one can notice a slight increase in mass and stiffness. The chord and thickness of aerofoils then gradually decrease from this point to the blade's tip.

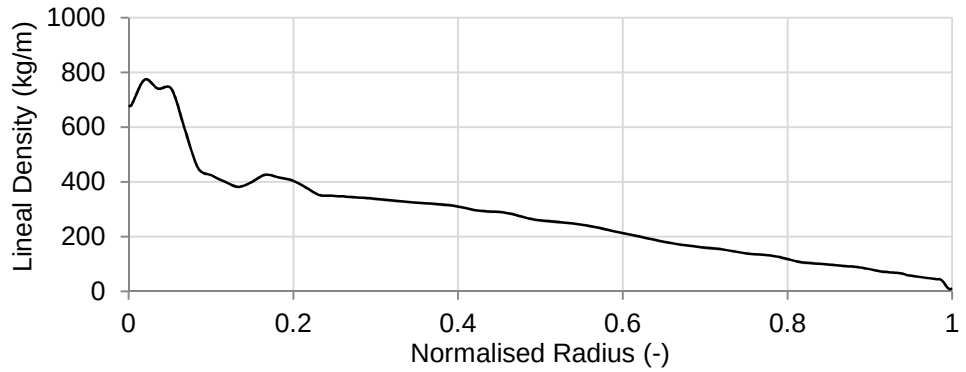


Figure 4.6 - NREL 5 MW wind turbine lineal density (kg/m)

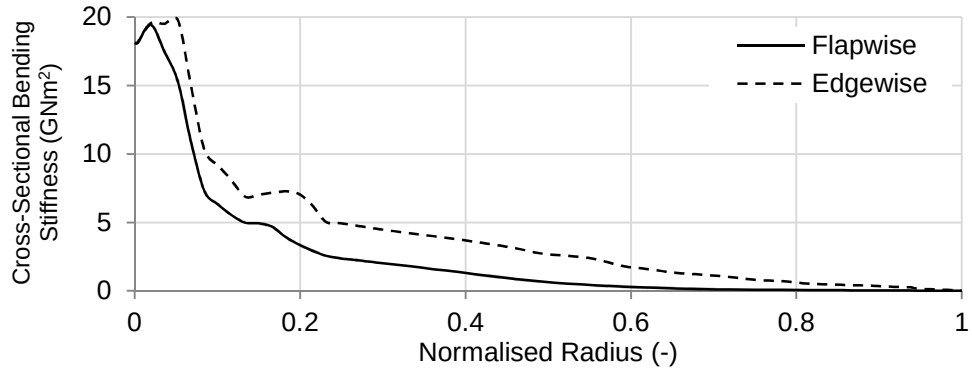


Figure 4.7 - NREL 5 MW wind turbine cross-sectional bending stiffness

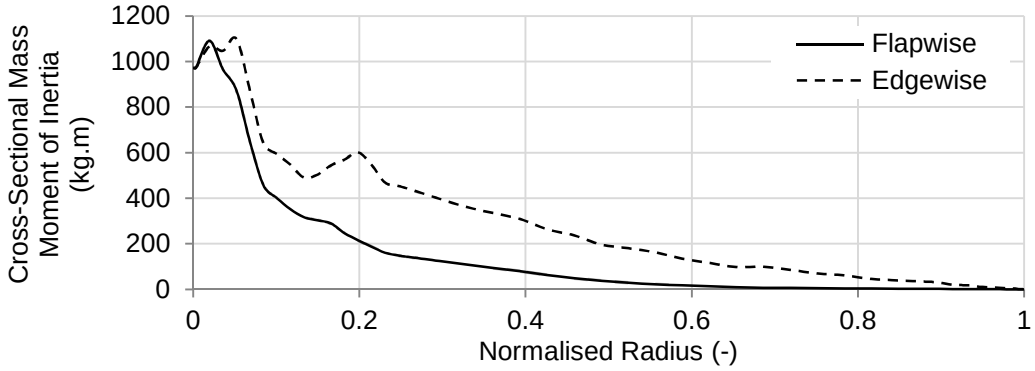


Figure 4.8 - NREL 5 MW wind turbine cross-sectional mass moment of inertia

## 4.5 WTAC - Validation of the Wind Turbine Blade Aero-Structural Model

In this section the results of our FE model coupled with the aerodynamic module are compared with FAST. This step is used to benchmark the aeroelastic module of WTAC before moving onto the aeroservoelastic problem of controlling a wind turbine blade equipped with control surfaces. All results presented in this section under the WTAC label are results which have generated using the in-house code developed during this research. The wind turbine models used for comparison are the variable speed pitch-controlled 1.5 MW WindPACT wind turbine and the NREL 5 MW wind turbines whose general features are given in Table 4.4.

Table 4.4 - Wind turbines' general features

| Wind Turbine | WindPACT 1.5 MW | NREL 5 MW |
|---|---|---|
| Hub height | 84.28m | 87.6m |
| Diameter | 70m | 126 m |
| Blade length | 33.25m | 61.5m |
| Blade mass | 3912.1kg | 17 740kg |
| Number of blades | 3 | 3 |
| Rated speed | 20.46rpm | 12.1rpm |
| Structural blade damping for all modes (in per-cent of critical) | < 3% | < 3% |

The natural frequencies calculated by WTAC and FAST are presented in Table 4.5. It can be observed that the primary modes of vibrations (i.e. first edgewise and flapwise natural frequencies) predicted by both software closely match.

Table 4.5 - Wind turbine blade natural frequencies (Hz)

| | WindPACT 1.5 MW | | NREL 5 MW | |
|---|---|---|---|---|
| | FAST | WTAC | FAST | WTAC |
| 1st Flapwise | 1.22 | 1.18 | 0.6993 | 0.7056 |
| 2nd Flapwise | 3.70 | 3.40 | 2.0205 | 2.0088 |
| 1st Edgewise | 1.88 | 1.79 | 1.0793 | 1.0943 |

In Figure 4.9, the author compare the steady state results of WTAC with FAST and DU-SWAMP. As it can be observed, the steady state results predicted using WTAC are in some cases closer to the predicted results by DU-SWAMP (e.g. rotor thrust force), while in some other cases closer to the results produced by FAST. The discrepancies between the flapwise displacements of WTAC, DU_SWAMP and FAST are likely caused by a combination of factors. In DU_SWAMP the tower top deflection is included in the blade tip displacement (Resor et al., 2010). WTAC does not include the flapwise and edgewise coupling. The three codes utilise different structural models (i.e. Super-Element, Finite Element, Multi-Body). Furthermore, non-linear structural phenomena are not considered in WTAC. On the other hand, in WTAC, the BEMT aerodynamic code employs a convergence accelerator algorithm ensuring convergence in its iteration loop.

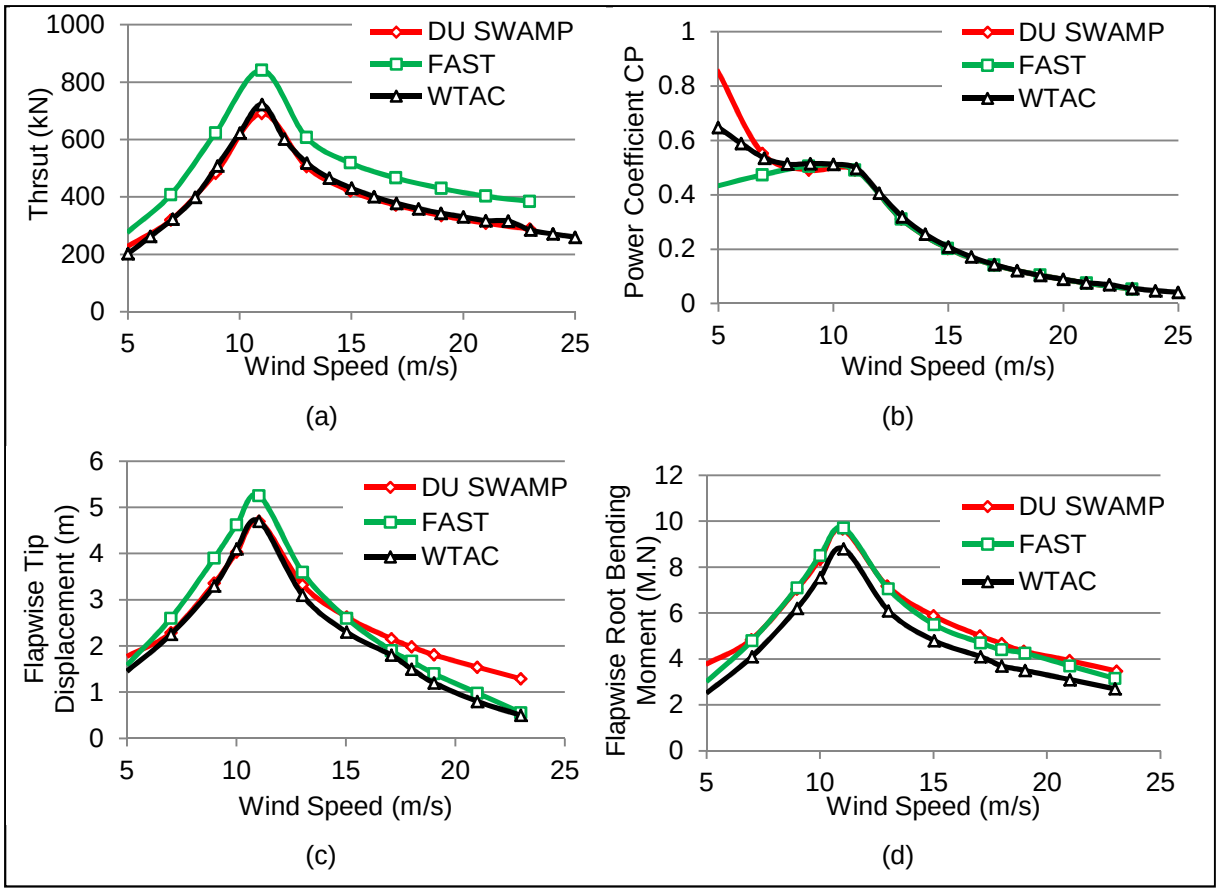


Figure 4.9 - Steady state results: (a) Thrust, (b) Power coefficient, (c) Flapwise tip deflection and (d) root bending moment

In addition to the steady state results, the author also compares the dynamic results obtained using WTAC against FAST. Figures 4.10 and 4.11 show the results obtained by WTAC and FAST for the WindPACT wind turbine operating in windshear conditions for the mean wind speeds of 7 m/s and 15m/s. Similarly, Figures 4.12 and 4.13 present the results obtained by WTAC and FAST for the NREL 5 MW wind turbine operating in windshear conditions for the mean wind speeds of 7 m/s and 10 m/s. In both cases it can be observed that while the periods of oscillation are similar, there is a constant phase shift between both predictions.

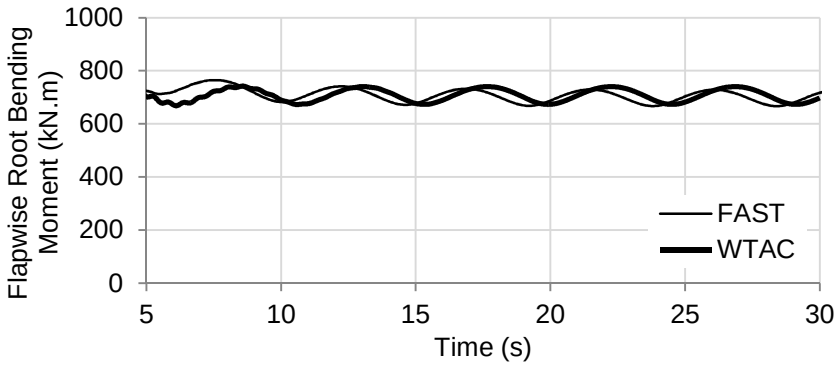


(a)

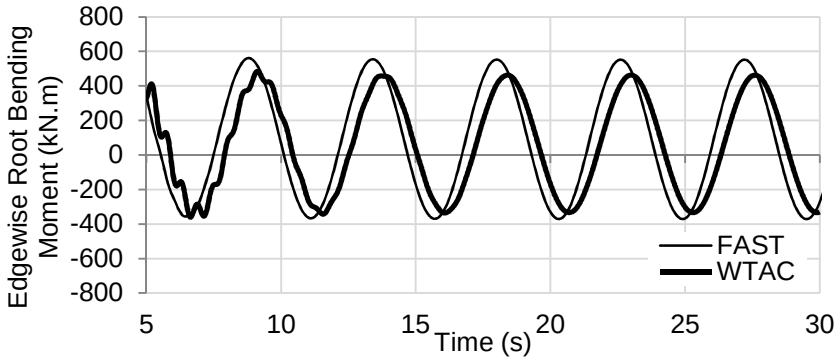


(b)

Figure 4.10 - (a) Flapwise and (b) Edgewise root bending moment
(WindPACT wind turbine operating at 7m/s mean wind speed windshear)

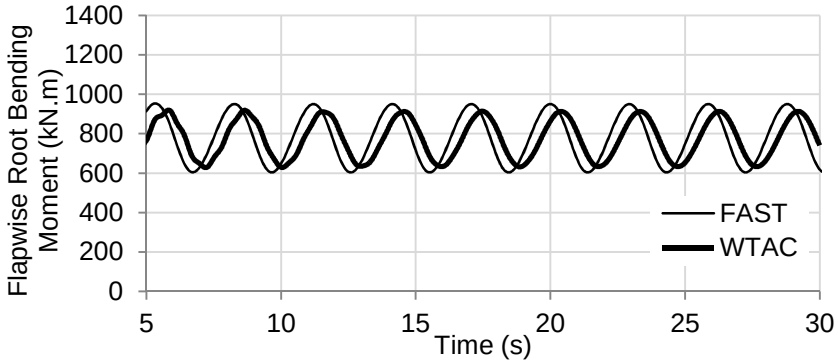


(a)

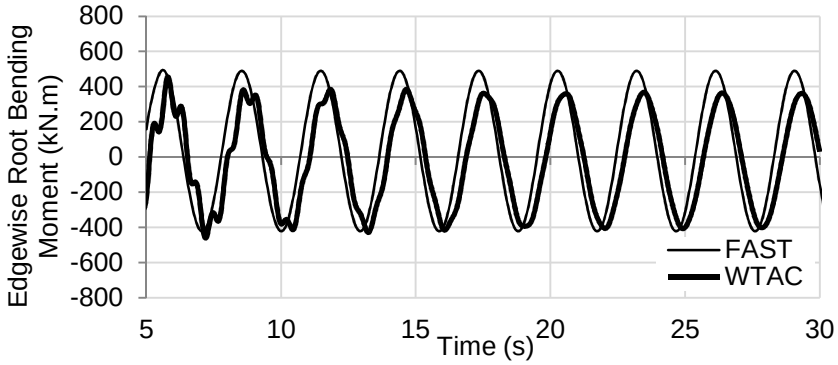


(b)

Figure 4.11 - (a) Flapwise and (b) Edgewise root bending moment
(WindPACT wind turbine operating at 15m/s mean wind speed windshear)

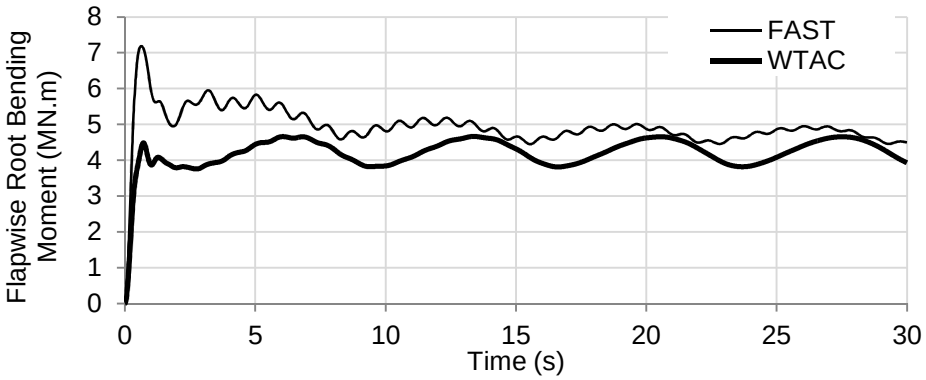


(a)

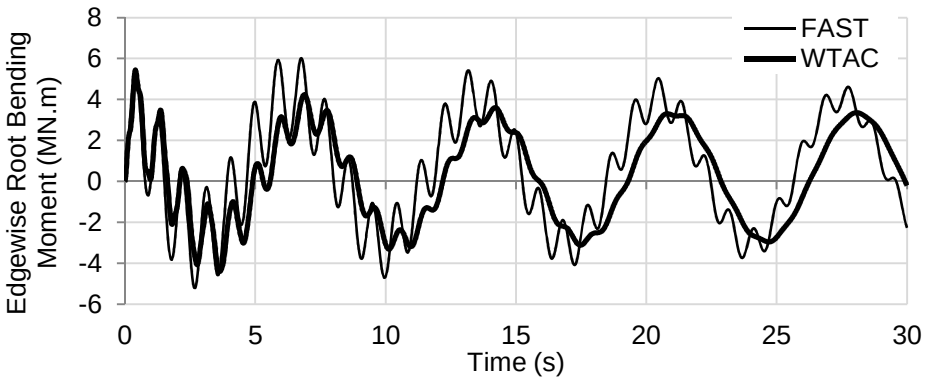


(b)

Figure 4.12 - (a) Flapwise and (b) Edgewise root bending moment
(NREL 5MW wind turbine operating at 7m/s mean wind speed windshear)

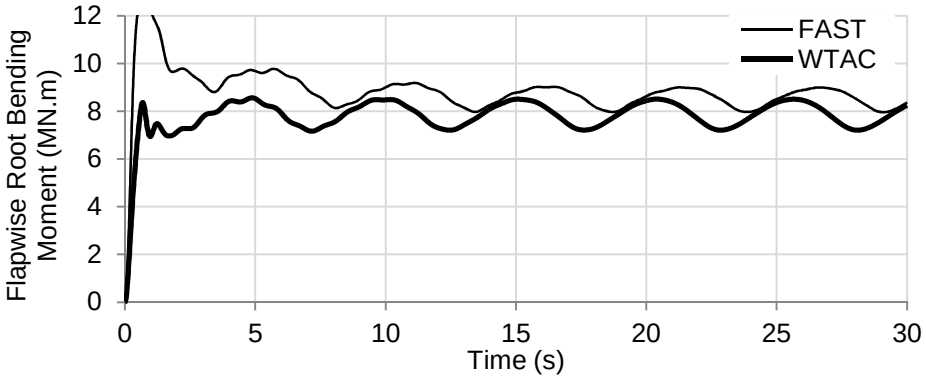


(a)

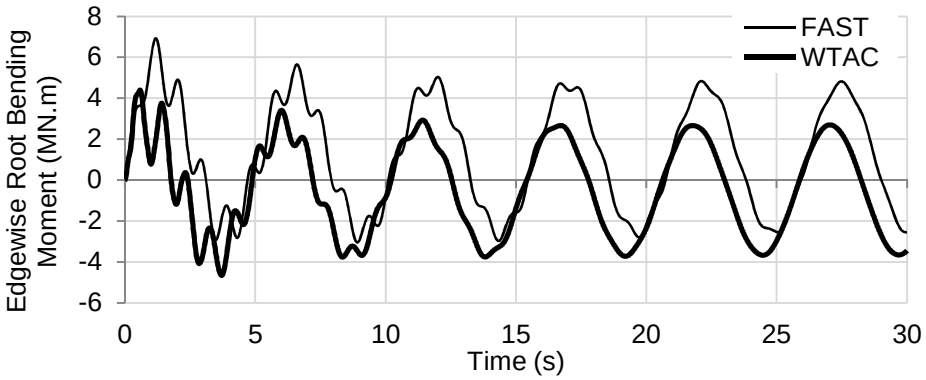


(b)

Figure 4.13 - (a) Flapwise and (b) Edgewise root bending moment
(NREL 5MW wind turbine operating at 10m/s mean wind speed windshear)

Further comparisons are made to evaluate the dynamic results of WTAC with FAST are presented in the following figures. Figure 4.14 compares both codes for the WindPACT wind turbine operating, in a turbulent wind field, at near rated wind speed. The time varying wind speed at hub, power, flapwise and edgewise root bending moments are respectively presented in Figure 4.14.a, b, c, and d. As shown in these figures, the low wind speed variations are well captured by both WTAC and FAST. As shown in Figure 4.14.c, the predicted flapwise root bending moment matches well at the start of the simulation before small discrepancies appear. Since the blade displacement at one given time instant is not only dependent on the aerodynamic forces at that time but also on all of the previous forces that have contributed to the blade motion, the discrepancies between both software are bound to increase as the time passes. Figure 4.15 presents similar results but for the NREL 5MW wind turbine operating in a turbulent wind field of mean wind speed of 15m/s. As for the WindPACT simulation, the low frequency variations are well captured by both codes. The flapwise root bending moment predicted by both codes show very similar trends before progressively accumulating disparities. On the other hand, the gravity dominated edgewise loads is well predicted. The comparisons between WTAC and FAST show that despite the fact that WTAC uses a linear model for wind turbine blades, it is able to capture the main variations (i.e. 1$P$ load amplitudes) of power and root bending moments.

Throughout this section, the author have validated the steady state and dynamic aeroelastic response of the developed in-house code WTAC. It was shown that WTAC captures the main flapwise and edgewise dynamics of the vibration problem at hand. This validation is critical since insights about the vibrating blade control problem and control strategies proposed in the followings are based on this model.

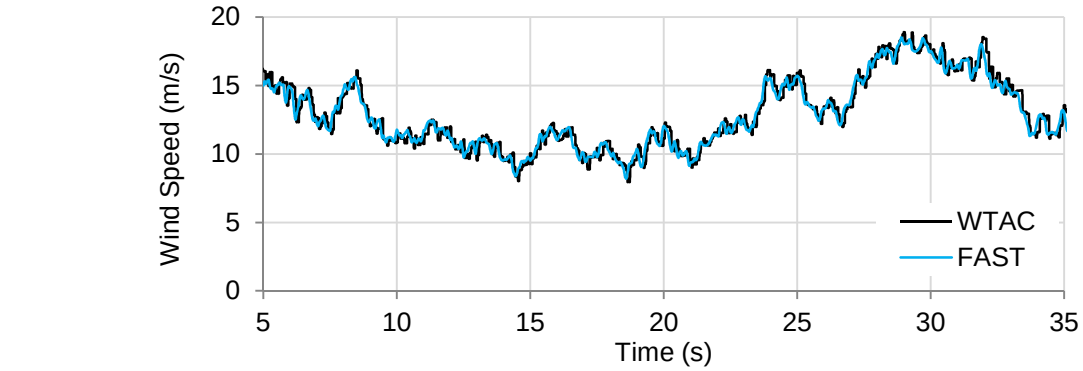


(a)

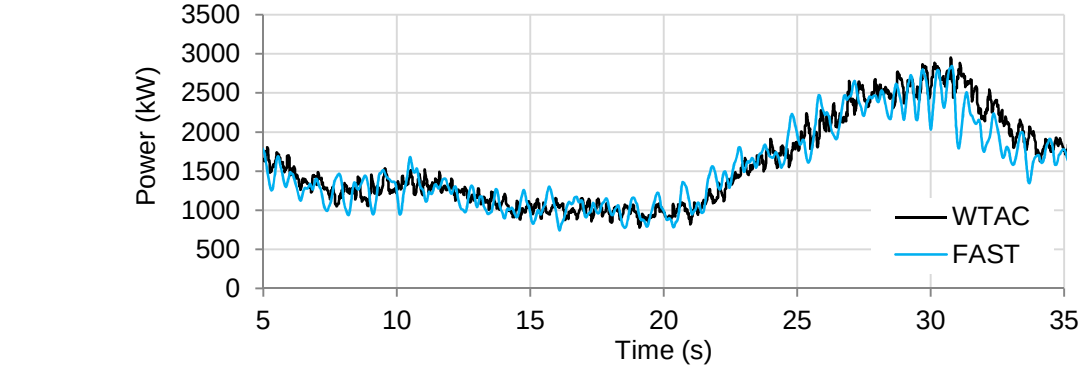


(b)

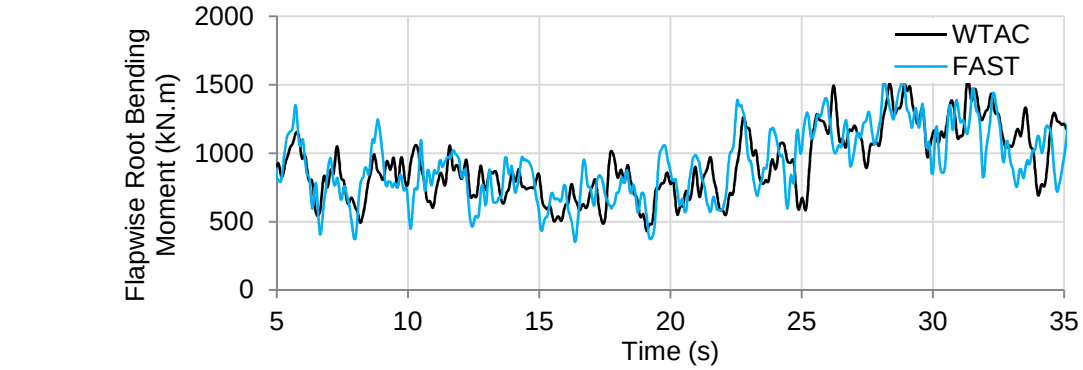


(c)

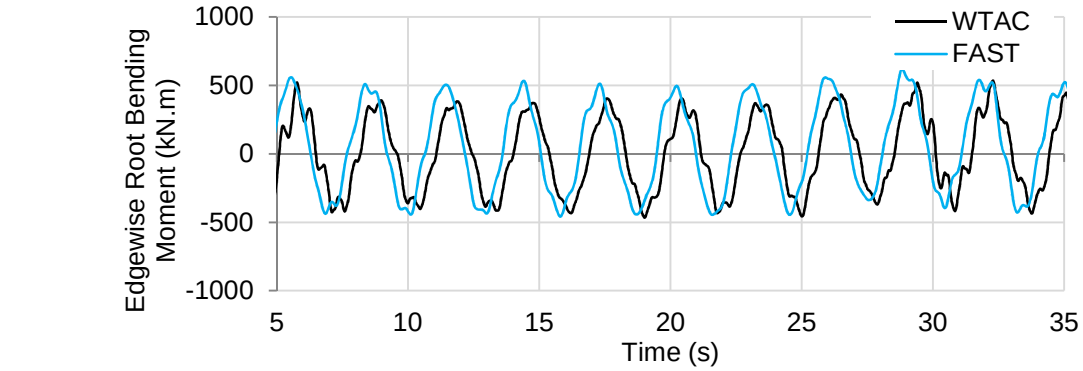


(d)

Figure 4.14 - (a) Wind Speed at Hub, (b) Power, (c) Flapwise and (d) Edgewise root bending moment (WindPACT wind turbine operating at 13m/s mean wind speed)

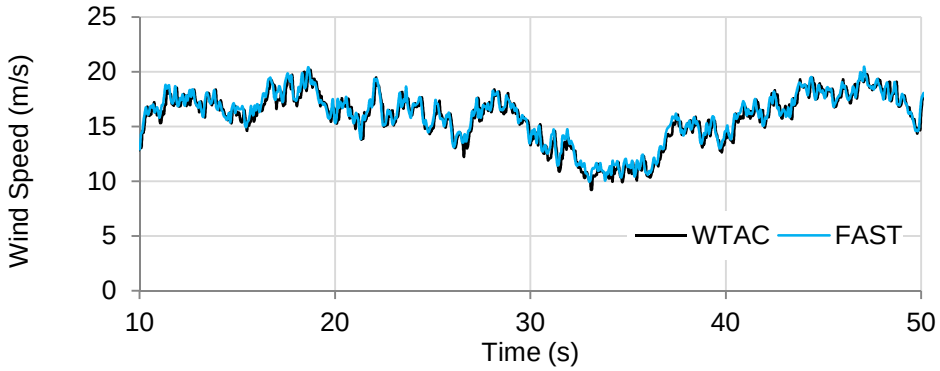


(a)

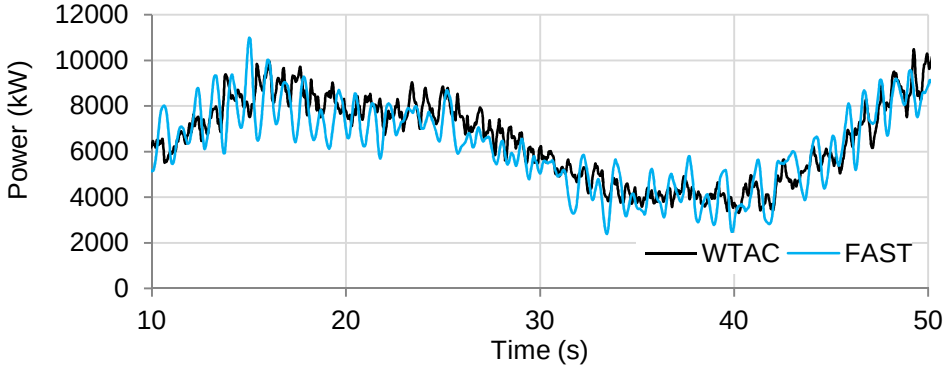


(b)

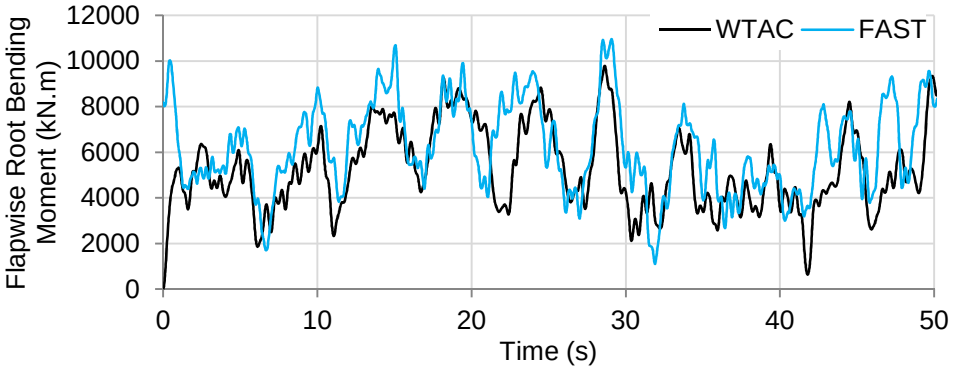


(c)

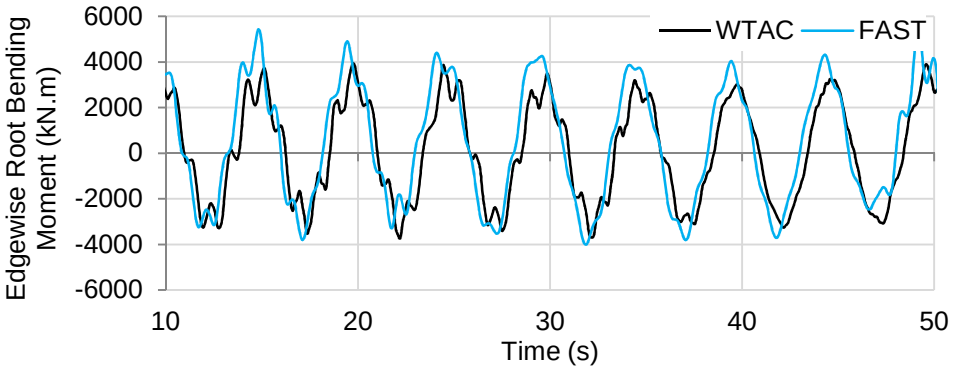


(d)

Figure 4.15 - (a) Wind Speed at Hub, (b) Power, (c) Flapwise and (d) Edgewise root bending moment (NREL 5MW wind turbine operating at 15m/s mean wind speed)

## 4.6 Aeroelastic Model of Wind Turbine Blades Equipped with Control Surfaces

In this section, the reduced structural model is coupled with the aerodynamic model of control surfaces. In doing so, the author's aim is twofold: (i) design control strategies which, for the first time in the literature, take into account the overall system dynamic (i.e. the blades structural dynamics and the control surfaces dynamics). (ii) Most importantly, the frequency response of the proposed coupled model is later on analysed and used in order to explain the dynamic response of actively controlled wind turbine blades. Understanding this dynamic response is critical for designing dedicated control systems.

According to BEMT the blade is divided into segments on which the external force on each element is assumed to be a uniformly distributed time varying force. It is also assumed that the implementation of the control surfaces on the planar frame element does not change its structural properties. The final system of equations obtained by combining both models in a state space form is described as follows:

$$\dot{\vec{X}}_{Ae} = [A_{Ae}]\vec{X}_{Ae} + [B_{Ae}][u] + \vec{D}_{Ae} \tag{4.45}$$

$$\vec{y}_{Ae} = [C_{Ae}]\vec{X}_{Ae} \tag{4.46}$$

$$\vec{X}_{Ae} = \begin{bmatrix} Q_r \\ \dot{Q}_r \\ X_{Fr} \end{bmatrix} \tag{4.47}$$

$$A_{Ae} = \begin{bmatrix} [A_{qr}] & [A_{As}] \\ 0 & [A_{Fr}] \end{bmatrix} \tag{4.48}$$

$$A_{As} = \begin{bmatrix} 0 \\ M^{-1}V_e^{\,T}\vec{F}C_{Fr} \end{bmatrix} \tag{4.49}$$

$$[B_{Ae}] = \begin{bmatrix} [0] \\ [B_{Fr}] \end{bmatrix} \tag{4.50}$$

$$C_{Ae} = \begin{bmatrix} [C_{qr}] & 0 \\ 0 & [C_{Fr}] \end{bmatrix} \tag{4.51}$$

The final system has a size of $2N_f + 3N_c$, where $N_f$ is the number of frequencies kept after the structural model reduction and $N_c$ is the number of elements equipped with a control surface.

The final system described in Equation (4.45) is naturally stable around the equilibrium point $X_{Ae} = \vec{0}$.

## 4.7 Summary - Aero-Structural Wind Turbine Blade Model

Chapter 4 served as a validation step for the developed finite element code employed for modelling the structural dynamics of wind turbine blades. The fundamental equations behind the structural model were briefly reminded and the calculations of blade cross-sectional properties were detailed. The finite element model was then transformed in its modal form in order to reduce computational effort while conserving high accuracy.

The main issues addressed in this chapter can be summarised as follows:

- First, the results generated by the newly developed aeroelastic simulator WTAC were verified against data reported in the literature and the NREL's code FAST.

- The author showed that the proposed linear structural model of wind turbine blades captures the prime vibratory dynamics. As a results, the developed model can confidently be used as an analogue for the purpose of controlling the main wind turbine blade loads.

- The author proposed a general mathematical description of the coupled aeroelastic problem of the blades equipped with control surfaces. This model and the information contained in it are crucial for designing dedicated control systems and clarifying the dynamics of actively controlled wind turbine blades.

- Finally, a general architecture for the coupling of the wind turbine blade aerodynamic model, structural model and the control surfaces is described. The flowchart of WTAC is shown in Figure 4.16. The proposed general architecture ease the implementation of control surfaces onto wind turbine blades. Moreover, it provides a guideline for other aeroelastic studies and support for developing and testing aeroelastic controllers for blades equipped with control surfaces

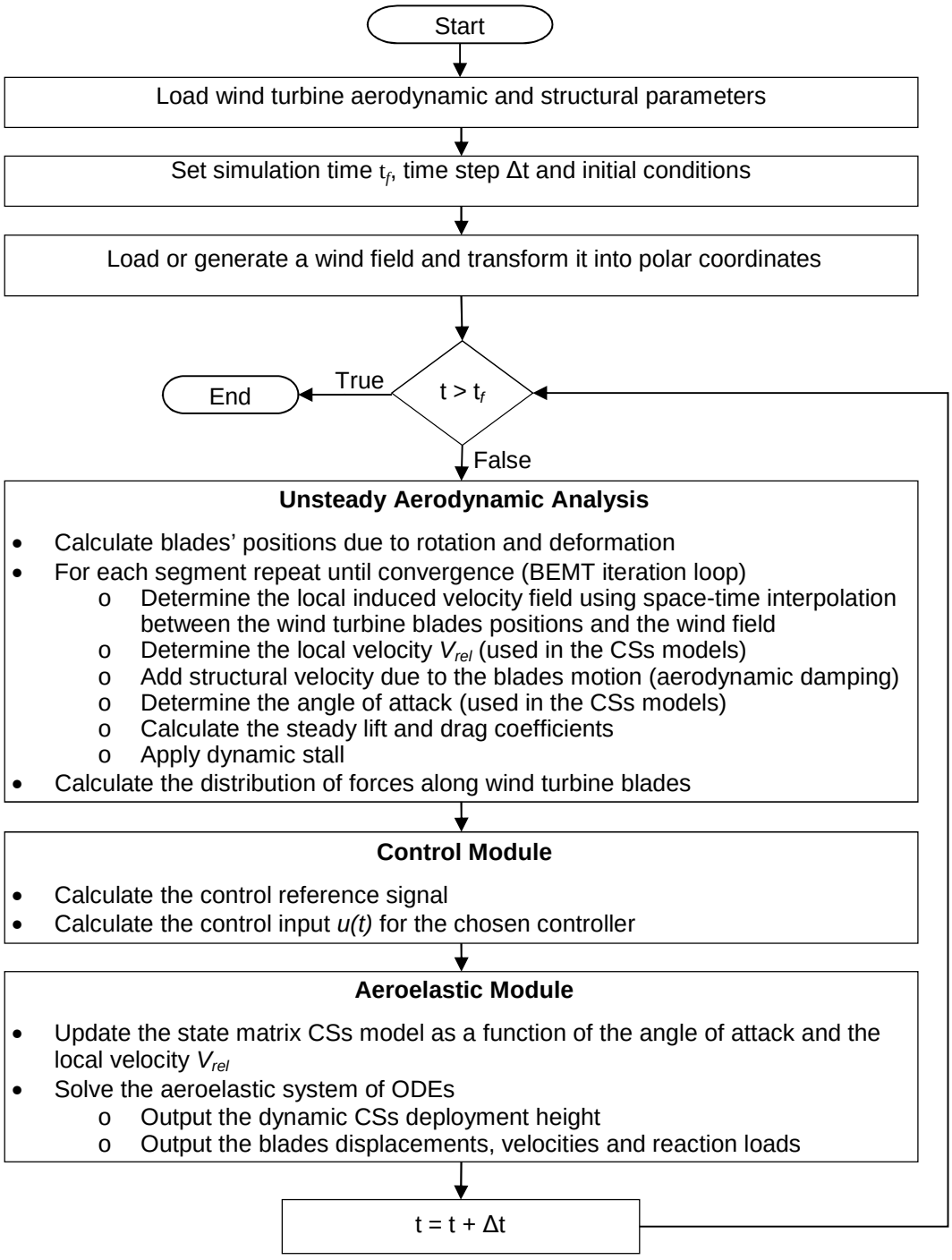


Figure 4.16 - WTAC wind turbine simulator flowchart

# 5. Control System Design

## 5.1 Introduction

As previously mentioned, several proof of concepts of CSs employed for load alleviation on wind turbine blades can be found in the literature. However, most of the proposed control strategies do not investigate their impact on the aeroelastic dynamic of actively controlled blades. This chapter intends to investigate the aeroelastic stability, observability (e.g. sensing system) and controllability of wind turbine blades equipped with CSs. The first objective of the present chapter, addressed in Section 5.2, is to investigate the aeroelastic stability of controlled wind turbine blades.

State-based controllers are commonly proposed in the literature. However, for those state-based control strategies to work properly it is crucial to ensure a sufficiently accurate state estimation. Moreover, it is known that the dynamic of wind turbine blades is driven by significant unknown forces and that those forces should not be considered known by the control system. In spite of these considerations, the system state estimation is often assumed fully known and is rarely considered a critical issue. The second objective of this chapter, addressed in Section 5.3, is therefore to investigate the types and numbers of sensors required for estimating the state vector of actively controlled wind turbine blades.

Section 5.4 is used to present the various controllers that will be employed in the next chapter. Controllers used for load alleviation are briefly described. In comparison to the literature, a particular distinction between continuous and discontinuous controllers is made in this research. Last but not least, the author proposes a frequency-based loop-shaping approach for analysing the dynamic of actively controlled aerodynamic surfaces. The proposed loop-shaping approach is key to many of the conclusions presented in the next chapter.

## 5.2 Blades Aeroelastic Stability

Aeroelastic instability due to the coupling of aerodynamic forces and structure motions results in self-sustainable vibrations and can lead to the damage and failure of wind turbines. Elements creating lift such as aircraft wings or wind turbine blades are especially prone to it. Amongst the various instabilities, wind turbine blades are particularly subject to flutter. The flutter instability refers to self-increasing amplitudes of oscillation of a structure due to negative aerodynamic damping. The wind turbine damping determines whether or not flutter will occur. A high damping value corresponds to rapidly dissipated energy and damped

vibrations, making the system stable. The damping of wind turbine blades is often distinguished between the structural and the aerodynamic damping. Aerodynamic forces responding in opposition to the blades motion (i.e. aerodynamic damping) are the major source of damping.

### 5.2.1 Structural Damping

Flapwise and edgewise DOFs are the main wind turbine blade dynamics. The blades structural dynamic can be analysed using the reduced modal form:

$$\left[M_{qr}\right]\ddot{\vec{Q}}_r + \left[C_{qr}\right]\dot{\vec{Q}}_r + \left[K_{qr}\right]\vec{Q}_r = \vec{F}_{qr} \tag{5.1}$$

As shown in Chapter 4, the blade dynamic response is a linear combination of mode shapes. Moreover, all modes are independent of each other. Hence, the calculation of the natural frequency and structural damping of each mode are straightforward. The structural dynamic of the three first flapwise mode shapes for the NREL 5 MW wind turbine is given by:

$$\begin{bmatrix} 269 & 0 & 0 \\ 0 & 284 & 0 \\ 0 & 0 & 248.5 \end{bmatrix}\ddot{\vec{Q}}_r + \begin{bmatrix} 406.5 & 0 & 0 \\ 0 & 83 & 0 \\ 0 & 0 & 10 \end{bmatrix}\dot{\vec{Q}}_r + \begin{bmatrix} 200000 & 0 & 0 \\ 0 & 41190 & 0 \\ 0 & 0 & 4747 \end{bmatrix}\vec{Q}_r = \vec{F}_{qr} \tag{5.2}$$

The above equation forms a system of three independent second-order equations for which the un-damped natural frequencies $\omega_{n,j}$ are calculated as:

$$\omega_{n,j} = \sqrt{\frac{k_j}{m_j}} \tag{5.3}$$

In case of damped oscillation, the modal coordinates can be found analytically as given by:

$$Q_j = A_i e^{\lambda_j t} \quad \text{with} \quad \lambda_j = \frac{-c_j}{2m_j} \pm i\frac{1}{2m_j}\sqrt{{c_j}^2 - 4{m_j}^2{\omega_{n,j}}^2}\,, \tag{5.4}$$

in which the damped natural frequency $\omega_j$ and the damping coefficient of each mode are defined as:

$$\omega_j = \frac{1}{2m_j}\sqrt{{c_j}^2 - 4{m_j}^2{\omega_{n,j}}^2} \tag{5.5}$$

$$C_j = \frac{-c_j}{2m_j} \tag{5.6}$$

The damping ratio is defined as the damping coefficient divided by the critical damping value as in:

$$\xi_i = \frac{C}{C_{cr}} = \frac{C_i}{2\omega_i m_i} \tag{5.7}$$

where, the critical damping $C_{cr}$ denotes the special case in which the system responds as fast as possible without oscillating. This occurs when the poles are both real (i.e. $c_j = 2m_j\omega_{n,j}$). Table 5.1 summarises the un-damped and damped natural frequencies as well as damping ratios for the first three flapwise modes of the NREL 5 MW wind turbine blades. It can be seen that the structural damping is small and therefore the un-damped and damped natural frequencies are almost identical. Because the damping ratio is low, the structural model is stable but will not strongly damp vibrations as shown in Figures 5.1 and 5.2.

Table 5.1 - Natural frequencies and damping ratio of the flapwise modes for the NREL 5 MW Wind Turbine blades (calculated by WTAC)

| Mode | Un-damped Natural Frequency (Hz) | Damped Natural Frequency (Hz) | Damping Ratio (%) |
|---|---|---|---|
| 1st Flapwise | 0.696 | 0.6956 | 0.460 |
| 2nd Flapwise | 1.920 | 1.9165 | 1.214 |
| 3rd Flapwise | 4.340 | 4.3381 | 2.772 |

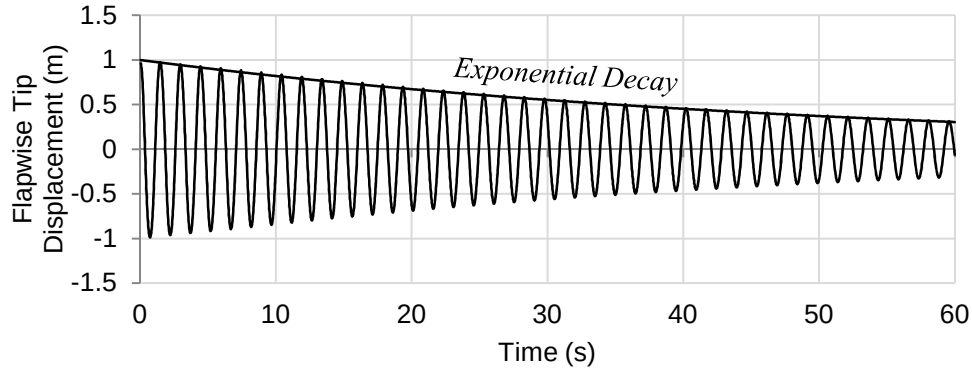


Figure 5.1 - Structural damping of the NREL 5 MW wind turbine blade flapwise vibration

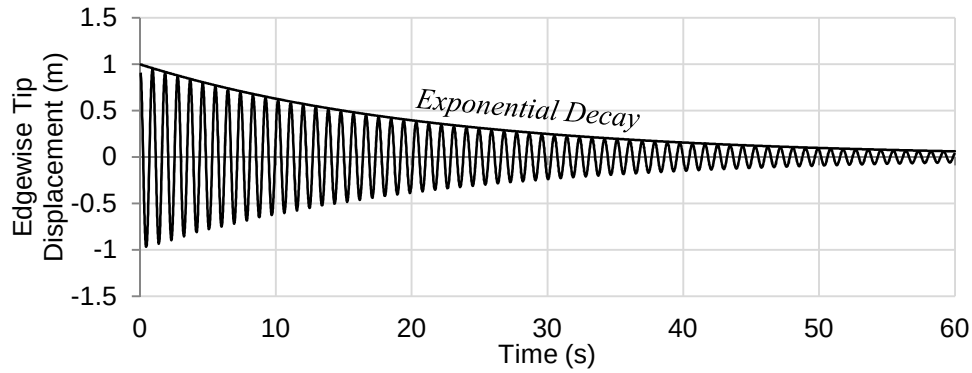


Figure 5.2 - Structural damping of the NREL 5 MW wind turbine blade edgewise vibration

### 5.2.2 Aerodynamic Damping

The aerodynamic damping is the main source of flapwise damping. The aerodynamic damping is an aeroelastic effect caused by the generation of an aerodynamic force resulting from a change in angle of attack, due to the structure motion. The damping is positive (i.e. stable dynamic) when the generated aerodynamic force is in opposition to the original structure motion. The stability analysis of a wind turbine blade as a whole is relatively complex to determine and therefore simplified two-dimensional methods are often used (Loewy, 2012). The blade is divided into segments along the span for which the damping is calculated based on two dimensional analysis. A simplified derivation of the aerodynamic damping is given by Salzmann and van der Tempel (Salzmann and Van der Tempel, 2005) who demonstrated that the slope of the lift coefficient is one of the critical parameters for aeroelastic stability. A more complete analysis carried out by Petersen et al. (Thirstrup et al., 1998) is based on the flow kinematic illustrated in Figure 5.3. The velocity induced by the aerofoil motion (i.e. $\dot{Y}_{ip}, \dot{Z}_{oop}$) is taken into account to modify the relative velocity $\left(V_{rel,stiff} \rightarrow V_{rel}\right)$ and the angle of attack.

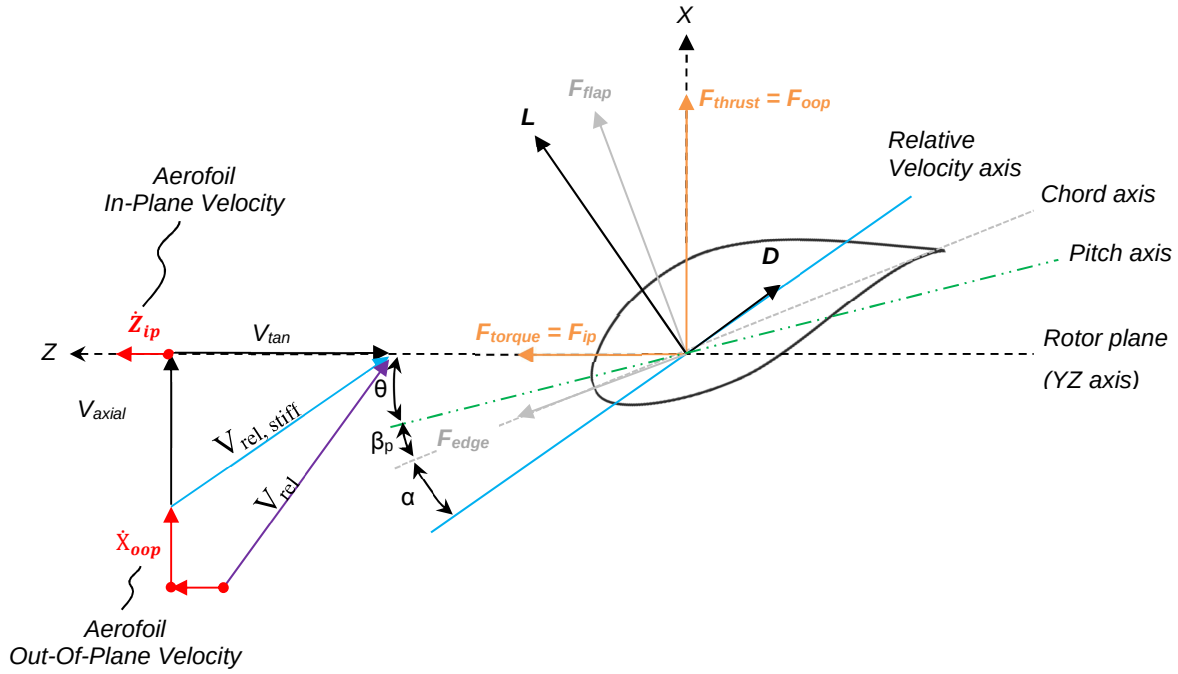


Figure 5.3 - Two dimensional aerodynamic forces acting on an aerofoil including the aerofoil speed

Both the lift and drag forces contribute to the in-plane and out-of-plane aerodynamic damping. That is, the in-plane and out-of-plane aerodynamic damping are coupled and can be defined by the two dimensional damping matrix $C_{Ad}$ as in (5.8). Note that the derivative with respect to the tangential velocity has a negative sign to account for the opposite direction of the in-plane aerofoil velocity as shown in Figure 5.3.

$$C_{Ad}\begin{bmatrix}\dot{x}_{oop}\\ \dot{z}_{ip}\end{bmatrix}=\begin{bmatrix}C_{oop} & C_{oop-ip}\\ C_{ip-oop} & C_{ip}\end{bmatrix}\begin{bmatrix}\dot{x}_{oop}\\ \dot{z}_{ip}\end{bmatrix}=\begin{bmatrix}\dfrac{\partial F_{oop}}{\partial V_{axial}} & -\dfrac{\partial F_{oop}}{\partial V_{\tan}}\\ \dfrac{\partial F_{ip}}{\partial V_{axial}} & -\dfrac{\partial F_{ip}}{\partial V_{\tan}}\end{bmatrix}\begin{bmatrix}\dot{x}_{oop}\\ \dot{z}_{ip}\end{bmatrix} \tag{5.8}$$

The out-of-plane aerodynamic damping corresponds to the aerodynamic force being generated due to the aerofoil velocity in the out-of-plane direction as described by:

$$C_{oop}=\frac{dF_{thrust}}{d\dot{x}_{oop}}=\frac{dF_{thrust}}{dV_{axial}}=\frac{\partial F_{thrust}}{\partial V_{axial}}+\frac{\partial F_{thrust}}{\partial V_{rel}}\frac{\partial V_{rel}}{\partial V_{axial}}+\frac{\partial F_{thrust}}{\partial C_L}\frac{\partial C_L}{\partial \alpha}\frac{\partial \alpha}{\partial V_{axial}}+\frac{\partial F_{thrust}}{\partial C_D}\frac{\partial C_D}{\partial \alpha}\frac{\partial \alpha}{\partial V_{axial}} \tag{5.9}$$

After derivation, Equation (5.9) can be written in terms of four coefficients as:

$$\begin{aligned}C_{oop}&=C_{oop,C_L}+C_{oop,C_D}+C_{oop,\partial C_L}+C_{oop,\partial C_D}\\&=\frac{1}{2}\rho c\frac{1}{V_{rel}}\left(C_L\left(V_{axial}V_{\tan}\right)+C_D\left({V_{rel}}^2+{V_{axial}}^2\right)+\frac{\partial C_L}{\partial \alpha}\left(V_{\tan}^2\right)+\frac{\partial C_D}{\partial \alpha}\left(V_{axial}V_{\tan}\right)\right),\end{aligned} \tag{5.10}$$

in which $C_{oop,CL}$, $C_{oop,CD}$, $C_{oop,\partial CL}$, $C_{oop,\ \partial CD}$ are the respective out of plane aerodynamic damping contribution from the lift and drag coefficients, and lift and drag slopes. Figure 5.4 presents the out-of-plane and in-plane aerodynamic damping coefficients of the aerofoil NACA 64-618 located on the NREL 5 MW wind turbine blades. It can be observed that the aerofoil lift slope is the main contributor of out-of-plane aerodynamic damping. Since the NREL 5 MW wind turbine is a variable-speed pitch-controlled turbine, the outer parts of the blades remain under attached flow where the lift slope and therefore the out-of-plane aerodynamic damping remain high. The total in-plane aerodynamic damping is mainly contributed to by the lift coefficient and the lift slope as shown in Figure 5.4.b. As the wind speed increases, however, the lift slope becomes the primary contributor of in-plane aerodynamic damping. The in-plane aerodynamic damping coefficient starts from a negative value and decreases until rated wind speed (i.e. 12 m/s) where the angle of attack reaches its maximum value. At higher wind speeds the pitch control system reduces the angle of attack which in turns increases the in-plane aerodynamic damping. The controlling parameters (i.e. rpm and pitch) are as shown in Figure 1.25.

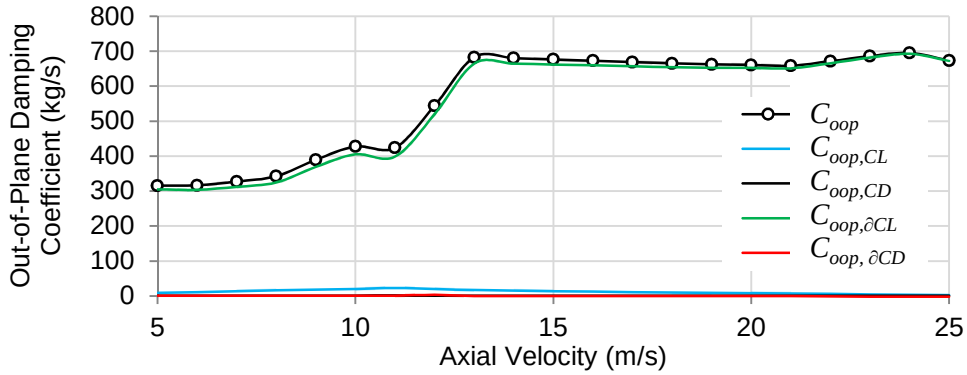


(a)

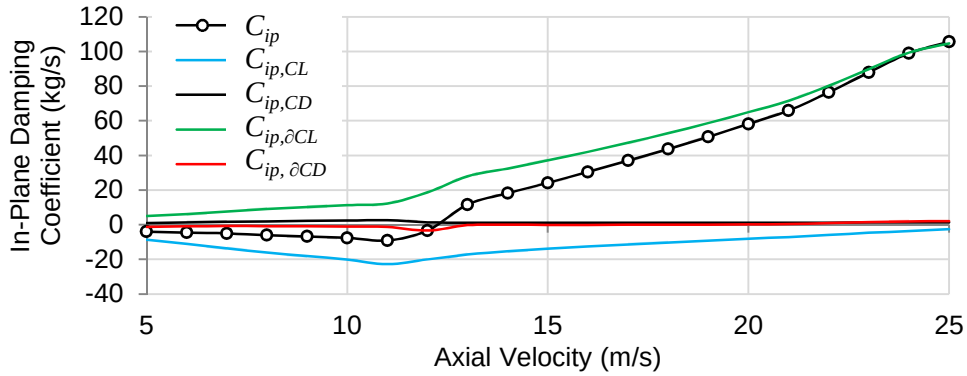


(b)

Figure 5.4 - Aerodynamic damping coefficients of the NACA 64-618 located on the NREL 5 MW wind turbine blade (r=50m) for the (a) out-of-plane and (b) in-plane axis

The behaviour observed in Figure 5.4 are explained by analysing the aerodynamic damping coefficients as functions of the angle of attack as shown in Figure 5.5 for a constant wind speed of 10m/s. As can be seen in Figure 5.5.a, operating under the attached flow a deflection of the blade in the out-of-plane direction will result in the generation of a strong aerodynamic force. This force acts in the opposite direction to the blade displacement and is maximal for low angles of attack (i.e. ±3°). As a result, it can be seen that in Figure 5.4.a the out-of-plane damping slowly increases from 5 m/s to 10 m/s as the angle of attack experienced by the aerofoil moves from 0 to 4°. A sudden increase of the out-of-plane damping coefficient is observed during the transition between the wind turbine operating region 2 and 3 (i.e. from 10 m/s to 13m/s). During this transition the wind turbine RPM increases while the angle of attack experienced by the aerofoil moves back from 4° to lower values resulting in a sudden increase of the $Coop_{,\partial CL}$ term in (5.10). Finally the out-of-plane damping remains high for higher wind speeds because the wind turbine RPM is maintained near rated value while the pitch control keeps lowering down the angle of attack experienced by the aerofoil. This is clearly visible in Figure 5.4.a towards 24 m/s where the local increase of the damping coefficient is linked to the lowering values of the angle of attack around -3°.

A similar line of reasoning can also be applied between the in-plane damping of Figure 5.4.b and the aerofoil damping coefficient of Figure 5.5.b. However, it should be noted that the in-plane damping is influenced by both $Cip_{,CL}$ and $Cip_{,\partial CL}$. As a result, both the lift coefficient value and its slope have to be considered. In low wind speed the in-plane aerodynamic damping coefficient is seen to steadily decrease as the angle of attack increases. A similar transition between the wind turbine operating region 2 and 3 is noticeable for the in-plane aerodynamic damping coefficient. That is, as the RPM increases and the angle of attack decreases the in-plane aerodynamic coefficient suddenly increases and keeps doing so thereafter.

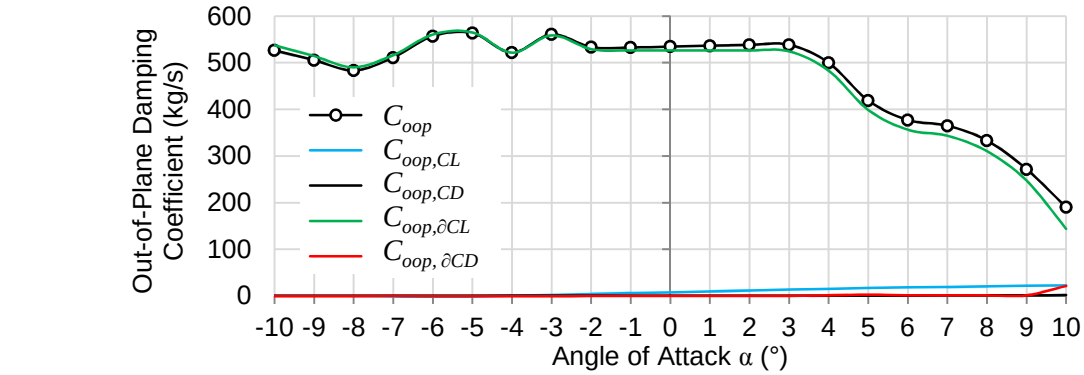


(a)

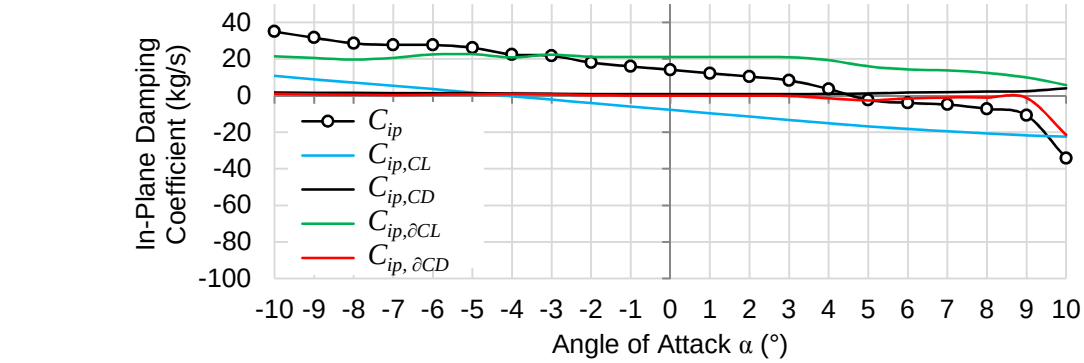


(b)

Figure 5.5 - Aerodynamic damping coefficient of the NACA 64-618 located on the NREL 5 MW wind turbine blade (r=50m) for the (a) out-of-plane and (b) in-plane axis as functions of the angle of attack

The wind turbine blade tangential velocity is normally higher than the axial velocity. As a result, the aerofoil edgewise velocity leads to a lower change of the angle of attack and therefore a lower aerodynamic damping. Furthermore, under attached flow conditions the flapwise aerodynamic damping is much greater than the structural damping alone. This can be observed from Figure 5.6 which shows flapwise vibrations, as damped by structural damping only, and by the aero-structural damping. On the other hand, wind turbines have a much lower edgewise aerodynamic damping as shown in Figure 5.7. Since CSs do not drastically alter the lift slope (see Chapter 3), the stability of variable-speed pitch-controlled wind turbine blades is likely to remain high when actively controlling CSs. However, ensuring that CSs do not excite the blades natural frequencies, when alleviating loads, is part of the control system design.

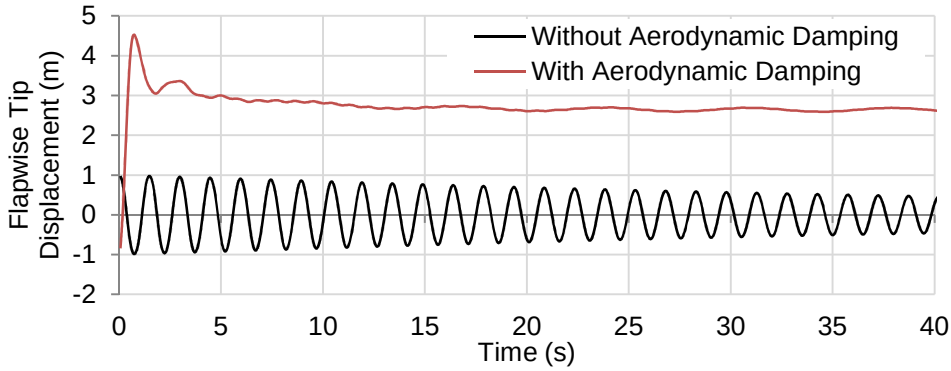


Figure 5.6 - Flapwise vibrations (NREL 5 MW wind turbine blade, 9m/s mean wind speed)

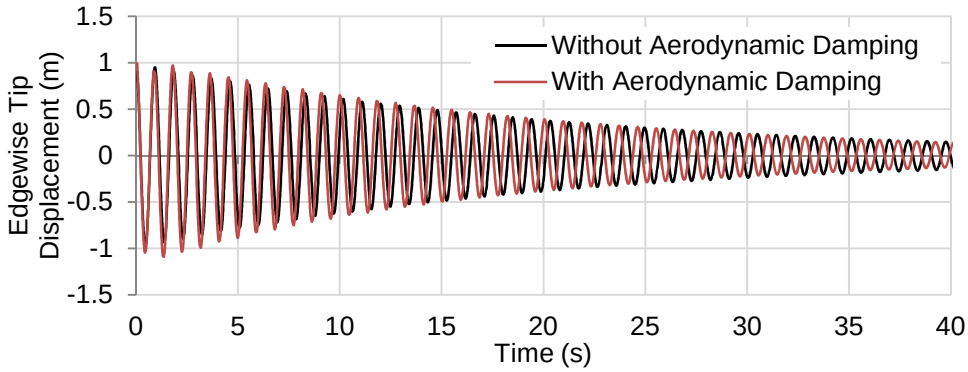


Figure 5.7 - Edgewise vibrations (NREL 5 MW wind turbine blade, 9m/s mean wind speed)

## 5.3 Blade Control - Measurements and Sensors

This section is devoted to the aerodynamic and structural sensing systems required for the control and state estimation of wind turbine blades equipped with CSs. Measurements and sensors are divided into the aerodynamic and structural types. Local aerodynamic measurements along the blade span (i.e. at CSs' location) are required in order to take into account the time dependence of the CSs models. They include the local angle of attack and relative velocity. Structural sensors, often strain gauges, are used to measure the blade displacement or bending moment and are necessary in order to calculate the CSs deployment control command. Several aerodynamic and structural sensing systems integrated to the NREL 5 MW wind turbine are investigated in the following subsections.

### 5.3.1 Aerodynamic Measurements

The CSs' aerodynamic models are time varying models depending on the instantaneous flow kinematics. The flow kinematics can be approximated via measured quantities by Pitot tubes, namely, the inflow angle $\phi$ and the local relative velocity $V_{rel}$. The Pitot-tubes measurement system is employed to approximate the angle of attack $\alpha$ and $V_{rel}$ as used in practice by Castaignet et al. (Castaignet et al., 2013). However, CSs may be distributed over a large blade

span (e.g. 20 %) and positioning a Pitot tube in front of each CS is not practically viable due to the increased installation and maintenance costs. There is, therefore, an interest in limiting the number of Pitot sensors distributed along each blade. In the rest of this section, sensing system configurations including a single, two, and three Pitot tubes are investigated.

**Single Pitot tube configuration**

In the first configuration, a single Pitot tube is used. As shown in Figure 5.8, the blade span neighbouring the Pitot tube is divided into 7 segments numbered from -3 to 3 and the Pitot tube is located on the leading edge of the blade in front of segment 0. Using TurbSim, 180-second unsteady wind fields are generated. For each time step, the Pitot tube measures the values of $\alpha$ and $V_{rel}$ in front of segment 0. The value of $\alpha$ and $V_{rel}$ for the neighbouring segments are assumed to be equal to those measured by the Pitot tube.

The performance of the aerodynamic sensing system is evaluated by comparing the measured and actual (i.e. as calculated by BEMT) values of $\alpha$ and $V_{rel}$ for each segment. Figure 5.9 presents the probability distribution function (PDF) of the error between the estimated and actual values of $\alpha$ and $V_{rel}$. As shown in this figure, assuming that $\alpha$ and $V_{rel}$ are constant around the Pitot tube results in significant approximation errors. Both the mean value and the standard deviation of the error of approximation of $\alpha$ and $V_{rel}$ are seen to increase as it is estimated further away from the Pitot tube.

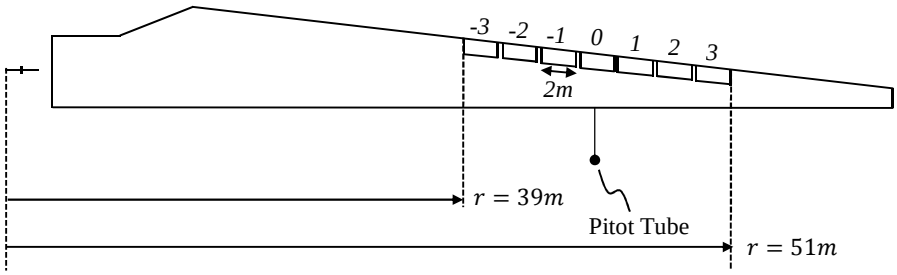


Figure 5.8 - Single Pitot tube configuration

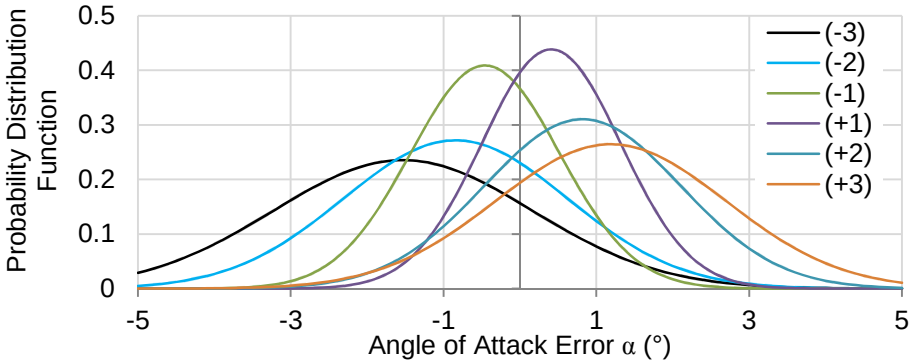


(a)

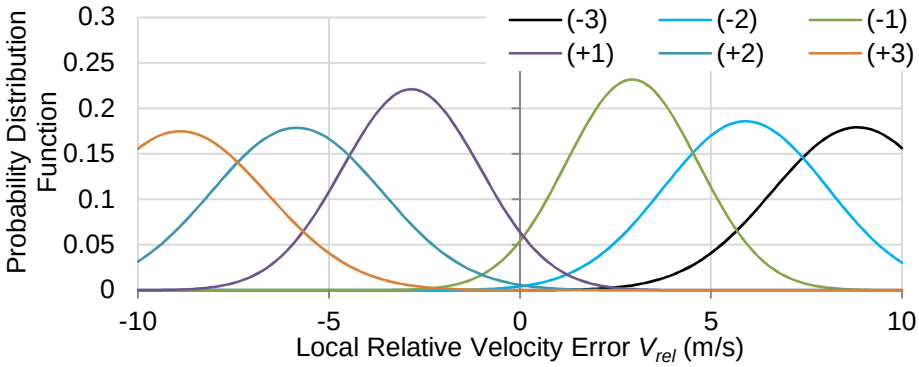


(b)

Figure 5.9 - Error of approximation of the (a) angle of attack and (b) relative velocity (single Pitot tube configuration)

**Two Pitot tubes configuration**

In the second configuration, two Pitot tubes are used. The Pitot tubes are located at the extremity of the segment span as shown in Figure 5.10. The flow kinematics at the neighbouring segments are interpolated based on the reading of these two measurements.

The performance of the Pitot sensing system is evaluated by comparing the measured and actual values of $\alpha$ and $V_{rel}$ for each segment as presented in Figure 5.11. As this figure shows, the postulation of flow kinematics obtained by interpolating the measurements between the two Pitot tubes is significantly better than the estimation achieved with the single Pitot tube configuration. Moreover, it can be seen that the probability distribution functions are almost centred at zero and the standard deviations have reduced to one degree for $\alpha$ and to 2.5m/s for *Vrel*.

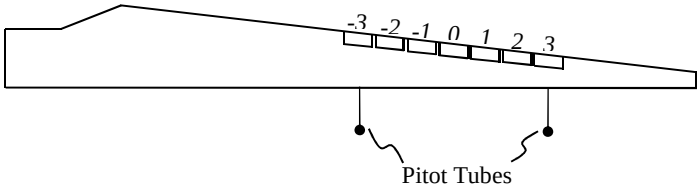


Figure 5.10 - Two Pitot tubes configuration

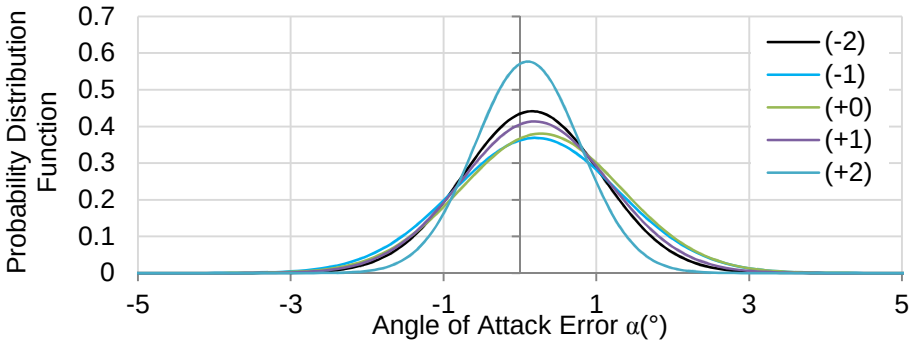


(a)

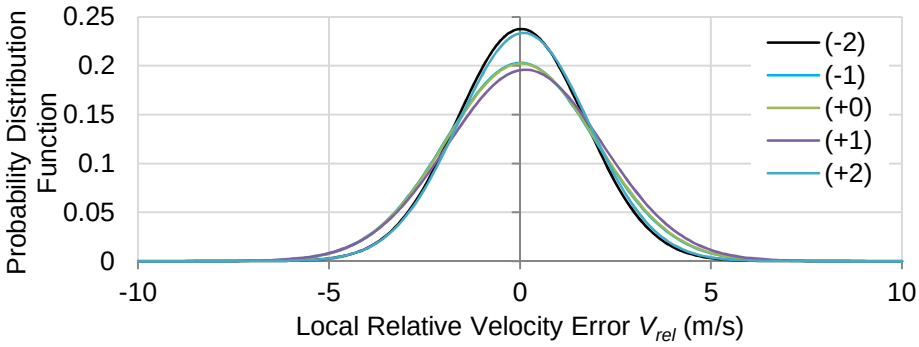


(b)

Figure 5.11 - Error of approximation of the (a) angle of attack and (b) relative velocity (two Pitot tubes configuration)

**Three Pitot tubes configuration**

The last sensing configuration considers the implementation of a third Pitot tube. In addition to the two pitot tubes located at the extremity of the segment span (i.e. Figure 5.10), a third Pitot tube is installed in front of segment 0. The flow kinematics are postulated by the interpolations of the three measurements and results for the three Pitot tubes configuration are shown in Figure 5.12.

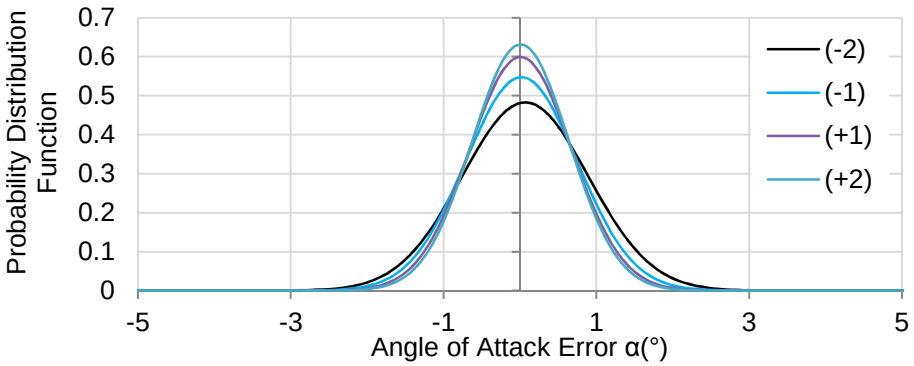


(a)

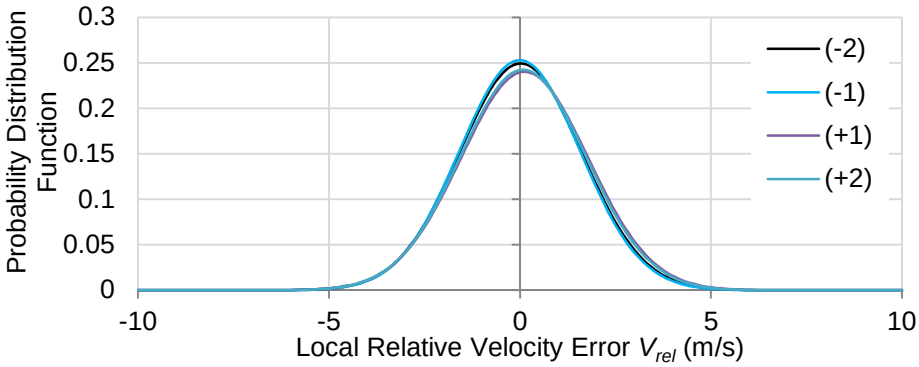


(b)

Figure 5.12 - Error of approximation of the (a) angle of attack and (b) relative velocity (three Pitot tubes configuration)

The observation of the three sets of results shows that by using two or three Pitot tubes, the standard deviation of the angle of attack estimation can be reduced to 1°, meaning that about 96% of the angle of attack approximations have error of estimations inferior to 2°. Similarly, the relative velocity measurements' standard deviation was reduced to 2 m/s and therefore about 96% of the estimations have less than 4m/s difference with the actual velocity. Since the steady state change in lift coefficient employing TEF and microtab is nearly constant under fully attached flow, a 2° angle of attack error of approximation in this range is assumed reasonably accurate. Similarly, flow kinematics at the outer section of blades, where the CSs are located, are mainly dictated by the magnitude of the tangential velocity. Since the tangential velocity at the outer blade span is high (e.g. 60-70 m/s), small errors up to ±4 m/s in wind velocity correspond to a relative error of approximately 5.5% which is deemed realistic.

Comparing the two and three Pitot tube configurations, it can be observed that the addition of the third Pitot tube does not significantly improve the aerodynamic sensing system performance. Consequently, the two Pitot tubes configuration seems a judicious choice that provides better accuracy than a unique sensor but also limits the number of Pitot tubes used.

### 5.3.2 Observer Design - Structural Measurement and State Estimation

Since the blade flapwise displacement and bending moment are strongly correlated as shown in Figure 5.13, most case studies reported in the literature assume the knowledge (e.g. through strain gauges) of at least one of them for control purposes (Castaignet et al., 2011, van Wingerden et al., 2011, Wilson et al., 2009, Barlas et al., 2012, Andersen, 2005). However, the estimation required by state-based controllers commonly proposed in the literature are generally not investigated. This section is therefore used to investigate the types, numbers of sensors and observers required for estimating the state vector of actively controlled wind turbine blades.

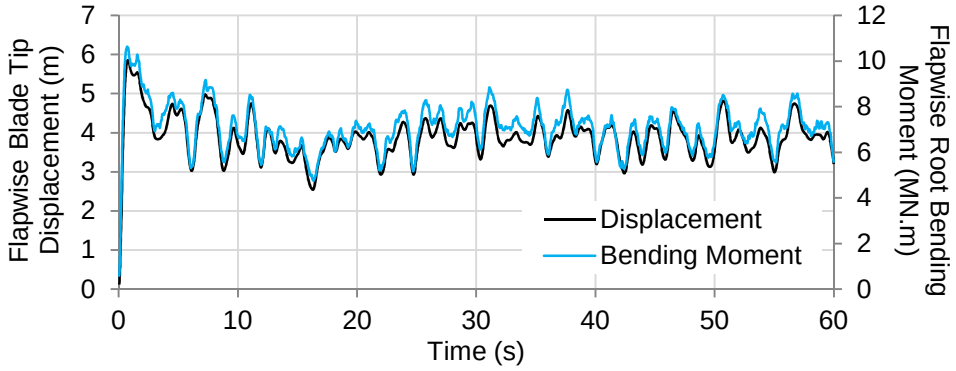


(a)

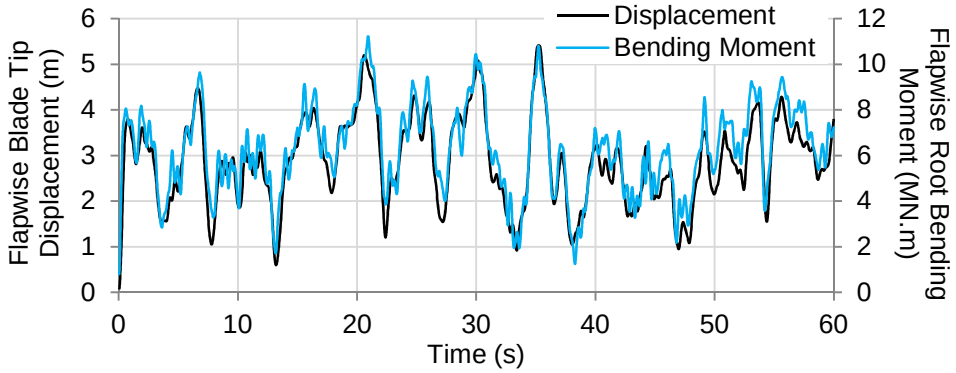


(b)

Figure 5.13 - Superposition of the blade flapwise tip displacement and root bending moment for a mean wind speed of (a) 9 m/s and (b) 15 m/s (NREL 5 MW wind turbine)

In order to alleviate the blade root bending moment strain gauges are generally installed at the blade root. However, under a bending load the root is only subject to small deflections and sensors therefore have to be very sensitive and accurate to precisely calculate the blade bending moment. On the other hand, a strain gauge located further down the blade would experience greater axial strain and therefore limit sensing errors.

Suitable locations for strain gauges can be found with the help of the structural blade mode shapes. As reiterated in Figure 5.14, the wind turbine blade mode shapes are known functions. Each mode shape *i* has (*i*-1) nodes at which the displacement of the corresponding mode is zero at all times. Because the blade displacement at $N_2$ is independent of the vibrations induced by mode 2, the second modal coordinate is not observable by a strain gauge located at $N_2$. Considering the above, strain gauges should be located at the location of high mode shape displacements in order to limit sensors inaccuracies and avoid zero displacement nodes (e.g. $N_2$, $N_1$). However, it is also worth considering that a sensor located along the blade span can be difficult to install and maintain. Consequently, locations such as 15 m (≈ 25%R) and 30 m (≈ 50%R) along the blade span may be preferred.

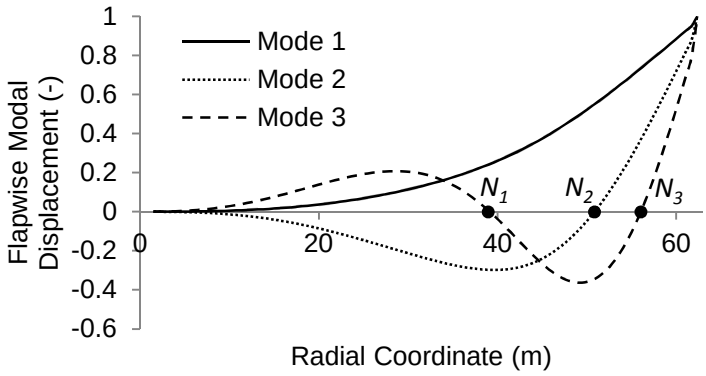


Figure 5.14 - Normalised mode shapes of the NREL 5 MW wind turbine blade

While local measurements are sufficient for classical controllers, state controllers require the knowledge of the system state in order to calculate the CSs control command. The state vector of a system is generally not known or only partially known. State estimation, based on local measurements, is therefore critical for the effective use of state controllers. However, adding new sensors onto wind turbine blades increases the installation and maintenance costs. Assuming instant and/or perfect measurements for load alleviation simulation, on the other hand, is likely to result in an over-prediction of the CSs' efficiency in rejecting loads. There is consequently an interest in limiting the number of strain gauges required for active load control.

State observers estimate the system state vector based on the available measurements. State observers are valuable for state controllers, fault detection and their robustness to state and output noises. A system is fully observable only if the condition of observability is satisfied. In the linear case, the observability is determined based on the state matrix $A_{Ae}$ and output matrix $C_{Ae}$. For wind turbine blades the system observability therefore depends on the blades

structural dynamic coupling with CSs and the position of structural sensors along the blades span.

For sake of clarity let us assume, for the observer design, that the NREL 5 MW blade displacement is approximated by the combination of the first two modes:

$$\vec{Y}_B \approx \vec{M}_1 Q_{r,1} + \vec{M}_2 Q_{r,2} \tag{5.11}$$

If noises are negligible compared to the primary system dynamics and the pair $(A_{Ae}, C_{Ae})$ is observable, then the error of estimation given by a Luenberger observer will converge towards zero (Andrieu and Praly, 2006). Equally, the unforced system-observer model of Equations (5.12) and (5.13) is stable and converges towards zero.

$$\begin{bmatrix} \dot{X}_{Ae} \\ \dot{e}_{Ae} \end{bmatrix} = \begin{bmatrix} A_{Ae} & 0 \\ 0 & A - K_o C_{Ae} \end{bmatrix} \begin{bmatrix} X_{Ae} \\ e_{Ae} \end{bmatrix} + \begin{bmatrix} B \\ 0 \end{bmatrix} U \tag{5.12}$$

$$Y_{Ae} = \begin{bmatrix} C_{Ae} & 0 \end{bmatrix} \begin{bmatrix} X_{Ae} \\ e_{Ae} \end{bmatrix} \tag{5.13}$$

where, $K_o$ denotes the observer gain matrix and $e_{Ae}$ is the dynamic error of estimation. Equation (5.14) shows the general form of the aero-structural blade-CS system output matrix when equipped with one CS and $N$ strain gauges. Additionally, the CSs deployment (i.e. microtab height or trailing edge flap angle) is also measured using a position sensor.

$$Y_{Ae} = C_{Ae} X_{Ae} = \begin{bmatrix} c_{11} & c_{12} & 0 & 0 & 0 \\ c_{21} & c_{22} & 0 & 0 & 0 \\ c_{31} & c_{32} & 0 & 0 & 0 \\ . & . & . & . & . \\ . & . & . & . & . \\ c_{N1} & c_{N2} & 0 & 0 & 0 \\ 0 & 0 & 0 & 0 & c_{Cs} \end{bmatrix} \begin{bmatrix} Q_2 \\ Q_1 \\ \dot{Q}_2 \\ \dot{Q}_1 \\ X_{Cs} \end{bmatrix} \tag{5.14}$$

In this example, there are only two modal coordinates, namely $Q_1$ and $Q_2$, to be estimated. In (5.14), it is clear that using more than two strain sensors is only useful to introduce some redundancy. That is, in the case of perfect measurements, the two modal coordinates can be precisely known using only two independent strain gauges. On the other hand, if a single strain gauge is used the best estimation is achieved using linear algebra is a root mean square approximation.

State and output noises are, however, unavoidable. In particular, wind turbine blades are subjected to substantial time dependent unknown forces (e.g. aerodynamic forces) that vary along the blade span. Including state and output noises, the state space system given by (4.45) is re-written in the following form:

$$\dot{\vec{X}}_{Ae} = [A_{Ae}]\vec{X}_{Ae} + [B_{Ae}][u] + \left(\vec{D}_{Ae} + \vec{S}_{noise}\right) \tag{5.15}$$

$$\vec{y}_{Ae} = [C_{Ae}]\vec{X}_{Ae} + \vec{O}_{noise} \tag{5.16}$$

where, $O_{noise}$ and $S_{noise}$, respectively, denote the output and state unknown bounded noises. The vector $D_{Ae}$, which stands for the transformed external force vector acting on the blades, is also unknown. However, the process noise $S_{noise}$ is assumed negligible since the external noise $D_{Ae}$ order of magnitude of kN is likely to be much greater than modelling errors and control input disturbances. For this system, the classical Luenberger observer would not provide an accurate estimation due to the significant unknown forces driving the system (i.e. $D_{Ae}$). The Kalman filter is a robust observer design that can be employed in order to provide an estimate of the state vector despite the state and output noises. Note that the Kalman filter has the same structure as the Luenberger observer, however the observer gains are calculated such that the square of the error of estimation is minimised. Weight matrices are used to quantify the confidence in the model and measurements from which the observer gains are calculated.

The robustness and accuracy of the Kalman filter state estimation as a function of the number and location of strain sensors is now examined. Two strain sensing system configurations employing one and two strain sensors are investigated. The strain sensors are chosen to be located at 25% and 50% of the blade span. It should be noted that due to the substantial disparity between state (i.e. aerodynamic forces) and output noise (i.e. sensors inaccuracies), the output noise is considered negligible in the rest of this section.

Figure 5.15 presents the error of state estimation results using two strain gauges. It can be seen that the first and second modal coordinates are well-estimated. Moreover, this figure shows that, while not totally converging towards zero, errors between the state space vector and its estimates are negligible.

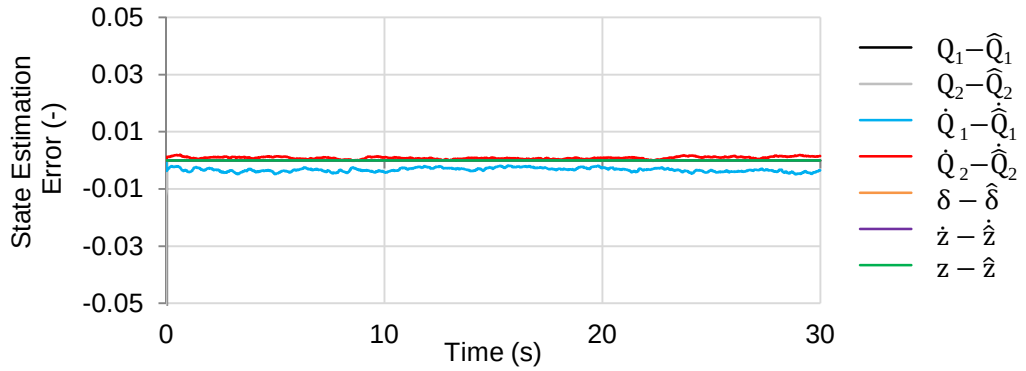


Figure 5.15 - State estimation of the blade-CSs system (NREL 5 MW wind turbine blade equipped with two strain gauges)

Results presented in Figure 5.16 show the state vector estimation using a single strain gauge located at the blade mid-span. As shown in this figure, the state estimation does not converge. Instead, the estimations of the first and second modal coordinates feature offset errors. On the other hand, the output estimation converges towards the actual output value as shown in Figure 5.16.c. As discussed previously, several linear combinations of mode shapes can be responsible for the measured displacement. Consequently, the offset error values of both modal coordinates cancel each other so that the output estimation matches the measured output.

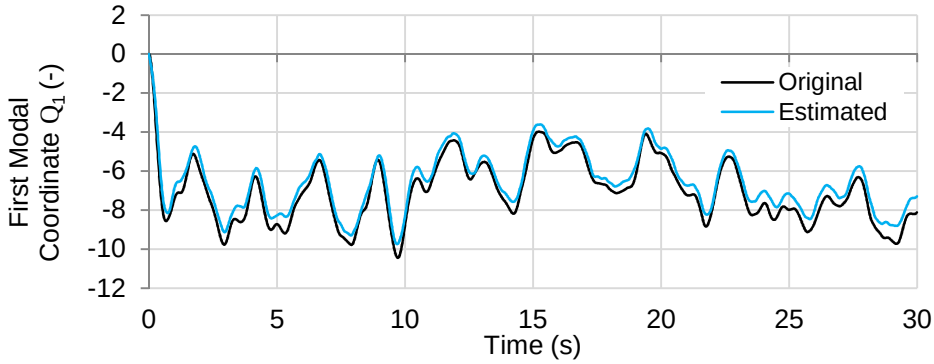


(a)

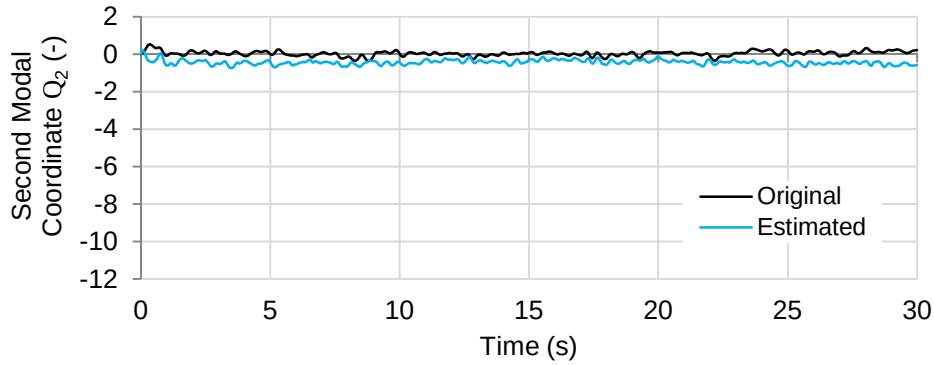


(b)

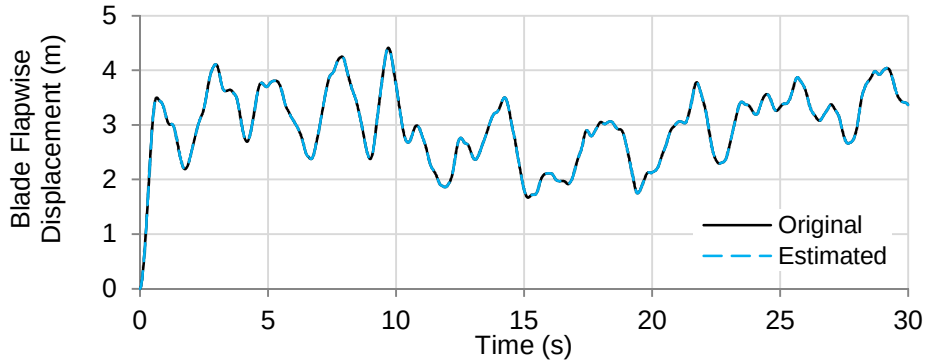


(c)

Figure 5.16 - Estimation of the blade-CSs system (a) first modal coordinates, (b) second modal coordinates, and (c) flapwise blade displacement (NREL 5 MW wind turbine blade equipped with a single strain gauge)

Employing two strain gauges ensures that there is a unique mode shape combination that can describe the output measurements. As a result, both estimated modal coordinates were shown to converge when employing two strain sensors. It was also shown that accurate state estimation can be achieved despite the substantial unknown state disturbances.

## 5.4 Controller Designs

In this section, the control strategies employed for the load alleviation of wind turbine blades are presented. The common Bang-Bang (BB), PID and LQR controllers found in the wind turbine blade load alleviation literature are briefly presented. Additionally, the use of sliding mode controllers is proposed as a potential improvement upon the BB controller.

Presently in the literature, there is no consensus about which type of CS actuation mechanisms should be used. To the best of the author's knowledge there is no previous researches that have investigated this question. Consequently, a clear distinction between continuous and discontinuous control systems is made during this research. The classical controllers such as PID and LQR are not suitable for discontinuous control systems, whereas the Bang-Bang controller and Sliding Mode Controller (SMC) can be used for both mechanism types. One of the objectives here is to compare the feasibility and efficiency of both types of control systems for wind turbine blade load alleviation.

Last but not least, the author proposes a frequency-based loop-shaping approach for analysing the dynamic of actively controlled aerodynamic surfaces. While most investigations available in the literature employ a time-based control system, the author believes that the load alleviation of wind turbine blades can more easily be described and

evaluated in the frequency-domain. The loop-shaping approach proposed at the end of this section is key to many of the conclusion presented in the next chapter.

During the control system design, the interactions between CSs and the classic wind turbine controllers are assumed negligible. This follows from the significant time difference between the dynamic response of the variable-speed system and the collective pitch control system compared with the CS dynamics. In other words, the variable-speed control dynamic is slow due to the rotor inertia and the collective pitch control system is not designed to reduce fatigue loads.

Although never more than one controller is used at the same time, the several controllers closed-loop can be represented in one illustration as in shown Figure 5.17. In this Figure, $Y_{filt}$ denotes the filtered output which contains frequencies to be alleviated. In other words, $Y_{filt}$ is the closed-loop error of the classical PID controller. The Kalman filter provides an estimate of the output $\hat{Y}_{Ae}$ and the state space $\hat{X}_{Ae}$. The control command $u$ calculations for the different controllers are now detailed.

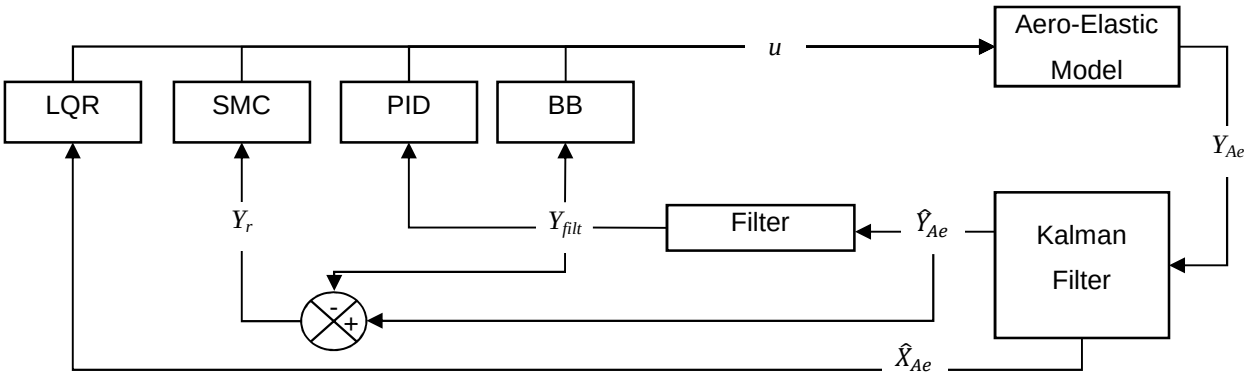


Figure 5.17 - Blade load alleviation closed loop control schematic of the four controllers

### 5.4.1 Discontinuous Controllers

**Bang-Bang Control (BB)**

BB controllers are used in a large range of applications, such as hysteresis or discontinuous systems and space applications, particularly, where the systems are constrained to work in either on or off position. Van Dam et al. (Van Dam et al., 2002) and Panesar and Weaver (Panesar and Weaver, 2012) suggest using discontinuous actuator mechanisms for microtabs and TEFs featuring fast actuation response, robustness and low cost. In comparison to more advanced controllers, the BB controller does not require long tuning, making it easier to

implement. The control law designed for BB controllers without hysteresis takes the following form:

$$u(t) = sign(\hat{Y}_{filt}) U_{sat} \tag{5.17}$$

where, $U_{sat}$ stands for the maximum control value corresponding to the maximum deployment value.

**Sliding Mode Controller (SMC)**

As for the BB controller, the SMC has been chosen because its discontinuous nature makes it a suitable control method for on-off actuators. In addition, the SMC can handle non-linearities and has advantageous features such as low sensitivity to uncertainties and noises. However, the chattering phenomenon is one of the main drawbacks of the SMC. The sliding surface is described by a 2nd order system dynamic of the system output:

$$S_1(x) = \ddot{Y}_{Ae} + \gamma_{SM} \dot{Y}_{Ae} + \beta_{SM} Y_{Ae} - \beta Y_r \tag{5.18}$$

with the condition of reaching the sliding surface in finite time:

$$S_1 \dot{S}_1 \leq -\kappa |S_1| \quad , \ \kappa > 0 \tag{5.19}$$

Parameters $\gamma_{SM}$ and $\beta_{SM}$ are the coefficients describing the desired output dynamic and $Y_r$ is the reference signal to track. As shown in Figure 5.17, the reference signal mostly contains the low frequencies of the estimated system output. By tracking $Y_r$ the controller activates the CSs in order to reduce 1*P* and higher frequency loads. The control ensuring that the condition given by Equation (5.19) is satisfied is denoted by $u_d$. Deriving the surface derivative $\dot{S}_1$, the equivalent control law $u_e$ is calculated by setting $\dot{S}_1 = 0$. The final control law is the summation of both controls:

$$u(t) = u_e(t) + u_d(t) \tag{5.20}$$

### 5.4.2 Continuous Controllers

Implementing continuous actuators for controlling the deployment of CSs is more challenging and costly in comparison to discontinuous actuators. However, this gives the possibility of deploying CSs to any given value within the operating boundaries, potentially

increasing the performance of CSs for active load control. In this study, both PID and LQR controllers assume the possibility of continuous CS deployment for comparison with the discontinuous controller performance.

**Proportional Integral Derivative Control (PID)**

PID controllers are well-known and widely used in a variety of applications. The control law for PID controllers is given by:

$$u(t) = K_P \varepsilon + K_D \varepsilon_D + K_I \varepsilon_I \tag{5.21}$$

in which, parameters $K_I, K_D$ and $K_P$ are respectively the integral, derivative and proportional tuning parameters. Similarly to the BB controller, $Y_{filt}$ is the closed-loop error ($\varepsilon$) of the classical PID controller.

**Linear Quadratic Regulator (LQR)**

Load alleviation employing LQR has been proposed in several studies (Castaignet et al., 2013, Castaignet et al., 2011, Barlas et al., 2012). In general, the control command consists of a linear combination of weighted signals. These signals represent the magnitudes of particular frequency bandwidths ($F_{b,i}$) to be rejected. By applying different weights ($w_{fi}$), specific frequency loads are alleviated. In order to take the filter dynamic into account during the feedback gain calculations, the system is augmented with filters $X_{filt}$ as shown in Equation (5.22). The numbers of filter and frequency bandwidths to filter often correspond to the number of weights in the criterion as in Equation (5.23).

$$\begin{bmatrix} \dot{X}_{Ae} \\ \dot{X}_{filt} \end{bmatrix} = \begin{bmatrix} A_{Ae} & [0] \\ & A_{filt} \end{bmatrix} \begin{bmatrix} X_{Ae} \\ X_{filt} \end{bmatrix} + \begin{bmatrix} B_{Ae} \\ 0 \end{bmatrix} u \tag{5.22}$$

$$J = \int_{t_0}^{t_f} \begin{bmatrix} X_{Ae} \\ X_{filt} \end{bmatrix}^T Q_{lqr} \begin{bmatrix} X_{Ae} \\ X_{filt} \end{bmatrix} + u^T R_{lqr} u = \int_{t_0}^{t_f} \left( w_{f1} F_{b,1} + w_{f2} F_{b,2} + \ldots + w_{fn} F_{b,n} + u^T R_{lqr} u \right) dt \tag{5.23}$$

in which, $Q_{lqr}$ and $R_{lqr}$ are weight matrices. Solving the Riccati's equation for $S_{lqr}$, the linear state feedback control law can be formulated as:

$$u = -R_{lqr}^{-1} \begin{bmatrix} B_{Ae}{}^T & [0] \end{bmatrix} S_{lqr} \begin{bmatrix} X_{Ae} \\ X_{filt} \end{bmatrix} \tag{5.24}$$

The stability of the observer-based control of the closed loop blade-CSs system can be studied with the help of the separation principle as explained as follows. Recalling that the system dynamic, the observer-based LQR control command and the state estimate error are respectively given by:

$$\dot{X}_{Ae} = A_{Ae} X_{Ae} + B_{Ae} u + D_{Ae} \tag{5.25}$$

$$u = -K\hat{X}_{Ae} = -K\left(X_{Ae} - \varepsilon\right) \tag{5.26}$$

$$\dot{\varepsilon} = \dot{X}_{Ae} - \dot{\hat{X}}_{Ae} = \left(A_{Ae} - LC_{Ae}\right)\varepsilon + D_{Ae} \tag{5.27}$$

The overall system can be written as:

$$\begin{bmatrix} \dot{X}_{Ae} \\ \dot{\varepsilon} \end{bmatrix} = \begin{bmatrix} A_{Ae} - B_{Ae}K & B_{Ae}K \\ 0 & A_{Ae} - LC_{Ae} \end{bmatrix} \begin{bmatrix} X_{Ae} \\ \varepsilon \end{bmatrix} + \begin{bmatrix} D_{Ae} \\ D_{Ae} \end{bmatrix} \tag{5.28}$$

The eigenvalues of the system are the combinations of the independent eigenvalues of the controlled blade-CSs system and of the observer. Choosing $K$ such that the controlled system is stable and $L$ such that the observer is stable is therefore sufficient to ensure the overall stability of the observer-based control blade-CSs system.

### 5.4.3 Frequency Based Control - Loop-Shaping

Amongst the load alleviation research found in the literature, most follow the same approach. In general, a load alleviation controller candidate is picked and tested without considerations being given to control analysis. The performance of the controller is then derived directly from comparisons of the load alleviation results. In other words, previous published studies generally do not explain or predict the impact of controllers on the dynamic of wind turbine blades equipped with CSs. While this approach is suitable for preliminary proof-of-concepts, detailed control analyses are required in order to gain an in-depth understanding of the load alleviation control problem and design dedicated load alleviation controllers.

In contrast to the literature, in this research the aim to understand and explain the dynamic of actively controlled wind turbine blades. The author believes that a better understanding of these dynamics will help in designing tailored control systems for load alleviation. For that purpose, a frequency-based approach is used to define the wind turbine blade load alleviation

as a loop-shaping control problem. Figure 5.18 is a typical representation of an aero-structural system where the plant ($P_L$), which stands for the aerodynamic surface equipped with CSs, is excited by external forces (e.g. aerodynamic, gravity). As for practical applications, these forces are rarely known. Hence, the controller cannot be positioned directly between the plant and the external forces (i.e. feed-forward control). The unknown forces driving the aeroelastic vibrations are generally alleviated by feedback control as shown in Figure 6.27.

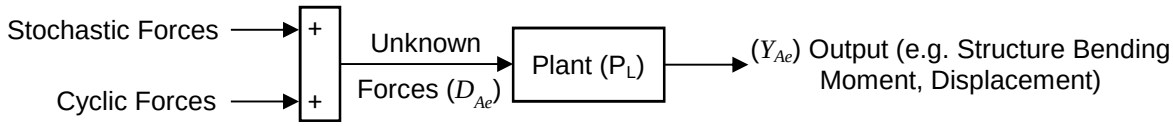


Figure 5.18 - Representation of an aerodynamic surface (plant) subject to unknown forces

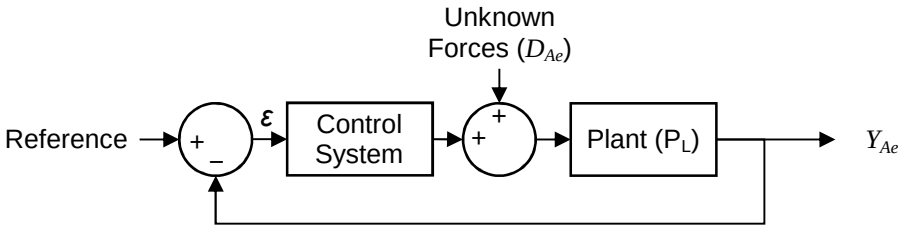


Figure 5.19 - Representation of the closed-loop control system of an aerodynamic surface equipped with AFCs

Figure 5.20 shows the frequency response of an open-loop and an ideally-controlled aeroelastic system. In this figure, 1*P* and 2*P* stand for the frequencies to be alleviated. Frequencies 1*N* and 2*N* denote the first and second natural frequencies. An ideal control system shapes the frequency response such that the frequencies to be alleviated are fully damped. Moreover, an ideal controller does not interact with other frequency bandwidths (i.e. $\Delta_f \rightarrow 0$). In other words, the ideal control system behaves like perfect notch filters.

While digital or electrical notch filters can reach substantial attenuation level, there are physical constraints imposed to electro-mechanical devices (i.e. active flow controllers) which limit their loop-shaping capabilities. Moreover, notch filters introduce significant phase shift near the attenuated frequency bandwidths, which in turn may reduce the closed-loop system stability. Not considering these two limitations when designing control systems is likely to result in poor trade-offs between performance and stability (Rice and Verhaegen, 2010). That is, the differences between the ideal and achieved frequency shapes can vary significantly as illustrated in Figure 5.21. One critical advantage of the frequency-based analysis (e.g. loop-shaping) over the time domain control approaches is the ability to clearly

explain and visualise the impact of proposed control strategies on the overall aeroelastic dynamic of the system. As a result, effective control systems dedicated to the vibration control of aerodynamic surfaces can be designed. In contrast to the literature, the proposed loop-shaping approach will be used for designing controllers dedicated to load alleviation in Chapter 6. Additionally, frequency analysis will be used to explain the observed dynamic responses of controlled wind turbine blades.

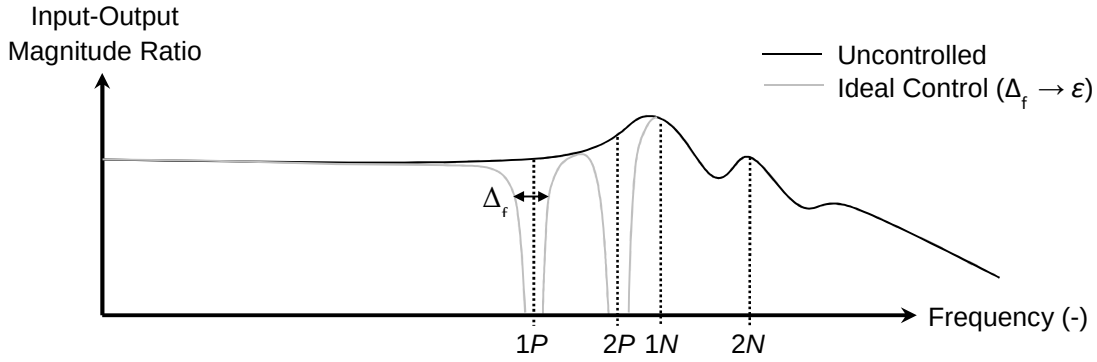


Figure 5.20 - Illustrative frequency response of an ideally controlled aeroelastic structure

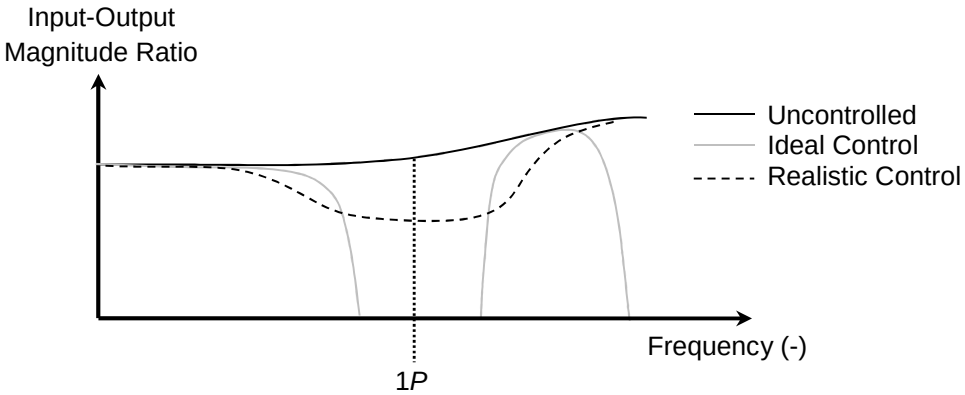


Figure 5.21 - Illustrative frequency response of an aeroelastic structure controlled with physical limitations

## 5.5 Summary - Control System Design

Chapter 5 was dedicated to the control analysis methodology of wind turbine blades equipped with CSs. The aeroelastic stability of wind turbine blades was investigated in Section 5.2. It was found that the aerodynamic damping remains high for variable-speed pitch-controlled wind turbines. As a result, is was assumed that the small changes in aerodynamic forces due to the deployment of CSs are not likely to lead to instability.

In this research, the author considered the aerodynamic and structural sensing systems, and the blade-CSs system state estimation as critical as the controller itself (see Section 5.3). It

was shown that a small number of Pitot tubes (i.e. two) could be used to reasonably approximate the local angle of attack and relative velocity distribution around CSs. This results is of particular interest since the number of sensors should be limited in order to reduce the control system cost. For the first time in the literature the influence of the number of strain sensors and their locations on the aeroelastic observability of wind turbine blades was also investigated. The author argues that strain sensors should be located at high mode shape displacements to avoid zero-displacement nodes and limit measurement errors. Additionally, it was shown that the number of necessary strain sensors depends on the type of control system used. Basically, state-based controllers require more strain sensors than classical controller due to the need for state estimation. Regarding the state estimation itself it was found that, despite the significant unknown forces driving wind turbine blades, the Kalman filter is a potential candidate for state estimation.

Four control architectures were described for the load alleviation of wind turbine blades equipped with CSs. Amongst them, it was decided to employ a sliding mode controller in order to improve the load alleviation performance of discontinuous CSs. In contrast to the mainstream literature, the author also makes a clear distinction between continuous and discontinuous actuation mechanisms with the objective to compare their feasibility and efficiency for load alleviation in the next chapter. Finally, it was chosen to shift from the usual time-based control paradigm to a frequency-based paradigm. The author argues that the load alleviation of wind turbine blades is more explicit in the frequency domain and that a frequency-based control approach will help in designing dedicated control system. The proposed control systems are now evaluated.

# 6. Performance Study of Microtabs and Trailing Edge Flaps in Load Alleviation

## 6.1 Introduction

In Chapter 6 the load alleviation analyses and results leading to the key contributions of this research are presented. The rest of this chapter is organised into five sections. The optimal location of CSs along the blade span in order to maximise load alleviation performance is investigated in Section 6.2. The aerodynamic and structural sensing systems required for the control of CSs are presented in Section 5.3. The wind turbine blade load alleviation results employing microtabs and trailing edge flaps are presented Section 6.3. The outcomes of the load alleviation investigations are summarised in Section 6.4.

The NREL 5 MW wind turbine is used as the main case study. For ease of reading, the main characteristics of the NREL 5MW wind turbine (Jonkman et al., 2009) are reiterated in Table 6.1.

Table 6.1 - NREL 5 MW wind turbine general features

| | | |
|---|---|---|
| General Characteristics | Hub height | 87.6m |
| | Diameter | 126 m |
| | Blade length | 61.5m |
| | Blade mass | 17 740kg |
| | Number of blades | 3 |
| | Rated speed | 12.1rpm |
| | blade structural damping (in % of critical damping) | < 3% |
| Blade Natural Frequencies (WTAC) | 1st Flapwise | 0.7056 Hz |
| | 2nd Flapwise | 2.0088 Hz |
| | 1st Edgewise | 1.0943 Hz |
| | 2nd Edgewise | 4.0918 Hz |

## 6.2 Control Surfaces Optimal Location

Since the positions of CSs determine their aerodynamic efficiency and their capability in alleviating loads, this section investigates the performance of CSs as a function of their locations along the blade span. The load alleviation efficiency of CSs is related to many factors such as the CS actuation time and control space, the local flow velocity, chord and aerodynamic twist. However, the link between these parameters and the CS load alleviation performance is not precisely known. While it is often assumed that CSs should be located in the blade aerodynamic region of efficiency (Andersen, 2005, Castaignet et al., 2011), the actual position at which CSs should be located in order to maximise load alleviation performance of a given wind turbine blade is yet unknown. In addition to increase the

performance, maximising load alleviation by appropriately positioning CSs can help in reducing the overall control system cost.

Since CSs are to be employed on modern wind turbines, only variable-speed pitch-controlled wind turbines are considered in the rest of this section. According to the BEMT formulation, the thrust force and bending moment along the blade span are calculated as follows:

$$F_{thrust}(r) = \frac{1}{2}\rho V_{rel}{}^{2}(r)c(r)(C_L \cos\phi + C_D \sin\phi) \tag{6.1}$$

$$M_{thrust}(r) = r\,F_{thrust}(r) \tag{6.2}$$

While not precisely defined, it is known that CSs should be located towards the blades outer section (i.e. aerodynamic region of efficiency). As a consequence, one can apply the following reasonable simplifications:

**(i)** In the outer blade part the dominant velocity is the tangential velocity (i.e. $V_{\tan}{}^{2} >> V_{axial}{}^{2}$) and therefore the local relative velocity can be assumed equal to:

$$V_{rel}{}^{2}(r) \approx V_{\tan}{}^{2} = (\omega_{rot} r)^2 \tag{6.3}$$

**(ii)** In order to simplify manufacturing as shown in Figure 6.1, the chord in the outer blade part is often linearised as:

$$c(r) = -ar + b, \quad (a,b) > 0 \tag{6.4}$$

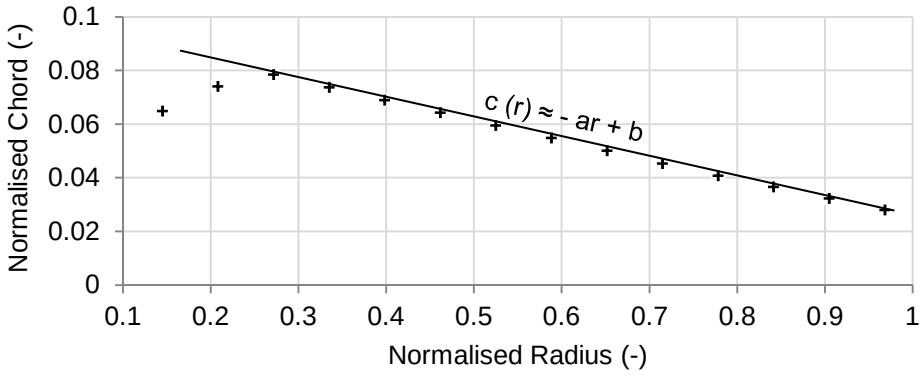


Figure 6.1 - Chord linear approximation (WindPACT 1.5MW wind turbine)

**(iii)** The pitch-control system (i.e. pitch to feather) maintains the outer part of the blades under attached flow where the lift-to-drag ratio remains high and therefore $C_L >> C_D$. Hence, the inflow angle remains small (i.e. $\cos\phi \approx 1$ and $\sin\phi \approx 0$ ).

**(iv)** The aerodynamic coefficient $C_L$ is a function of the angle of attack $\alpha(V_\infty, r)$ which is a function of the wind speed, rotor speed and blade radial coordinate. On the other hand, the steady state lift coefficient generated by the CS (i.e. $\Delta C_{L,ss}$) is nearly constant under attached flow (see Chapter 3).

Rewriting Equation (6.2) while considering the above assumptions, one obtains:

$$M_{thrust}(r) = \frac{1}{2} r \rho (\omega_{rot} r)^2 (-ar + b) C_L (\alpha(V_\infty, r)) \tag{6.5}$$

The moment solely generated by the deployment of the CS is written as:

$$\Delta M_{thrust}(r) = \frac{1}{2} r \rho (\omega_{rot} r)^2 (-ar + b) \Delta C_L (\alpha(V_\infty, r)) \tag{6.6}$$

The only difficulty left consists of expressing the lift generated by the CS as a function of the blade radial coordinate and the steady state lift coefficient. The lift coefficient that can be generated by the CS in the operating condition is distinguished from the CS steady state lift coefficient $\Delta C_{L,ss}$ as follows:

$$\Delta C_L (\alpha(v, r)) = \Delta C_{L,ss} \gamma(V_\infty, r) \tag{6.7}$$

The lift ratio function (i.e. gamma function) is the ratio between the dynamic and steady state lift coefficients generated by the CS:

$$\gamma(v, r) = \frac{\Delta C_L (\alpha(V_\infty, r))}{\Delta C_{L,ss}} \tag{6.8}$$

Substituting (6.8) into (6.6), the moment generated by the CS can be expressed as:

$$\Delta M_{thrust}(r) = \frac{1}{2} r \rho (w_{rot} r)^2 (-ar + b) \Delta C_{L,ss} \gamma(V_\infty, r) \tag{6.9}$$

Differentiating (6.9) with respect to radial coordinate r and equating to zero one obtains:

$$0 = (-4ar + 3b) \gamma(V_\infty, r) + (-ar^2 + br) \gamma'(V_\infty, r) \tag{6.10}$$

If the lift ratio function is known, the optimal location of a CS along the wind turbine blades is obtained by solving the roots of Equation (6.10). A priori the lift ratio function is dependent on the wind turbines to which the CSs are equipped. Two variable-speed pitch-

controlled wind turbines (i.e. NREL 5 MW and WindPACT 1.5 MW) are used as case studies.

The lift ratio function is calculated using WTAC steady-state BEMT code modified to include the extra lift generated by CSs. Figures 6.2 and 6.3 illustrate the lift ratio function as a function of the wind speed and the radial coordinate. Note that the lift ratio function does not reach 1, and consequently, using the steady state lift coefficient to predict the force generated by the CS is certain to result in over-prediction. Furthermore, it can be seen that the lift ratio function has two main distinguishable parts. At low wind speed, the lift ratio function is relatively low (< 0.5). Moreover, it first decreases from root to mid-span before increasing until the blade tip. On the other hand, one can notice a sudden increase of the CS aerodynamic efficiency above rated wind speed. In addition, above rated wind speed the lift ratio function starts at about 0.7 and increases up to 0.85 towards 85% of the blade span before decreasing towards the tip. Since the two states (i.e. before and after rated wind speed) of the lift ratio function are so different, it is chosen to use a function for each state in order to solve (6.10). Two second order functions are used to approximate the lift ratio function for low and high wind speeds as:

$$\gamma_1(r) = d_1 r^2 + e_1 r + f_1 \tag{6.11}$$

$$\gamma_2(r) = d_2 r^2 + e_2 r + f_2 \tag{6.12}$$

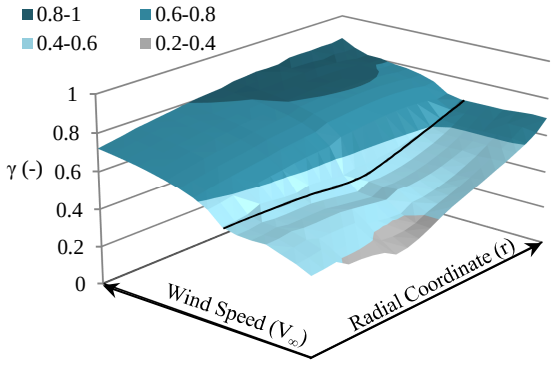


Figure 6.2 - NREL 5MW wind turbine lift ratio function

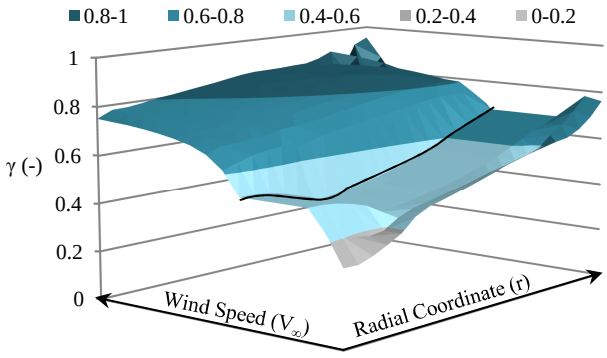


Figure 6.3 - WindPACT 1.5MW wind turbine lift ratio function

A particular solution of (6.10) is obtained when assuming that the lift coefficient generated by the CS is independent of the radial coordinate (i.e. $\gamma'(r) = 0$). Solving for this particular scenario, the solution of (6.10) is obtained as:

$$r_{opt} = 0.75\frac{b}{a} \tag{6.13}$$

In comparison to the general approach, the result obtained in (6.13) is solely dependent on of the chord geometry and does not require calculating the wind turbine corresponding lift ratio function. The optimal location results obtained using the general Equation (6.10) and the simplified Equation (6.13) are now evaluated and compared for the two wind turbine case studies.

**First Case Study**

For the first wind turbine case study (i.e. NREL 5 MW), the blade chord can be approximated by:

$$c(r) = -0.0596r + 5.7 \tag{6.14}$$

Moreover the lift ratio functions for low and high wind speeds are given by:

$$\gamma_1(r) = 0.0002721r^2 - 0.01745r + 0.7683 \tag{6.15}$$

$$\gamma_2(r) = -0.00009452r^2 + 0.01063r + 0.4961 \tag{6.16}$$

The results for the first wind turbine design using a constant $\Delta C_{L,ss}$ value of 0.2 are shown in Figure 6.4. It can be observed that the approximated moment generated by the CS is close to WTAC numerical results. Both optimal locations predicted by the simplified and general

analytical methods are shown to be similar. Moreover, both results predict that the CS optimal location is greater than the wind turbine blade radius (R = 63 m). That is, the optimal location should therefore be the blade tip. However, it can be observed that the numerical results predict a sudden decrease of CS performance towards the blade tip due to a substantial chord reduction (i.e. assumption **ii**) at the NREL 5MW wind turbine blade tip

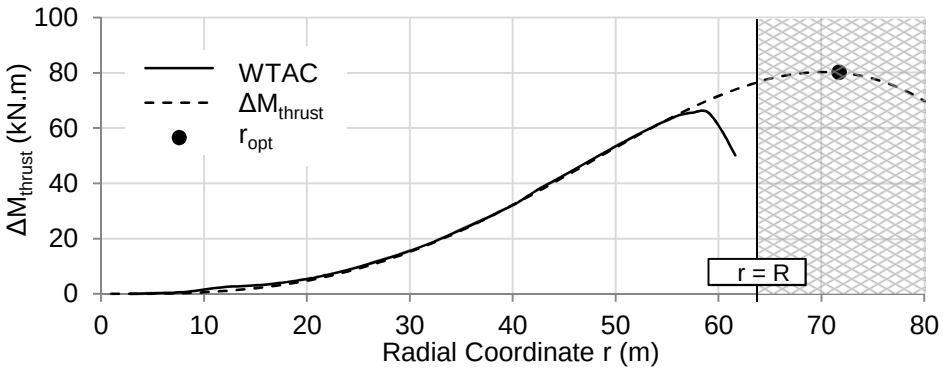


Figure 6.4 - NREL 5MW bending moment generated along blade span by CSs

In order to further evaluate the proposed analytical approach the original wind turbine chord distribution of (6.14) is modified as follows:

$$c(r) = -0.08r + 6 \tag{6.17}$$

The results obtained between the simplified prediction and WTAC for a constant value of $\Delta C_{L,ss}$ are presented in Figure 6.5. As this figure shows, the simplified approximation of optimal CS location using Equation (6.13) matches WTAC results.

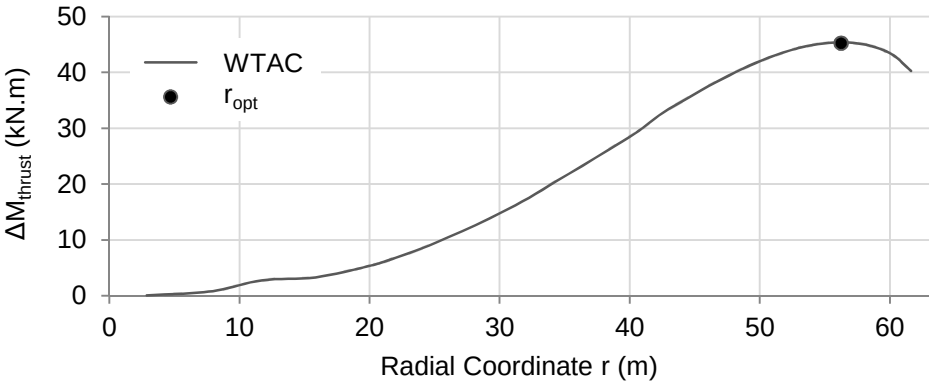


Figure 6.5 - Optimal CS location for the NREL 5 MW modified chord

**Second Case Study**

The optimal location of CS for the second wind turbine design (Malcolm and Hansen, 2002) is now calculated. The chord of the second wind turbine design (i.e. WindPACT 1.5 MW) is approximated by:

$$c(r) = -0.072r + 3.4 \tag{6.18}$$

Moreover the lift ratio functions for low and high wind speeds are:

$$\gamma_1(r) = 0.001214r^2 - 0.04346r + 0.84 \tag{6.19}$$

$$\gamma_2(r) = -0.0004864r^2 + 0.0265r + 0.4662 \tag{6.20}$$

The results for the second wind turbine design using a constant $\Delta C_{L,ss}$ value of 0.2 are shown in Figure 6.6. Similarly to the first case study, the approximation of the moment generated by the CS is close to the WTAC calculations (Figure 6.6). Moreover, the two analytical methods suggest positioning the CS at a radial location greater than the blade tip. As for the first case study, a small reduction of the CS performance near blade tip is observed.

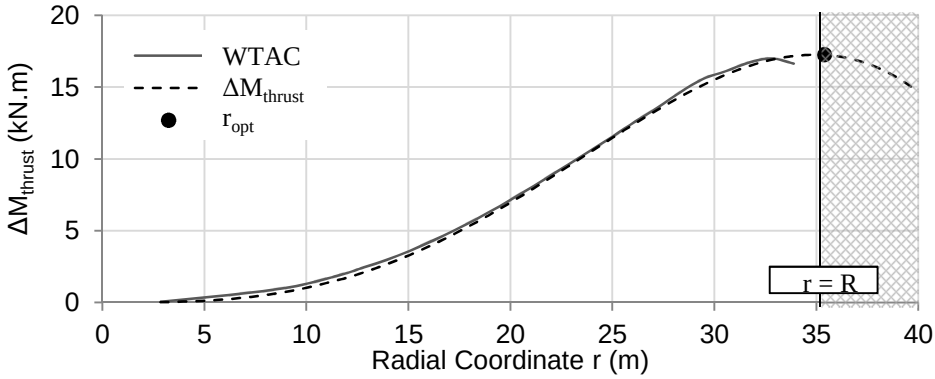


Figure 6.6 - WindPACT 1.5 MW bending moment generated along blade span by CSs

In order to further evaluate the proposed analytical approach the original wind turbine chord distribution of Equation (6.18) is modified as follows:

$$c(r) = -0.092r + 3.4 \tag{6.21}$$

The results obtained between the simplified method and the numerical approach for a constant value of $\Delta C_{L,ss}$ are presented in Figure 6.7. It can be seen that the simple approximation of optimal location using Equation (6.13) matches the numerical results.

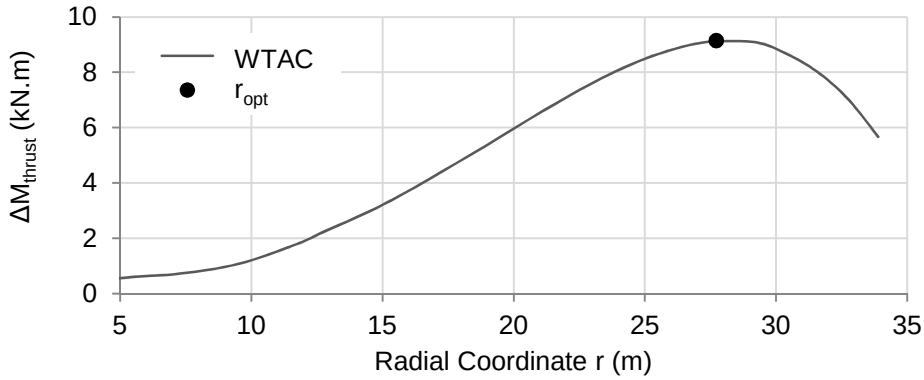

Figure 6.7 - Optimal CS location for the WindPACT 1.5 MW modified chord

**Section Summary**

In this section, the author developed an analytical approach for calculating the optimal location of CSs along the blade span in order to maximise load alleviation. To the best of the author's knowledge, no such formula has been proposed before. By deriving the formula, it was demonstrated that in order to maximise their efficiency, CSs should be located near the blade tip. A simplified analytical solution for determining the optimal location of CSs described by Equation (6.13) was also derived. Surprisingly, it was shown that the current trends in wind turbine blade design leads to (6.13) sole dependency on the blade chord. This equation provides a quick way to calculate the optimal location of CSs and can be used as a preliminary estimate for including CSs in the early wind turbine design phase.

## 6.3 Load Alleviation Employing Control Surfaces

The load alleviation of wind turbine blades employing microtabs and TEFs is evaluated in this section. In contrast to the mainstream literature, the author not only evaluates the controllers performances but also provide in-depth details about the dynamics of actively controlled wind turbine blades. For that purpose, it was decided to shift from the usual time-based control paradigm to a frequency-based paradigm. In addition, particular attention is paid to the different behaviours exhibited by continuous and discontinuous control systems.

This section is divided into 4 subsections. The load alleviation study starts in Section 6.3.1 with wind turbine blades equipped with single CSs. The load alleviation results are extended to multiple CSs in Section 6.3.2. The frequency analysis of the closed-loop control design of wind turbine blades equipped with CSs is carried out in Section 6.3.3. Section 6.3.4 presents the quantitative load alleviation results obtained for the NREL 5 MW wind turbine equipped with microtabs and TEFs.

For sake of simplicity, the load alleviation on wind turbine blades equipped with CSs is first studied without considering the CSs' deployment and speed constraints. These constraints are taken into account for the quantitative evaluation in Section 6.3.4.

### 6.3.1 Load Alleviation Employing a Single Control Surface

This section explores the load alleviation of wind turbine blades equipped with single CSs. The high-pass filter design used for rejecting low frequency loads is also evaluated. In contrast with the current literature, the filters used herein are low-order real time filters in order to limit the phase-lag added to the closed-loop system. Filters are also directly integrated into the state space so that their dynamics are taken into account when designing controllers.

The aero-structural state space system augmented with a simple first order high-pass filter can be defined as:

$$X_A = \begin{bmatrix} Q_2 & Q_1 & \dot{Q}_2 & \dot{Q}_1 & z & \dot{z} & \delta_F & y_f \end{bmatrix}^T \tag{6.22}$$

$$A = \left[\begin{array}{cccc:ccc:c} 0 & 0 & 1 & 0 & 0 & 0 & 0 & 0 \\ 0 & 0 & 0 & 1 & 0 & 0 & 0 & 0 \\ r_2 & 0 & s_2 & 0 & t_{21} & t_{22} & t_{23} & 0 \\ 0 & r_1 & 0 & s_1 & t_{11} & t_{12} & t_{13} & 0 \\ \hline 0 & 0 & 0 & 0 & 0 & 1 & 0 & 0 \\ 0 & 0 & 0 & 0 & a_{F6} & a_{F7} & a_{F4} & 0 \\ 0 & 0 & 0 & 0 & 0 & 0 & \tau_F & 0 \\ \hline 0 & 0 & c_2 & c_1 & 0 & 0 & 0 & \gamma_{filt} \end{array}\right] \tag{6.23}$$

where the new state variable $y_f$ stands for the filtered output. The filter dynamic is set by $\gamma_{filt}$ and the derivative of the state space output (i.e. $\dot{y}_{Ae} = c_2\dot{Q}_2 + c_1\dot{Q}_1$) is used as input to the high-pass filter. The Bode magnitude and phase plots of the filter are shown in Figure 6.8 and the filtered blade flapwise displacement is shown in Figure 6.9. It can be observed that a low order high-pass filter is suitable for the rejection of low frequency loads while conserving the 1*P* loads without adding any significant amount of phase-lag.

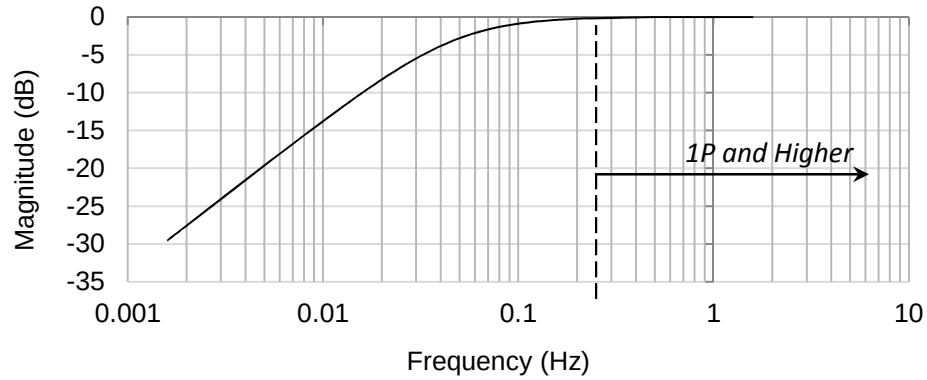


(a)

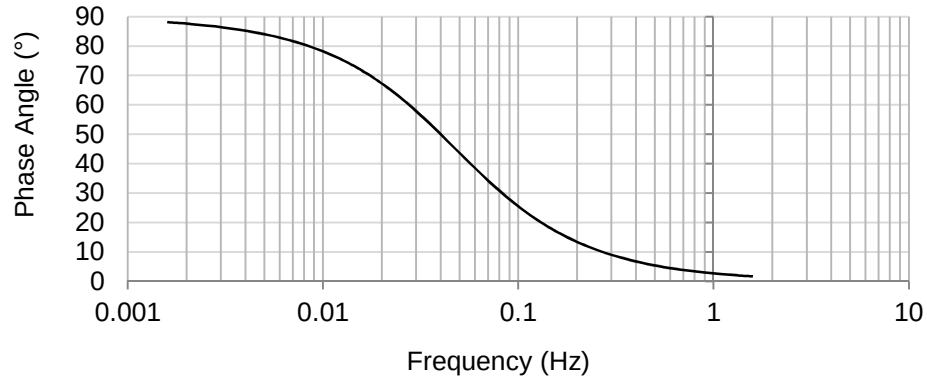


(b)

Figure 6.8 - (a) Magnitude and (b) phase plots of the first order high-pass filter

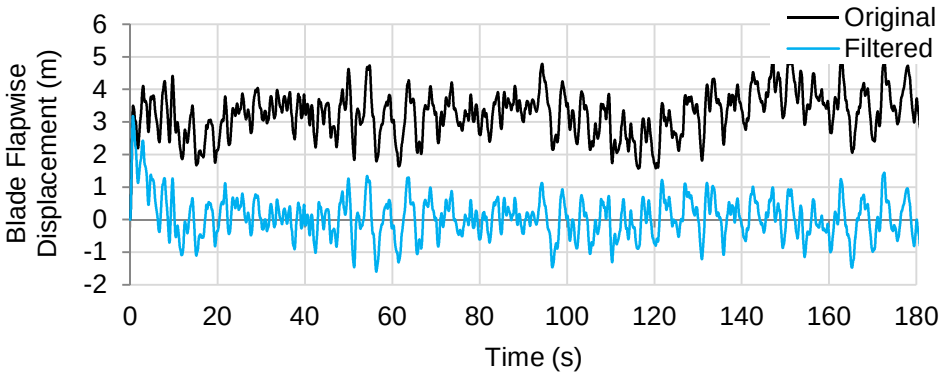


Figure 6.9 - Time domain results of the first order high-pass filter

The rest of this section is divided into the continuous and discontinuous control investigations.

**Continuous Controllers**

The results presented above have demonstrated that a first order high-pass filter can be employed to remove the flapwise displacement low frequency content while conserving the 1*P* loads. The filtered signal is now used for controlling the CS deployment. A proportional P

controller, with a gain $K_p$ multiplying the filtered system output $y_f$, is employed to control the CS deployment as described by:.

$$u = K_p y_f \tag{6.24}$$

and in the state matrix form as :

$$A = \left[\begin{array}{cccc:ccc:c} 0 & 0 & 1 & 0 & 0 & 0 & 0 & 0 \\ 0 & 0 & 0 & 1 & 0 & 0 & 0 & 0 \\ r_2 & 0 & s_2 & 0 & t_{21} & t_{22} & t_{23} & 0 \\ 0 & r_1 & 0 & s_1 & t_{11} & t_{12} & t_{13} & 0 \\ \hdashline 0 & 0 & 0 & 0 & 0 & 1 & 0 & K_p \\ 0 & 0 & 0 & 0 & a_{F6} & a_{F7} & a_{F4} & 0 \\ 0 & 0 & 0 & 0 & 0 & 0 & \tau_F & 0 \\ \hdashline 0 & 0 & c_2 & c_1 & 0 & 0 & 0 & \gamma_{filt} \end{array}\right] \tag{6.25}$$

The comparison between the original and controlled flapwise root bending experienced by the NREL 5 MW wind turbine blade is presented in Figure 6.10. As this figure shows, a simple closed-loop control design consisting of a P controller combined with a first order high-pass filter can successfully be used for the load alleviation of wind turbine blades employing a CS. This is most likely one of the simplest closed-loop controls that can be used for load alleviation purposes.

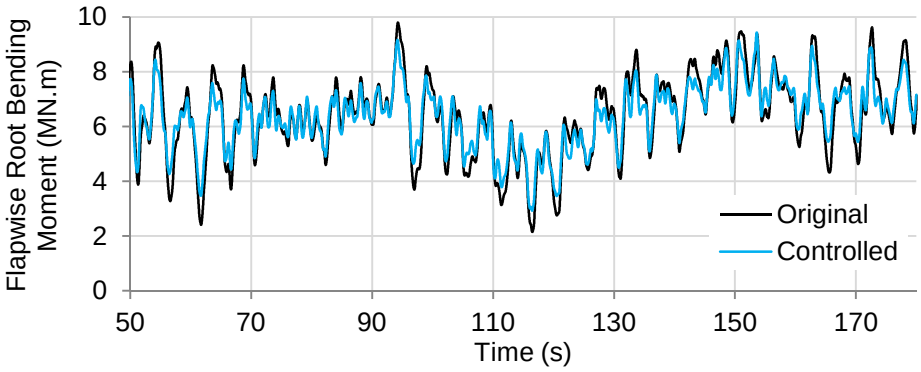


Figure 6.10 - Flapwise root bending moment (NREL 5MW wind turbine, P controller, 10 m/s turbulent wind field)

The general form of the classical controller, namely the PID controller, is now investigated. The integral term, however, is not useful for rejecting highly turbulent, zero mean wind turbine blade flapwise loads. That is, the system dynamic never reaches steady state and, the slow response and zero steady state error brought by the integral term are not useful in our case. Instead, a proportional derivative PD controller is used. In addition to the proportional

gain $K_p$, the derivative gain $K_d$ multiplies the filtered output derivative $\dot{y}_f$. Since the first modal coordinate includes the majority of loads to be rejected as illustrated in Figure 6.11, for sake of clarity and without loss of accuracy the first modal coordinate is used instead of system output as described by:

$$u = \mathbf{K_p} y_f + \mathbf{K_d} \dot{y}_f \approx \mathbf{K_p} c_1 Q_{1f} + \mathbf{K_d} c_1 \dot{Q}_{1f} = K_p Q_{1f} + K_d \dot{Q}_{1f} \tag{6.26}$$

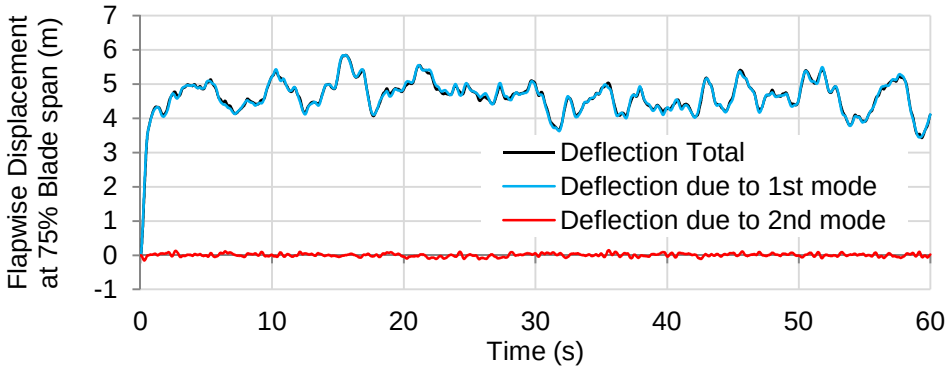


Figure 6.11 - Decomposition of the blade flapwise displacement into modes

In order to include the PD controller into the system, the first order high-pass filter is replaced by a second order high-pass filter for the derivative of the filtered modal coordinate $\dot{Q}_{1f}$ to appear in the state vector as follows:

$$X_A = \left[ Q_2 \quad Q_1 \quad \dot{Q}_2 \quad \dot{Q}_1 \quad \ddot{Q}_1 \quad z \quad \dot{z} \quad \delta_F \quad Q_{1f} \quad \dot{Q}_{1f} \right]^T \tag{6.27}$$

Moreover, the first modal coordinate dynamic of the state matrix must also be augmented as:

$$A = \left[\begin{array}{cccc:c:ccc:cc}
0 & 0 & 1 & 0 & 0 & 0 & 0 & 0 & 0 & 0 \\
0 & 0 & 0 & 1 & 0 & 0 & 0 & 0 & 0 & 0 \\
r_2 & 0 & s_2 & 0 & 0 & t_{21} & t_{22} & t_{23} & 0 & 0 \\
0 & 0 & 0 & 0 & 1 & 0 & 0 & 0 & 0 & 0 \\
\hdashline
0 & \tau r_1 & 0 & r_1 + \tau s_1 & -\tau + s_1 & \tau t_{11} & \tau t_{12} & \tau t_{13} & 0 & 0 \\
\hdashline
0 & 0 & 0 & 0 & 0 & 0 & 1 & 0 & 0 & 0 \\
0 & 0 & 0 & 0 & 0 & a_{F6} & a_{F7} & a_{F4} & 0 & 0 \\
0 & 0 & 0 & 0 & 0 & 0 & 0 & \tau_F & 0 & 0 \\
\hline
0 & 0 & 0 & 0 & 0 & 0 & 0 & 0 & 0 & 1 \\
0 & 0 & 0 & 0 & 1 & 0 & 0 & 0 & \gamma_1 & \gamma_2
\end{array}\right] \tag{6.28}$$

where, a fast dynamic is added for the second derivative $\ddot{Q}_1$ to appear in the state vector and to be used by the high-pass filter. Adding the fast dynamic, the system is augmented such that

the original system poles remain unchanged (i.e. only a fast dynamic pole is added). The fast dynamic pole (i.e. parameter $\tau$) is chosen to ensure the added dynamic is at least ten times faster than the original system dynamic. In doing so, the fast dynamic follows the original system dynamic as illustrated in Figure 6.12. The filtered output of the second order high-pass filter is shown in Figure 6.13.

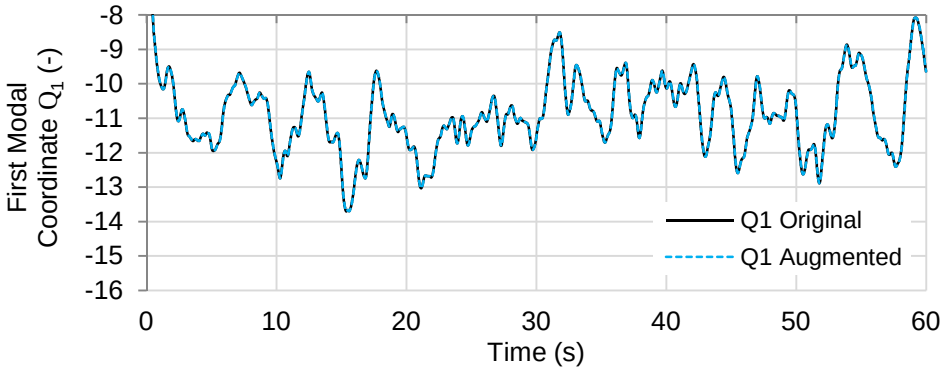


Figure 6.12 - Augmented and original first modal coordinate

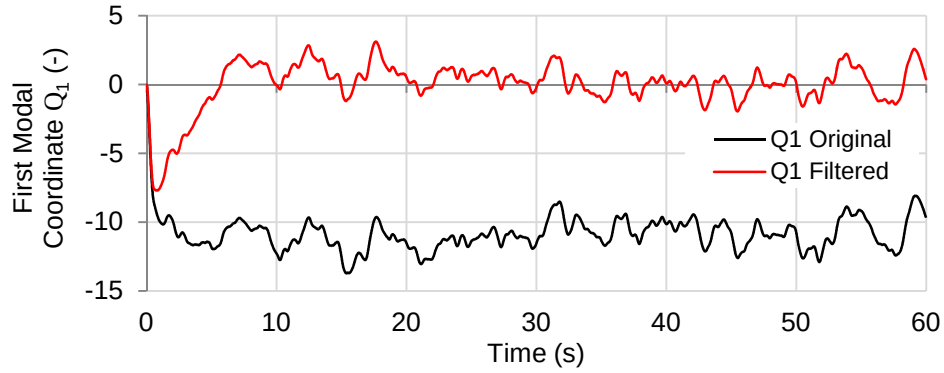


Figure 6.13 - Filtered and original first modal coordinate

The PD controller is incorporated into the state space model by substituting the control signal of (6.26) into the state matrix as:

$$A=\left[\begin{array}{cccc|c|cccc|cc}
0 & 0 & 1 & 0 & 0 & 0 & 0 & 0 & 0 & 0\\
0 & 0 & 0 & 1 & 0 & 0 & 0 & 0 & 0 & 0\\
r_2 & 0 & s_2 & 0 & 0 & t_{21} & t_{22} & t_{23} & 0 & 0\\
0 & 0 & 0 & 0 & 1 & 0 & 0 & 0 & 0 & 0\\
\hline
0 & \tau r_1 & 0 & r_1+\tau s_1 & -\tau+s_1 & \tau t_{11} & \tau t_{12} & \tau t_{13} & 0 & 0\\
\hline
0 & 0 & 0 & 0 & 0 & 0 & 1 & 0 & K_p & K_d\\
0 & 0 & 0 & 0 & 0 & a_{F6} & a_{F7} & a_{F4} & 0 & 0\\
0 & 0 & 0 & 0 & 0 & 0 & 0 & \tau_F & 0 & 0\\
\hline
0 & 0 & 0 & 0 & 0 & 0 & 0 & 0 & 0 & 1\\
0 & 0 & 0 & 0 & 1 & 0 & 0 & 0 & \gamma_1 & \gamma_2
\end{array}\right] \qquad (6.29)$$

Results of the PD controlled system on the NREL 5 MW wind turbine subjected to cyclic loadings due to windshear are presented in Figure 6.14. The PD controller is activated from the start (i.e. t = 0) and consequently first alleviates the fast transient and mean loadings before the system reaches its normal operating condition at about 30 s. As expected from the P controller results, a PD controller combined with a high-pass filter is also suitable for the alleviation of wind turbine blades equipped with a CS.

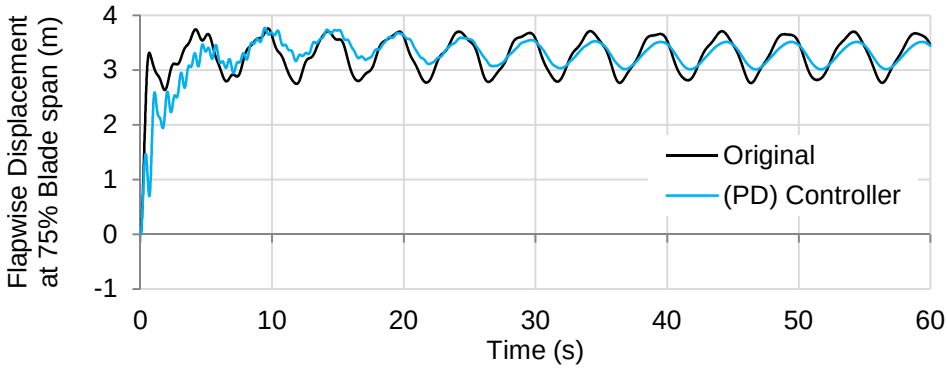


(a)

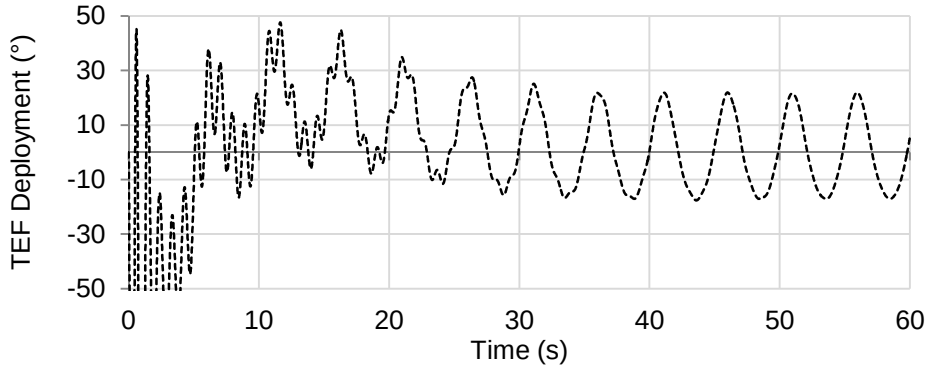


(b)

Figure 6.14 - Load alleviation employing a high-pass filter and a PD controller (NREL 5 MW wind turbine, windshear condition)

**Discontinuous Controllers**

All previous results considered the use of continuous controllers (i.e. P and PD) which could be integrated into the state space model. In this research, a particular attention is given to the effects of discontinuous controllers on the dynamic of actively controlled wind turbine blades. These have yet to be investigated in the literature. The use of discontinuous controllers that can only deploy in either maximal or minimal positions is therefore investigated.

The Bang-Bang (BB) controller is designed to deploy the CS as a function of the reference signal sign. Figure 6.15 presents the load alleviation results of a wind turbine blade equipped

with a single CS deploying accordingly to the BB control command. Moreover, Figure 6.16 compares the CS deployment controlled by the P and BB controllers. As expected, the CS actuation of the discontinuous actuator matches the zero crossing of the P controller. That is, the BB controller can be viewed as a very high gain P controller constrained in between the maximal CS deployment boundaries. While such abrupt actuations may cause significant wear on the actuators, the load alleviation results presented in Figure 6.15 do not show any clear disadvantage when using a single CS.

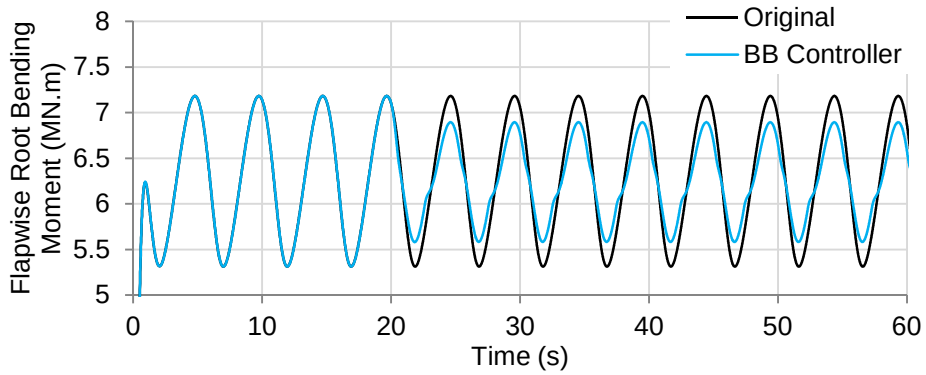


(a)

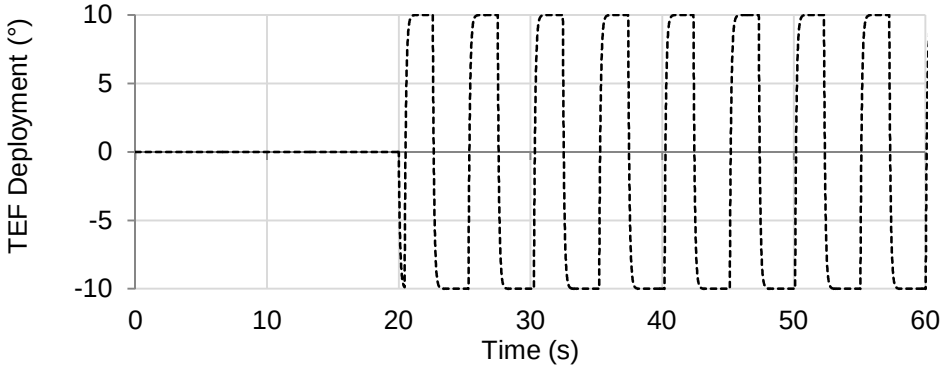


(b)

Figure 6.15 - BB controller load alleviation employing one TEF

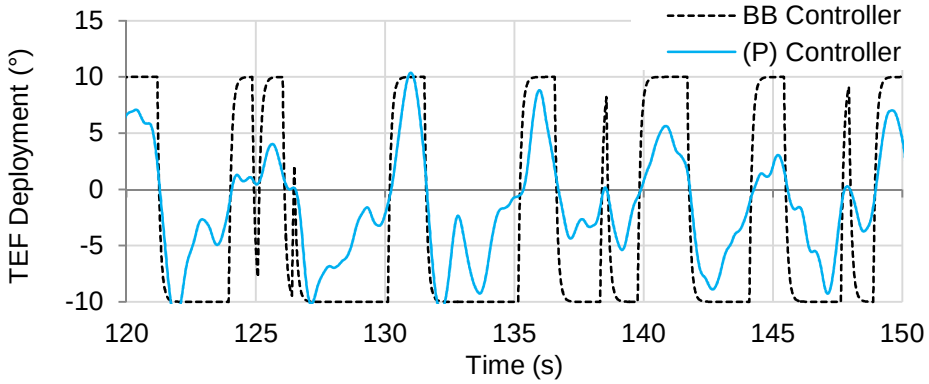


Figure 6.16 - Comparison between the proportional and the BB controller TEF actuation

**Section Summary**

Throughout this section, the author showed that the trivial combination of a proportional controller and a high-pass filter can be used to shape the plant frequency response for load reduction purposes. This is likely one of the simplest yet most effective control system that can be used for the SISO case (i.e. single CS). Our result is not entirely in agreement with recent literature which often suggests the use of high-order band-pass or non-real time zero-phase band-pass filters as well as advance controllers. Clearly, the results obtained do not encourage the use of high-order filters that would destabilise the controlled blades and therefore increase natural frequency loads. The author argues that it is not necessary to precisely extract the loads at frequencies of interest. First, the 1P, 2P and 3P frequencies are relatively close to each other (e.g. within a 1Hz bandwidth for large wind turbine) which makes the extraction of each of these individual loads difficult. Second, the approaches commonly used in literature are based on the ideal assumption that each frequency can be extracted and controlled independently. However, in practice this is often incorrect and the control systems will have a general influence on the system rather than on each individual load. The author therefore recommends using low-order filters which encompass all the frequencies (e.g. 1P, 2P and 3P) to be rejected together. Since the 1P loads are much greater than the other frequencies, the control system will naturally focus more control effort on rejecting 1P loads. At the same time, by employing low-order filters, the system stability will not be degraded.

In this section it was also demonstrated that both continuous and discontinuous control systems could be effectively used for load alleviation employing a CS. At this stage, the author does not see any drawbacks in using cheaper discontinuous actuation mechanisms.

### 6.3.2 Load Alleviation Employing Multiple Control Surfaces

The load alleviation of wind turbine blade loads employing multiple CSs is investigated in this section. According to Section 6.2, the wind turbine blades are assumed equipped with a string of control surfaces covering $S_{CS}$ (20% or ≈12m) of the total span of the NREL-5 MW wind turbine blades, extending from the outer radial location (56.5m or about 90% of the blade span) to the inner blade part as shown in Figure 6.17. The string of CSs is divided into *n* segments, each segment with a length of $\Delta S_{CS}$. Without loss of accuracy, CS segments are chosen of the same length as the blade segments defined for BEMT analysis.

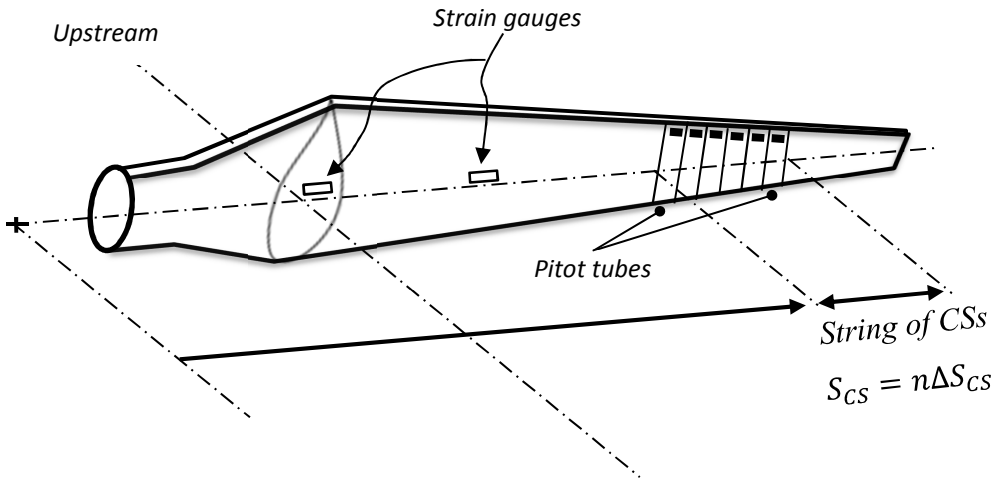


Figure 6.17 - Control surfaces and sensors locations along the blade span

**Control Effort Distribution**

The control effort distribution amongst CSs is explored in this section. In the research carried out by Barlas and van Kuik (Barlas and van Kuik, 2009), different strategies are proposed in order to control multiple CSs. One strategy, referred to as the *decentralised individual flap control*, assumes that all CSs deploy simultaneously based on the root bending moment measurements. This strategy is similar to the large CS assumption presented above in which all CSs deploy simultaneously. A second control strategy, referred to as the *decentralised multiple flap control*, controls each CS individually based on local bending measurements.

CSs located at different blade span locations have slightly different aerodynamic responses and therefore may require independent tuning to perform effectively. In both proposed control strategies the CSs' deflections is based on the blade bending moment measured either at the root or along the blade span. However, it was previously shown that the NREL 5 MW wind turbine blade dynamic is dominated by the first structural mode (see Section 5.3). The measurements of various bending moments along the blade span are, therefore, in-phase as illustrated in Figure 6.18. Consequently, the author argues that using multiple sensors that carry the same information should not significantly influence the load alleviation performance. Since different measurements are in-phase but have different amplitudes, the controller gains must simply be adjusted so that the control inputs have the same magnitudes. As a result, it was decided to consider classical controllers and the large CS assumption for investigating the dynamic analyses of wind turbine blades equipped with multiple CSs in the

rest of Section 6.3.2. The load alleviation results employing multi-input multi-output (MIMO) controllers are explored in the next sections.

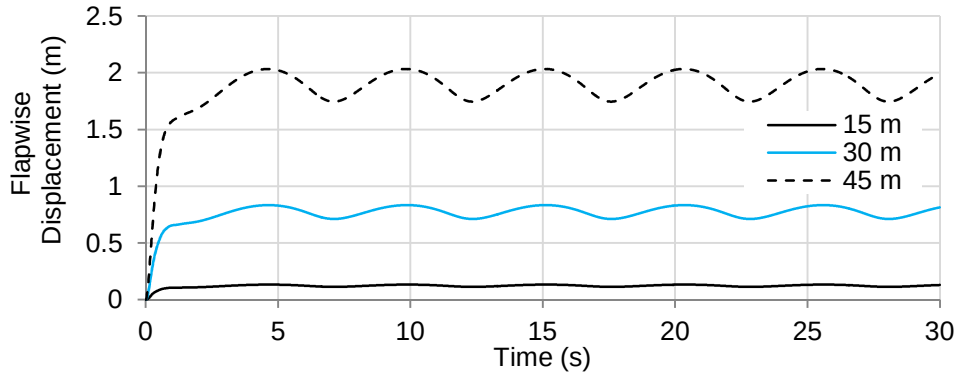


(a)

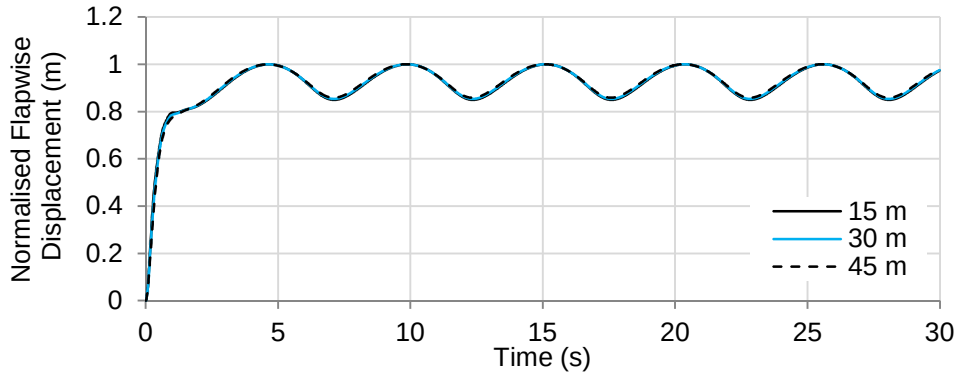


(b)

Figure 6.18 - Flapwise blade measurements along the NREL 5 MW wind turbine blade span

**Control Effort Distribution using Continuous Controllers**

The control effort distribution and load alleviation capability of the continuous control system in terms of the number of equipped CSs is examined in this section. As discussed before, all CSs are assumed to deploy simultaneously (i.e. large CS assumption) as controlled by a simple P controller combined with a high-pass filter. In Figure 6.19 the load alleviation results obtain with WTAC as the number of CSs increases are presented. The overall load alleviation capability is shown to increase as the number of TEFs increases while the actual capability of each newly added CS decreases. Similar results were observed when employing one CS and increasing the proportional gain $K_p$ as shown in Figure 6.20.

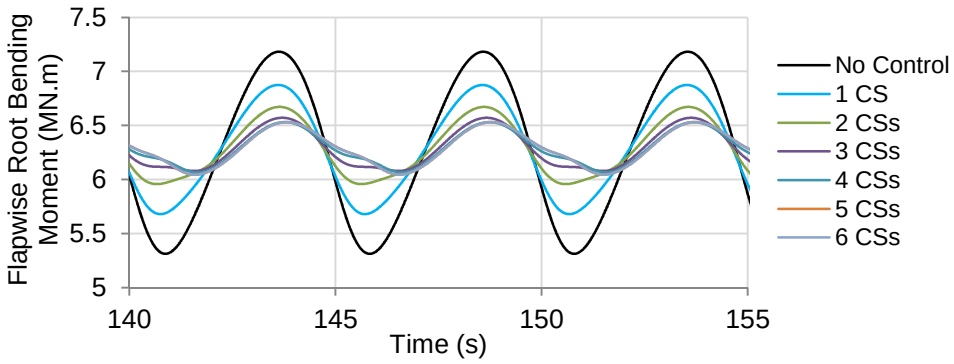


Figure 6.19 - Load alleviation performance as a function of the number of CSs employed

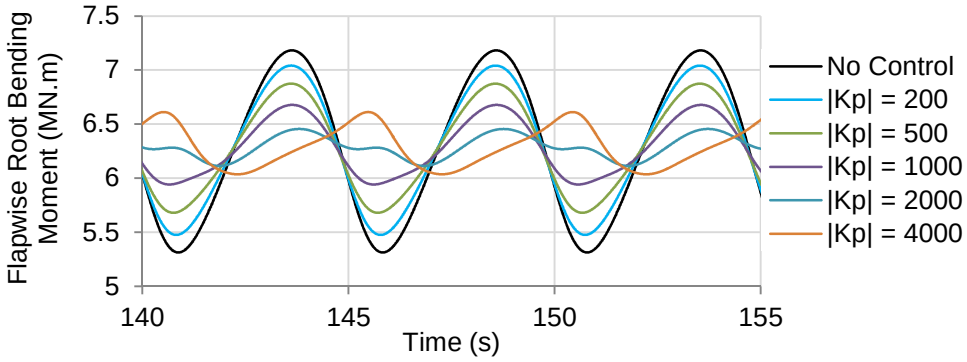


(a)

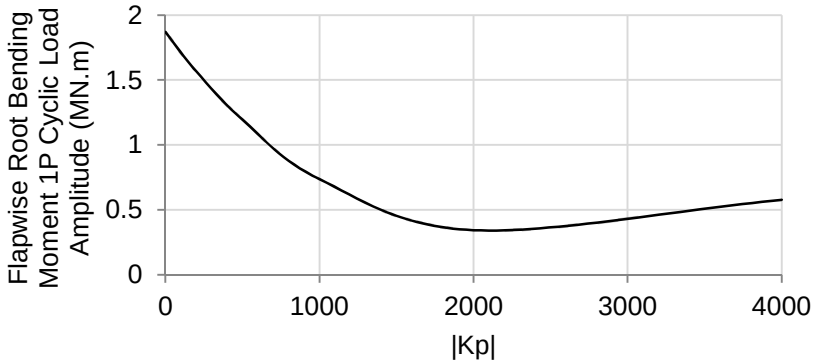


(b)

Figure 6.20 - Load alleviation performance of a single CS as a function of the proportional gain

The results presented in the above figures can be explained as follows. Each CS produces an independent controllable aerodynamic force; in these figures it is shown that adding these limited forces or utilising one unlimited force produced by a unique CS have similar consequences on the blade-CSs system dynamic. That is, the reduction of the load alleviation performance as the number of CS increases is due to the blade-CSs system poles moving towards instability. As $K_p$ or the number of CS increases, the blade-CSs system poles move towards instability and the natural frequencies becomes more and more excited and out-of-phase as observed in Figure 6.20.a. The author, therefore, concludes that the load alleviation

capabilities of a wind turbine blade equipped with multiple CSs does not increase linearly with the available control effort (i.e. number of CSs) as highlighted by Figure 6.20.b.

Since the high gain of the P controller is the cause of the excitation of higher frequencies, the PD controller load alleviation results are investigated as shown in Figure 6.21. It can be seen that the PD controller load alleviation outperforms the P controller. In particular, the PD controller reduces the excitation of higher frequencies due to the virtually added damping.

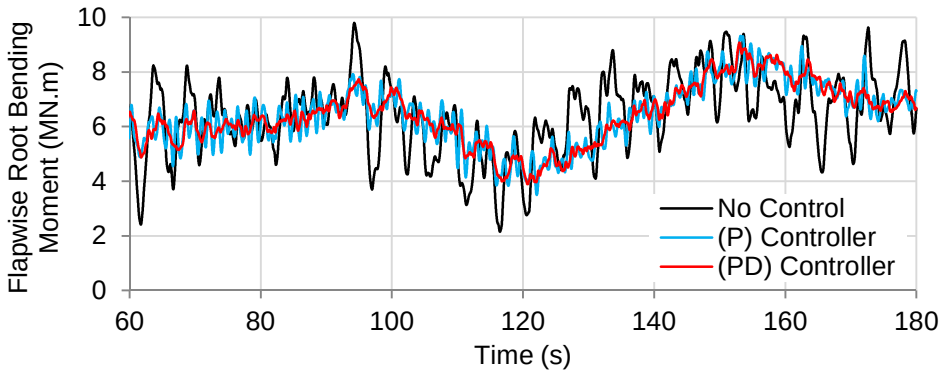


Figure 6.21 - Single CS load alleviation of the NREL 5MW wind turbine using P and PD controllers (13m/s turbulent wind field)

The same behaviour as the one observed for a single CS in Figure 6.21 is also observed for a wind turbine blade equipped with multiple CSs and controlled using the PD controller as shown in Figure 6.22. These results suggest that the interaction between CSs may be negligible and that the "large CS assumption" could be used for designing suitable load alleviation controllers.

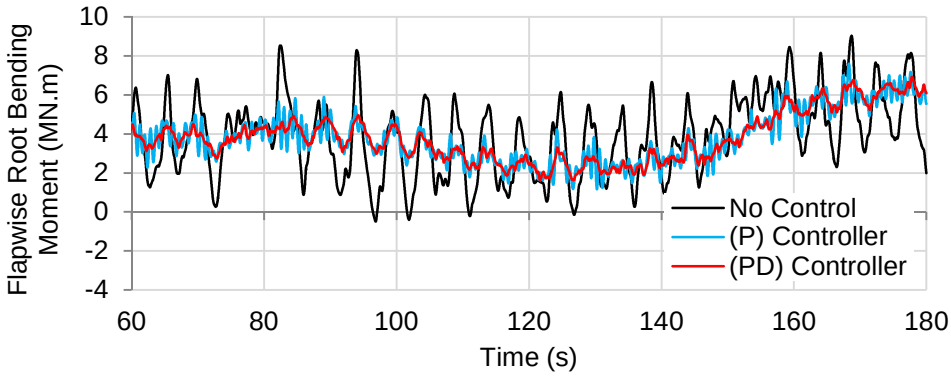


Figure 6.22 - Multiple CSs load alleviation of the NREL 5MW wind turbine blade using P and PD controllers (18m/s turbulent wind field)

**Control Effort Distribution using Discontinuous Controllers**

As for the previous section, the discontinuous controller (i.e. bang-bang) control effort distribution for load alleviation employing multiple CSs is explored herein. Figure 6.23 shows the load alleviation results as the number of CSs increases. As the number of CSs increases, the flapwise root bending moment shows significant discrepancies compared to the results obtained with the continuous P controller. In particular, one can observe a rapid excitation of the blade natural frequencies as the overall control capability increases. This result was expected as the BB controller was previously shown to behave similarly to a constrained high gain P controller.

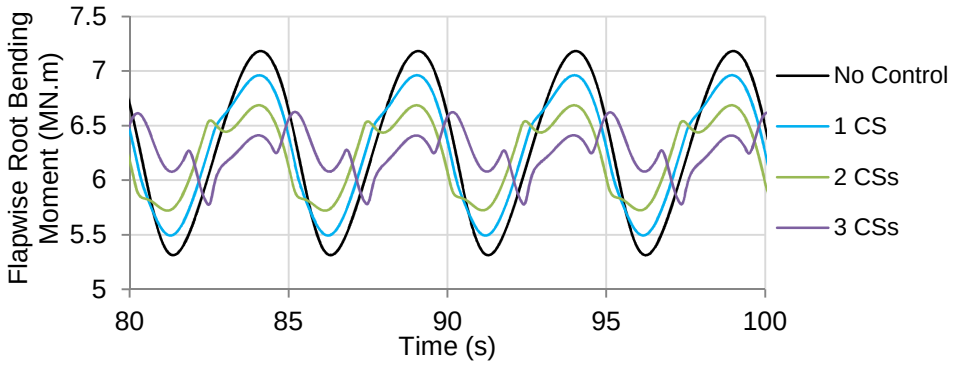


Figure 6.23 - Turbulent load alleviation results employing several CSs deploying according to a discontinuous BB controller

**Section Summary**

In this section, the author showed that the load alleviation capability of wind turbine blades equipped with CSs does not increase linearly as the number of CSs increases. This observation is critical in the sense that the control system should be efficient yet cheap. Determining the optimal number of CSs that should be installed on wind turbine blades is therefore crucial. These preliminary results suggest that the maximum 1P load alleviation of the NREL 5 MW wind turbine can be achieved with 3 to 4 CSs for a total covered span of about 12%. While it is not possible to directly calculate the optimal number of CSs based on our results, it is argued that a similar load alleviation trend will occur on other wind turbine blades. That is, the author demonstrated that the load alleviation performance of wind turbine blades equipped with multiple CSs is limited due to the increased closed-loop instability.

The author also observed that the load alleviation dynamic of several CSs was equivalent to the load alleviation dynamic of a single CS. These results suggest that the interaction between CSs may be negligible and that the “large CS assumption” could be used for designing

suitable load alleviation controllers. The frequency analyses of the load alleviation control problem is now carried out in order to investigate the dynamic of the actively controlled wind turbine blades. Additionally, the frequency analyses will be used to verify the preliminary results obtained so far based on the time approach.

### 6.3.3 Frequency Based Control Evaluation

In this section the influences of the control architectures presented in Figure 5.17 on the dynamic of the blade-CSs system are investigated. The frequency analyses carried out in this section are divided into the *simplified frequency control analysis*, the *individual CS frequency control analysis*, and the *multiple CS frequency control analysis*.

**Simplified Frequency Control Analysis**

The simplified frequency control analysis is a method that is proposed in order to gain insights into the dynamic of the blade-CSs system based on a simplified model. Results obtained for the simplified frequency control analysis are later compared with the *multiple CS frequency control analysis* of the aero-structural wind turbine blade model. The following assumptions are made during the simplified frequency analysis:

**Assumption (i)**

According to Section 6.3.2, blades equipped with multiple CSs are assumed to be dynamically equivalent to blades equipped with single CSs. This assumption permits writing the aero-structural system in a single-input single-output (SISO) form for which the frequency analysis is simplified.

**Assumption (ii)**

In WTAC, the aerodynamic damping is simulated by feedback of the blades velocity to the aerodynamic module. In order to include the aerodynamic damping in the model used for the frequency analysis, it is assumed that a virtual damping term is added to the structural model of Equation (4.45). A comparison between WTAC and the stand-alone aero-structural model flapwise calculation is shown in Figure 6.24.

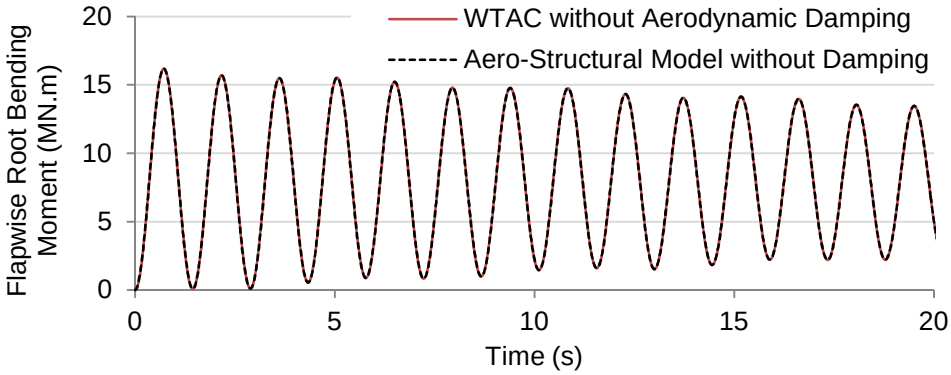


(a)

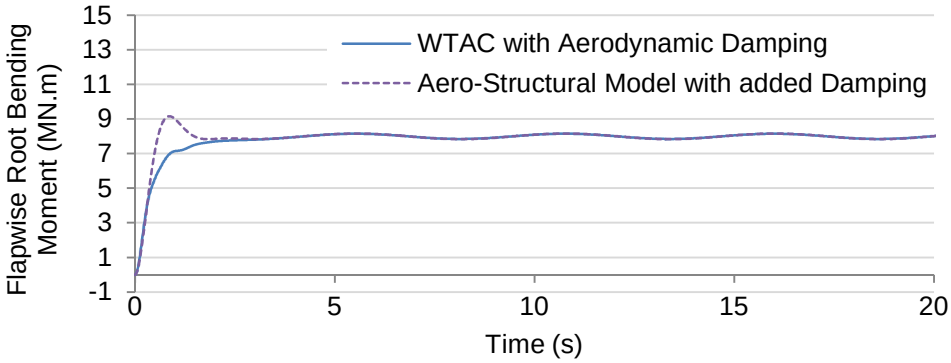


(b)

Figure 6.24 - Flapwise root bending moment predicted by WTAC and the standalone aero-structural wind turbine blade model

Resulting from assumption (ii), Figure 6.25 shows the frequency response of the structural and the aero-structural (i.e. with aerodynamic damping) blade models. The magnitude plot static gain is about -60dB because the input considered is the transversal load and the output is the transversal displacement. The aero-structural model dynamic, due to the substantial amount of aerodynamic damping, is approximated by a low-pass filter dynamic. In other words, the aero-structural natural frequencies are not subject to self-increasing excitations due to the substantial amount of energy being dissipated by the aerodynamic damping.

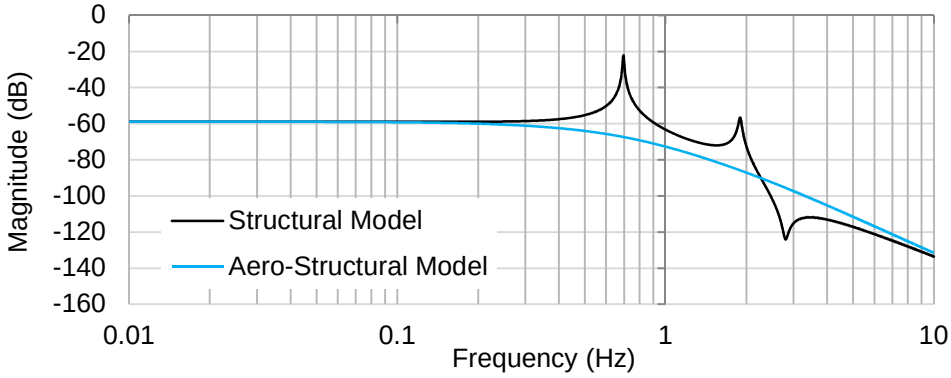


Figure 6.25 - Frequency response of the structural and aero-structural wind turbine blade models

Based on these assumptions, the simplified frequency analysis is now carried out. Figure 6.26 illustrates the open-loop aero-structural system of Equation (4.45). The plant $P_L$, which stands for the wind turbine blades equipped with CSs, is excited by unknown external forces.

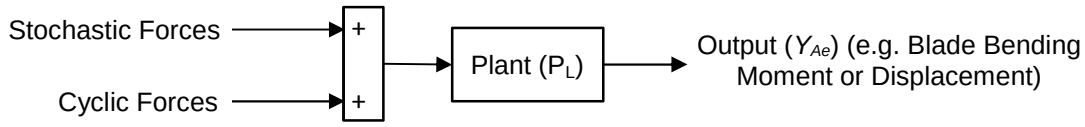


Figure 6.26 - Representation of the open-loop wind turbine blade (plant) subject to unknown forces

Consider the control architecture of Figure 6.27. Since the external forces are assumed unknown, the controller cannot be positioned directly between the plant and the unknown forces (feed-forward). In other words, the unknown forces driving the wind turbine dynamics can only be alleviated by closing the loop. In doing so, the blade displacement generated by the unknown external forces is fed back to the controller that deploys CSs in order to counteract the unknown disturbances. Since the mean load and low frequency loads are not to be alleviated, the output is generally filtered.

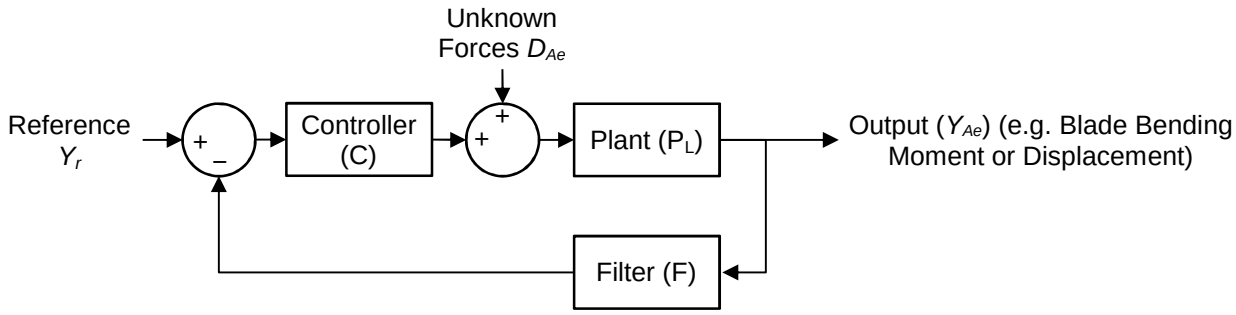


Figure 6.27 - SISO closed-loop structure for wind turbine blades equipped with a control surface

If the filtered signal contains all frequencies to be rejected, the reference is set to zero and the control structure can be presented as in Figure 6.28.

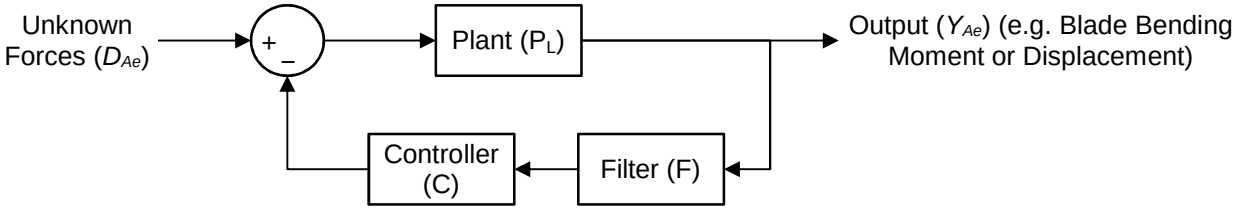


Figure 6.28 - SISO closed-loop structure for wind turbine blades equipped with a control surface ($Y_r = 0$)

Utilising a single order low-pass filter as plant (i.e. assumption **ii**), the closed-loop transfer function illustrated in Figure 6.28 is given by:

$$H_{cl} = \frac{Y_{Ae}}{D_{Ae}} = \frac{P_L}{1 + P_L CF} \tag{6.30}$$

Employing a P controller in the feedback loop, the closed-loop system equation can be calculated as:

$$H_{cl} = \frac{Y_{Ae}}{D_{Ae}} = \frac{P_L}{1 + P_L K_p} \tag{6.31}$$

The magnitude plots of the open and closed-loop systems are presented in Figure 6.29. It can be seen that the P controller alleviates all frequencies from the mean value up to the first natural frequency.

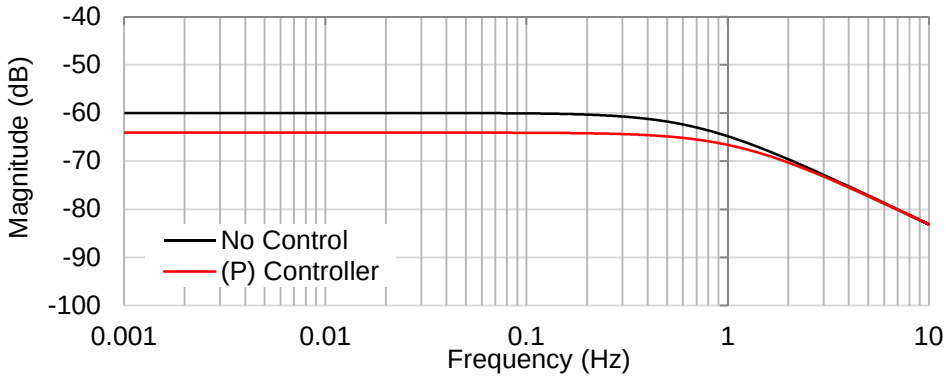


Figure 6.29 - Magnitude plots of an open-loop and closed-loop (P controller) low-pass filter

Integrating the high-pass filter into the feedback loop one obtains:

$$H_{cl} = \frac{P_L}{1 + P_L CF} = \frac{P_L}{1 + P_L K_p \dfrac{s}{s + \gamma}} \tag{6.32}$$

The Bode plot corresponding to (6.32) is shown in Figure 6.30. As expected, the high-pass filter stops the controller from rejecting low frequency loads. Moreover, it can be seen that the added phase remains low.

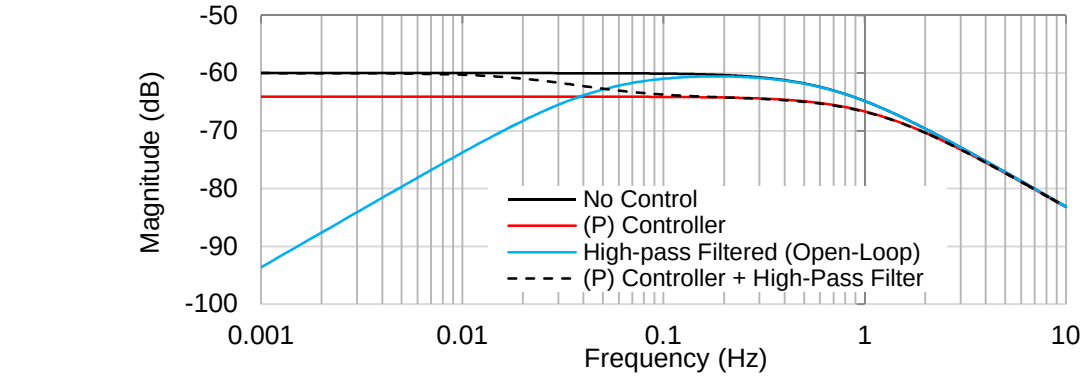


(a)

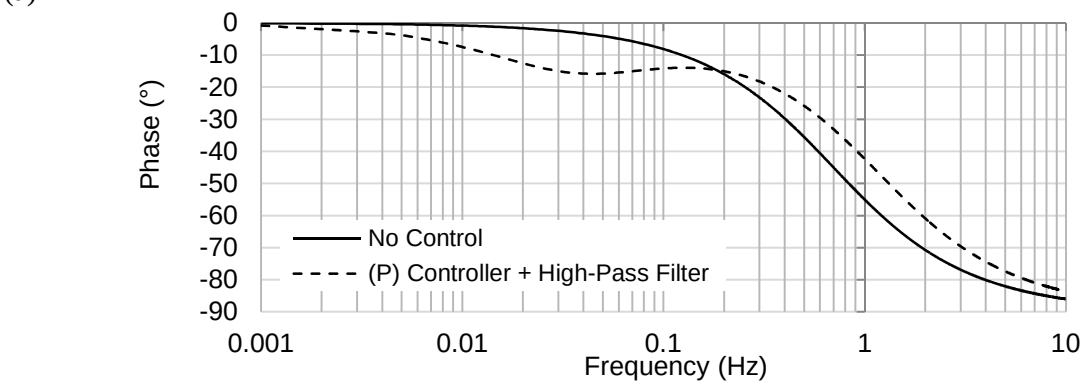


(b)

Figure 6.30 - Bode plot of an open and closed-loop (P controller and high-pass filter) low-pass filter

**Individual Control Surface Frequency Control Analysis**

With reference to the simplified frequency analysis presented above, one can conclude that a simple combination of a P controller and a high-pass filter can be used to modify the plant frequency response in order to achieve load alleviation. The same procedure is now applied to the wind turbine blade aero-structural model equipped with a single CS (i.e. SISO case).

Figure 6.31 shows the magnitude plot of the blade-CS system equipped with a P controller as the gain $K_p$ increases. As this figure shows, a similar behaviour to the simplified frequency analysis is observed. That is, as the proportional gain increases the alleviation of the rotational frequencies load increases. In addition, an amplification of the natural frequency loads is observed because, in comparison to the single order low-pass filter, the blade-CS system becomes unstable as the proportional gain increases. Without any filter, the P controller also rejects low frequency loads.

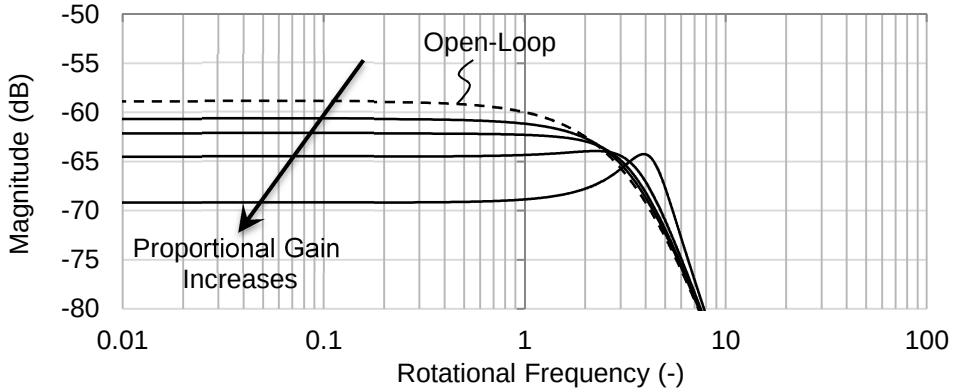


Figure 6.31 - Wind turbine blade closed-loop dynamic response to control surface (P controller)

As expected from the simplified frequency analysis, by combining the high-pass filter with the P controller in the feedback loop the load alleviation frequency bandwidth is reduced as shown in Figure 6.32.

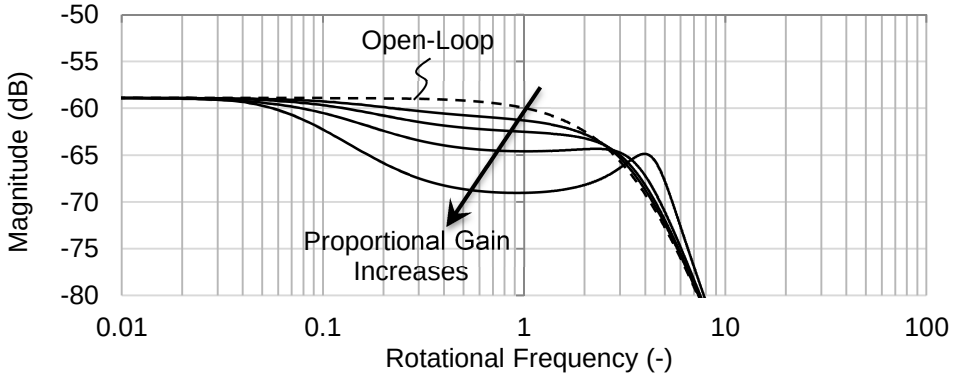


Figure 6.32 - Wind turbine blade closed-loop dynamic response to control surface (P controller with a high-pass filter - pole at 0.3rad/s)

In order to increase the closed-loop system stability, the derivative controller can be added to the closed-loop control frequency response as shown in Figure 6.33. According to the load alleviation results presented in Section 6.3.2, it can be observed that the derivative gain increases the virtual damping and therefore reduces the excitation of the blade natural frequencies.

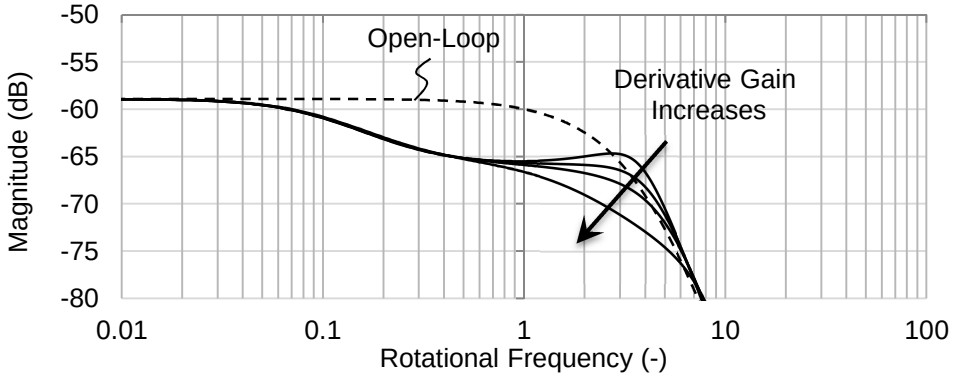


Figure 6.33 - Wind turbine blade closed-loop dynamic response to control surface (PD controller with a high-pass filter - pole at 0.3rad/s)

The above results show that the loop-shaping control method used for the simplified frequency analysis can also be successfully applied to a wind turbine blade equipped with a single CS. These results suggest that a feedback control consisting of a PD controller and a high-pass filter may be one of the simplest yet most effective control strategies for the SISO load alleviation of wind turbine blades.

**Multiple Control Surfaces Frequency Control Analysis**

So far, the control analyses were limited to SISO cases. However, wind turbine blades may be equipped with many CSs. In which case, the author represents the control structure as in Figure 6.34. Here the chief advantage of MIMO controllers is evident. The classical controllers form a repeated SISO control structure where each controller (C1, ... , Cn) must be tuned individually. On the other hand, the MIMO controller calculates the deployment of all CSs in a straightforward manner while taking the overall system dynamic into account.

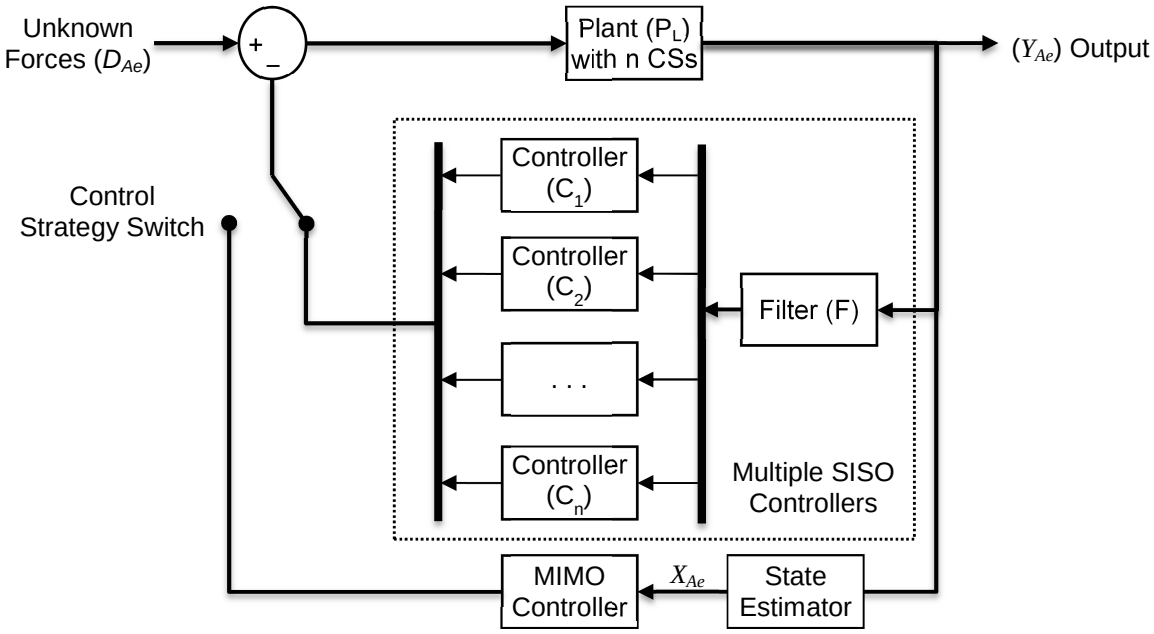


Figure 6.34 - Control structures for a wind turbine blade equipped with multiple control surfaces

In this multiple CS case, the loop-shaping control using the classical SISO controller remains identical to the one presented in the previous sections. In comparison, the LQR criterion is designed to weigh the first filtered modal coordinate $Q_{1f}$ of the augmented wind turbine blade model of Equation (6.28). For preliminary comparison, the LQR control strategy is

evaluated for a wind turbine blade equipped with a single CS (i.e. SISO case). The magnitude plot and flapwise root bending moment of the blade-CS system are shown in Figure 6.35. The criterion weight is increased tenfold between LQR 1 and LQR 2, and LQR 2 and LQR 3. As it can be observed, the magnitude plot of the LQR shows obvious similarities with the PD controller Bode plot of Figure 6.33.

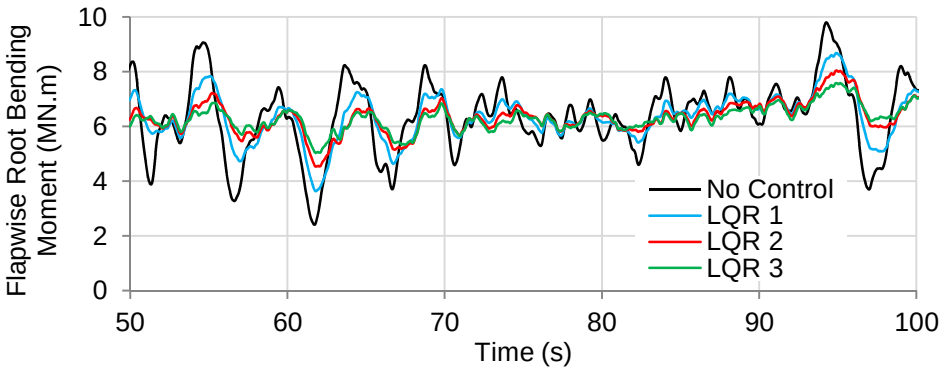


(a)

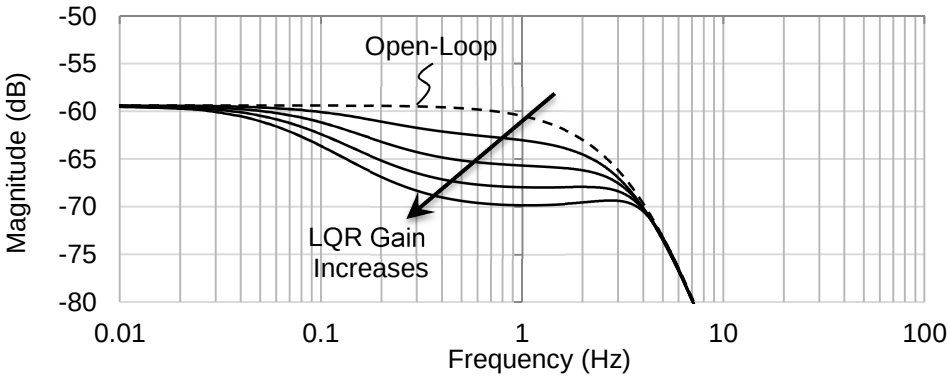


(b)

Figure 6.35 - SISO wind turbine blade flapwise root bending moment and magnitude plots (LQR)

The LQR control strategy is now applied to wind turbine blades equipped with multiple CSs. The load alleviation achieved using the MIMO control strategies are presented in Figure 6.36. The criterion weight is increased tenfold between LQR - A and LQR - B, and LQR - B and LQR - C. As illustrated in this figure, the flapwise root bending moment alleviation using the MIMO controller is similar to the one achieved for the SISO case.

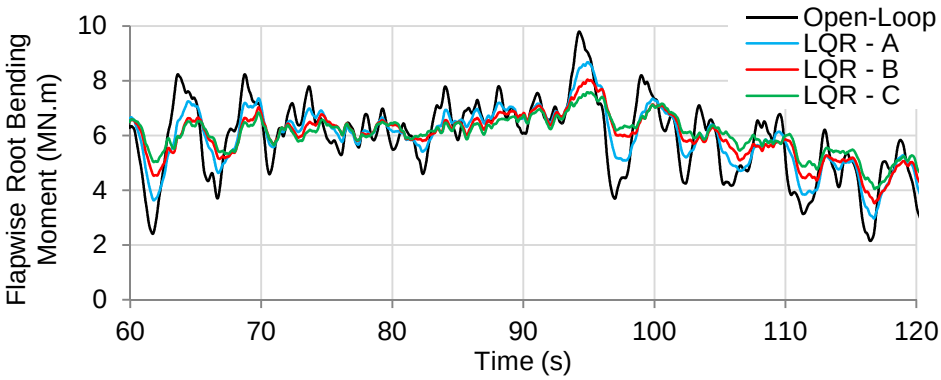


(b)

Figure 6.36 - MIMO wind turbine blade flapwise root bending moment as controlled by the (a) PD and (b) LQR controllers

Employing PD controllers with a reference signal based on a flapwise sensor located towards the blade root, all CSs deploy in-phase. The magnitude of each CS deployment may however vary due to small changes in models and controller tuning. By contrast, a MIMO controller such as the LQR is able to control each CS independently. Nevertheless, the deployments of TEFs controlled using the LQR are also in-phase with each other as shown in Figure 6.37. This is in accordance with Section 6.3.2 which showed that flapwise measurements made along the blade span are in-phase.

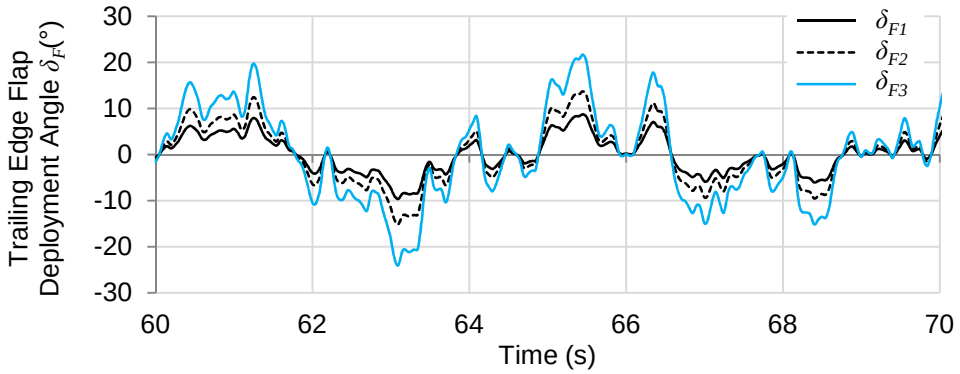


Figure 6.37 - Unconstrained trailing edge flap deployment angle $\delta_F$ according to the LQR control

**Section Summary**

The prime conclusion of our frequency analyses follows: The dominant vibrating mode and the limited control capabilities and interactions between CSs are such that the original MIMO control problem can “effectively” be decoupled into SISO control problems. Note that the MIMO control problem has not been mathematically decoupled but the particularities of this vibration problem permits to assume an “effective” decoupling. In other words, it was found

that the interaction between CSs is negligible due to the dominant vibrating dynamic of large blades.

This “effective” decoupling is one of the key results of this research. By demonstrating that the complex MIMO load alleviation control problem can be decoupled, the author infers that advanced time-based control system are not necessary to achieved good performance. In contrast to the current state of literature, the present research points towards a better understanding of the dynamic of controlled blades, and simple yet efficient control structures. In particular, the author recommends the use of classical control structures combined with low order filters. Load alleviation results will be as good as, if not better than, for advanced controllers while the stability of the blade will not be degraded.

Quantitative analyses of the control structure are now carried out to validate the frequency results.

### 6.3.4 Quantitative Load Alleviation Performance

A quantitative assessment of the load alleviation achieved employing microtabs and TEFs is carried out in this section. In order to evaluate the control systems performance over the several frequency bandwidths of interest (i.e. rotational and natural frequencies), the load alleviation performance is calculated in the frequency domain. Since loads are usually spread over a frequency bandwidth, the load alleviation is calculated by averaging the load reduction in separate intervals centred at the rotational and natural frequencies as described by:

$$LA = 100\left(\frac{\sum_{nP-\mu}^{nP+\mu}\left(f_{noc}(\omega) - f_{c}(\omega)\right)}{\sum_{nP-\mu}^{nP+\mu} f_{noc}(\omega)}\right) \tag{6.33}$$

where, $f_{noc}(\omega)$ and $f_{c}(\omega)$ respectively denote the flapwise root bending moment frequency spectrum for the uncontrolled and controlled case and $[nP-\mu, nP+\mu]$ is the interval over which the results are averaged for the first, second and third rotational frequencies ($n = 1, 2$ and 3) as well as the first natural frequency.

During the load alleviation simulation, the NREL 5 MW wind turbine blade is equipped with CSs and sensors as in Figure 6.17. The CSs primary features are summarised in Table 6.2.

The simulations are carried out over 10 minutes with a time step of 0.01s. Representing the bending moment at the root of the blades by two components, the mean value $\overline{M}$ and the variable part $\hat{M}$ ($M = \overline{M} + \hat{M}$), the frequency domain figures in this section show the frequency spectrum of the variable part of the controlled bending moment only. This choice is justified as the CSs control system does not interact with low frequency loads.

Table 6.2 - Control surfaces features

| | Trailing Edge Flap | Microtabs |
|---|---|---|
| Covered Span (in percent of radius) | 20% | 20% |
| Size (in percent of local chord) | 10% | $\in$ [1, 2]% |
| Maximum Deployment | ±10° | ±1 (normalised) |
| Maximum Deployment Speed | ±100°/s | ±10/s (normalised) |
| Maximum $\Delta C_L$ | ≈ 0.38 ± 0.02 | ≈ 0.17 ± 0.02 |

**Microtabs**

Microtab load alleviation results are the first to be investigated. Figure 6.38 presents the flapwise root bending moment of the NREL 5 MW wind turbine blade equipped with microtabs. The corresponding frequency spectrum is shown in Figure 6.39. Since load alleviation results are difficult to evaluate visually, these figures are presented as a typical load alleviation example. Results obtained for other scenarios are directly presented in tables in terms of quantitative load alleviation performance. The quantitative load alleviation performance of the BB, PD, LQR, and SMC controllers are calculated using (6.33) with a 10% interval around the rotational and natural frequencies.

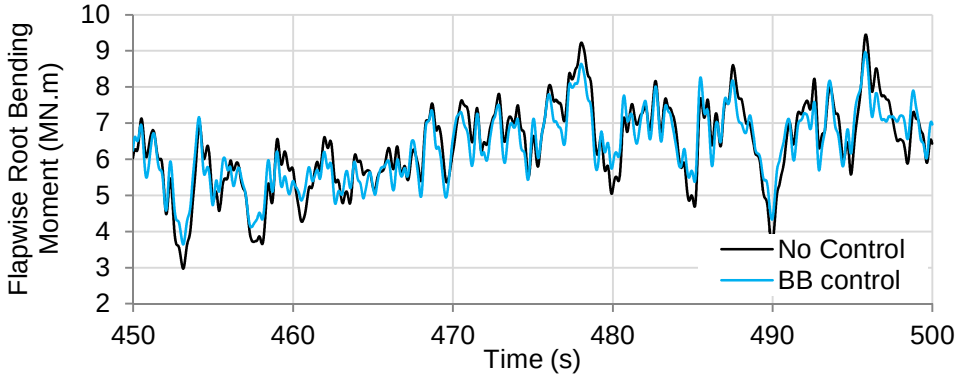


Figure 6.38 - Load alleviation of the NREL 5 MW wind turbine blade equipped with microtabs (10m/s turbulent wind field, BB control)

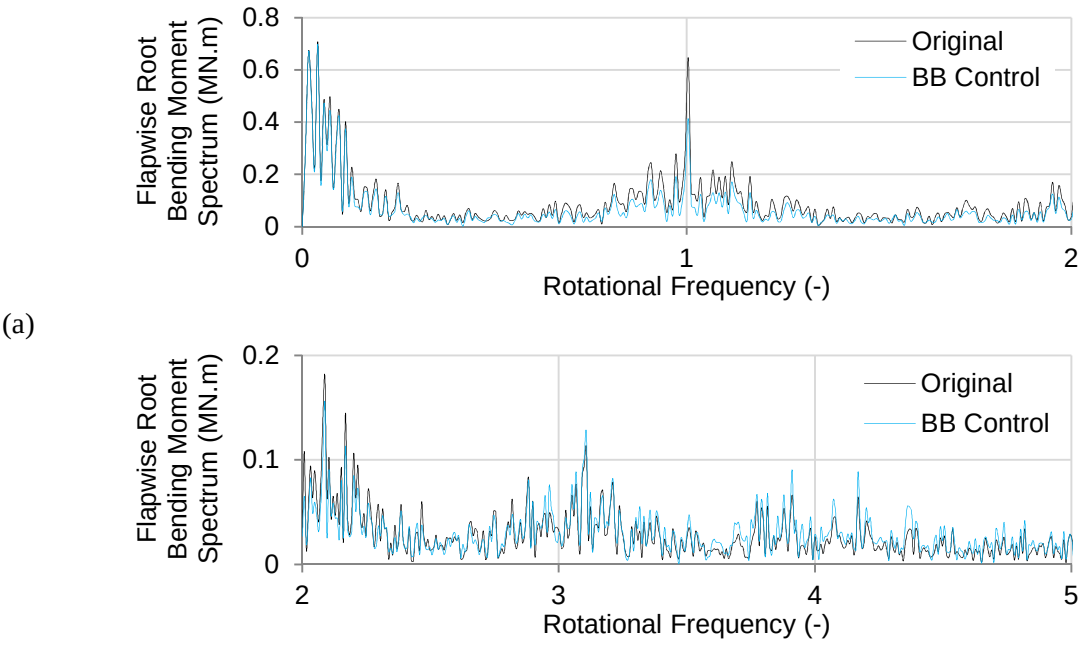


Figure 6.39 - Frequency spectrum of the NREL 5 MW wind turbine blade load alleviation (10m/s turbulent wind field, BB control)

The load alleviation achieved using several PD tunings are shown in Table 6.3. According to Equation (6.33), a positive percentage denotes a load reduction while a negative percentage refers to an increased load excitation. As can be observed, the maximum 1*P* load alleviation occurs when the derivative gain $K_d$ is equal to zero. At the same time, according to the frequency analysis of Section 6.3.3, the excitation of the blade first natural frequency is amplified as the proportional gain $K_p$ increases. Furthermore, as $K_d$ increases the 1*P* load alleviation reduces and the load alleviation of higher frequency loads such as 3*P* and 1*N* increases. The wind turbine blade load alleviation results presented in Table 6.3 are in complete agreement with the frequency analyses of Section 6.3.3.

Table 6.3 - Load alleviation of the NREL 5 MW wind turbine employing microtab (10m/s turbulent wind, PD controller)

| | **PD Controller - Microtabs Load Alleviation** | | | |
|---|---|---|---|---|
| | $K_p$=250 $K_d$=100 | $K_p$=250 $K_d$=200 | $K_p$=250 $K_d$=0 | $K_p$=500 $K_d$=0 |
| 1*P* | 34.53 % | 28.43 % | 37.52 % | 37.39 % |
| 2*P* | 38.39 % | 39.51 % | 30.14 % | 28.84 % |
| 3*P* | 32.83 % | 37.60 % | 6.79 % | 3.22 % |
| 1*N* | 23.99 % | 29.74 % | -8.44 % | -14.60 % |

The load alleviation results for different LQR weights are shown in Table 6.4. If the LQR weights are non-sufficiently high, the control system does not exploit the whole control effort and the load alleviation performance is poor as seen for the *LQR - 4*. According to the LQR frequency analysis (Section 6.3.3), if unsuitable weights are used the LQR controller may

focus the majority of control effort on 1*P* and neglect higher frequency loads as observed for the *LQR - 3*. Finally, if the weights are properly chosen, the LQR closed-loop feedback shapes the dynamic response of the blade-CSs system to effectively alleviate loads as shown for *LQR - 1* and *LQR - 2*.

Table 6.4 - Load alleviation of the NREL 5 MW wind turbine employing microtab (10m/s turbulent wind, LQR)

| | **LQR Controller - Microtabs Load Alleviation** | | | |
|---|---|---|---|---|
| | *LQR - 1* | *LQR - 2* | *LQR - 3* | *LQR - 4* |
| 1*P* | 37.64 % | 36.03 % | 37.48 % | 8.35 % |
| 2*P* | 34.80 % | 33.57 % | 32.29 % | 6.90 % |
| 3*P* | 23.09 % | 23.75 % | 12.36 % | 3.22 % |
| 1*N* | 13.43 % | 14.63 % | -0.92 % | 1.12 % |

The load alleviation performance of the SMC for several sliding surfaces is shown in Table 6.5. Recall that the sliding surface parameters ( $\gamma_{SM}$ and $\beta_{SM}$ ) are related to the damping and stiffness of the desired output dynamic as in Equation (5.18). As a consequence, modifying these two parameters is similar to changing the PD controller tuning gains. If the stiffness surface parameter $\beta_{SM}$ is small, the 1*P* load alleviation is low as seen for the *SMC - 4*. As the stiffness surface parameter increases, the SMC focuses more control effort in rejecting 1*P* loads and drives the system towards instability as seen for the *SMC - 3* and *SMC - 2.* A trade-off between these two parameters gives the best load alleviation performance as observed for the *SMC - 1.*

Table 6.5 - Load alleviation of the NREL 5 MW wind turbine employing microtab (10m/s turbulent wind, SMC)

| | **SMC Controller - Microtabs Load Alleviation** | | | |
|---|---|---|---|---|
| | *SMC - 1* (γ=2, β=15) | *SMC - 2* (γ=1, β=20) | *SMC - 3* (γ=10, β=20) | *SMC - 4* (γ=10, β=2) |
| 1*P* | 35.97 % | 32.74% | 27.69% | 18.32% |
| 2*P* | 26.98 % | 22.93% | 31.49% | 36.99% |
| 3*P* | 18.84 % | 6.23% | 27.94% | 40.43% |
| 1*N* | 16.57 % | 3.72% | 22.16% | 33.24% |

The best found load alleviation performances of the NREL 5 MW wind turbine equipped with microtabs are presented in Table 6.6. It can be observed that the controllers, irrespective of the actuation mechanism (discontinuous and continuous) and controller type (BB, LQR, SMC and PD), have similar performances in easing 1*P* loads. The 1*P* counter-acting loads to be generated by the string of microtabs are greater than the microtabs reachable space (maximum achievable moment by the string of microtabs) and consequently all microtabs deploy to their maximum heights and saturate as shown in Figure 6.40 for the BB and PD

controllers. In other words, the microtabs deployment height time history is dominated by the effect of low frequency loads (1*P*-2*P*) as observed in Figure 6.40.b. This figure shows 1*P* and 1*P*-2*P* loads after filtering all other frequencies.

Table 6.6 - Load alleviation of the NREL 5 MW wind turbine utilising microtabs (10m/s turbulent wind)

| | **Microtabs Load Alleviation - Summary** | | | |
|---|---|---|---|---|
| | BB | PD | LQR | SMC |
| 1*P* | 34.93 % | 34.53 % | 37.64 % | 35.97 % |
| 2*P* | 23.98 % | 38.39 % | 34.80 % | 26.98 % |
| 3*P* | -7.16 % | 32.83 % | 23.09 % | 18.84 % |
| 1*N* | -28.81 % | 23.99 % | 13.43 % | 16.57 % |

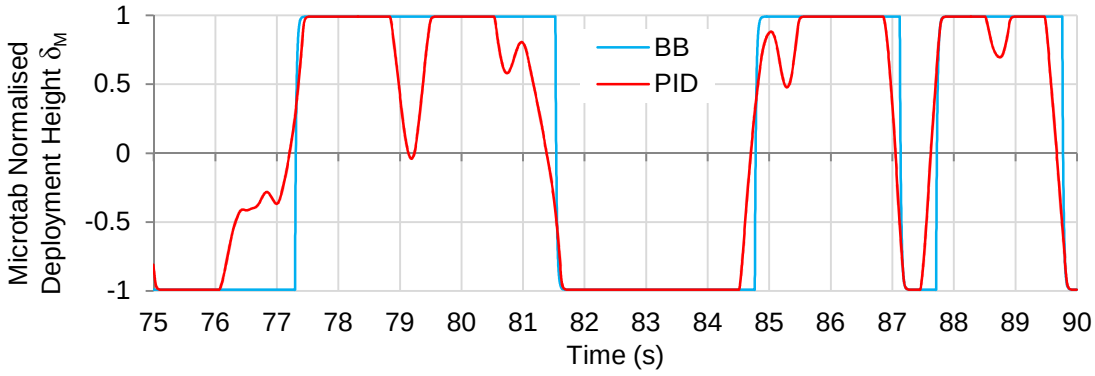


(a)

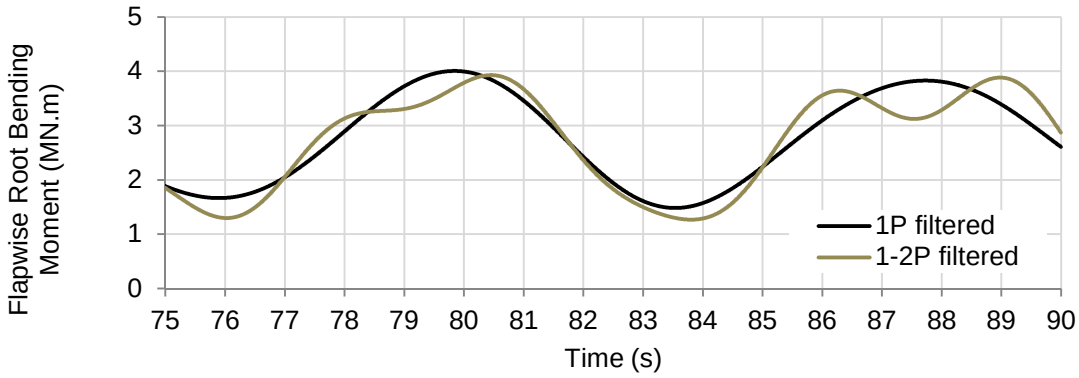


(b)

Figure 6.40 - (a) Microtab normalised deployment height and (b) root bending moment alleviation employing BB and PID controllers for a 15 seconds time window

According to the results presented in Table 6.6, the BB controller significantly increases the amplitudes of the 3*P* and 1*N* frequency loads. As mentioned in Section 6.3.2, discontinuous microtabs can deploy abruptly which results in step-like aerodynamic forces. If these forces are not properly controlled, they will excite the wind turbine blade natural frequencies as shown for the BB controller. Despite the discontinuous actuation mechanism for which the BB controller was shown to over-excite the blade natural frequencies, the SMC controller shows load alleviation capability similar to the continuous controllers.

In view of Table 6.6 one can also notice differences between the SMC, PD and LQR controllers in alleviating 2*P*+ frequency loads. The PD controller shows a load alleviation spread from 1*P* to 1*N*. On the other hand, the effectiveness of the SMC and the LQR controllers decrease more as the frequency increases. While it was shown (Section 6.3.3) that the controllers can shape the blade-CSs for load alleviation, difference in tuning results are likely responsible for the small differences observed in Table 6.6. For instance, alleviating 1*N* loads in addition to 1*P* loads requires faster actuation as shown when comparing the PD and LQR microtab deployment time history in Figure 6.41.

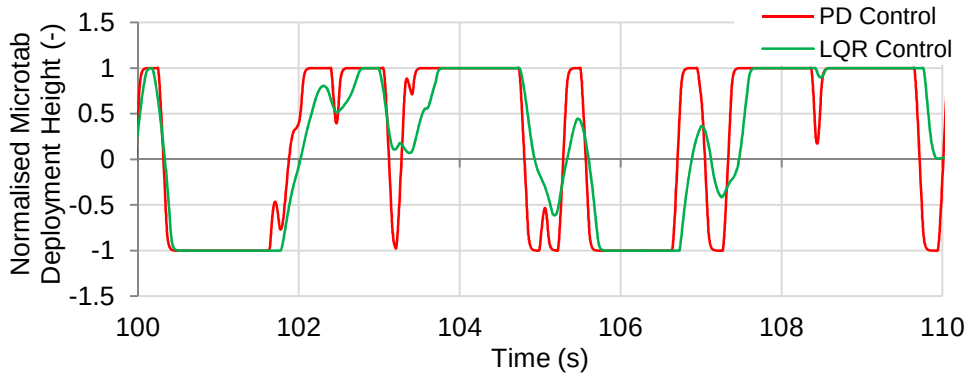


Figure 6.41 - Microtab deployment time history of the PD and LQR controllers

**Trailing Edge Flaps**

The load alleviation performance of the NREL 5 MW wind turbine blades equipped with TEFs is now examined. The previous results obtained for microtabs are repeated to allow a comparison of the two CSs performance and to highlight similarities. First, the PD controller load alleviation results are presented in Table 6.7. As expected, TEFs have a greater control space and therefore show higher load alleviation performance compared to microtabs. However, it can be observed that similar trends in the results are obtained for both CSs. That is, the maximum load alleviation occurs when the derivative gain is set to zero and the best performance is achieved through the PD trade-off tuning parameters.

Table 6.7 - Load alleviation of the NREL 5 MW wind turbine employing microtab and TEF (10m/s turbulent wind, PD controller)

| | Microtabs | | | | Trailing Edge Flaps | | |
|---|---|---|---|---|---|---|---|
| | $K_p$=250 $K_d$=100 | $K_p$=250 $K_d$=200 | $K_p$=250 $K_d$=0 | $K_p$=500 $K_d$=0 | $K_p$=500 $K_d$=200 | $K_p$=250 $K_d$=200 | $K_p$=250 $K_d$=0 |
| 1*P* | 34.53 % | 28.43 % | 37.52 % | 37.39 % | 55.89 % | 51.11 % | 58.06 % |
| 2*P* | 38.39 % | 39.51 % | 30.14 % | 28.84 % | 55.02 % | 56.65 % | 46.36 % |
| 3*P* | 32.83 % | 37.60 % | 6.79 % | 3.22 % | 45.15 % | 50.46 % | 14.25 % |
| 1*N* | 23.99 % | 29.74 % | -8.44 % | -14.60 % | 31.48 % | 40.45 % | -19.19 % |

The results obtained employing the LQR are now presented in Table 6.8. As for the PD controllers, TEF results indicate higher load alleviation potential. Moreover, it can be seen that similar LQR criteria result in similar load alleviation pattern.

Table 6.8 - Load alleviation of the NREL 5 MW wind turbine employing microtab and TEF (10m/s turbulent wind, LQR controller)

| | Microtabs | | | Trailing Edge Flaps | | |
|---|---|---|---|---|---|---|
| | *LQR - 1* | *LQR - 2* | *LQR - 3* | *LQR - 1* | *LQR - 2* | *LQR - 3* |
| 1*P* | 37.64 % | 36.03 % | 37.48 % | 55.52 % | 43.76 % | 57.24 % |
| 2*P* | 34.80 % | 33.57 % | 32.29 % | 55.03 % | 40.09 % | 47.17 % |
| 3*P* | 23.09 % | 23.75 % | 12.36 % | 47.07 % | 25.76 % | 22.49 % |
| 1*N* | 13.43 % | 14.63 % | -0.92 % | 35.00 % | 14.43 % | -7.48 % |

The load alleviation performance of the SMC employing TEF is presented in Table 6.9. As expected, similarities between the microtab and TEF aerodynamic models are also observed for the sliding mode controller.

Table 6.9 - Load alleviation of the NREL 5 MW wind turbine employing microtab and TEF (10m/s turbulent wind, SMC controller)

| | Microtabs | | | Trailing Edge Flaps | | |
|---|---|---|---|---|---|---|
| | *SMC - 1* ($\gamma$=2, $\beta$=15) | *SMC - 2* ($\gamma$=1, $\beta$=20) | *SMC - 3* ($\gamma$=10, $\beta$=20) | *SMC - 1* ($\gamma$=2, $\beta$=15) | *SMC - 2* ($\gamma$=1, $\beta$=20) | *SMC - 3* ($\gamma$=20, $\beta$=2) |
| 1*P* | 35.97 % | 32.74% | 27.69% | 60.79% | 48.59% | 48.71% |
| 2*P* | 26.98 % | 22.93% | 31.49% | 49.50% | 39.29% | 59.86% |
| 3*P* | 18.84 % | 6.23% | 27.94% | 31.55% | 8.36% | 56.86% |
| 1*N* | 16.57 % | 3.72% | 22.16% | 27.75% | 6.79% | 46.83% |

The best found load alleviation controllers for microtabs and TEFs are summarised in Table 6.10. Similar to the microtab results, the TEFs 1*P* load relief achieved with the four controllers are very close due to the limited TEFs control capability. Due to the greater load alleviation capabilities of TEFs compared to microtabs, the BB controller excitation of the first natural frequency is seen to drastically increase when employing TEFs. According to the TEF and microtab aerodynamic model similarities observed in Chapter 3, it is logic that similar patterns are observed between the load alleviation results of both CSs.

Table 6.10 - Best found load alleviation results of the NREL 5 MW wind turbine employing microtab and TEF (10m/s turbulent wind)

| | Microtabs | | | | Trailing Edge Flaps | | | |
|---|---|---|---|---|---|---|---|---|
| | BB | PD | LQR | SMC | BB | PD | LQR | SMC |
| 1*P* | 34.93 % | 34.53 % | 37.64 % | 35.97 % | 53.29 % | 55.89 % | 55.52 % | 60.79% |
| 2*P* | 23.98 % | 38.39 % | 34.80 % | 26.98 % | 34.54 % | 55.02 % | 55.03 % | 49.50% |
| 3*P* | -7.16 % | 32.83 % | 23.09 % | 18.84 % | -25.49 % | 45.15 % | 47.07 % | 31.55% |
| 1*N* | -28.81 % | 23.99 % | 13.43 % | 16.57 % | -100.84 % | 31.48 % | 35.00 % | 27.75% |

Finally, the load alleviation performance of the NREL 5 MW wind turbine blades obtained over five different operating conditions are presented in Table 6.11. It can be seen that similar CSs load alleviation results are found for the different wind speeds. That is, as the wind speed increases both the magnitude of cyclic loads and the capacity of CSs to generate aerodynamic forces increase. Hence, the general load alleviation trends remain the same.

Table 6.11 - PD controller load alleviation performance of trailing edge flaps and microtabs as a function of the mean wind speed

| | Trailing Edge Flaps | | | | | Microtabs | | | | |
|---|---|---|---|---|---|---|---|---|---|---|
| | 10m/s | 13m/s | 15m/s | 18m/s | 22m/s | 10m/s | 13m/s | 15m/s | 18m/s | 22m/s |
| 1*P* | 55.89% | 53.68% | 54.41% | 50.07% | 51.64% | 35.92% | 35.65% | 36.81% | 34.02% | 32.69% |
| 2*P* | 55.02% | 55.04% | 54.16% | 49.02% | 45.62% | 33.67% | 35.28% | 37.10% | 34.11% | 29.11% |
| 3*P* | 45.15% | 44.62% | 44.32% | 38.00% | 38.16% | 23.63% | 30.02% | 27.38% | 23.39% | 25.23% |
| 1*N* | 31.48% | 24.09% | 33.46% | 27.55% | 20.84% | 17.45% | 16.33% | 20.73% | 17.13% | 14.19% |

## 6.4 Load Alleviation Results Summary

The optimal positioning of CSs along the blade span in order to maximise load alleviation was investigated in Section 6.2. In this section, the author developed an analytical approach for calculating the optimal location of CSs along the blade span in order to maximise load alleviation. To the best of our knowledge, no such formula has been proposed before. By deriving the formula, it was demonstrated that in order to maximise their efficiency CSs should be located near the blade tip. A simplified analytical solution for determining the optimal location of CSs was also derived (6.13). This equation provides a quick way to calculate the optimal location of CSs and can be used as preliminary estimate for including CSs in the early wind turbine design phases.

The load alleviation of wind turbine blades employing single and multiple CSs was considered in Section 6.3.1. Throughout this section, the author showed that the simple combination of a proportional controller and a high-pass filter can be used to shape the plant frequency response in order to achieve load reduction. It is argued that this is likely to be one of the simplest yet most effective control systems that can be used for controlling a wind turbine blade equipped with a single CS. In contrast to the literature, the author does not encourage the use of high-order filters that would destabilise the controlled blades and therefore increase natural frequency loads. Instead, the author suggests using low-order filters designed to encompass all the frequencies to be rejected together. Additionally, it was

demonstrated that both continuous and discontinuous control systems could be effectively used for load alleviation employing a single CS.

The load alleviation of wind turbine blades employing single and multiple CSs was considered in Section 6.3.2. In this section, it was first showed that the load reduction of wind turbine blades equipped with CSs does not increase linearly with the number of CSs employed. The author argued that this behaviour is likely to occur on other wind turbines and is a critical factor in determining the number of CSs that should be used. Moreover, our preliminary load alleviation results suggested that the interaction between CSs may be negligible.

The frequency-based approach proposed in this research was assessed in Section 6.3.3. This approach gave us key insights into the dynamic of the actively controlled wind turbine blades. First, it was shown that the dynamic response of a wind turbine blade can be approximated, due to the aerodynamic damping, by a low-pass filter dynamic. This analogous dynamic can be used to gain insights and quickly design and test control systems. Based on the present investigation, the prime conclusion of the proposed frequency analyses was that the dominant vibrating mode and the limited control capabilities and interactions between CSs are such that the original MIMO control problem can “effectively” be decoupled into SISO control problems. Consequently, the author inferred that advanced time-based control system are not necessary to achieve good performance. In contrast to the current state of literature, this research points towards a better understanding of the dynamic of controlled blades, and simple yet efficient control structures. The author recommends the use of classical control structures combined with low order filters.

The quantitative load alleviation results of the proposed control architectures were explored in Section 6.3.4. In this section, the results obtained with the frequency-based approach were validated by comparing them with the frequency spectrum of actively controlled blades employing WTAC. It was confirmed that all the control strategies are strongly dominated by the blade first vibrating mode containing 1P and 2P loads. Moreover, it was also demonstrated that the overall control capability of CSs is insufficient for rejecting 1P loads. Considering these two statements, the author confirmed the necessary assumptions supporting our idea of an “effectively” decoupling of the MIMO problem into SISO control

problems. Furthermore, our quantitative results also confirmed that well-designed classical control structures (e.g. PID) can be very efficient at reducing wind turbine blade loads.

The results obtained in Section 6.3.4 also helped us demonstrate that both continuous and discontinuous control systems could be used. However, it is recommended to avoid simple BB controller and employed more advanced controllers such as the SMC in order to retain a better stability.

In terms of numbers, it was found that the *1P* loads experienced by the NREL 5MW blades equipped with CSs covering 20% of the blade span could be alleviated by up to about 35% employing microtabs and by up to 56% for TEFs.

# 7. Summary of Achievements, Contributions and Critical Appraisal

## 7.1 Summary of Achievements and Contributions

To achieve the aim of this research: "Aeroelastic Analysis of Wind Turbine Smart Blades Utilising Multiple Control Surfaces", a software-tool WTAC capable of simulating the aeroelastic dynamic of wind turbine blades equipped with control surfaces was developed. WTAC was then used to explore the capability of control surfaces in controlling wind turbine blade loads. A detailed achievement and contribution summary resulting from this research is listed below:

**Contributions**

- A dynamic model describing the aerodynamic response of microtab deployment was developed and published. The aerodynamic response of microtab is defined as the combination of two dynamics. First, the fast transient dynamic which corresponds to sharp increase in lift and drag as the microtab deploys. Second, the slow dynamic during which the flow reaches a steady state at a much slower rate.

- An analytical formula was developed in order to quickly estimate the optimal location of control surfaces along wind turbine blade span.

- The author demonstrated that state estimations of actively controlled wind turbine blades can be achieved with a limited number of sensors and robust estimators such as the Kalman filter. Moreover, it was also shown that the overall performance of the control system does not necessarily increase with the number of control surfaces used.

- The author showed that the dominant vibrating mode and the limited control capabilities and interactions between CSs are such that the original MIMO control problem can "effectively" be decoupled into SISO control problems. Well-designed SISO control structures are, therefore, very efficient as reducing wind turbine blade loads.

**Achievements**

- CFD and panel methods have been used to expand the available numerical data of aerofoils equipped with control surfaces. Aerodynamic results obtained with these methods were also benchmarked with data available in the literature.

- A trailing edge flap aerodynamic response model previously published in literature was used. The original equations were, however, modified to improve the model steady state accuracy. A new parameter integrated into the aerodynamic model was proposed in order to control the slope of the lift coefficient. Using an iterative search method, the error between the model and data published or produced by CFD and XFoil were minimised.

- The original steady state wind turbine simulator WTAero was modified for unsteady aerodynamic simulations. The unsteady aerodynamic simulator has the capability to simulate wind turbines operating in wind fields of constant velocity, shear flow and fully turbulent wind fields. A dynamic stall model was implemented to simulate the aerodynamic responses of aerofoils. In this aerodynamic module, blades are dynamically rotating in the wind fields and normal vectors are used to calculate the local wind field velocity. A convergence accelerator algorithm (CAA) was developed in order to enhance the convergence accuracy and speed of the BEMT iteration loop. Using a variable relaxation factor, the CAA was shown to effectively reduce the numbers of iteration required for convergence. The aerodynamic steady state module results were validated with the NREL code WT_Perf for three wind turbine case studies.

- In order to include the structural dynamics of blades, a finite element code modelling wind turbine blades as rotating tapered beams was developed and validated with data reported in the literature. Developing the finite element model was extremely useful for understanding the vibratory dynamics of high aspect-ratio aerodynamic surfaces and in particular of wind turbine blades. A standalone code was also developed in order to calculate the cross-sectional properties of blades to be used by the finite element model.

- WTAC suit is the combination of the unsteady aerodynamic module, the finite element blade structural module, the control surface models, and the control module. WTAC is used in order to simulate the aeroelastic dynamics of wind turbine blades. The unsteady aeroelastic wind turbine simulator results were validated with the NREL code FAST and DU_SWAMP.

- WTAC was then used to investigate:
    - The control system properties of the wind turbine blades equipped with control surfaces
    - The aerodynamic sensing system (i.e. location and numbers of Pitot tubes) required for estimation of the local angle of attack and flow velocity.
    - The structural sensing system (i.e. location and numbers of strain gauges) necessary for classical output and state controllers (i.e. state estimation).
    - The optimal location of control surfaces along the blades span.
    - Controllers and control architectures for the load alleviation of wind turbine blades equipped with control surfaces including:
        - The use of discontinuous actuation mechanism and controllers such as
            - The Bang-Bang Controller
            - The Sliding Mode Controller
        - The use of continuous control actuation mechanism and controllers such as
            - The Proportional Integral Derivative controller
            - The Linear Quadratic Regulator

- The capability of the proposed control structures (PD, BB, SMC and LQR) for load alleviation was evaluated and the following conclusion were made:
    - Results showed that both continuous and discontinuous actuation mechanisms may be used to alleviate wind turbine blade loads. However, the discontinuous actuation mechanism often results in more wear of the actuators.
    - Using the frequency-based approach, it was shown that simple SISO control structures can effectively alleviate wind turbine blade loads. A proportional derivative controller combined with a high-pass filter was shown to be one of the simplest control structures suitable for alleviating wind turbine blade loads employing multiple control surfaces.
    - The BB controller was found to significantly increase the amplitude of the natural frequency loads due to impulse like changes in aerodynamic forces.
    - Both continuous controllers (i.e. PD and LQR) and the SMC have shown very similar load alleviation potential.

- While more advanced controllers have been suggested as a means to increase the load alleviation performance, simple control designs were shown to be very efficient at alleviating wind turbine blade loads.
- Poor design of the closed-loop blade-CSs system was shown to result in the excitation of the blades first natural frequency. For instance, using a *1P* notch filters in the control loop removes the natural frequency load feedback, which in turns permits the control surface to excite natural frequency when alleviating *1P* frequency loads.

- Regarding the NREL 5MW wind turbine blade equipped with control surfaces covering 20% of the blade span, it was found that:
  - The blade flapwise dynamic is dominated by the blade first mode (i.e. first natural frequency and mode shape)
  - The MIMO blade-CSs control problem could be decoupled into multiple SISO control problems.
  - Microtab, as active control surfaces, can be effective in alleviating loads with a wide range of frequencies (1*P* to 1*N*).
  - Trailing edge flaps, as active control surfaces, can be effective in alleviating loads with a wide range of frequencies (1*P* to 1*N*).
  - Discontinuous and continuous actuation methods can both produce load relief from 1*P* to 1*N*.
  - It was shown that using simplified steady state flow models can lead to inaccurate results in the form of both under- and over-predictions
  - The 1*P* load alleviation achieved by the different control structures were found to be similar. This was explained due to the limited control surfaces capability in generating aerodynamic forces.
  - The effectiveness of all types of controllers in alleviating loads reduces with the frequency of load.
  - As expected, the small control space of microtabs lead to lower load alleviation capability in comparison to trailing edge flaps. Microtabs were found to alleviate the 1*P* loads up to about 35% whereas the trailing edge flap alleviated the 1*P* loads up to 56%.

## 7.2 Critical Appraisal and Future Work

**Wind Turbine and Control Surface Aerodynamic Model**

WTAC is a BEMT-based code used to describe the aerodynamics of wind turbines. It has been chosen as a trade-off between computational efficiency and accuracy. Nevertheless, it is known that the unsteady aerodynamic modelling of wind turbine is still an on-going research topic. Unsteady aerodynamic effects occurring on rotating wind turbine blades (e.g. 3D dynamic stall) are still poorly understood. Moreover, there is a substantial lack of experiments involving the dynamic use of control surfaces on wind turbine blades.

**Finite Element Wind Turbine Blade Model**

The finite element model used to represent blades as rotating tapered beams is a linear model. Although the model has shown reasonable accuracy, it is known that non-linear effects are likely to become pre-dominant as wind turbine blades become longer. More advanced, two or three dimensional, models would allow the coupling between the primary vibratory modes as well as between the translational and torsional degrees of freedom.

**Load Alleviation Controllers**

The present investigation did not consider the use of feed-forward controllers. That is, the external forces feeding fatigue loads to the wind turbine blades were assumed unknown. Feed-forward control structures are advantageous to use for slow and/or delayed dynamic systems with large control space such as the individual pitch control system. On the other hand, control surfaces are fast acting devices that have limited capacity in controlling aerodynamic forces. As a consequence, the gain provided by a feed-forward control structure for load alleviation of wind turbine blades using control surfaces was assumed to be negligible.

Actuators of control surfaces implemented on wind turbine blades are required to meet some design constraints in order to be considered as potential solutions for load alleviation. Actuators must have short time responses to counteract high frequency aerodynamic loadings. On the other hand, while subject to high frequency deployment, actuators must maintain their reliability over the long lifespan of wind turbines. Future investigation should include the calculation of actuators wear. However, such calculation requires a good understanding and a model of the mechanism used.

The control investigation carried out during this research is mostly linear. As the structural model fidelity increases, non-linear phenomena are likely to appear in the structural dynamics. The frequency-based analysis proposed in this research can, however, be applied to non-linear systems when combined with gain scheduling control methods.

# 8. References


Abdullah MA, Yatim AHM, Tan CW & Saidur R (2012). A review of maximum power point tracking algorithms for wind energy systems. *Renewable and Sustainable Energy Reviews,* 16**,** 3220-3227.

Abdullah, M. A., Yatim, A. H. M., Tan, C. W. & Saidur, R. (2012). A review of maximum power point tracking algorithms for wind energy systems. *Renewable and Sustainable Energy Reviews,* 16**,** 3220-3227.

Adhikari, S. 2001. *Damping models for structural vibration.* University of Cambridge.

Andersen, P. B. 2005. *Load alleviation on wind turbine blades using variable airfoil geometry (2D and 3D study).* Master, Technical University of Denmark.

Andersen, P. B. (2010a). Advanced load alleviation for wind turbines using adaptive trailing edge flaps: sensoring and control.

Andersen, P. B. (2010b). Advanced Load Alleviation for Wind Turbines using Adaptive Trailing Edge Flaps: Sensoring and Control *Riso DTU.*

Andersen, P. B., Gaunaa, M., Bak, C. & Hansen, M. H. (2009). A dynamic stall model for airfoils with deformable trailing edges. *Wind Energy,* 12**,** 734-751.

Andersen, P. B., Henriksen, L., Gaunaa, M., Bak, C. & Buhl, T. (2010). Deformable trailing edge flaps for modern megawatt wind turbine controllers using strain gauge sensors. *Wind Energy,* 13**,** 193-206.

Andrieu, V. & Praly, L. (2006). On the Existence of a Kazantzis--Kravaris/Luenberger Observer. *SIAM Journal on Control and Optimization,* 45**,** 432-456.

Bæk, P. & Gaunaa, M. (2011). Modeling the Temporal Response of a Microtab in an Aeroelastic Model of a Wind Turbine. *AIAA,* 49.

Bæk, P., Gaunaa, M., Sørensen, N. N. & Fuglsang, P. (2010). Comparative Study of Distributed Active Load Control Concepts for Wind Turbine Blades. *Science of Making Torque from Wind***,** 611-617.

Baker, J. P., Standish, K. J. & van Dam, C. P. (2007). Two-dimensional wind tunnel and computational investigation of a microtab modified airfoil. *Journal of Aircraft,* 44**,** 563-572.

Bang, D., Polinder, H., Ferreira, J. A. & van Rooij, R. P. J. O. M. (2007). New active speed stall control compared to pitch control for a direct-drive wind turbine. *Europe,* 5**,** 11.

Barbarino, S., Pecora, R., Lecce, L., Ameduri, S. & Calvi, E. (2009). A novel SMA-based concept for airfoil structural morphing. *Journal of materials engineering and performance,* 18**,** 696-705.

Barlas, T. K., van der Veen, G. J. & van Kuik, G. A. M. (2012). Model predictive control for wind turbines with distributed active flaps: incorporating inflow signals and actuator constraints. *Wind Energy,* 15**,** 757-771.

Barlas, T. K. & Van Kuik, G. A. M. (2007). State of the art and prospectives of smart rotor control for wind turbines. *Journal of Physics: Conference Series,* 75**,** 012080.

Barlas, T. K. & van Kuik, G. A. M. (2009). Aeroelastic modelling and comparison of advanced active flap control concepts for load reduction on the Upwind 5MW wind turbine. *European Wind Energy Conference, Marseille, France***,** 16-19.

Barlas, T. K. & van Kuik, G. A. M. (2010). Review of state of the art in smart rotor control research for wind turbines. *Progress in Aerospace Sciences,* 46**,** 1-27.

Barlas, T. K., Wingerden, W., Hulskamp, A. W., Kuik, G. A. & Bersee, H. E. (2013). Smart dynamic rotor control using active flaps on a small-scale wind turbine: aeroelastic modeling and comparison with wind tunnel measurements. *Wind energy,* 16**,** 1287-1301.

Bertagnolio, F., Sørensen, N. N., Johansen, J. & Fuglsang, P. (2001). *Wind turbine airfoil catalogue*.

Bettini, P., Airoldi, A., Sala, G., Landro, L. D., Ruzzene, M. & Spadoni, A. (2010). Composite chiral structures for morphing airfoils: Numerical analyses and development of a manufacturing process. *Composites Part B: Engineering,* 41**,** 133-147.

Bossanyi, E. A. (2003). Individual blade pitch control for load reduction. *Wind Energy,* 6**,** 119-128.

Bottasso, C. L., Croce, A., Nam, Y. & Riboldi, C. E. D. (2012). Power curve tracking in the presence of a tip speed constraint. *Renewable Energy,* 40**,** 1-12.

Breton, S. P., Coton, F. N. & Moe, G. (2008). A study on rotational effects and different stall delay models using a prescribed wake vortex scheme and NREL phase VI experiment data. *Wind Energy,* 11**,** 459-482.

Buhl, M. L. (2004). WT_Perf User's Guide. *National Wind Technology Center, National Renewable Energy Laboratory, Golden, CO*.

Buhl ML (2004). WT_Perf User's Guide. *National Wind Technology Center, National Renewable Energy Laboratory, Golden, CO*.

Burton, T., Sharpe, D., Jenkins, N. & Bossanyi, E. (2001). *Wind Energy Handbook,* John Wiley & Sons.

Cansizoglu, O., Harrysson, O., Cormier, D., West, H. & Mahale, T. (2008). Properties of Ti–6Al–4V non-stochastic lattice structures fabricated via electron beam melting. *Materials Science and Engineering: A,* 492**,** 468-474.

Castaignet, D., Barlas, T., Buhl, T., Poulsen, N. K., Wedel Heinen, J. J., Olesen, N. A., Bak, C. & Kim, T. (2013). Frequency-Weighted Model Predictive Control of Trailing Edge Flaps on a Wind Turbine Blade. *IEEE transaction on control system technology,* 21.

Castaignet, D., Barlas, T., Buhl, T., Poulsen, N. K., Wedel Heinen, J. J., Olesen, N. A., Bak, C. & Kim, T. (2014). Full-scale test of trailing edge flaps on a Vestas V27 wind turbine: active load reduction and system identification. *Wind Energy,* 17**,** 549-564.

Castaignet, D., Poulsen, N. K., Buhl, T. & Wedel-Heinen, J. J. (2011). Model Predictive Control of Trailing Edge Flaps on a Wind Turbine blade. *2011 American Control Conference***,** 4398-4403.

Changliang, X. & Zhanfeng, S. (2009). Wind energy in China: Current scenario and future perspectives. *Renewable and Sustainable Energy Reviews,* 13**,** 1966-1974.

Chaviaropoulos, P. K. & Hansen, M. (2000). Investigating three-dimensional and rotational effects on wind turbine blades by means of a quasi-3D Navier-Stokes solver. *Journal of Fluids Engineering,* 122**,** 330-336.

Chow, R. & van Dam, C. P. (2007). Computational Investigations of Deploying Load Control Microtabs on a Wind Turbine Airfoil. *American Institute of Aeronautics and Astronautics*.

Corrigan, J. J. & Schillings, J. J. (1994). Empirical model for stall delay due to rotation. *American Helicopter Society Aeromechanics Specialist Conf*.

Deodatis, G. (1996). Simulation of ergodic multivariate stochastic processes. *Journal of Engineering Mechanics-Asce,* 122**,** 778-787.

Di Paola, M. (1998). Digital simulation of wind field velocity. *Journal of Wind Engineering and Industrial Aerodynamics,* 74-6**,** 91-109.

Diaconu, C. G., Weaver, P. M. & Mattioni, F. (2008). Concepts for morphing airfoil sections using bi-stable laminated composite structures. *Thin-Walled Structures,* 46**,** 689-701.

Drela, M. (1989). XFOIL: An Analysis and Design System for Low Reynolds Number Airfoilsii.

Du, Z. & Selig, M. S. (1998). A 3-D stall-delay model for horizontal axis wind turbine performance prediction. *AIAA Paper,* 21.

Dumitrescu, H. & Cardos, V. (2012). Inboard stall delay due to rotation. *Journal of aircraft,* 49**,** 101-107.

Duraisamy, K., McCroskey, W. J. & Baeder, J. D. (2007). Analysis of wind tunnel wall interference effects on subsonic unsteady airfoil flows. *Journal of Aircraft,* 44**,** 1683-1690.

Eggers, A. J., Digumarthi, R. & Chaney, K. (2003). Wind shear and turbulence effects on rotor fatigue and loads control. *ASME 2003 Wind Energy Symposium***,** 225-234.

National Renewable Energy Laboratory Golden, CO (2006). Wind turbine design cost and scaling model.

Foley, J. T. & Gutowski, T. G. (2008). TurbSim: Reliability-based wind turbine simulator. *IEEE International Symposium on Electronics and the Environment***,** 315-319.

Frederick, M., Kerrigan, E. C. & Graham, J. M. R. (2010). Gust alleviation using rapidly deployed trailing-edge flaps. *Journal of Wind Engineering and Industrial Aerodynamics,* 98.

Risø National Laboratory (2006). Unsteady 2D Potential-flow Forces on a Thin Variable Geometry Airfoil Undergoing Arbitrary Motion.

González, L. G., Figueres, E., Garcerá, G. & Carranza, O. (2010). Maximum-power-point tracking with reduced mechanical stress applied to wind-energy-conversion-systems. *Applied Energy,* 87**,** 2304-2312.
Greenpeace and the Global Wind Energy Council (2010). Global Wind Energy Outlook 2010.

Greenpeace and the Global Wind Energy Council (2012). Global Wind Energy Outlook 2012.

Gunda, J. B., Singh, A. P., Chhabra, P. S. & Ganguli, R. (2007). Free vibration analysis of rotating tapered blades using Fourier-$ p $ superelement. *Structural Engineering and Mechanics,* 27**,** 243-257.
National Renewable Energy Laboratory (2006). User's guide to PreComp (pre-processor for computing composite blade properties).

National Renewable Energy Laboratory, Golden, CO (US) (1999). Variable-speed wind turbine controller systematic design methodology: a comparison of non-linear and linear model-based designs.

Hansen, C. (2012). NWTC design codes (AirfoilPrep).
Hau, E. & von Renouard, H. (2013). *Wind turbines: fundamentals, technologies, application, economics*, Springer.
Hong, M.-K. & Lee, H.-H. (2010). Adaptive maximum power point tracking algorithm for variable speed wind power systems. *Life System Modeling and Intelligent Computing.* Springer.
Hui, J. & Bakhshai, A. (2008). A new adaptive control algorithm for maximum power point tracking for wind energy conversion systems. *Power Electronics Specialists Conference, 2008. PESC 2008. IEEE***,** 4003-4007.
International Renewable Energy Agency (IRENA) (2012). Renewable Energy Cost Analysis - Wind Power.

Johnson, S. J., Baker, J. P., van Dam, C. P. & Berg, D. (2010). An overview of active load control techniques for wind turbines with an emphasis on microtabs. *Wind Energy,* 13**,** 239-253.
National Renewable Energy Laboratory Colorado (2009). Definition of a 5-MW reference wind turbine for offshore system development.

Jonkman, J. M. & Buhl, M. (2005). FAST user's guide. *Golden, CO: National Renewable Energy Laboratory*.
National Renewable Energy Laboratory Colorado (2009). Definition of a 5-MW reference wind turbine for offshore system development.

Kaminsky, G. & Schmukler, S. L. (2002). Emerging market instability: do sovereign ratings affect country risk and stock returns? *The World Bank Economic Review,* 16**,** 171-195.
Kooijman, H. J. T., Lindenburg, C., Winkelaar, D. & van der Hooft, E. L. (2003). DOWEC 6 MW pre-design. *Energy Research Center of the Netherlands (ECN).*
Koomey, J. (2011). Growth in data center electricity use 2005 to 2010. *A report by Analytical Press, completed at the request of The New York Times*.
Lachenal, X., Daynes, S. & Weaver, P. M. (2013). Review of morphing concepts and materials for wind turbine blade applications. *Wind Energy,* 16**,** 283-307.
Lafountain, C., Cohen, K. & Abdallah, S. (2012). Use of XFOIL in design of camber-controlled morphing UAVs. *Computer Applications in Engineering Education,* 20**,** 673-680.
Laino, D. J. (2005). NWTC Design Codes (AeroDyn). *NWTC. July,* 5.
Laks, J. H., Pao, L. & Wright, A. D. (2009). Control of wind turbines: Past, present, and future. *American Control Conference, 2009***,** 2096-2103.
Lantz, E., Wiser, R. & Hand, M. (2012). The past and future cost of wind energy. *IEA Wind Task,* 26.
Lanzafame, R. & Messina, M. (2007). Fluid dynamics wind turbine design: Critical analysis, optimization and application of BEM theory. *Renewable Energy,* 32**,** 2291-2305.

Larsen, J. W., Nielsen, S. R. K. & Krenk, S. (2007). Dynamic stall model for wind turbine airfoils. *Journal of Fluids and Structures,* 23**,** 959-982.
Larsen, T. J., Madsen, H. A. & Thomsen, K. (2005). Active load reduction using individual pitch, based on local blade flow measurements. *Wind Energy,* 8**,** 67-80.
Leishman, J. G. (1994). Unsteady lift of a flapped airfoil by indicial concepts. *Journal of Aircraft,* 31**,** 288-297.
Leishman, J. G. (2002). Challenges in modelling the unsteady aerodynamics of wind turbines. *Wind Energy,* 5**,** 85-132.
Leishman, J. G. & Beddoes, T. S. (1989). A Semi-Empirical Model for Dynamic Stall. *Journal of the American Helicopter Society,* 34**,** 3-17.
Liebeck, R. H. (1978). Design of subsonic airfoils for high lift. *Journal of Aircraft,* 15**,** 547-561.
Lindenburg, C. (2004). Modelling of rotational augmentation based on engineering considerations and measurements. *European Wind Energy Conference, London***,** 22-25.
Liserre, M., Sauter, T. & Hung, J. Y. (2010). Future energy systems: Integrating renewable energy sources into the smart power grid through industrial electronics. *Industrial Electronics Magazine, IEEE,* 4**,** 18-37.
Loewy, R. G. (2012). A two-dimensional approximation to the unsteady aerodynamics of rotary wings. *Journal of the Aeronautical Sciences (Institute of the Aeronautical Sciences),* 24.
Maheri, A., Noroozi, S., Toomer, C. & Vinney, J. (2006a). Damping the fluctuating behaviour and improving the convergence rate of the axial induction factor in the BEMT-based rotor aerodynamic codes. *European Wind Energy Conference & Exhibition, Athens, Greece,* 27**,** 1-4.
Maheri, A., Noroozi, S., Toomer, C. A. & Vinney, J. (2006b). WTAB, a computer program for predicting the performance of horizontal axis wind turbines with adaptive blades. *Renewable Energy,* 31**,** 1673-1685.
Maki, K., Sbragio, R. & Vlahopoulos, N. (2012). System design of a wind turbine using a multi-level optimization approach. *Renewable Energy,* 43**,** 101-110.
Malcolm, D. J. & Hansen, A. C. (2002). *WindPACT Turbine Rotor Design Study: June 2000--June 2002,* National Renewable Energy Laboratory.
Maniaci, D. C. (2011). An Investigation of WT_Perf Convergence Issues. *AIAA Aerospace Sciences Meeting***,** 2011-150.
Mayda, E. A., van Dam, C. P. & Yen-Nakafuji, D. (2005). Computational investigation of finite width microtabs for aerodynamic load control. *AIAA Paper,* 1185**,** 2005.
DTIC Document (1987). A critical assessment of wind tunnel results for the NACA 0012 airfoil.

Merz, K. O. (2011). Conceptual design of a stall-regulated rotor for a deepwater offshore wind turbine.
National Renewable Energy Lab., Golden, CO (United States) (1995). Wind turbine trailing edge aerodynamic brakes.

Mohd Jani, J., Leary, M., Subic, A. & Gibson, M. A. (2014). A review of shape memory alloy research, applications and opportunities. *Materials & Design,* 56**,** 1078-1113.
Moriarty PJ & Hansen AC (2005). *AeroDyn theory manual,* National Renewable Energy Laboratory Golden, Colorado, USA.
Moriarty, P. J. & Hansen, A. C. (2005). *AeroDyn theory manual,* National Renewable Energy Laboratory Golden, Colorado, USA.
Muljadi, E. & Butterfield, C. P. (2001). Pitch-controlled variable-speed wind turbine generation. *IEEE Transactions on Industry Applications,* 37**,** 240-246.
Nakafuji, D. T. Y., van Dam, C. P., Bräeuchle, F., Smith, R. L. & Collins, S. D. (2000). Active load control and lift enhancement using MEM translational tabs. *AIAA Paper,* 2422**,** 2000.
Nakafuji, D. T. Y., van Dam, C. P., Smith, R. L. & Collins, S. D. (2001). Active load control for airfoils using microtabs. *Journal of solar energy engineering,* 123**,** 282-289.
Nakamura, T., Morimoto, S., Sanada, M. & Takeda, Y. (2002). Optimum control of IPMSG for wind generation system. *Power Conversion Conference, 2002. PCC-Osaka 2002. Proceedings of the,* 3**,** 1435-1440.

Nema, P., Nema, R. K. & Rangnekar, S. (2009). A current and future state of art development of hybrid energy system using wind and PV-solar: A review. *Renewable and Sustainable Energy Reviews,* 13**,** 2096-2103.

Panesar, A. S. & Weaver, P. M. (2012). Optimisation of blended bistable laminates for a morphing flap. *Composite Structures,* 94**,** 3092-3105.

Pierce, K. G. & Migliore, P. G. (2000). *Maximizing energy capture of fixed-pitch variable-speed wind turbines*, National Renewable Energy Laboratory.

Poore, R. Z. (2000). *NWTC AWT-26 Research and Retrofit Project: Summary of AWT-26/27 Turbine Research and Development*, National Renewable Energy Laboratory.

Raza Kazmi, S. M., Goto, H., Guo, H.-J. & Ichinokura, O. (2010). Review and critical analysis of the research papers published till date on maximum power point tracking in wind energy conversion system. *Energy Conversion Congress and Exposition (ECCE), 2010 IEEE,* 4075-4082.

Resor, B., Wilson, D., Berg, D., Berg, J., Barlas, T. K., van Wingerden, J. W. & van Kuik, G. A. M. (2010). Impact of higher fidelity models on simulation of active aerodynamic load control for fatigue damage reduction. *Proceedings of the 48th AIAA/ASME*.

Rice, J. K. & Verhaegen, M. (2010). Robust and distributed control of a smart blade. *Wind energy,* 13**,** 103-116.

Şahin, A. D. (2004). Progress and recent trends in wind energy. *Progress in Energy and Combustion Science,* 30**,** 501-543.

Salzmann, D. & Van der Tempel, J. (2005). Aerodynamic damping in the design of support structures for offshore wind turbines. *Paper of the Copenhagen Offshore Conference*.

Schubel, P. J. & Crossley, R. J. (2012). Wind turbine blade design. *Energies,* 5**,** 3425-3449.

Sieros, G., Chaviaropoulos, P., Sørensen, J. D., Bulder, B. H. & Jamieson, P. (2012). Upscaling wind turbines: theoretical and practical aspects and their impact on the cost of energy. *Wind energy,* 15**,** 3-17.

Simms, D. A., Schreck, S., Hand, M. & Fingersh, L. J. (2001). *NREL unsteady aerodynamics experiment in the NASA-Ames wind tunnel: a comparison of predictions to measurements,* National Renewable Energy Laboratory Colorado, USA.

Snel, H., Houwink, R. & Bosschers, J. (1994). *Sectional prediction of lift coefficients on rotating wind turbine blades in stall,* Netherlands Energy Research Foundation.

Stanewsky, E. (2001). Adaptive wing and flow control technology. *Progress in Aerospace Sciences,* 37**,** 583-667.

National Renewable Energy Laboratory, Golden, CO (United States) (1996). Considerations for an integrated wind turbine controls capability at the National Wind Technology Center: an aileron control case study for power regulation and load mitigation.

Tan, K. & Islam, S. (2004). Optimum control strategies in energy conversion of PMSG wind turbine system without mechanical sensors. *Energy Conversion, IEEE Transactions on,* 19**,** 392-399.

Tangler, J. & Kocurek, J. D. (2005). Wind turbine post-stall airfoil performance characteristics guidelines for blade-element momentum methods. *43rd AIAA Aerospace Sciences Meeting and Exhibit,* 10-13.

Tangler, J. L. (2002). The nebulous art of using wind-tunnel airfoil data for predicting rotor performance. *ASME 2002 Wind Energy Symposium,* 190-196.

Theodorsen, T. (1935). General theory of aerodynamic instability and the mechanism of flutter.

Thiel, M., Lesieutre, G. A., Maughmer, M. D. & Koopmann, G. H. 2006. *Actuation of an active Gurney flap for rotorcraft applications.* Pennsylvania State University.

Thill, C., Etches, J. A., Bond, I. P., Potter, K. D. & Weaver, P. M. (2010). Composite corrugated structures for morphing wing skin applications. *Smart Materials and Structures,* 19**,** 124009.

Thirstrup, P. J., Aagaard, M., Björck, A., Enevoldsen, P., Øye, S., Ganander, H. & Winkelaar, D. (1998). *Prediction of dynamic loads and induced vibrations in stall*.

Timmer, W. A. (2009). An overview of NACA 6-digit airfoil series characteristics with reference to airfoils for large wind turbine blades. *AIAA Paper,* 268**,** 2009.

Turner, J. A. (1999). A realizable renewable energy future. *Science,* 285**,** 687-689.

Van Dam, C. P., Nakafuji, D. Y., Bauer, C., Chao, D. & Standish, K. (2002). Computational Design and Analysis of a Microtab Based Aerodynamic Loads Control System for Lifting Surfaces. *SPIE International Society for Optical Engineers*.

Van Dam, C. P., Yen, D. T. & Vijgen, P. M. (1999). Gurney flap experiments on airfoil and wings. *Journal of aircraft,* 36**,** 484-486.

van der Hoven, I. (1957). Power spectrum of horizontal wind speed in the frequency range from 0.0007 to 900 cycles per hour. *Journal of Meteorology,* 14**,** 160-164.

van Engelen, T. G. (2006). Design model and load reduction assessment for multi-rotational mode individual pitch control (higher harmonics control). *Wind Energy Conference*.

van Wingerden, J. W., Hulskamp, A., Barlas, T., Houtzager, I., Bersee, H., van Kuik, G. & Verhaegen, M. (2011). Two-degree-of-freedom active vibration control of a prototyped "smart" rotor. *Control Systems Technology, IEEE Transactions on,* 19**,** 284-296.

Veers, P. S., Ashwill, T. D., Sutherland, H. J., Laird, D. L., Lobitz, D. W., Griffin, D. A., Mandell, J. F., Musial, W. D., Jackson, K. & Zuteck, M. (2003). Trends in the design, manufacture and evaluation of wind turbine blades. *Wind energy,* 6**,** 245-259.

National Aeronautics and Space Administration, Cleveland, OH (USA). Lewis Research Center (1982). Theoretical and experimental power from large horizontal-axis wind turbines.

Wang, G. & Wereley, N. M. (2004). Free vibration analysis of rotating blades with uniform tapers. *AIAA journal,* 42**,** 2429-2437.

Wang, J. J., Li, Y. C. & Choi, K.-S. (2008). Gurney flap—Lift enhancement, mechanisms and applications. *Progress in Aerospace Sciences,* 44**,** 22-47.

Weisshaar, T. A. (2013). Morphing aircraft systems: Historical perspectives and future challenges. *Journal of aircraft,* 50**,** 337-353.

Wilson, D. G., Berg, D. E., Barone, M. F., Berg, J. C., Resor, B. R. & Lobitz, D. W. (2009). Active aerodynamic blade control design for load reduction on large wind turbines. *European Wind Energy Conference, Marseille, France***,** 26-19.

Wilson, D. G., Berg, D. E., Lobitz, D. W. & Zayas, J. R. (2008). Optimized Active Aerodynamic Blade Control for Load Alleviation on Large Wind Turbines. *AWEA WINDPOWER.*

Wilson, D. G., Resor, B. R., Berg, D. E., Barlas, T. K. & van Kuik, G. A. M. (2010). Active Aerodynamic Blade Distributed Flap Control Design Procedure for Load Reduction on the UpWind 5MW Wind Turbine. *Proceedings of the 48th AIAA Aerospace Sciences Meeting***,** 4-7.

Yang, X., Sotiropoulos, F., Conzemius, R. J., Wachtler, J. N. & Strong, M. B. (2014). Large-eddy simulation of turbulent flow past wind turbines/farms: the Virtual Wind Simulator (VWiS). *Wind energy*.

Yen, D. T., van Dam, C. P., Bräeuchle, F., Smith, R. L. & Collins, S. D. (2000). Active load control and lift enhancement using MEM translational tabs. *AIAA Paper,* 2422**,** 2000.

Zayas, J. R., van Dam, C. P., Chow, R., Baker, J. P. & Mayda, E. A. (2006). Active aerodynamic load control for wind turbine blades. *European Wind Energy Conference*.

Zhang, J., Cheng, M., Chen, Z. & Fu, X. (2008). Pitch angle control for variable speed wind turbines. *Electric Utility Deregulation and Restructuring and Power Technologies, 2008. DRPT 2008. Third International Conference on***,** 2691-2696.

# Appendix A - List of Publications

**Journal Articles-Published**

J1. Macquart T, Maheri A, Busawon K, **"Microtab Dynamic Modelling for Wind Turbine Blade Load Rejection",** *Renewable Energy 64 (2014): 144-152* **(Elsevier, Q1, IF 3.361)**

J2. Macquart T, Maheri A, "**Integrated aeroelastic and control analysis of wind turbine blades equipped with microtabs**", *Renewable Energy 75* (2015): 102-114. **(Elsevier, Q1, IF 3.361)**

**Journal Articles - Under Review**

J3. Macquart T, Maheri A, "**A Stall-Regulated Wind Turbine Design to Reduce Fatigue**", Wind Energy **(Wiley, Q1, IF 2.556)**

**Journal Articles - Submitted**

J4. Macquart T, Maheri A, Busawon K, "**Damping the Vibrations of Aerodynamic Surfaces Employing Flow Controllers : A Loop-Shaping Approach**", Journal of Sound and Vibrations **(Wiley, Q1, IF 1.857)**

**Journal Articles - Under Preparation**

J5. Macquart T, Maheri A, Busawon K, **"Which Controller for the Load Alleviation of Wind Turbine Blades Employing Control Surfaces? "**

J6. Macquart T, Maheri A, "**A Pitch-Less 5MW Wind Turbine Design using Active Flow Controllers**"

J7. Macquart T, Maheri A, "**Morphing Aerofoils for Wind Turbine Blades : Proof of Concept**"

**Book Sections - Published**

*B1.* Macquart T, Maheri A, Busawon K, **"Improvement of the Accuracy of the Blade Element Momentum Theory Method in Wind Turbine Aerodynamics Analysis"**, Environment Friendly Energies and Applications (EFEA), 2012 IEEE

**Conference Papers - Published**

C1. Maheri A, Macquart T, Safari D, Maheri M, **"Phenotype Building Blocks and Geometric Crossover in Structural Optimisation"**, "The Eighth International Conference on Engineering Computational Technology (ECT), 2012 Croatia

**Conference Papers - Accepted**

C2. Macquart T, Maheri A, "**A Simple Method to Determine the Optimal Location of Active Flow Controllers on Wind Turbine Blades**", Environment Friendly Energies and Applications (EFEA), 2014

C3. Stylianidis N, Macquart T, Maheri A, **"Aerodynamic Design of Wind Turbine Blades Considering Manufacturing Constraints"**, Environment Friendly Energies and Applications (EFEA), 2014

C4. Somoza M.H, Macquart T, Maheri A, "**Reduction of Tidal Turbines Hydrodynamic Loads Employing Bend-Twist Adaptive Blades**", Environment Friendly Energies and Applications (EFEA), 2014